# Broadband, Ultra-sparse Array Processing for Low Complexity Multibeam Sonar Imaging

**Raghav Menon**

A Thesis submitted for the degree of

Doctor of Philosophy

in the School of Electrical, Electronic and Computer

Engineering

2010

# Abstract

Imaging sonar systems have become increasingly popular in numerous applications associated with underwater imaging. Though multibeam sonar systems have been used in a variety of applications, the cost of these systems limits their use. The reason for the high costs has been identified to the use of large number of hydrophone array elements and hence large number of associated analogue channels and analogue-to-digital converters (ADC) that are required in high resolution imaging.

In this thesis, an imaging sonar system has been developed with as few as four array elements to minimise cost. The inter-element spacing between any two array elements was chosen to be much greater than half the wavelength. In order to avoid phase ambiguity associated with wide array element spacing, the time difference of arrival is determined. Hence, for this purpose a wideband chirp signal was used. The return signals were divided into range cells to determine the target range. The time difference of arrival was obtained by correlating the range cells. Using the time difference of arrival, the direction of arrival (DOA) angle was calculated. The image of the target being illuminated was formed using the calculated range and the DOA values. The image pixel intensity at any pixel position was determined from the correlation result between the range cells. A simulation model was built to test the theory developed. Simulations were performed for various inter-element spacing and for four different target profiles types. Two objective metrics (signal to noise (SNR) ratio and peak signal to noise (PSNR) ratio) and a subjective metric (Structural Similarity (SSIM) index) were used to determine the performance of the algorithm and image quality.

Image formed from the simulations using two hydrophone elements showed the presence of artefacts in the form of correlation sidelobes. The SNR metric showed a low gain of -5dB on comparison against a test image. PSNR and SSIM ratio showed a constant image quality over all the array spacing. The number of array elements was increased and linear operation like averaging was applied. The results showed no improvement in the gain and image quality.

To overcome the problem of correlation sidelobes, a non-linear combining process has been proposed. Using the non-linear combining process it was found that the SNR showed an average gain of 10 dB on simulated data over the images formed without it. The PSNR and SSIM also showed a small increase in the image quality. The computational complexity of the proposed non-linear combining process was calculated by determining the number of multiplications and additions. The time taken to perform these operations on a SHARC ADSP 21261 chip was calculated theoretically. The calculations showed the feasibility of using this algorithm on a digital signal processing (DSP) hardware.

An experimental prototype was built and performance was tested during sea trials. The data obtained was processed using a computer. The experimental results verified that the processing algorithm was effective in a practical system.

# Contents

# List of Figures

## Chapter 1

## Chapter 2

## Chapter 3

## Chapter 4

## Chapter 5

## Chapter 6

## Chapter 7

# List of Tables

## Chapter 1

## Chapter 3

## Chapter 5

## Chapter 6

## Chapter 7

## Chapter 8

# List of Abbreviations

| | | |
|---|---|---|
| Sonar | - | **SO**und **Na**vigation and **R**anging |
| ADC | - | **A**nalogue to **D**igital **C**onverter |
| Lidar | - | **Li**ght **D**etection **A**nd **R**anging |
| DOA | - | **D**irection **O**f Arrival |
| dB | - | **D**eci**b**els |
| TVG | - | **T**ime **V**arying **G**ain |
| CW | - | **C**ontinuous **W**ave |
| LFM | - | **L**inear **F**requency **M**odulation |
| NLFM | - | **N**on-**L**inear **F**requency **M**odulation |
| LPM | - | **L**inear **P**eriod **M**odulation |
| SAS | - | **S**ynthetic **A**perture **S**onar |
| MVDR | - | **M**inimum **V**ariance **D**istortionless **R**esponse |
| MUSIC | - | **MU**ltiple **S**ignal **C**lassification |
| ESPRIT | - | **E**stimation of **S**ignal **P**arameters via **R**otational **I**nvariance **T**echnique |
| Matlab | - | **MAT**rix **LAB**oratory |
| FR | - | **F**ull **R**eference |
| RR | - | **R**educed **R**eference |
| NR | - | **N**o **R**eference |
| SNR | - | **S**ignal to **N**oise **R**atio |
| PSNR | - | **P**eak **S**ignal to **N**oise **R**atio |
| SSIM | - | **S**tructural **SIM**ilarity |
| HVS | - | **H**uman **V**isual **S**ystem |
| FIR | - | **F**inite **I**mpulse **R**esponse |

| | | |
|---|---|---|
| FFT | - | **F**ast **F**ourier **T**ransform |
| op-amp | - | **OP**erational **AMP**lifier |
| USB | - | **U**niversal **S**erial **B**us |

# List of Publications

[1] Neasham J A, Menon R and Hinton O R, Broadband Ultra-Sparse Array Processing for Low Complexity Multibeam Sonar Imaging, Oceans 2007 – Europe, 18-21 June 2007, pp.1-6.

# Acknowledgements

I would like to thank Mr. Jeffrey Neasham and Prof. Oliver Hinton for their guidance, encouragement and support during the four and half years of association.

I also would like to thank my colleagues in Communications and Signal Processing group of Newcastle University who have helped me through this research by constant encouragement. I would like to express my gratitude to the Universities UK institution, Newcastle University and the School of Electrical Electronic and Computer Science Engineering for funding this research through ORS scheme, IRS scheme and School Scholarship. I would like to express my thanks to Tritech International.

I am very grateful to my parents Mr. T K Narayana Menon and Mrs. Rathi Devi Menon for their love, encouragement and without whom I would not have had this opportunity. I would like to thank my wife Mrs. Dipthi Raghav who has always been on my side encouraging and supporting me in the most difficult times. I would like to thank my sister Mrs. Remya Rajesh for her constant support. I would like to thank all my other friends and flatmates who made my four year stay in Newcastle a memorable one.

# List of Symbols

| | |
|---|---|
| $c$ | Speed of sound (m/s) |
| $f$ | Frequency of sound (Hz) |
| $\lambda$ | Wavelength (m) |
| $Z_1, Z_2$ | Specific acoustic impedance of the medium |
| $\rho_1, \rho_2$ | Densities of medium |
| $rc$ | Reflection coefficient |
| $r$ | Range (m) |
| $s(t), g(t)$ | Signals |
| $P_{Loss}$ | Total loss in dB |
| $I$ | Sound Intensity |
| $I_{ref}$ | Reference intensity; $0.67 \times 10^{-18}$ Wm$^{-2}$ |
| $S_L$ | Spreading loss dB |
| $A_T$ | Attenuation dB |
| $P$ | Source power (watts) |
| $A$ | Attenuation coefficient dB/km |
| $SL$ | Source level dB |
| $TS$ | Target strength dB |
| $TL$ | Transmission loss dB |
| $RL$ | Received level dB |
| $NL$ | Noise level dB |
| $NSL$ | Noise spectral level db/Hz |
| $B$ | Signal bandwidth Hz |
| $\Delta r$ | Range resolution m |
| $\Delta \theta$ | Angular resolution |
| $\tau$ | Pulse length |
| $\Omega$ | Signal amplitude |
| $\gamma$ | Chirp rate |
| $\chi(t,f)$ | Ambiguity function |
| $\delta(t)$ | Impulse function |
| $S(\omega)$ | Fourier transform of $s(t)$ |
| $H(\omega)$ | Fourier transform of $h(t)$ |
| $h(t)$ | Matched filter impulse response |
| $\upsilon(t)$ | Noise signal |
| $\mathbf{x}(n) = [x_1(n) \dots x_n(n)]$ | Input to the array |
| $y(n)$ | Array output |
| $a(\theta)$ | Steering vector or array manifold vector |
| $A(\theta)$ | $[a(\theta_1) \dots \dots a(\theta_m)]$ |
| $w$ | Weight vector |
| $\hat{\boldsymbol{R}}$ | Data covariance matrix |
| $\boldsymbol{V}$ | Eigen vector matrix |
| $\boldsymbol{Q}$ | Eigen value matrix |
| $d$ | Array element separation (m) |
| $x_{MF}(t)$ | Output from matched filter |
| $x_{TVG}(t)$ | Output from time varying gain amplifier |
| $G(t)$ | TVG amplifier Gain |
| $\delta x$ | Difference in distance travelled (m) |
| $\delta t$ | Difference in time due to $\delta x$ (sec) |

| | |
|---|---|
| $n_d$ | Number of samples due to $\delta x$ |
| $R_{ss}$ | Signal correlation |
| $h_{LP}$ | Impulse response of lowpass filter |
| $x_r$ | Range cell size (m) |
| $N_I$ | Number of range cells |
| $N_A$ | Number of angular cells |
| $p$ | Percentage overlap between the range cells |
| $n_{RC}$ | Number of samples corresponding to a range cell |
| $n_{d\_max}$ | Maximum number of samples on one side of range cell |
| $K$ | Number of hydrophone elements |
| $\theta_b$ | Half-beam angle |
| $\boldsymbol{r\theta}$ | Matrix obtained by correlating the range cells |
| $N_{IMG}$ | Number of images that can be formed |
| $B$ | Threshold |
| $\boldsymbol{W}$ | Matrix containing true or false values |
| $\cap$ | And operator |
| $\varDelta n_d$ | Difference between the number of samples arriving at the hydrophones from two targets |
| $F$ | Sampling frequency Hz |
| $T$ | Sampling interval (sec) |
| $N_{samp}$ | Factor relating sampling frequency and bandwidth |
| $r_{c1}$ | Radius of cluster |
| $r_{c2}$ | Maximum radius of point targets in the cluster |
| $V_{rms}$ | RMS value of voltage |
| $V_A$ | Peak value of voltage |
| $SNR$ | Signal-to-noise ratio |
| $PSNR$ | Peak signal to noise ratio |
| $SSIM$ | Structural similarity |
| $\mu$ | Mean |
| $\sigma$ | Standard deviation |
| $MSE$ | Mean square error |
| $l$ | Luminance measure |
| $Ct$ | Contrast measure |
| $st$ | Structural measure |
| $D_y$ | Dynamic range of image |
| $C_{\boldsymbol{r\theta}}$ | Complexity in the formation of $\boldsymbol{r\theta}$ matrix |
| $C_{IM}$ | Complexity of image formation process |
| $C_S$ | Complexity of signal processing procecss |
| $FB$ | Fractional bandwidth |

# Chapter 1
# Introduction

## 1.1    Overview

Multibeam sonar is one of the popular types of imaging sonar system which is widely used in applications where the scanning rate of mechanically scanned systems is considered too slow. Some of the examples where these systems are of utmost importance are profiling/bathymetry, seabed characterization and obstacle avoidance systems. These high resolution systems achieve better performance due to large number of receiver channels of the order of 100 to 200 with each channel having their own set of transducers, amplifiers, analogue-to-digital converters (ADC) etc. The construction of large number of analogue receiver channels is costly. Apart from the large number of analogue channels, the contemporary multibeam imaging sonar system requires dedicated hardware for data storage. This further adds to the cost of the system. With the application of imaging sonars being widespread in the areas of fishery, marine archeology etc it has thus been impossible to procure these high resolution systems.

State-of-art signal processing chips are available at lower cost. The possibility of reducing the number of channels by giving more importance to processing is yet to be investigated. Thus the distinct advantage of using these low cost and powerful signal processing chips to its maximum capacity remains unexploited.

The prime motivation and contribution of this research has been to build a cost-effective imaging sonar system. The research has paved the way in building an imaging sonar system which is ultra-sparse which uses true time delay, stereoscopic and spatial-diversity techniques for forming the image of the target scene. The reduction in the number of channels is achieved through use of the novel algorithm developed. This reduction in the number of channels comes at the cost of increased computational complexity which allows the use of the modern signal processing chips to its maximum processing capacity. The low cost system built can be used for applications like profiling and for those applications where high resolution of multibeam system is not required.

## 1.2    Problem description

Underwater imaging is an important technology for offshore oil/gas, scientific and military operations worldwide. Underwater imaging provides recognizable images of objects which are under water thereby providing a means to explore the marine environment, the knowledge of which is limited. In marine applications, the use of underwater imaging is growing because of significant untapped resources which are under the sea. Underwater imaging is used by the navy for the detection, identification and classification of approaching targets, mine detection, collision avoidance and navigation.

For underwater imaging, non-acoustic methods like photography have been used and tested. To improve the optical visibility and imaging range, laser based imaging techniques like Light Detection and Ranging (LIDAR) are being researched [1 2 3 4]. But due to the high frequency of the optical signals, they experience severe attenuation in water [1]. These along with the scattering and the absorptive nature of the sea water degrade the visibility of optical imaging instruments [4]. Optical imaging methods can work well when the medium of transmission (water) is clear and hence turbidity is another issue which causes degradation of the optical images [5]. In [5] a comparison of the performance of an airborne LIDAR and multibeam sonar was performed. It was concluded in [5] that LIDAR was unable to fully identify high relief features and differentiate between fine and coarse sediments. Thus these non-acoustic imaging techniques are still in the development stage and are only expected to make an impact in the future [1, 5].

SONAR remains the dominant technology for underwater imaging. SONAR is the acronym for SOund NAvigation and Ranging. There has been a lot of interest in the use of sound as a source for underwater imaging. This is because sonar has the advantage of long range visibility in water and hence is able to provide details of the objects that cannot be obtained using non-acoustic methods. A comparison of operational performance between acoustic and the non-acoustic methods of imaging is presented by Sutton in [6]. Sutton [6] in 1979 has shown that of the

methods available for underwater imaging, imaging using sonar provides the best results.

Initially when developed, sonar had been considered as an instrument to indicate the position of the target. A number of researches have been performed on acoustic imaging techniques and improvements have been made over the past few decades in the areas of beamforming, data collection and fusion methods and imaging algorithms. With the improvements in the technology along with the advancement of signal processing techniques for the underwater imaging, it is now possible for the modern sonar systems to produce high resolution images of the seafloor, sunken objects etc. These developments in the sonar system technology have thus enabled to view the marine environment with improved clarity. Thus with the substantial progress in the field of acoustic imaging, sonar has matured from being a position indicator to being the most reliable system for underwater imaging.

All researches performed on sonar systems have aimed at improving the imaging resolution of the system with less importance given to form a reasonable image by decreasing the number of channels. These improvements come at the cost of using a large number of projectors and hydrophones. In the multibeam system, beamforming algorithms are used to form narrow beams which are transmitted in desired directions and the returns are obtained from each specific direction. These returns are in turn processed to form an image. These highly directional beams are generated using large number of projectors and hydrophones. Some multibeam sonar systems are equipped with global positioning facility in order to determine the path of the sonar system and hence further improve the quality of the final image formed. A few examples of modern high resolution multibeam imaging sonar systems are given in table 1.1 below. This table has been formed by collecting the technical specifications of the common multibeam systems that have been used in number of researches.

Table 1.1 shows that the multibeam systems have a small effective beamwidth as a result of beamforming but the number of transmitter and receiver channels is large. Building of these analog channels is very costly. Another matter of concern

is the storage of the data obtained from these channels which further increases the cost of the system.

| Multibeam Sonar System | Operating Frequency | Range | Beamwidth | Number of Channels |
|---|---|---|---|---|
| *Simrad SM2000 [7 8]* | *200 kHz* | *1000m* | *0.87°* | *TX Channels ~ 80* <br> *RX Channels ~ 80* |
| *Reson Seabat 8101 system [8]* | *240 kHz* | *300m* | *1.5°* | *TX Channels ~ 36* <br> *RX Channels ~ 176* |

**Table 1.1 Multibeam sonars and specifications**

It is thus attractive to aim for a system having qualities comparable to that of a high resolution multibeam system but at a lower cost. In order to build a cost effective system it is necessary to reduce the number of analogue channels in the high resolution systems. Thus it is required to design a system which is ultra-sparse and whose processing algorithm is efficient enough to obtain an acceptable image. The modern beamforming algorithms are capable of producing highly directional beams only in the presence of large number of array elements. Using fewer array elements decreases the directivity thereby increasing the beamwidth which in turn would decrease the angular accuracy.

The mainlobe width also depends on the length of the array. Increasing the spacing between the array elements increases the total array length but gives rise to grating lobes. Grating lobes occur when the phase shift between the adjacent elements is greater than -/+$\pi$ or when the elemental spacing is greater than $\lambda/2$ [9]. The presence of grating lobes introduces ambiguity in the determination of DOA. Thus it is usual to keep the elemental spacing $d < \lambda/2$ [9]. In sparse arrays, the array elements are widely spaced. High resolution beamforming algorithms make use of the phase difference between the signals arriving at the hydrophone elements in order to determine their DOA. Hence, the existing algorithms would

hardly be of any use if the aim is to decrease the number of array elements to a sparse number.

### 1.2.1   Focus into the problem – Literature Survey

As discussed in the previous section, the cost of the imaging sonar system can be reduced by decreasing the number of hydrophone elements and hence the number of analogue channels available. Sparse arrays have been receiving a lot of attention lately due to the advantage it provides from the economic point of view.

Investigation on the concept of array thinning or sparse arrays have been carried on for years [10 11 12 13]. Array thinning has been achieved by using a normal array with large number of elements and turning *off* certain elements and keeping the rest of the elements *on*. The elements to be switched *on* or *off* are selected based on conditions like low sidelobe level, minimizing grating lobes etc. Ant colony optimization algorithm is used in [10, 11] in order to switch the elements *on* or *off*.  In [12] evolutionary algorithms are applied in order to achieve the same. In [13] an adaptive method using linearly constrained minimum power method has been suggested for array thinning. All the methods described contain large number of elements but by switching *on* and *off* certain number of elements the processing load is reduced. Thus these array thinning procedures reduce the requirement of large processing power but do not reduce the number of channels in the array. Hence the cost of the array remains high.

The sparse array have their array elements spaced wide apart to obtain a longer array but with small number of antenna elements. The angular resolution would be better for a longer array as angular resolution is inversely proportional to the array length. But when the array length and hence the number of array elements increases so does the cost. Decreasing the number of elements in order to form a sparse array would result in the formation of grating lobes. The problem of eliminating the grating lobes has been studied for decades. Array shading has been effectively used in decreasing the sidelobes but since the grating lobes occur at multiples of the mainlobe angles, shading is not useful in keeping the grating lobes down [14]. In many research publications the problem of grating lobes has

been overcome by unequal placement of the array elements [14 15 16]. In [16 17] it has been shown that unequal spacing of elements would bring down the grating lobes but the average spacing between the elements should be less than or equal to $\lambda/2$ where $\lambda$ is the wavelength and also the total number of elements should be equal to a certain number. Researches have also been performed which use evolutionary algorithms to choose the array weighing using which lower sidelobe levels are attained [18]. In [19] evolutionary algorithm has been used to reduce the grating lobe by introduction of a small perturbation to the elemental positions of uniform linear array.

The type of signal considered in the above cases is narrowband signal. Narrowband signals are one in which the bandwidth is small when compared to center frequency of the signal. They can also be defined as signals whose time-bandwidth product is small. In the case of narrowband signals the time difference of arrival is translated to phase difference [20]. This is because in the case of narrowband signals the time taken for a significant change in the modulation envelope is large. Number of algorithms for the determination of DOA using narrowband signals is described in [21]. All the methods for the narrowband DOA estimation described in [21] make use of the phase difference and hence the sensors should be separated by a distance $d < \lambda/2$.

In [22 23 24] 3D imaging sonar has been developed. Array thinning in [22 23 24] of a full array is achieved using simulated annealing process. The thinned planar array (containing 584 array elements) in which the elements were distributed in a circular pattern was used for imaging. It is found that even though the array is thinned the number of elements is still very large.

### 1.2.2   Interferometry in sonar

One other method that has become very popular during recent years is the interferometric method [25 26 27]. The inspiration for applying interferometry techniques to sonar for determining the DOA and hence depth information was drawn from the field of radar. The application of interferometry to these systems

came from the principle of stereoscopic photography [27]. The principle of stereoscopy is shown in the figure 1.1.

When looked at the objects 'a' and 'b' from position Y they seem to be in a straight line and look as though they are a single object. But when parallax is introduced and then observed from the position X it is possible to resolve the objects 'a' and 'b'. This is the principle which the human eye is based on where the eyes are separated by a small distance to introduce the parallax. In the case of radar or sonar, the parallax is obtained using receivers separated by a small distance. Some factors that led to the eventual development and the application of the interferometric methods to sonar have been discussed below.
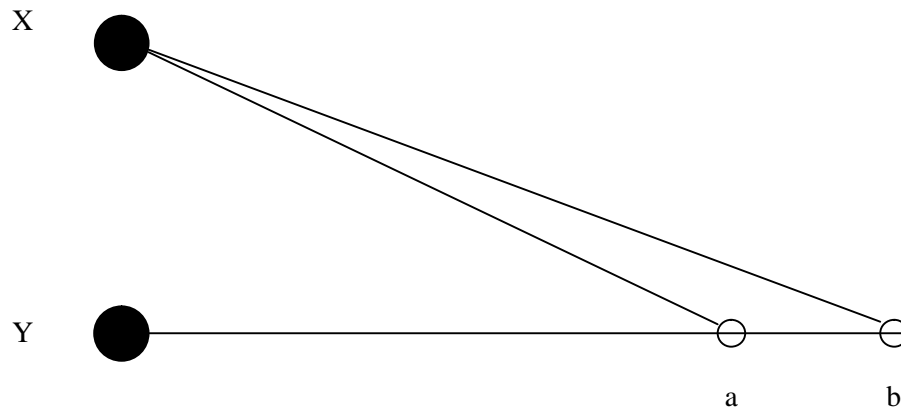


**Figure 1.1 Principle of stereoscopic imaging [27]**

The usual side-scan sonar provides images of the seabed without any depth information [28]. This shortcoming was overcome with the development of multibeam sonar. As discussed in section 1.2, these systems are very costly. To reduce the cost, interferometric technique is used along with side-scan sonar systems to yield a system which was more compact than multibeam systems.

The interferometry effect is usually described with reference to Young's experiment [29]. In this experiment, a monochromatic light source was diffracted into two by means of slits made in a cardboard. The slits act as two coherent sources of light. When light falls on paper screen it creates patterns at locations where two waves from the slits are superposed on each other. From Young's

experiment it can be shown that the resulting intensity depends on the phase difference between the waves from the two sources.

In the case of applying this principle to sonars, the slits made in the cardboard is replaced by receiver elements. Thus the most basic form of interferometric sonar consists of a transmitter and two hydrophones which act as receivers [30]. The transmitted acoustic wave travels and strikes the seabed and is received by the hydrophones. This results in a phase difference because of the difference in distance travelled to the hydrophones. From the phase difference measured, it is possible to determine the DOA and thus the angle at which the target is located.

The first interferometric system using the interference patterns were based on the Lloyds mirror effect observed from the conventional side-scan sonar records [27, 31]. Figure 1.2 shows the principle behind Lloyds mirror effect. The Lloyds mirror effect is noticeable due to interference between signals that are backscattered directly from the target and return signal reflecting off from the surface of the sea [27 31]. This effect is particularly noticeable when the sea surface is flat [27]. It was noted by Chesterman et al and by Heaton and Haslett that each fringe could provide useful information on the declination angle and hence depth can be calculated [27 31]. However, the Lloyds mirror effect is produced only when the sea surface is smooth and therefore this effect cannot always be noticed [27 31].

In order to overcome this problem, Strubbs et al in 1974 introduced a more satisfying scheme for the formation of interference fringes [27]. They gave it the name 'telesounding'. The operation of the telesounder is similar to that of side-scan sonar except that it has a plane acoustic reflector which projects from its side and allows for the formation of more controlled fringes. The difficulty here is that the reflector projects out. Subsequently the idea of using two receivers stacked vertically to obtain depth from the interferometric fringes was put forward. The modern bathymetric system is shown in figure 1.3.
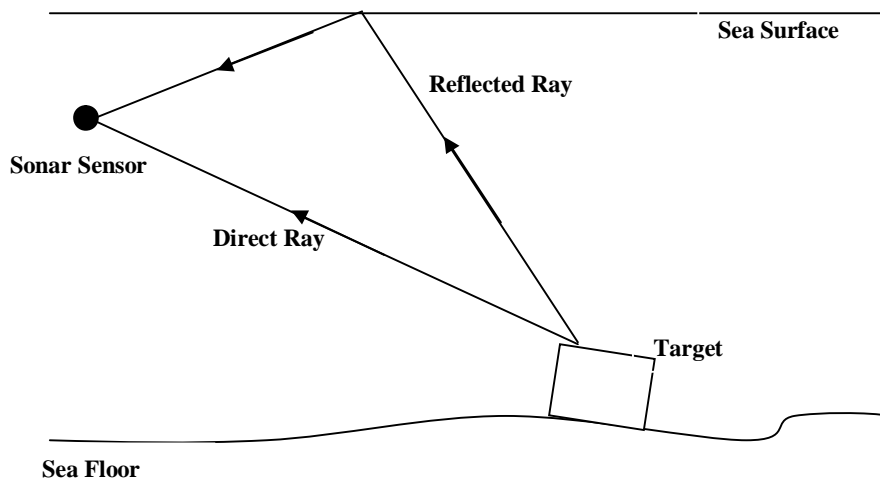
**Figure 1.2 Lloyds mirror effect**
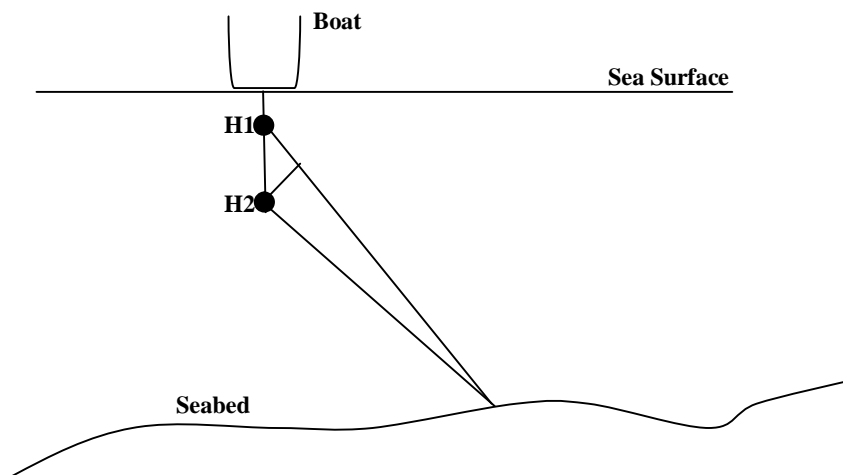


**Figure 1.3 Principle of operation of bathymetric system**

The interferometric fringes in the telesounding system are formed by the addition of signals received [31]. It was Denbigh who in his paper [31] in 1977 had suggested use of phase difference. In figure 1.3 the phase difference is calculated between the signals arriving at hydrophones H1 and H2. The method suggested had an advantage over the telesounder in that it could measure the depth instantaneously for every resolution cell of the side-scan sonar data record [31]. Thus the modern day bathymetric systems came into existence which [27 31]

measure the declination angle by measuring phase difference as suggested by Denbeigh in [31].

In [32 33] side-scan systems were used to mimic the operation of multibeam systems. Two signals projected into the medium add up when the signals are in phase with each other. When the signals add up constructive interference occurs and they form a maximum. The signals which are out of phase cancel each other and destructive interference takes place. Nulls are formed at points were the destructive interference takes place. The points where the constructive interference occurs serve as separate beams and behave as a multibeam system.

The interferometric technique has been applied to a number of sonar applications. With its successful application to side-scan sonar, the technique has been applied to Synthetic Aperture Sonar (SAS) for achieving high resolution 3D imaging and a simulation model was reported in [34] together with its implementation in [35]. With its large number of applications, the use of interferometric principle has still not led to a cost effective system.

The problem with using interferometry in determining the DOA is that it uses phase difference which would result in phase ambiguity if the array elements are spaced greater than $\lambda/2$. The interferometry technique is quite sensitive to phase and would cause severe errors if the phase difference is not accurately determined. Hence interferometry is a narrowband technique and thus for the reduction of phase ambiguity the receivers should be separated by less than half the wavelength. Hence interferometric technique is not suitable for application with sparse arrays.

From the discussion above it is seen that high resolution sonars available use a large number of array elements for obtaining higher resolution. These high resolution systems have regular arrays which follow the basic wavelength criterion of array element placement i.e. $d < \lambda/2$.

### 1.2.3 Possible Solution

Wideband signals are signals that have a large bandwidth over small time duration. Wideband signals are becoming popular [20, 21] and have been successfully used in high resolution imaging in radar [20, 21], tracking targets [20, 21] and detection of buried objects using seismic sensors [20, 21]. Wideband signals are preferred because they provide high resolution and better probability of detection in the presence of correlated noise [36]. DOA estimation available for wideband signals uses traditional narrowband approaches [20, 21]. Here the wideband signals are split into a series of narrowband signals and the DOA algorithms for narrowband signals are applied for each frequency [20, 21]. Wideband signals are split into a series of narrowband frequencies because the bandwidth of the signals is comparable to the center frequency and hence the relationship between the phase difference and time delay no longer holds [20, 21]. Thus the distance traveled $dsin\theta$ ($d$ is the distance between the array elements and $\theta$ is the direction of arrival) cannot be approximated by phase as the phase is dependant on the wavelength $\lambda$.

There has not been much research into the use of wideband signals with sparse arrays. The use of narrowband techniques for wideband DOA estimation would require the array elements to be separated by less than $\lambda/2$ failing which grating lobes would appear. The problem arising due to grating lobes like ambiguity, false detections/artifacts in the reconstructed scene might be resolved by the use of time difference of arrival to calculate the DOA instead of using the phase difference.

Stereoscopic principle discussed in section 1.2.2 requires a parallax to be introduced between the sensors in order to determine the height of the object. Here two hydrophone elements are separated by a distance in order to obtain the parallax. Thus the same point on the target is viewed from different hydrophone positions. Stereoscopic technique requires the identification of the reference point where the height or depth is required to be calculated. For the DOA estimation, the target being insonified using wideband signal returns a unique pattern in the backscattered signal which are received by the receiver elements. The lead or lag time of the pattern in one signal with respect to the other would give the time

difference of arrival from which the DOA can be calculated. Correlation has been widely used for comparing the similarity between two received signals [37]. Depending on where the correlation peak occurs, the time difference of arrival can be obtained. Thus the reference point is the pattern that occurs in the signals received. An advantage of using the time difference of arrival is that the separation between the sensors does not require to be less than $\lambda/2$.

Wide bandwidth signals provide a high range resolution as the range resolution is proportional to the signal bandwidth. It would be interesting to determine whether this high range resolution obtained due to large excess bandwidth can be traded off for a better angular resolution when using sparse arrays.

From the survey presented in sections 1.2.1 and 1.2.2 it is clear that improvement of imaging resolution has been the main focus in the researches on imaging sonar. Sparse arrays have been used to decrease the processing power required at the time when the powerful signal processing chips where more expensive than the cost of building the receiver channels. The reduction in the price of these high performance chips has not been exploited to build systems with reduced number of channels. It is also clear from the discussion in section 1.2.1 and section 1.2.2 that the use of sparse arrays have been widely investigated using narrowband signals.

All the above factors directed this research in building a sparse array 2D imaging sonar system with as few receiver elements as possible. The problems like phase ambiguity etc. which arise resulting from the use of narrowband signals with sparse arrays prompted the use of very wide bandwidth signals where true time delay can be used for the determination of DOA of the signals. Thus it is desired to build an ultra-sparse array with as few as four elements which are spaced many wavelengths apart. Figure 1.4 tries to summarize the requirements of the problem diagrammatically

Requirements            End Result           Properties
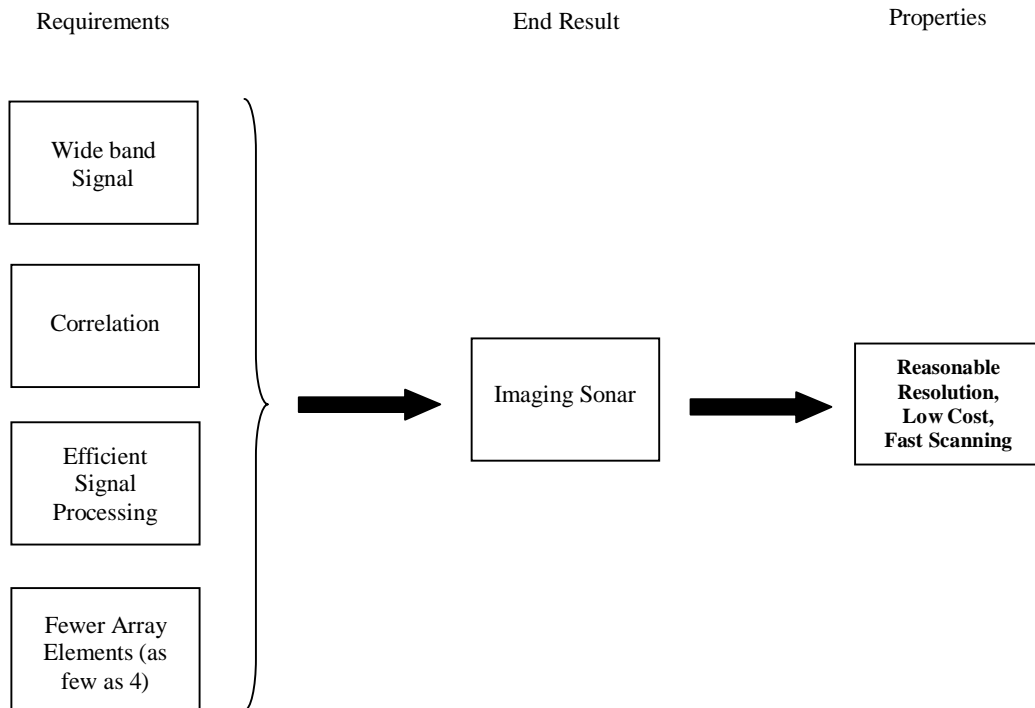
**Figure 1.4 Basic design requirements**

## 1.3  Summary of research objectives

Some of the important objectives of the imaging system being developed in this project are listed below:

a) The imaging system should be capable of forming an image which could be easily recognized and interpreted by the operator. The performance of the imaging system is tested using simulation by forming the image and determining the SNR, PSNR and SSIM index of the image formed.

b) It is one of the objectives of this research to keep the hydrophones to a minimal number. The use of an ultra sparse array with few hydrophone elements as low as four is investigated. The array element spacing is such that $d >> \lambda$. The number of projectors used for target insonification is one. The projector is considered to have a fan

beampattern. Minimizing the number of hydrophone channels is a key drive to keep the system cost down.

c) Wide bandwidth signals have been used because of their ability to achieve high range resolution. It is desired to investigate whether this high range resolution available can be traded for obtaining a better angular resolution.

d) Investigate techniques to determine multiple target angle of arrival from the same range cell.

e) Since the properties of the ocean environment change quickly with time it is difficult to predict or derive a statistical model of the return signal. Hence it is one of the objectives of the research to keep any statistical model assumptions to a bare minimum.

f) Test the algorithm developed using data obtained under realistic conditions.

## 1.4　Thesis outline

The structure of the thesis is discussed in the following paragraphs.

Chapter 2 discusses the background related to sonar, the two different types of sonar in existence and the related equations. The chapter discusses the signals that are commonly employed in active sonar systems. The main components of a sonar system are described with the help of a block diagram. This chapter closes with the description of operation of common imaging sonar types along with their advantages and disadvantages.

Chapter 3 describes the principle of different types of beamformers available. This chapter then discusses the drawbacks of these beamformers. The chapter then

describes the broadband and narrowband signals drawing a comparison between them. Finally the chapter describes the near-field and far-field conditions.

Chapter 4 discusses the theory behind the DOA estimation used in this research. The novel correlation technique is explained and analysed, focusing particularly on the issues of data registration between hydrophones. The chapter also describes the fundamentals of digital image followed by the method of transition of raw data into an image. This chapter describes the signal processing method used in the research. The chapter closes with the explanation of the novel non-linear combining process developed.

Chapter 5 explains the structure of the simulation model used in this research. The range resolution and angular resolution obtained using this method is also discussed. The chapter also describes the measurement metrics that are used in this research.

Chapter 6 presents the simulation results and discusses the result obtained.

Chapter 7 describes the hardware developed. The results of the experiments performed in real time are presented in this chapter.

Chapter 8 concludes this research and presents the areas where future work could be performed related to this topic.

# Chapter 2
# Background and Literature Review

Acoustic imaging is accepted as the most reliable method for underwater imaging and has grown into a separate field by itself. In underwater imaging, the received sound signals are processed in order to investigate and explore unknown domains inaccessible to humans. Just like scattered light is used in building up the image of the scene in optical imaging, acoustic imaging uses sound scattered by the target to build up the image [1]. Image obtained by using acoustic method is not affected by the turbidity in water [1]. Developments in underwater acoustic imaging technology has made it possible to view the ocean environment, although with an accuracy of only a fraction of that obtained with radar imaging [38]. In this chapter, some of the basics of sonar are introduced. This chapter concludes with the description of a few existing imaging sonars.

## 2.1    Sonar

Sonar utilizes the fact that sound waves can propagate in water. Acoustic waves travel more effectively in water than the electromagnetic waves. This is because, in the case of electromagnetic waves, water being an excellent conductor of electricity, results in rapid dissipation of the electrical energy as heat [39]. Thus, electromagnetic waves experience greater attenuation than acoustic waves of the same frequency [39]. Optical imaging techniques are not suitable for the purpose of underwater imaging as they would be able to cover only small distances due to scattering and is also affected by the turbidity in water [1]. Due to these reasons sound is widely used for the exploration of the seas and hence the name Sound Navigation and Ranging.

### 2.1.1   Principle of operation of sonar systems

The fact that the sound wave can travel effectively through water makes it useful for detection and exploration. Sound propagates in water as a series of pressure fronts known as the compressional waves, i.e. they are transmitted in the form of

compression and rarefaction. Sound waves propagate through the water at local speeds (the speed of sound varies as the medium changes). The speed of sound in water has been determined to be approximately 1500 m/s. The speed is found to vary with salinity, temperature and pressure. The frequency of an acoustic wave is the number of pressure fronts that pass a fixed point per second. The relation between speed ($c$ $m/s$), wavelength ($\lambda$ $m$) and frequency ($f$ $Hz$) is given by

$$c = f\lambda \qquad\qquad\qquad 2.1$$

When the speed of sound changes in the medium only its wavelength changes while its frequency remains constant. Therefore sound waves are usually expressed in terms of frequency rather than wavelength.

Sound waves carry acoustic energy which can be detected using a hydrophone. The amplitude of the sound waves is related to the acoustic energy being transmitted and the energy is proportional to the square of the amplitude of the sound waves. As the sound wave travels through the medium it loses some of its energy. This loss is called attenuation. This is because energy transfer is not perfect and some of the energy is lost as heat. The attenuation level depends on the frequency of the sound waves. The higher the frequency the higher the attenuation and thus higher frequency sound waves can be used only for small distance applications. Low frequency sound waves would travel long distances without considerable loss in energy. A plot showing the attenuation coefficient and the frequency is shown in figure 2.4 in section 2.1.2.2.

Acoustic energy travelling through a medium gets interrupted if it encounters obstacles or if there is a sudden change in the medium in its path. This results in absorbtion, reflection or scattering of acoustic energy. The extent of absorbtion, reflection or scattering depends on the nature of the material or the medium. This scattered or reflected energy has to go back into the original medium through which it had been traveling and is called the '*echo*'. It is shown diagrammatically in figure 2.1. Thus if $Z_1$ and $Z_2$ are the specific acoustic impedances of the respective mediums as labeled in figure 2.1 then

$$Z_1 = \rho_1 c_1 \qquad\qquad\qquad\qquad 2.2$$

$$Z_2 = \rho_2 c_2 \qquad\qquad\qquad\qquad 2.3$$

where $\rho_1$, $\rho_2$ are the densities of the medium and $c_1$, $c_2$ are the velocities of the acoustic waves in the respective medium. From the above equation it is seen that acoustic impedances are related to the density of the medium. The reflection coefficient (*rc*) which determines the amount of energy that goes back into the medium1 is given by

$$rc = \frac{Z_2 - Z_1}{Z_1 + Z_2} \qquad\qquad\qquad\qquad 2.4$$

The hydrophones which collect the reflected or scattered sound waves, convert them into electrical signals. These signals are further processed to obtain the range, the location and in some cases the image of the target which causes the echo. Thus in the terms of A.A.Winder [39] sonar can be defined as a *'method or equipment for determining by means of underwater sound the presence, location and the nature of the objects'*.
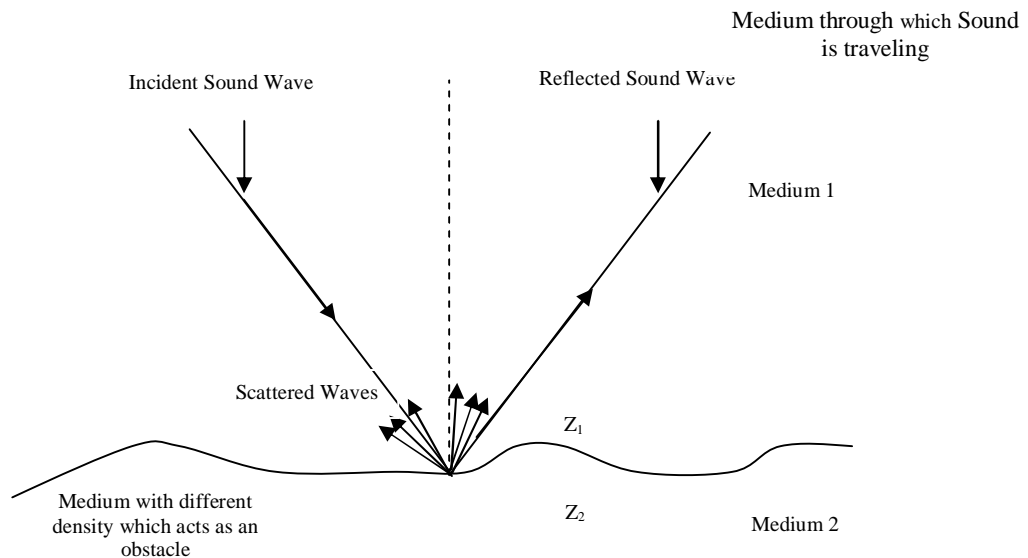


**Figure 2.1 Sound traveling through a medium being interrupted by another medium**

18

Sonar systems can be classified into two types depending on their mode of operation. They are a) Passive sonar and b) Active sonar. The principle of operation of both is described below.

### 2.1.1.1    Passive sonar

A passive sonar system listens to the sound transmitted by other objects and does not transmit any signal of its own.  The targets are considered to radiate sound with a certain signature or frequency by means of which it can be detected and distinguished [39]. Hence this becomes a detection problem to isolate the desired signal from noise which may have the same energy spectrum as the desired signal. A block diagram depicting operation of passive sonar is shown in figure 2.2.
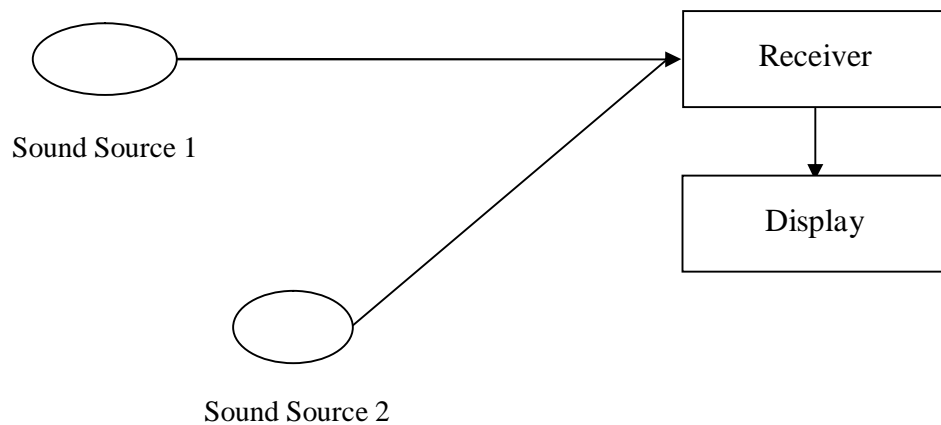


**Figure 2.2 Principle of operation of passive sonar**

Passive sonar systems usually have large sonic databases which contain details of sounds produced by many common targets and mammals found in the sea. During processing of the return signals, the sonar system compares them with signatures stored in the database and associates them to known classes of ships, submarines etc. The final decision is dependant on the operator.

### 2.1.1.2    Active sonar

Active sonar systems send out well defined pulsed signals of particular frequencies in a desired direction. The signal transmitted illuminates the obstacles

in its path which scatter the signal. Scattered signals detected by the receiver are processed and then displayed. The operation of an active sonar system is shown in figure 2.3. The signal received contains not only the useful signal but also noise.
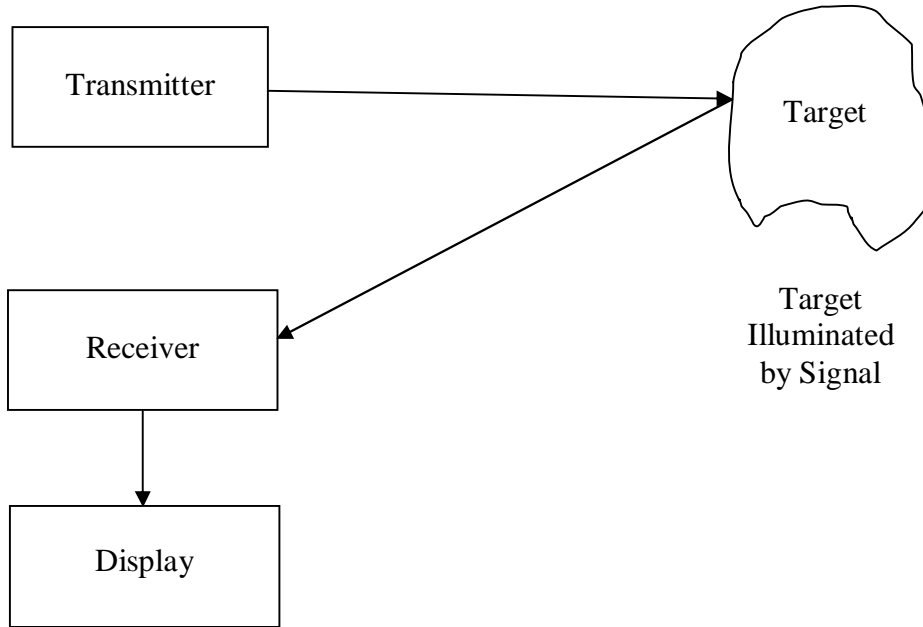


**Figure 2.3 Principle of operation of active sonar**

When the transmitter and the receiver are located in the same place the sonar operation is called monostatic [40]. Most of the active sonar systems are monostatic. If the sonar's transmitter and receiver are at a distance apart, their operation is said to be bistatic [40]. When either multiple transmitters or receivers are used with a separation between them the operation is said to be multistatic [41]. When active sonar is used to measure the depth, it is said to function as an echo sounder.

Consider a pulse *s(t)* transmitted in water that hits a target and gets scattered. This echo is detected by the receiver after *2r/c* seconds where *r* is the range, i.e. the distance between transmitter and target, and *c* is the velocity of sound in water. The factor of '*2*'denotes the two way distance travelled in case of a monostatic operation.  In other words, a pulse similar to the transmitted pulse is received after a delay of *2r/c* which can be mathematically written as

$$g(t) = s(t - 2r/c) + \upsilon(t) \hspace{3cm} 2.5$$

where $g(t)$ is the received signal and $v(t)$ is the noise. Equation 2.5 does not take into account various other factors like the attenuation, dispersion, multi-path reflections, etc, which have to be considered.

### 2.1.2 Losses experienced by the signal while traveling through the medium

The transmitted signal while travelling through the medium experiences a loss in energy due to a number of factors such as attenuation, spreading, multi-path reflections, etc. Some of the common causes of losses which affect the signal are described in the following paragraphs along with the relevant mathematical equations. The effects of these losses can be grouped together in a single equation, $P_{Loss}$, which is expressed in decibels (dB). This can be described as the propagation loss which is the decrease in intensity of the radiated signal when it arrives at the receiver. Thus

$$P_{Loss} = 10 \log \left( \frac{I_0}{I_r} \right) dB \qquad 2.6$$

where $I_0$ is the intensity of the signal at the source and $I_r$ is the intensity at the receiver. The intensity of the sound is always expressed relative to the reference intensity $I_{ref}$ (*watts per square meter ($Wm^{-2}$)*) whose value is given by [42 43 44]

$$I_{ref} = 0.67 \times 10^{-18} Wm^{-2} \qquad 2.7$$

The reference intensity can be defined as the intensity of the plane wave which has a RMS value of $1\mu Pa$ [42 44].

The main contributors of the loss $P_{Loss}$ are the

    a) Spreading loss ($S_L$)
    b) Attenuation ($A_T$)

Thus the total loss ($P_{Loss}$) can be written as

$$P_{Loss} = S_L + A_T \qquad\qquad 2.8$$

where all the terms in equation 2.8 are in decibels (dB). Each of these losses is briefly explained in the following paragraphs.

### 2.1.2.1    Spreading loss

When the source is located in an unbounded and lossless medium, the power is radiated equally in all directions and will radiate spherically from the source. If the power of the source is given by $P$, then it is possible to write [42 44]

$$P = Area \times Intensity \qquad\qquad 2.9$$

$$= 4\pi r^2 \times I(r) \qquad\qquad 2.10$$

where intensity is defined as power per unit area. $I(r)$ is the intensity at distance $r$. Hence the spreading loss can be written as [42 44]

$$Loss = 10\log\left(\frac{I(1)}{I(r)}\right) \qquad\qquad 2.11$$

Thus [42 44]

$$Loss(S_L) = 10\log\left(r^2\right) \qquad\qquad 2.12$$

$$= 20\log(r)\,\text{dB} \qquad\qquad 2.13$$

### 2.1.2.2    Attenuation

The propagation of sound in water is subjected to losses due to absorption. Absorption losses occur mainly due to two factors i.e. a) viscosity of the fluid and b) molecular relaxation [42]. Experiments carried out on these losses have resulted in empirical formula which relates them to frequency, salinity and depth. The total loss was expressed as an attenuation coefficient $\alpha$ with the units of *dB/km*.

The attenuation coefficient increases rapidly with frequency and changes with temperature. In order to calculate the loss it is necessary to multiply the range $r$ (in km) with the attenuation coefficient $\alpha$ from the graph shown in figure 2.4. The formula for the attenuation loss, $A_T$, is given as follows [42 44]

$$A_T = \alpha r (dB) \qquad\qquad 2.14$$
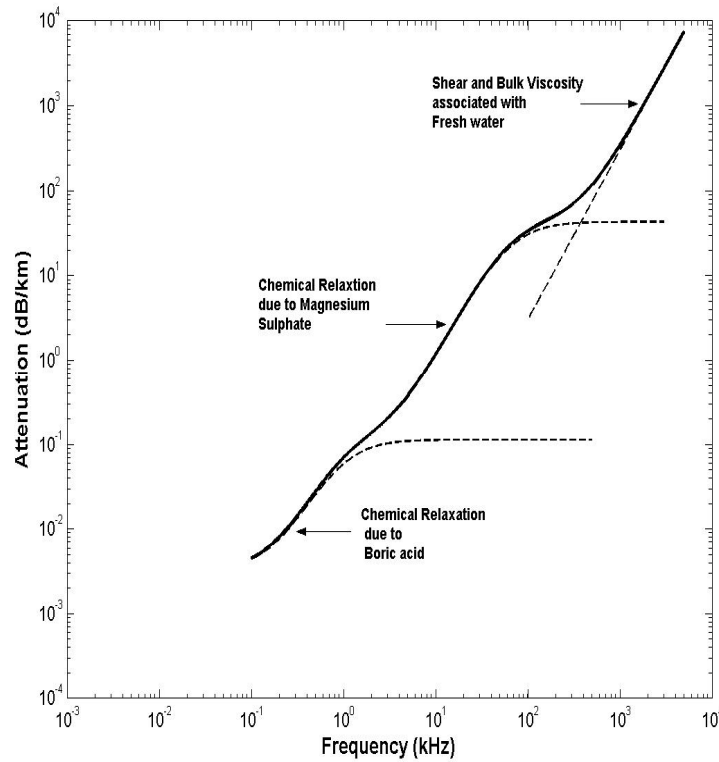


**Figure 2.4 Attenuation coefficient vs. Frequency**

Figure 2.4 shows the plot between the attenuation coefficient $\alpha$ and frequency (kHz). The effects that are dominant at the various frequency ranges are shown in the figure. From the figure 2.4 it is clear that as the frequency increases so does the attenuation coefficient and the attenuation. The graph in figure 2.4 is calculated using the equation 2.15 which gives the approximate value of the absorption coefficient [44 45]

$$\alpha = 3.3 \times 10^{-3} + \frac{0.11 f^2}{1 + f^2} + \frac{43 f^2}{4100 + f^2} + 2.98 \times 10^{-4} f^2 \, dB/km \qquad 2.15$$

The second term in equation 2.15 gives the contribution of relaxation due to boric acid and the third term gives the contribution of relaxation due to magnesium sulphate. The fourth term in the equation 2.15 gives an idea about the contribution of shear and bulk viscosity associated with fresh water.

### 2.1.3   Target strength

Target strength is the echo returned by an underwater target [43 44]. Target strength is the intensity of sound returned to the receiver by the target. It is defined as the ratio, in *dB*, of the reflected intensity at a distance of 1m from the target to that of the incident intensity. It can be given mathematically as follows [42 44].

$$TS = 10\log\left(\frac{I_r}{I_i}\right) \qquad 2.16$$

where $I_r$ is the reflected intensity and $I_i$ is the incident intensity. Target strength depends on the geometry and orientation of the target.

### 2.1.4   Active sonar equation

Previous sections discussed the various parameters required for obtaining the sonar equation. The sonar equation defines the received signal strength as a sum of the source level (*SL dB*), transmission loss (*TL dB*) from the source to the receiver and back and the target strength (*TS dB*) [42 44 46].
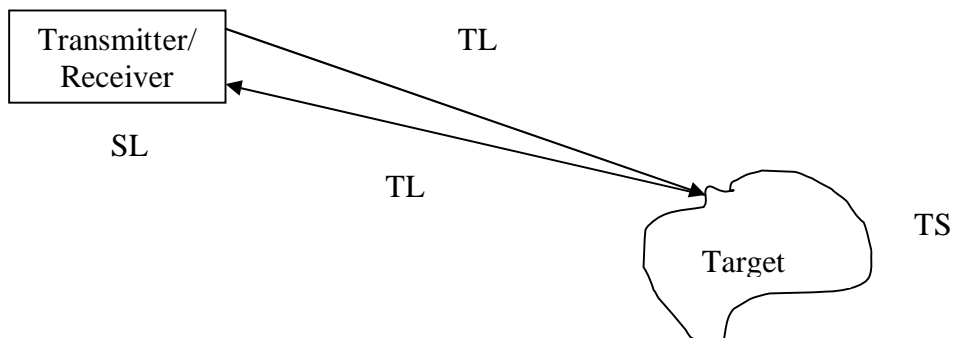


**Figure 2.5 Figure showing the various effects on the transmitted signal**

Consider figure 2.5; the transmitter emits a signal with a source level $SL$ $dB$. When traveling through the medium the emitted signal undergoes losses indicated as $TL$ $dB$ due to spreading and absorption which reduces the intensity of the signal. The remaining signal $(SL\text{-}TL)$ $dB$ hits the target and the signal which is reflected back into the medium depends on the target strength ($TS$ $dB$). During its return journey towards the receiver it further undergoes transmission losses ($TL$ $dB$) which may be the same if the system is monostatic. Thus the equation for the received signal level ($RL$ $dB$) of active sonar can be given by the following equation [42 44]

$$RL = ((SL - TL) + TS - TL)dB \qquad\qquad 2.17$$
$$= (SL - 2TL + TS)dB \qquad\qquad 2.18$$

The transmission loss ($TL$ $dB$) is the sum of the absorption losses and the loss due to spreading. If the noise level at the receiver is $NL$ $dB$ then the equation for the signal to noise ratio can be given as [42 44]

$$SNR = (SL - 2TL + TS - NL)dB \qquad\qquad 2.19$$

Previously in section 2.1.2.1, source level was described as intensity which is the pressure per unit area. When the source level is calculated it is assumed that the sound from the source undergoes spherical spreading omnidirectionally. At 1m from the acoustic center (standard range) the source is surrounded by a sphere of surface area $4\pi r^2 = 4\pi = 12.6 m^2$. Thus if the power output is $P$ watts then the intensity of the source at 1m is $\left(\dfrac{P}{12.6}\right)$ W/m$^2$. Hence the source level becomes [42]

$$SL = 10\log\left(\frac{P/12.6}{I_{ref}}\right) \qquad\qquad 2.20$$

Substituting the value of $I_{ref}$ from equation 2.7

$$SL = 10\log(P) + 170.8 dB.re.1\mu Pa\, @\, 1m \qquad\qquad 2.21$$

This gives the equation for the calculation of the source level. The source level is expressed as **re.1μPa** as the reference intensity is the intensity related to 1 μPa.

### 2.1.5   Noise

There are many sources of noise like the ambient noise, shipping noise, thermal noise, turbulence noise and the noise due to surface agitation [42 44]. All these are frequency dependant and would be dominant in a certain frequency range [42 44]. There are number of equations that have been hypothesized for determining the noise spectral level. The noise level can be calculated from the noise spectral levels (*NSL dB re 1μPa*). Thus the equation for the noise level is given by [42]

$$NL = NSL + 10\log(B) \qquad\qquad 2.22$$

where $B$ is the bandwidth of the signal in Hz. A plot showing the ambient noise i.e. the noise due to the sea is shown in figure 2.6.
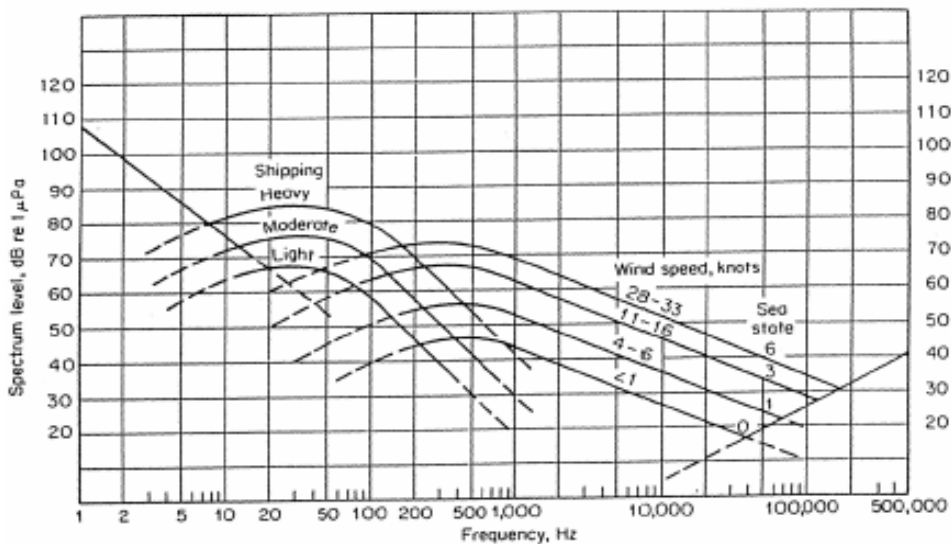


**Figure 2.6 Ambient noise (Wenz Curves) [44]**

From figure 2.6 it is seen that the low frequency regions are affected by the shipping noise which varies from 2 to 200 Hz. As the frequency increases the

shipping noise rolls off and the noise region is dominated by the wind speed which occupies the frequency region from 200 Hz to 100 kHz. The very high frequency region is dominated by the thermal noise. In the very low frequency region the noise is dominated by seismic activity.

## 2.2 Active sonar waveform types

Active sonar systems transmit their own pulses. The signals that are most commonly used are the continuous wave (CW) and linear frequency modulated wave (LFM) or chirp [39 47]. The signals used depend on the application as well. In the following paragraphs each of these signals is explained briefly.

### 2.2.1 Continuous wave pulse (CW pulse)

The CW pulse is characterized by its amplitude, width and constant frequency. A CW pulse can be represented mathematically as

$$
\left.\begin{aligned}
CW(t) &= \Omega \sin(2\pi f t),\ 0 < t \leq \tau \\
&= 0, \quad t > \tau
\end{aligned}\right\}
\tag{2.23}
$$

where $\Omega$ is the signal amplitude. The range resolution (the ability to distinguish between two targets in the same bearing but separated in range) that can be obtained using a CW pulse is given by

$$
\Delta r = \frac{c\tau}{2}
\tag{2.24}
$$

where $\tau$ is the pulse length. In order to obtain a good range resolution it is necessary to decrease the pulse length and thus the range resolution depends on the pulse length [47]. The problem with the CW pulse is that when the signals from two targets, separated by a small distance, overlap it becomes difficult to determine which pulse arrived earlier. An example of CW signal is shown in

figure 2.7. The signal has a frequency of 250 kHz and is sampled at 1 MHz. Power spectrum of the CW signal is shown in figure 2.8.
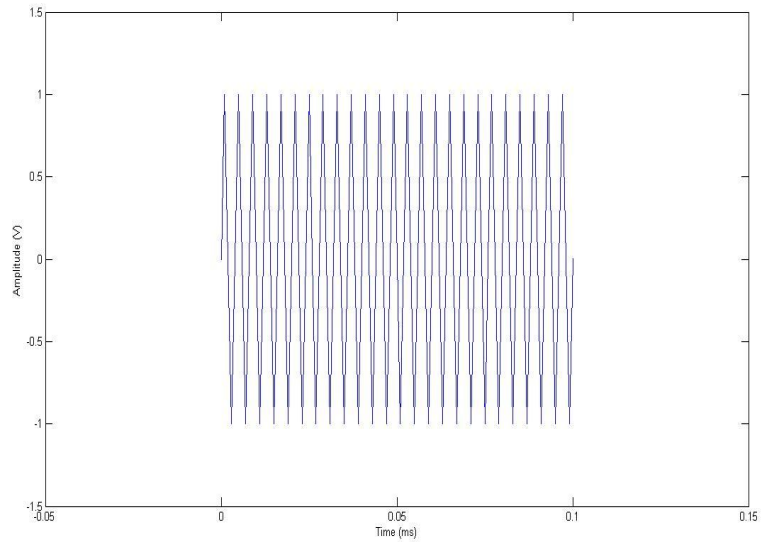


**Figure 2.7 CW signal**
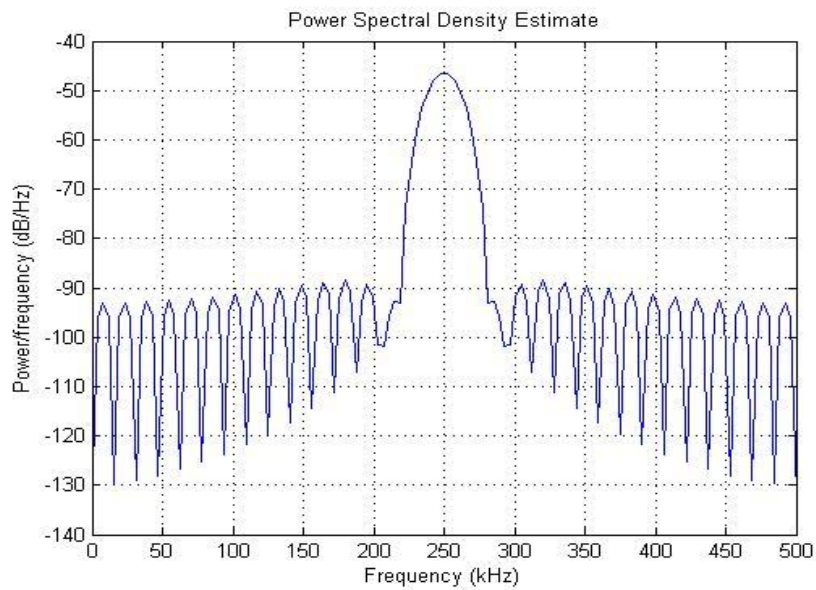


**Figure 2.8 Power spectrum of the CW signal in figure 2.7**

The spectrum in figure 2.8 shows a peak at 250 kHz which is the center frequency of the signal.

### 2.2.2 Linear frequency modulated signals (LFM signals or CHIRP)

The linear frequency modulated signals or chirp (Compressed High Intensity Radar Pulse) is a frequency modulated signal in which the frequency of the signal varies linearly with the time. The equation for a LFM pulse can be given as [48 49]

$$s(t) = \Omega \cos(2\pi(f_0 + \frac{\gamma t}{2})t) \qquad 2.25$$

where $f_0$ is the start frequency, $\Omega$ is the signal amplitude and $\gamma$ is the chirp rate which is calculated using the relation

$$f = f_0 + \gamma t \qquad 2.26$$

where $f$ is the instantaneous value of the frequency. An example of a chirp signal is given in figure 2.9.
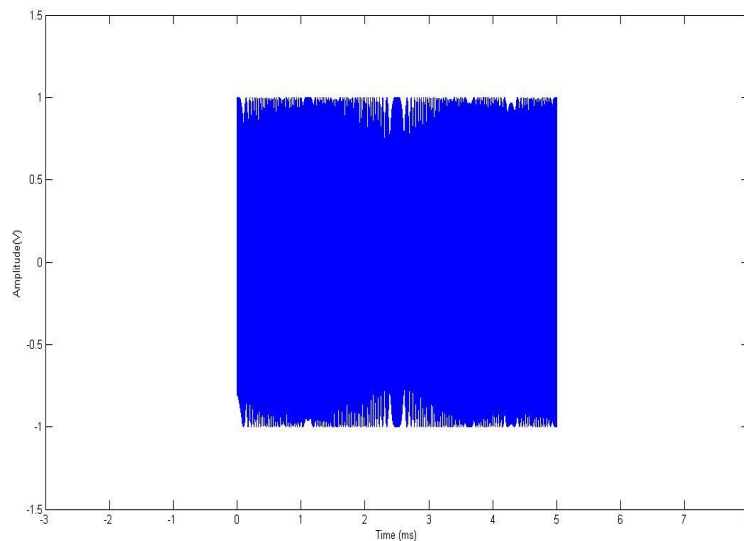


**Figure 2.9 Chirp waveform**
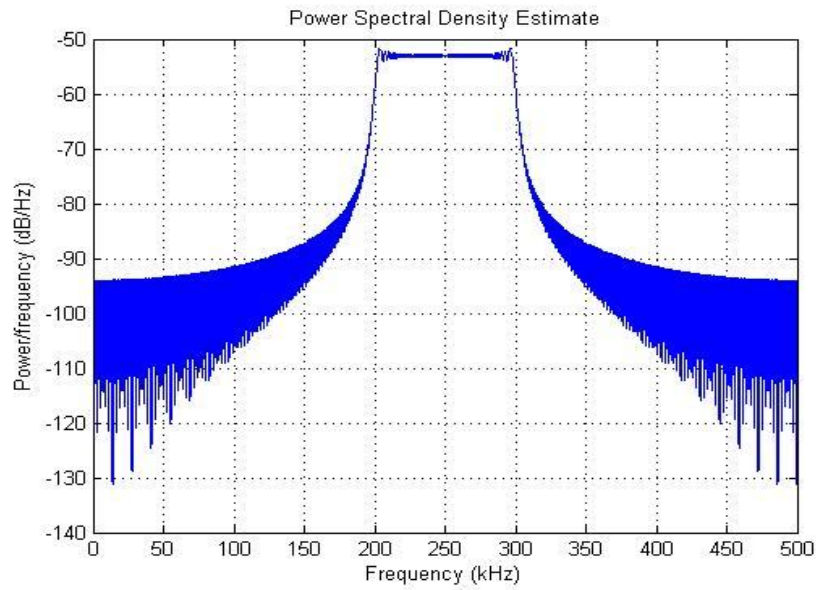
**Figure 2.10 Spectrum of the chirp signal in figure 2.9**
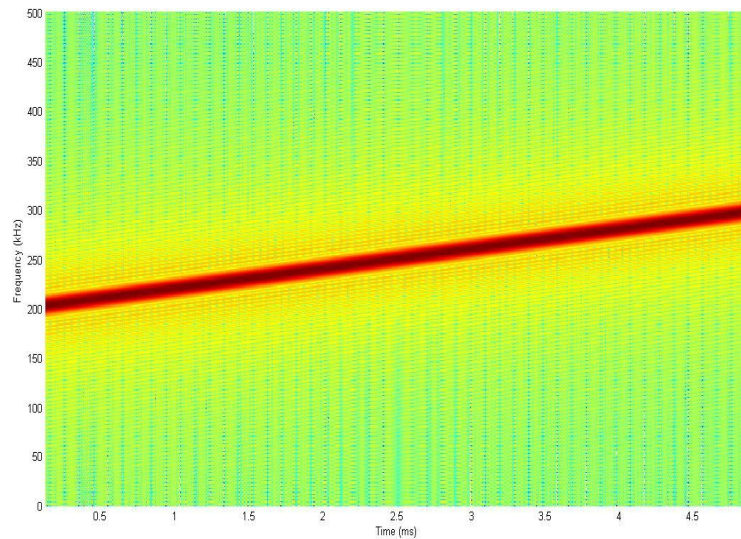


**Figure 2.11 Spectrogram of chirp**

Figure 2.9 shows a chirp signal with a frequency sweep between 200 – 300 kHz in 5ms time interval. The bandwidth of the LFM can be confirmed from the spectrum of the chirp which is shown in figure 2.10. The spectrogram in figure 2.11 shows that the frequency of the chirp signal varies linearly w.r.t. time.

Chirp signals are detected by correlating it with the copy of the signal that is transmitted. This process is called chirp compression. Compression of the chirp

signal would yield a processing gain of $B.\tau$ where $B$ is the bandwidth of the chirp signal and $\tau$ is the duration of the chirp [50]. The range resolution in the case of a LFM signal is given by [49]

$$\Delta r = \frac{c}{2B} \qquad\qquad 2.27$$

Thus from equation 2.27 it is seen that the range resolution does not depend on the pulse length. In case of a chirp signal, since the frequency of the pulse transmitted varies over the pulse length this acts as a signature. Thus, even when returns from two targets merge, the processing is able to distinguish between the two closely spaced temporal returns because of the signature.

### 2.2.3   Other waveforms

Apart from the signals mentioned above, there are other signals like the Non-linear frequency modulated signals (NLFM) and the linear period modulated (LPM) signals [46] which are used in active sonar system. These signals are used for obtaining low range sidelobe level [51] and a good Doppler tolerance. The design of NLFM signals is complicated and the signal has to be designed for specific sidelobe levels [51]. NLFM signals by itself are no better Doppler tolerant than LFM but have to use hybrid methods (used in LFM) like shading, amplitude windowing etc to improve Doppler tolerance [51]. In [51] a hybrid NLFM signal is designed in order to obtain the advantages of NLFM i.e. low range sidelobes and also to obtain Doppler tolerance. As mentioned it can be seen from [51] that the design of such a waveform is rigorous. Also designing signals with low sidelobe level would  hardly be a solution as we are considering a complex target as a collection of point targets and even if the sidelobe level is down, the final image formed may have significant sidelobes (unless the waveforms are perfectly orthogonal where they match only when perfectly aligned). Whereas Linear period modulation signals (also called hyperbolic frequency modulation) are very Doppler tolerant [51]. In the absence of Doppler the performance of LFM and LPM are similar [51]. Doppler frequency comes into account only when the sonar platform is in motion. In this project, it is desired to

build sonar from the basic principles for a sparse array and hence we are concerned only with sonar on stationary platform. Hence further investigations into these waveforms are not made and would be considered as a part of future work. LFM forms a signal which can be obtained with ease with a function generator. Thus this project considers a broadband LFM chirp signal for analysis. Doppler can be tackled in these cases with the help of Doppler filters which can estimate the frequency range of the return signal. LFM signal itself is Doppler tolerant to a certain extent [51].

### 2.2.4   Ambiguity Function

An ambiguity function is a two dimensional function of time-delay and Doppler frequency $\chi(t,f)$ showing distortion of the received pulse due to matched filtering at the receiver. The ambiguity function is determined by the properties of the pulse and the matched filter. The ambiguity function can be given by the equation [49]

$$\chi(\tau, f_D) = \int_{-\infty}^{\infty} s(t)s^*(t-\tau)e^{-i2\pi f_D t} dt \qquad\qquad 2.28$$

The ambiguity function reduces to autocorrelation between the signals when $f_D = 0$ and it reduces to the Fourier transform of the square of the pulse considered when $\tau = 0$. When $f_D = 0$ and $\tau = 0$ equation 2.28 gives the energy of the pulse. A few examples of the ambiguity function of some waveforms are given in figure 2.12.

From figure 2.12 it is found that for long CW pulse the Doppler ambiguity is small whereas for a short pulse the Doppler ambiguity is large. In case of a LFM pulse it is seen that small Doppler mismatches does not affect the detection. Ideally the ambiguity function should be of the form

$$\chi(\tau, f_D) = \delta(f_D)\delta(\tau) \qquad\qquad 2.29$$
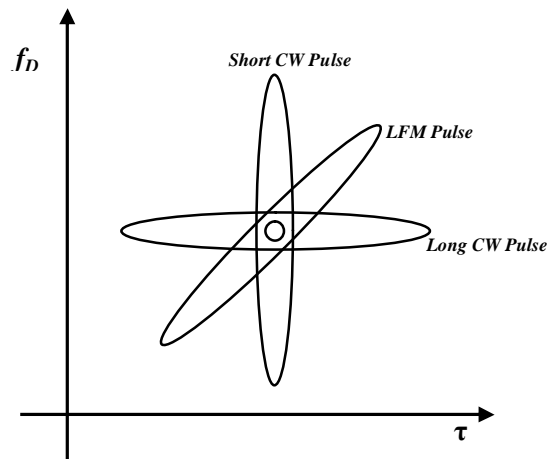
**Figure 2.12 Diagram of ambiguity function of different signals [39]**

## 2.3    Block diagram of a complete sonar system

Figure 2.13 gives the block diagram of a sonar system. The block diagram would be generic for all the equipments and only differs in the way in which the data is collected and returns are processed. In this section some of the basic functions performed by the units in the block diagram are discussed briefly.

The function of the hydrophones is to convert the received pressure signals into electrical signals suitable for processing. Most of the hydrophones available today are made of piezo-electric materials which convert mechanical energy into electrical energy and vice-versa.

The signal processing unit consists of amplifiers, filter, beamformer and matched filter. The function of each of these blocks is described.
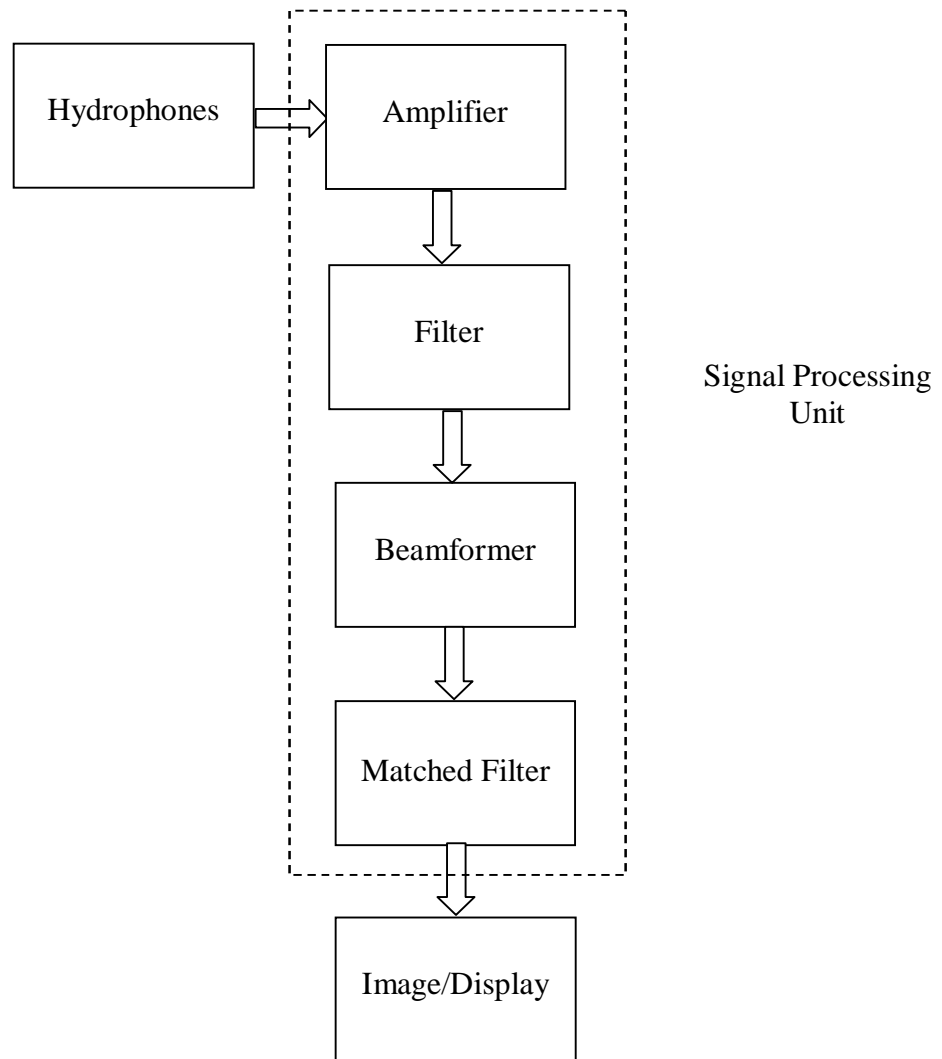
**Figure 2.13 Block diagram of a sonar receiver system**

### 2.3.1 Amplifier

The transmitted signal experiences losses and attenuation and hence the signal received at the receivers would be very small. The function of the amplifier is to amplify the signal at the receiver to the required level.

### 2.3.2 Filter

The signals received by the hydrophones not only contain the desired signal but also other signals at various other frequencies. Since in an active sonar system a signal of a specific frequency or a range of frequencies are sent out, it is necessary

to separate the desired signal from unwanted noise signals. For this purpose a bandpass filter is used which allows a range of frequencies to pass through. When a signal is applied to the filter only those frequencies within the passband are allowed to pass through.

### 2.3.3 Beamformer

Beamforming can be defined as a process which enhances signals impinging on array from a particular direction. Thus beamforming techniques coherently sum the signal arriving from a particular direction. There are number of beamforming methods and these are further discussed in Chapter 3.

### 2.3.4 Matched Filter

The technique of matched filtering provides optimum linear processing of the received signals [52 53]. Matched filter utilizes the knowledge of transmitted signal to detect the existence of reflected targets [53]. Matched filters are linear filters whose impulse response can be obtained such that they maximize the signal to noise ratio (SNR) at the output [53 54]. Matched filter processing converts the desired signal received at the receiver with noise additions into a form that can be used to distinguish the presence of desired signals in presence of noise. Thus the probability of detection of the matched filter is related to the SNR rather than the exact waveform of the signal [54]. Consider figure 2.14
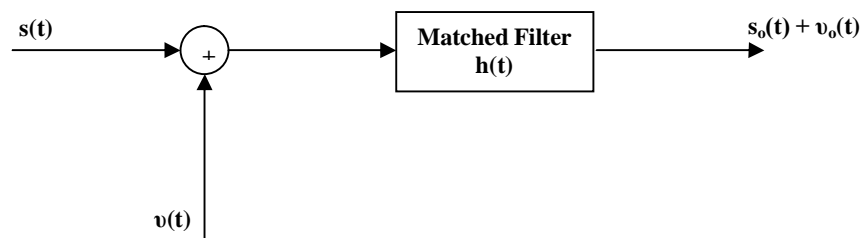
**Figure 2.14 Matched filter operation**

Let $s(t)$ be the transmitted signal and $n(t)$ be the AWGN noise added. It is required to maximize the SNR at the output. If the Fourier transform of the transmitted

signal is $S(\omega)$ then the output signal at $t_o$, where $t_o$ is the signal delay, is given by [53]

$$s_o(t_o) = \frac{1}{2\pi} \int_{-\infty}^{\infty} H(\omega)S(\omega)e^{j\omega t_o} d\omega \qquad 2.30$$

where $H(\omega)$ is the Fourier transform of the filter response. The mean squared value of noise which is independent of time is [53]

$$\upsilon_o^2(t) = \frac{N_o}{4\pi} \int_{-\infty}^{\infty} |H(\omega)|^2 d\omega \qquad 2.31$$

where $\dfrac{N_o}{2}$ is the power spectral density of noise. The SNR at the output is given by [53]

$$SNR = \frac{\left| \dfrac{1}{2\pi} \int_{-\infty}^{\infty} H(\omega)S(\omega)e^{j\omega t_o} d\omega \right|^2}{\dfrac{N_o}{4\pi} \int_{-\infty}^{\infty} |H(\omega)|^2 d\omega} \qquad 2.32$$

If $A(\omega)$ and $B(\omega)$ are two complex signals then according to *Schwarz inequality* [53]

$$\left| \int_{-\infty}^{\infty} A(\omega)B(\omega)d\omega \right|^2 \leq \int_{-\infty}^{\infty} |A(\omega)|^2 d\omega \times \int_{-\infty}^{\infty} |B(\omega)|^2 d\omega \qquad 2.33$$

And the equality holds iff

$$A(\omega) = kB^*(\omega) \qquad 2.34$$

where $k$ is a constant. Using 2.33 and 2.34 in equation 2.32

$$SNR \leq \frac{\frac{1}{4\pi^2} \int\limits_{-\infty}^{\infty} |H(\omega)|^2 d\omega \times \int\limits_{-\infty}^{\infty} |S(\omega)|^2 d\omega}{\frac{N_o}{4\pi} \int_{-\infty}^{\infty} |H(\omega)|^2 d\omega} = \frac{2E}{N_o}$$  2.35

where $E$ is the signal energy. Thus it is shown that the filter response is maximum if

$$H(\omega) = kS^*(\omega)e^{-j\omega t_o}$$  2.36

Taking inverse Fourier transform of equation 2.36 yields

$$h(t) = ks^*(t_o - t)$$  2.37

### 2.3.5   Image processing

Sonar image processing is another area that has been gaining importance. Image processing is required for improving the quality of the image formed. It is sometimes necessary to have an experienced operator in order to interpret the target returns.  In the case of automating the process of detection and target identification, image processing plays an important role. In case of autonomous underwater vehicles (AUV), it is required for the collision avoidance, for seafloor characterization, etc. Thus image processing techniques can help the operators who are less experienced in deciding what to look for.

## 2.4    Imaging sonars

In this section, principle of operation behind few imaging sonars are discussed. Advanced radar imaging algorithms have been applied to the sonar domain since similar principles apply except that now acoustic signals are involved.

### 2.4.1 Side scan sonar

Many active sonar systems with different configuration have been designed but one that has gained popularity is the side scan sonar [43 55]. It can be considered as the traditional method of imaging the seafloor using very short pulses. Here a transducer array is mounted on a towed towfish which sends out the acoustic pulses called the pings. The arrays are mounted in such a way that the acoustic pulses are transmitted towards the sides [56]. When a ping is transmitted, it travels and strikes the sea bed and gets scattered. After transmitting the pulse, the transducer goes into the receive mode to receive scattered signals. The image is built up one line at a time. Thus the signal is transmitted continuously from the either sides of the towfish and the strength of the return signal which is recorded is used to form the image of the scene being illuminated.

#### 2.4.1.1    Advantages

1)    The image produced is of high quality.

#### 2.4.1.2    Disadvantages

1)    Must be moved and cannot look in the forward direction.
2)    They are sensitive to motion.
3)    Does not have the capability to provide accurate information of the depth.

### 2.4.2 Synthetic aperture sonar

Synthetic aperture sonar, based on the principle of synthetic aperture radar, has grown in popularity by producing a number of promising results in sea floor mapping applications [57 58 59]. Synthetic aperture sonar (SAS) illuminates the area to be imaged by sending out acoustic pulses. The platform on which the array elements are mounted moves along a heading direction and the respective received signals are added coherently, hence the name 'Synthetic Array'.

### 2.4.2.1 Advantages

1) Generates a large aperture by coherent addition of received signals.

### 2.4.2.2 Disadvantages

1) Medium instability which arises due to change in pressure, temperature and salinity gives rise to phase ambiguities [59 60 61].
2) Slow mapping rate in order to avoid ambiguity in range and azimuth.
3) Sensitive to platform motion.

### 2.4.3 Doppler Sonar

Doppler sonar is based on the principle that the signal which is transmitted to or received from a moving object experiences a change in frequency [62]. Underwater vehicles need to have an accurate knowledge of their position. This becomes necessary when vehicles remain under water for longer durations. In Doppler sonar, the vehicle's velocity is calculated relative to the sea floor. The transmitter transmits a high frequency narrow beam signal and estimates the center frequency of the returned signal. The transducer generates four beams each at 60 degree depression angle, which are arranged facing opposite directions. By calculating the Doppler shift in the frequency it is possible to determine the velocity of the vehicle. In [62] it has been shown that the Doppler sonar can be used to build a navigational system which determines the coordinates of an underwater vehicle relative to a reference system.

### 2.4.4 Blazed array sonar

Blazed array sonar was invented by R Lee Thompson and W J Zehner [63]. In blazed array sonar, a broadband signal is dispersed in frequency. The dispersed beam forms independent acoustic beams which are transmitted. The transmitted acoustic beam is such that each frequency determines a particular direction. The received signals combine at the receiver but each frequency in the received signal has angular information embedded in it. Image is formed through time-frequency or time-scale processing. Thus this process is a frequency steered acoustic

beamforming. Blazed array sonars have been used for the purpose of two dimensional imaging. They have also been used along with the synthetic aperture sonar for three dimensional imaging [64]. This technology has been licensed to Blueview Technologies and some of the practical results could be seen in [65].

### 2.4.4.1    Advantages

1) Blazed array sonar has the angular information embedded in each of the return frequencies. Thus they can form the image by using time-frequency transforms without any other complicated processing techniques.

### 2.4.4.2    Disadvantages

1) The blazed array sonar covers only a narrow swath. In order to have a large area covered, it is required to have two such arrays fixed in such a way so that it can cover a wide swath. With such an array it is difficult to obtain a good orientation.

### 2.4.5    Multibeam sonar

Multibeam sonar uses high resolution beamforming techniques in order to steer the beam to a particular direction. Multibeam sonar uses separate arrays for transmission and reception [66]. The transmitter array consists of hundreds of elements which produces pencil like beams in each direction [66]. The receiver array interrogates each direction illuminated by the transmitted acoustic pulses for an acoustic return and collects the backscattered data. Multibeam sonar records data in the form of elevation and acoustic backscatter. Multibeam sonar is usually mounted on the ship's hull.

### 2.4.5.1    Advantages

1) The advantage of the multibeam sonar is that they have 100% bottom coverage.
2) They have the ability to cover large areas in a short period of time.

3) Their resolution is independent of the speed of the vessel.

4) In multibeam sonar, the complication which arises from the towing is reduced.

5) Improved coverage in areas which are difficult to survey.

### 2.4.1.5    Disadvantages

1) As the multibeam system uses a large number of transducers, the cost is very high.

2) Multibeam system requires special software and dedicated hardware for processing and storing.

## 2.5    Summary

In this chapter, the basics of sonar have been introduced. The two broad classifications of sonar are then discussed. The working of active sonar along with the equations which govern them is then explained in detail. Some of the common types of active sonar waveforms are then discussed. From the discussion of the other types of signals available, it was found that NLFM require rigorous design and LPM signals have the same performance as the LFM signal when platform motion is not considered. The ambiguity function discussed in the next section showed that LFM chirp is Doppler tolerant to a certain extent.

A block diagram of a generic sonar system was presented. The functionality of each block in the block diagram is described with the beamforming block to be discussed in Chapter 3. This chapter concludes with a brief discussion on the working of few imaging sonars along with their advantages and disadvantages. Understanding the sonar basics and working of different imaging sonars is required in order to build the sonar simulation model.

# Chapter 3

# Direction of Arrival (DOA) Estimation – Some Existing Techniques

In signal processing, direction of arrival (DOA) denotes the direction in which the propagating waves arrive at the receiver. DOA estimation has been studied for a number of years and finds application in diverse fields. In this section some of the literature of DOA associated with sonar is presented. DOA is usually estimated using the beamforming techniques.

Beamforming can be compared to spatial filtering which helps in detecting signals coming from specific direction while attenuating the signals from the other directions. There are number of beamforming methods which can be classified under two general heading

i)      Mechanical beamsteering and

ii)     Electronic beamforming

## 3.1  Mechanical beamsteering

In mechanical beamsteering, a single directional element or sensor array connected in parallel is rotated either mechanically or manually to the required direction. The signals arriving from that direction are processed in order to determine if the information contained is useful.

## 3.2  Electronic beamforming

Electronic beamforming is a process by which the signals from the array sensors are combined coherently by weighing, delaying and summing the signals in order to enhance the detection process [67]. Electronic beamformer can be considered as a spatial filter which concentrates the beam in a particular direction [68]. The electronic beamforming process can be sub-classified as spectral methods and

parametric methods. The spectral methods can be further classified as conventional beamforming and high resolution beamforming.

### 3.2.1 Conventional beamforming

The conventional beamforming includes the delay and sum beamformer. In this type of beamformer, appropriate time delays are inserted and the signals arriving from a particular direction are added coherently. The inserted time delay is proportional to the DOA and hence can be determined. This helps to reinforce the signals coming from a particular direction while the noise contribution is reduced. A simple delay and sum beamformer is shown in figure 3.1
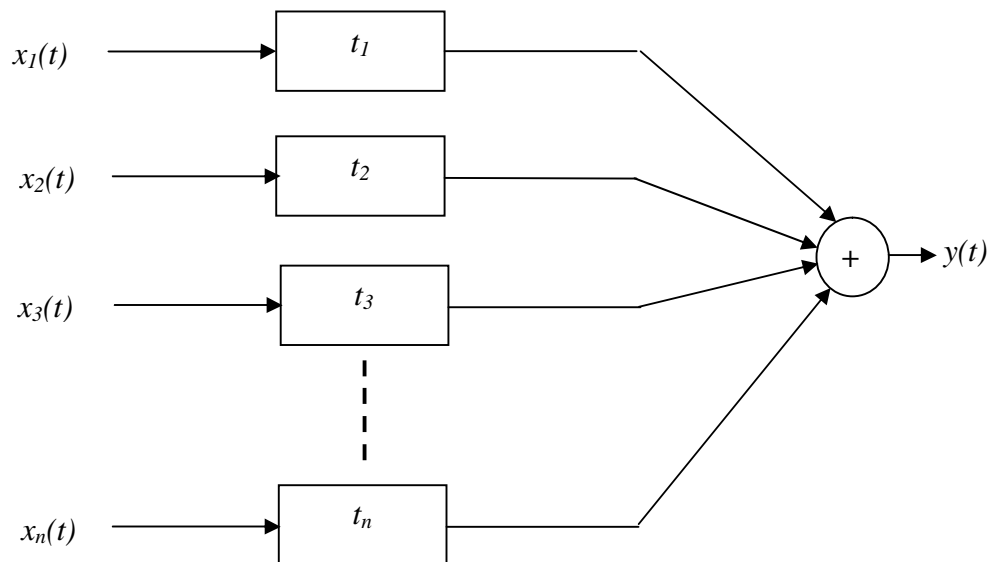


**Figure 3.1 Delay and sum beamformer**

Thus the output $y(t)$ in the delay and sum beamformer can be written as [69]

$$y(t) = \sum_{i=1}^{n} x(t - t_i)$$
3.1

where $t_n$ is the time delay between the first element and the $n^{th}$ element of the array. Let $d$ be the separation between the array elements, then it can be shown

that by adjusting $t_i$ in equation 3.1, the signals from various directions can be aligned and coherently added [69]

$$t_n = \frac{(n-1)d \sin \theta}{c} \qquad\qquad 3.2$$

$\theta$ is the steering angle.

### 3.2.2 High resolution beamforming

For applications that demand high resolution it is not possible to use conventional beamforming technique. Other types of high resolution beamforming methods are available for this purpose. The main idea behind this type of beamformer is to localize the signal coming from a particular direction by maximizing the power in that direction. Thus the array response is the linear combination of weighed outputs from the sensors. This can be mathematically explained as follows [70]

Let $\mathbf{x}(n) = [x_1(n) \; x_2(n) \ldots\ldots\ldots\ldots x_n(n)]^T$ be the inputs.

$$\mathbf{x}(n) = \mathbf{a}(\theta)s(n) + \mathbf{v}(n) \qquad\qquad 3.3$$

where $s(n)$ is the signal impinging on the array and $\mathbf{v}(n)$ is the added noise. The vector $\mathbf{a}(\theta)$ is called the steering vector and is given by the equation [70]

$$\boldsymbol{a}(\theta) = \left[ 1 \quad e^{\frac{j2\pi d \sin \theta}{\lambda}} \quad e^{\frac{j4\pi d \sin \theta}{\lambda}} \quad . \; . \; . \quad e^{\frac{j2\pi(n-1)d \sin \theta}{\lambda}} \right]^T \qquad\qquad 3.4$$

Suppose there are $M$ signals impinging on the array then equation 3.3 can be written as

$$\mathbf{x}(n) = \mathbf{A}(\theta)\mathbf{s}(n) + \mathbf{v}(n) \qquad\qquad 3.5$$

where

$$\mathbf{A}(\theta) = \begin{bmatrix} \mathbf{a}(\theta_1) & \mathbf{a}(\theta_2) & \mathbf{a}(\theta_3) & . & . & . & \mathbf{a}(\theta_M) \end{bmatrix}$$ 3.6

$\theta_1, \theta_2, ....., \theta_M$ are the DOA of the $M$ signals impinging on the array and $\mathbf{s}(n)$ is a matrix containing $M$ signals. Let $y(n)$ be the output of the beamformer. Then the relation between output and input is given by [70]

$$y(n) = \sum_{i=1}^{n} w_i^* x_i(n)$$ 3.7

or,

$$y(n) = \mathbf{w}^{\mathbf{H}} \mathbf{x}(n)$$ 3.8

$\mathbf{w}^{\mathbf{H}}$ is the weight vector and the superscript $\mathbf{H}$ represents the Hermitian transpose. The power $P(\mathbf{w})$ is calculated from the following equation [70]

$$P(\mathbf{w}) = \frac{1}{N} \sum_{n=1}^{N} |y(n)|^2$$ 3.9

$$P(\mathbf{w}) = \frac{1}{N} \sum_{n=1}^{N} w^{\mathbf{H}} \mathbf{x}(n) \mathbf{x}^{\mathbf{H}}(n) \mathbf{w}$$ 3.10

$$P(\mathbf{w}) = \mathbf{w}^{\mathbf{H}} \hat{\mathbf{R}} \mathbf{w}$$ 3.11

where $N$ is total number of samples and $\hat{\mathbf{R}}$ is the data covariance matrix [70]

$$\hat{\mathbf{R}} = \frac{1}{N} \sum_{i=1}^{N} \mathbf{x}(n) \mathbf{x}^{\mathbf{H}}(n)$$ 3.12

This forms the basis of the principle behind most of the high resolution beamformers. Different beamformers use different values of the weight vector **w**.

### 3.2.2.1 Minimum Variance Distortionless Response (MVDR)

The goal of MVDR beamformer is to optimize its response so that the output contains minimum contributions due to the noise and the signals arriving from direction other than the required directions. [70 71]. For this purpose it is required that the weights in equation 3.11 are chosen so that the signals arriving from the required direction is passed on with a specified gain. Thus the MVDR weights can be obtained using the following criterion

$$\min_{w} P(\mathbf{w}) \text{ subject to the condition } \mathbf{w}^H \mathbf{a}(\theta) = 1 \qquad 3.13$$

Thus the weight matrix is obtained to be [68 71 72]

$$\mathbf{w}_{MVDR} = \frac{\hat{\mathbf{R}}^{-1}\mathbf{a}(\theta)}{\mathbf{a}^H(\theta)\hat{\mathbf{R}}^{-1}\mathbf{a}(\theta)} \qquad 3.14$$

Substituting equation 3.14 in equation 3.11

$$P_{MVDR}(\mathbf{w}) = \frac{1}{\mathbf{a}^H(\theta)\hat{\mathbf{R}}^{-1}\mathbf{a}(\theta)} \qquad 3.15$$

### 3.2.2.2 Eigen-Vector beamforming

The equation for this type of beamformer can be obtained by modifying the equation for the MVDR beamformer. The data covariance matrix can be written in the form [73 74]

$$\hat{\mathbf{R}} = \sum_{i=1}^{n} q_i \mathbf{v}_i \mathbf{v}_i^H \qquad 3.16$$

where $q_i$, $\{i = 1,2,3....n\}$ are the eigen values and the corresponding eigen vectors are given by $\mathbf{v}_i$, $\{i = 1,2,3....n\}$. The data covariance matrix is partitioned into signal subspace and noise subspace matrices [73 74]. Equation 3.16 can be written as

$$\hat{\mathbf{R}} = \mathbf{V}\mathbf{Q}\mathbf{V}^{\mathbf{H}} \qquad\qquad 3.17$$

$$\hat{\mathbf{R}} = \mathbf{V_s}\mathbf{Q_s}\mathbf{V_s^{H}} + \mathbf{V_n}\mathbf{Q_n}\mathbf{V_n^{H}} \qquad\qquad 3.18$$

where $\mathbf{V}_s$ and $\mathbf{Q}_s$ are the eigenvectors and eigenvalues of signal subspace. $\mathbf{V}_n$ and $\mathbf{Q}_n$ are the eigenvector and eigenvalues of noise subspace. The noise subspace is orthogonal to the signal subspace and hence orthogonal to the steering vectors which lie in the signal subspace [73 74]. Hence

$$P_{Eigen}(\mathbf{w}) = \frac{1}{\mathbf{a}^{H}(\theta)\mathbf{V}_n\mathbf{Q}_n^{-1}\mathbf{V}_n^{H}\mathbf{a}(\theta)} \qquad\qquad 3.19$$

One advantage of decomposing the $\hat{\mathbf{R}}$ matrix into eigenvectors and eigenvalues is that the inverse of the covariance matrix is the inverse of its eigenvalues. The eigenvectors of the covariance matrix and its inverse are the same. It should be noted from equation 3.19 that only the noise subspace is considered. Writing the equation of the beamformer in terms of noise subspace values as in equation 3.19 improves the angular resolution [73]. The disadvantage of this method is that it requires knowing the number of sources in order to divide the matrix into signal and noise subspace [74].

### 3.2.2.3   MUSIC algorithm

The Multiple Signal Classification is also a noise subspace frequency estimator method [21]. The Music algorithm can be obtained by further modifying the equation for the Eigen Vector type of beamforming. The equation for the Music algorithm can be obtained by making the eigen values of the noise $\mathbf{Q}_n = \mathbf{I}$ thus making it simpler so that it is not necessary to calculate the inverse. Here the

47

smallest eigen values which correspond to noise are set to unity which causes it to whiten those portions of the signal that do not correspond to the signal [73]. MUSIC has the same resolution capability as that of eigen vector beamformer. The equation for the power spectrum of MUSIC can be given as [73 74 75 76]

$$P_{Music}(\mathbf{w}) = \frac{1}{\mathbf{a}^H(\theta)\mathbf{V}_n\mathbf{V}_n^H\mathbf{a}(\theta)}$$

3.20

Thus it is possible to determine the DOA ($\theta$) of the signal by finding the peak of the Music spectrum. MUSIC is popular for its generality i.e. they can be applied to arbitrary but known configurations of the array [77]. The problem with MUSIC is that the array has to be calibrated [77]. MUSIC is found to underperform at very low SNRs [77].

### 3.2.2.4   ESPRIT

Estimation of Signal Parameters via Rotational Invariance Technique (ESPRIT) is another high resolution DOA determination technique. The method of determining the DOA using this technique can be described as follows. ESPRIT algorithm assumes that the $N$ element array is divided into identical subarrays each having elements $N_1$ and $N_2$ [77]. The individual elements in each subarray can have arbitary responses provided that each one have an identical twin or doublets in the companion subarray [77]. The doublets are assumed to be separated by a distance $d$. The signal received given by the equation 3.5 can be written as [77]

$$\mathbf{x}(n) = \begin{bmatrix} \mathbf{A}_1(\theta) \\ \mathbf{A}_2(\theta) \end{bmatrix}\mathbf{s}(n) + \begin{bmatrix} \mathbf{v}_1(n) \\ \mathbf{v}_2(n) \end{bmatrix}$$

3.21

where $\mathbf{A}_1(\theta)$ and $\mathbf{A}_2(\theta)$ are the array manifold vectors for the subarrays. Where

$$\mathbf{A}(\theta) = \begin{bmatrix} \mathbf{A}_1(\theta) \\ Last \end{bmatrix} = \begin{bmatrix} First \\ \mathbf{A}_2(\theta) \end{bmatrix}$$

3.22

where *First* and *Last* indicates the first and last rows of the $A(\theta)$ matrix. Thus [70 77]

$$\mathbf{A}_2 = \mathbf{A}_1 \mathbf{\Phi} \tag{3.23}$$

where $\mathbf{\Phi}$ is a diagonal matrix with elements $e^{\frac{j2\pi}{\lambda} md \sin \theta}$ where $m = 1...M$.

If $\mathbf{V_s}$ is the eigenvectors of the $M$ largest eigenvalues of the received signal auto-covariance matrix, it can be shown that [70 77]

$$\mathbf{V}_s = \begin{bmatrix} \mathbf{V}_1 \\ \mathbf{V}_2 \end{bmatrix} = \begin{bmatrix} \mathbf{A}_1(\theta) \\ \mathbf{A}_1(\theta)\mathbf{\Phi} \end{bmatrix} \mathbf{T} \tag{3.24}$$

where $\mathbf{T}$ is some full rank matrix. Writing $\mathbf{V_2}$ in terms of $\mathbf{V_1}$

$$\mathbf{V}_2 = \mathbf{V}_1 \mathbf{T}^{-1} \mathbf{\Phi} \mathbf{T} \tag{3.25}$$

$$\mathbf{V}_2 = \mathbf{V}_1 \mathbf{\Psi} \tag{3.26}$$

where

$$\mathbf{\Psi} = \mathbf{T}^{-1} \mathbf{\Phi} \mathbf{T} \tag{3.27}$$

Thus [70 77]

$$\mathbf{\Phi} = \mathbf{T} \mathbf{\Psi} \mathbf{T}^{-1} \tag{3.28}$$

Thus, since $\mathbf{\Phi}$ and $\mathbf{\Psi}$ are related by a similarity transformation, the eigenvalues of $\mathbf{\Psi}$ must be equal to the diagonal elements of $\mathbf{\Phi}$. Furthermore, the columns of $\mathbf{T}$ are the eigenvectors of $\mathbf{\Phi}$ [70 77]. Thus the DOA can be estimated from the eigenvalues of $\mathbf{\Psi}.$

ESPRIT uses the underlying data model just like MUSIC but overcomes the disadvantages of MUSIC by using the constraint of displacement invariance [77] i.e. sensor occurs in matched pairs. It can be seen that the equation for determining the value of DOA is independent of $\mathbf{A}(\theta)$ and hence calibration of the array is not required. ESPRIT is less sensitive to array imperfections than MUSIC [77].

### 3.2.3 Parametric beamforming

The parametric method of beamforming uses the fact that the medium behaves non-linearly in the presence of two high pressure sound levels [44 78 79 80 81 82 83]. This non-linear nature of the medium is used to generate the sum and the difference frequencies [44 78 79 80 81 82 83]. As the high frequencies are attenuated faster, the sum components are absorbed by the medium and the result would contain the difference component [44 78 79 80 81 82 83]. They have a very narrow beam which is as narrow as or narrower than the primary sources that are used for its generation. The sidelobe level is very small [44 78 79 80 81 82 83]. The beamwidth at the difference frequency depends on the two high primary frequencies and the absorption coefficient of the medium at these frequencies [44 83].

### 3.3 Evaluation of beamforming techniques

The disadvantage of mechanical beamformers is that they are slow. Hence there is a possibility that by the time these arrays are manually rotated to the required direction any useful signals would be lost.

The conventional delay and sum beamformer requires a large number of time delay elements to steer the beam. This would make it bulky. The resolution of this beamformer depends on the length of the array and hence they cannot be used to form a narrow beam [77]. This beamformer cannot resolve signal coming from

electrical angles less than $\dfrac{2\pi}{N}$ [77]. This is the weakness of the method and hence this beamformer cannot be used for high resolution purposes.

The high resolution beamformers provide good resolution in determining the DOA. But in spite of all the advantages it offers, they have their own limitations. One major disadvantage is that these beamformers require the estimation of auto covariance matrix. The estimation of this matrix is more accurate if there are large number of signal samples. With improper estimation the performance of these arrays degrades and it might also result in the cancellation of the desired signal. The high resolution obtained using these beamformeer is due to large number of array elements. As stated in Chapter 1 one of the main objective of this work is to reduce the cost of the hardware and by having hundreds of transducers it becomes contradictory to our objective.

As discussed in section 3.2, the high resolution beamformers require the array to be calibrated. The Eigen-Vector and MUSIC beamformer achieves better resolution by using the condition that the signal and noise subspace are orthogonal to each other. Thus the knowledge of number of sources is required to divide the auto-correlation matrix into signal and noise subspace. Thus if the number of sources are not known in advance, the performance of these beamformers degrades.

The high resolution beamformers are mainly used in narrowband signal applications. In the case of broadband signals, they have to be treated as a combination of narrowband signals [20, 21]. Thus the application of these high resolution beamforming methods to broadband signals demands large memory requirements. This is a distinct disadvantage when it is required to analyse data at sea-trials. All the beamformers discussed suffer from ambiguity in determination of DOA if the separation between the array elements is greater than $\dfrac{\lambda}{2}$.

The drawback of parametric array principle is that it is difficult to generate complicated waveforms [83]. Parametric arrays are not suitable for multibeam

operations [83]. Another problem with this type of beamformer is that only a small portion of the acoustic power generated at the primary frequencies appears at the difference frequency [44 82 83]. Increasing the power in primary frequencies in order to increase the difference frequency power would result in cavitation [44 82]. Another disadvantage of parametric sonar is that it requires a highly linear amplifier at high powers [84].

## 3.4 Broadband signals vs Narrowband signals

The active sonar systems available assume that the signal used is narrowband. Many problems like range resolution etc which arise due to the use of narrowband signals can be avoided by the use of broadband signals. There is no standard definition to classify the signal as narrowband or broadband. The best way to classify a signal as narrowband or broadband is using their fractional bandwidth. Fractional bandwidth can be defined as the ratio of bandwidth to its center frequency. The definition of fractional bandwidth is given mathematically as follows [85]

$$FB = \frac{2(f_h - f_l)}{(f_h + f_l)} \qquad\qquad 3.29$$

where $FB$ is the fractional bandwidth, $f_h$ is the higher side frequency; $f_l$ is the lower side frequency. Thus the signal can be classified as a broadband signal if the ratio exceeds a certain value otherwise it is considered as a narrowband signal.

Bandwidth can be defined as a spectral region where most of the signal energy is concentrated. For detecting targets at long distances, sufficient energy should be backscattered from the target. Increasing the transmitted signal power is one way to make certain that sufficient energy returns from the target. For narrowband signals, the peak power transmitted can be increased by using a pulse with a very long duration. Though increasing the pulse width increases the amount of detectable energy scattered by the target, this would in turn further degrade the range resolution, as the range resolution depends on the pulse length of the signal.

Broadband signals can be of long duration. The range resolution of the broadband signals depends on the bandwidth of the signal used. Hence the range resolution of the broadband signals is not affected by the increase in the signal length.

Thus the use of narrowband signals presents a trade off between reliable detection and better range resolution. Both factors are important and hence it would be advantageous to use signals with greater bandwidth.

### 3.4.1   Comparison of broadband signals with narrowband signals

Table 3.1 provides a comparison between broadband signals and narrowband signals.

| *Broadband Signals* | *Narrowband Signals* |
|---|---|
| *Time delay processing:* Because the center frequency is comparable to the signal bandwidth, phase difference cannot be used to determine DOA. Thus time difference has to be used and this aids in avoiding problems like phase ambiguity. | *Phase shift processing:* Narrowband signals uses phase shift between the received signals to determine DOA. Using phase difference gives rise to phase ambiguity if the phase difference between the signals is outside $\pm\pi$ |
| *Rich Target Returns:* The target returns contain information regarding the target at different frequencies. | *Simple target returns:* The bandwidth of the narrowband signals being very small, the amount of information returned is also small. |
| *Wideband signals provide better noise immunity [86]* | *Susceptible to noise* |
| Large bandwidth enables the pulse energy to be distributed over the range of frequencies and hence the pulse length can be short. | Narrowband signals require a longer duration to have the same amount of energy as that of the broadband signals. |

**Table 3.1 Comparison of broadband and narrowband signals**

## 3.5    Near-field and Far-field

In most of the cases, for the purpose of ease in calculation, it is usually assumed that the target which backscatters the signals is situated in the far-field. The echoes from the targets situated in the near field would be spherical and hence the assumption of the return signals to be a plane wave would lead to the necessity of applying error-corrections.

In [87], definition of near-field and far-field is given as

$$0 \leq Near - field \leq 2d \qquad\qquad 3.30$$

$$Far - Field \geq \frac{2d^2}{\lambda} \qquad\qquad 3.31$$

where $d$ is the aperture length which is the distance between the two hydrophone elements and $\lambda$ is the wavelength. The wavelength of a chirp signal whose frequency varies linearly from 200 kHz-300 kHz is calculated at the center frequency $f_c$. The distance $d$ (aperture length) between the array elements is assumed to be 0.3m. Thus the center frequency $f_c$ is calculated using the formula,

$$f_c = \frac{f_l + f_h}{2} = 250kHz \qquad\qquad 3.32$$

From the relationship between the velocity, frequency and wavelength,

$$c = f\lambda \qquad\qquad 3.33$$

$$\lambda = \frac{c}{f} = \frac{1500}{f_c} \qquad\qquad 3.34$$

$$= 0.006\text{m} \qquad\qquad 3.35$$

Thus according to far field definition [87], the near-field ends at *2d* i.e. 0.6m and the far-field begins at

$$Far - Field = \frac{2d^2}{\lambda} \qquad\qquad 3.36$$

$$= \frac{2 \times 0.3^2}{0.006} = 30m \qquad\qquad 3.37$$

The explanations of near-field and far-field are diagrammatically shown in figure 3.2 and figure 3.3 respectively. Figure 3.2 and figure 3.3 shows how the sound waves reflected from a target located at the near-field and the far-field would appear at the receivers. When the target is located in the near-field, it is seen that the sound waves arriving at the receivers cannot be considered as a plane wave. But when the target is located in the far-field, the separation between the two receivers is very small when compared to the distance to the target and hence the points on the spherical surface impinging on the two receivers can be considered close enough in order to approximate them into a plane wave. Thus in the case of a 0.3m aperture spacing the far-field is supposed to start at 30m and therefore any acoustic waves backscattered from a target beyond 30m can be assumed as plane waves. Returns from a target at the near-field can be processed by taking into account the spherical nature of the returned signals.



**Figure 3.2 Near-field**

$Rx_1$     d     $Rx_2$

Far-Field $(>2d^2/\lambda)$

Target
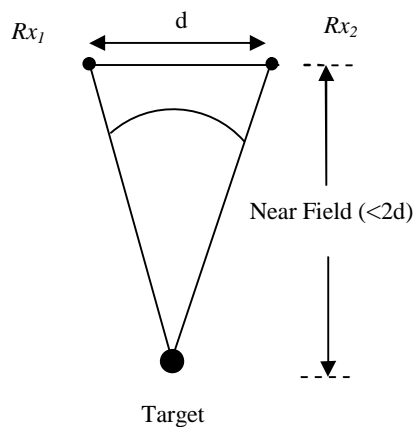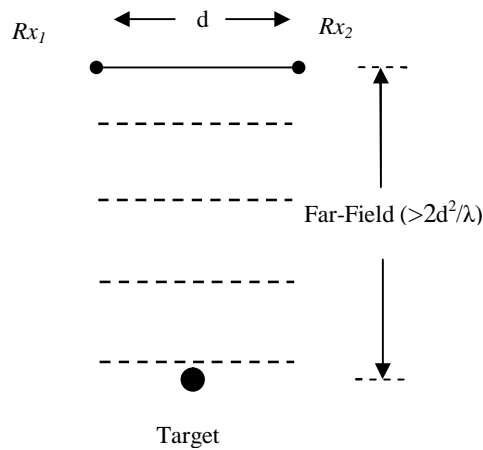
**Figure 3.3 Far-field**

## 3.6    Summary

This chapter explains the key DOA algorithms available in literature. It was found from the literature that these beamforming algorithms work well for narrowband signals due to their reliance on processing using phase difference. In order to use these beamformers with broadband signals, the signals have to be divided into narrowband signals and considered separately. Applying these beamformers to the sparse array considered in this project, the problem of phase ambiguity would arise as the array used has elements separated by $d >> \lambda$. It was also found that these high resolution beamformers require reliable estimation of the noise correlation matrix which is possible only in the presence of large number of array elements. With the number of array elements in this project very small, the estimation of the covariance matrix would be prone to errors. For these reasons the existing high resolution algorithms was found unsuitable for this project.

Broadband signals and their comparison with narrowband signals are presented in the next section. The chapter concludes with the explanation of the near and far field criterion which is useful for classifying whether the backscattered signal arriving at the receivers from the target can be approximated to plane waves.

# Chapter 4
# Direction of Arrival Estimation and Image Formation

From the description of beamforming processes in chapter 3, it is clear that most work is based on narrowband assumption. Hence the spacing between the array elements cannot be greater than $\lambda/2$. It has been noted in [30 86 87] that widely spaced array elements have more tolerance in measurements and hence more accuracy. But widely spaced array elements would give rise to phase ambiguity. Thus for wider array element spacing time difference of arrival has to be used.

Using broadband signals it is possible to accurately determine the time difference of arrival of signals between two receivers. Thus with broadband signals, problems which arise due to phase ambiguities can be avoided. Hence widely spaced receiver elements can be used thus guaranteeing better performance [30 86 87]. Keeping in view the other advantages of broadband signals over narrowband signals, the use of broadband signals was selected.

## 4.1    Structure of receiver

Figure 4.1 shows the block diagram of the receiver structure used in this research. Figure 4.1 shows the receiver structure having two channels.
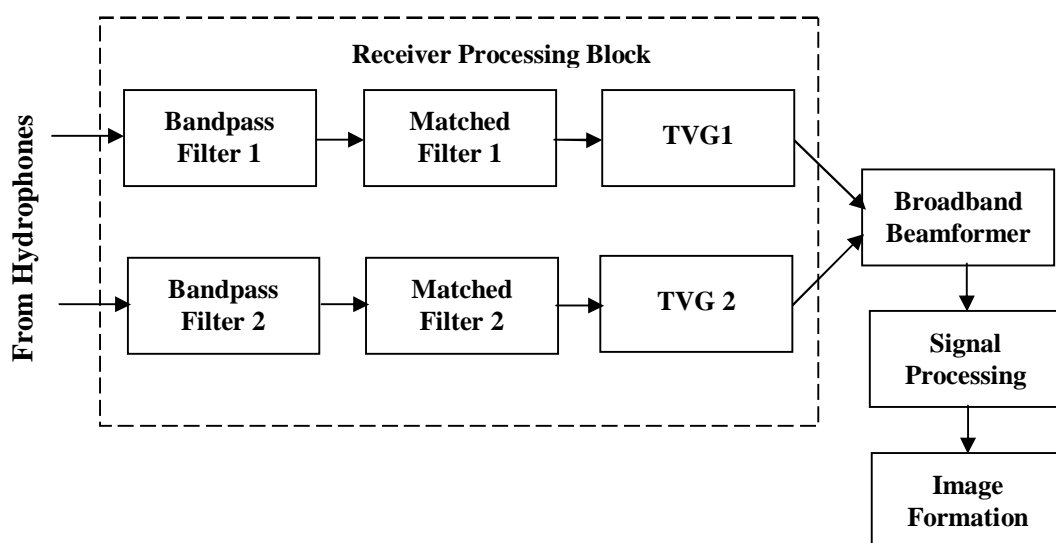


**Figure 4.1 Structure of receiver**

Figure 4.1 shows the structure of a receiver having two channels. The signals from the hydrophones are passed on to the receiver processing block. The receiver processing block contains i) Bandpass filter ii) Matched filter and iii) Time Varying Gain (TVG). As described in Chapter 2, section 2.3, the hydrophones convert pressure signals impinging on them into electrical signals. The signals from each hydrophone then pass through the bandpass filter where unwanted signals are removed.

### 4.1.1   Matched filter operation

Let the transmitted signal be $s(t)$. As described in Chapter 2 section 2.3.4, the impulse response of the matched filter is

$$h(t) = s^*(T - t) \hspace{4cm} 4.1$$

The signals considered in this project are real signals. Therefore the impulse response of the matched filter would be time reversed form of the transmitted signal. Let $x_{MF1}(t)$ and $x_{MF2}(t)$ be the matched filter responses from the channel 1 and channel 2. Therefore,

$$x_{MF1}(t) = h(t) * \tilde{s}_1(t) \hspace{3cm} 4.2$$

$$x_{MF2}(t) = h(t) * \tilde{s}_2(t) \hspace{3cm} 4.3$$

where $\tilde{s}_1(t)$ and $\tilde{s}_2(t)$ are the signals obtained after passing through the bandpass filter. Matched filtering provides a processing gain of $B\tau$ where $B$ is the bandwidth of the transmitted signal and $\tau$ is the signal duration. For a wide bandwidth signal the time bandwidth product is always greater than unity. Processing gain can also be defined as the ratio of the signal duration before compression to that after compression.

Consider a chirp signal sweeping from 200 kHz – 300 kHz in 5ms. The bandwidth of the signal is 100 kHz. The time bandwidth product is

$$B \times \tau = 100kHz \times 5ms = 500 \qquad\qquad 4.4$$

Thus there is a processing gain of 500. This is demonstrated using figure 4.2 to figure 4.5.
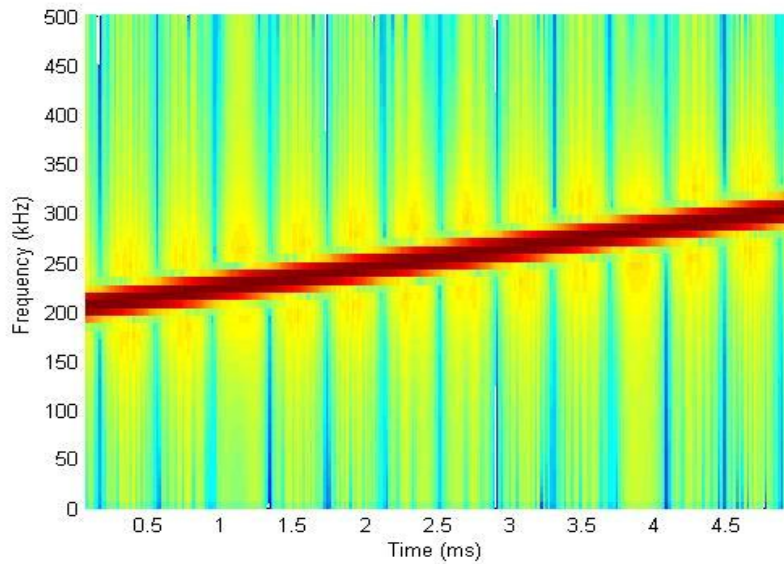


**Figure 4.2 Spectrogram of a 100 kHz bandwidth chirp signal**
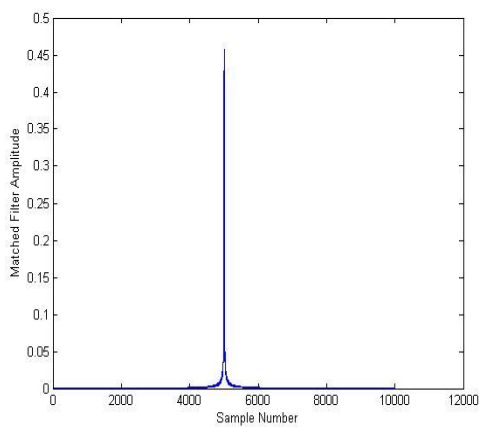


| **Figure 4.3 Matched filter output** | **Figure 4.4 Matched filter output in dB** |
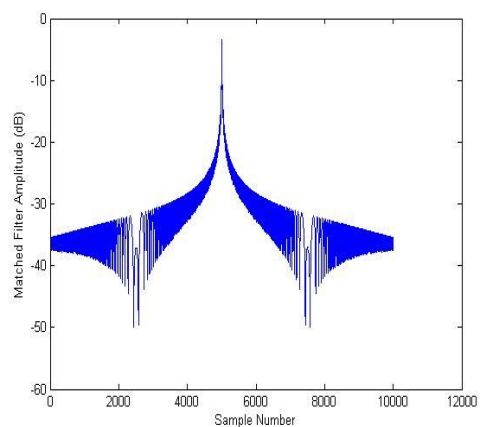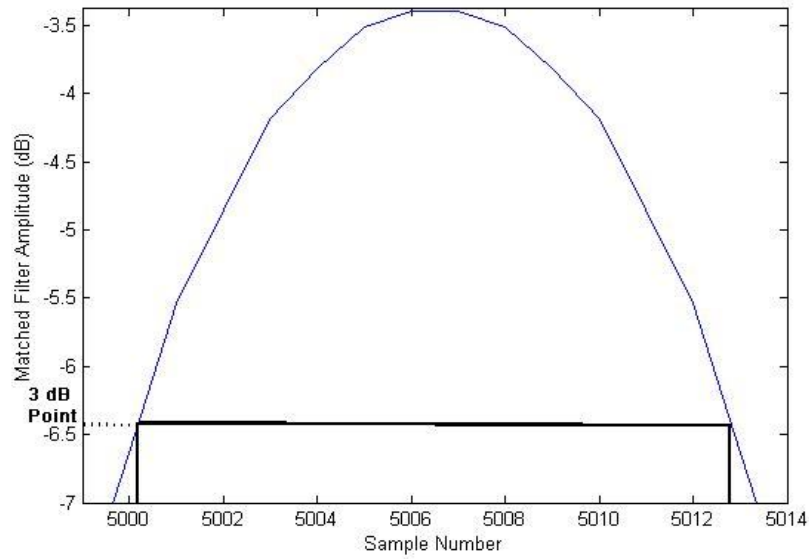
**Figure 4.5 Matched filter output in dB showing 3 dB point**

Figure 4.5 is the expanded version of matched filter output in dB in figure 4.4 showing the 3 dB point. The mainlobe size is approximately 12.5 samples. The sampling frequency used was 1 MHz. Thus the size of compressed pulse (at -3 dB) is 12 μs. The compression ratio is

$$Ratio = \frac{5ms}{12.5\mu s} \approx 400 \qquad\qquad 4.5$$

which is almost equal to the time bandwidth product. Thus it is seen that the pulse is compressed by a factor determined by the compression ratio.

## 4.1.2   Time Varying Gain (TVG)

Because of the spreading losses the signal peaks formed after the matched filtering process would be very small. In order to compensate for the loss a TVG amplifier is applied to the output of the matched filter. The gain of the TVG amplifier varies with time. From section 2.1.2.1, the loss due to spherical spreading is proportional to square of the distance travelled by the signal. Hence to compensate for the spherical spreading loss, the gain of the amplifier varies as

the square of the distance travelled to the target. The gain of the amplifier can be given by the following equation.

$$G(t) = r(t)^2 \qquad\qquad 4.6$$

$$G(t) = \left[\frac{ct}{2}\right]^2 \qquad\qquad 4.7$$

In the above equation $r(t)$ is the distance travelled by the signal. Equation 4.7 gives the square of the distance travelled to the target. The travel time $t$ can be determined by

$$t = \frac{n}{F} \qquad\qquad 4.8$$

where $n$ is the sample number and $F$ is the sampling frequency. Applying the TVG to the matched filter output in equation 4.2 and equation 4.3,

$$x_{TVG1}(t) = G(t)x_{MF1}(t) \qquad\qquad 4.9$$

$$x_{TVG2}(t) = G(t)x_{MF2}(t) \qquad\qquad 4.10$$

where $x_{TVG1}(t)$ and $x_{TVG2}(t)$ are the outputs of the TVG amplifier. This output is then used as the input to the beamforming block. The variation of the gain of TVG amplifier w.r.t. time is shown in figure 4.6. Figure 4.6 shows time in milliseconds (*ms*) along the X axis and gain along the Y axis.

The process of estimating the DOA and image formation is described in the next section.
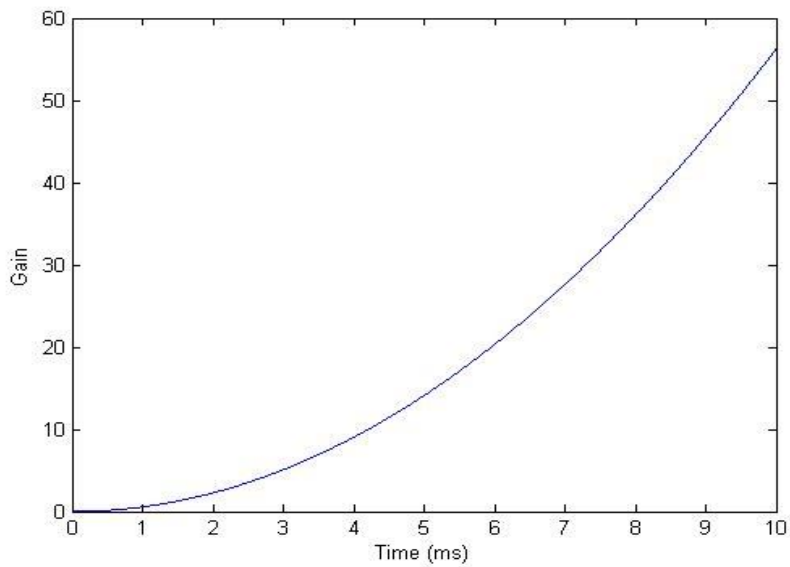
**Figure 4.6 Time varying gain**

## 4.2 Direction of arrival (DOA) estimation for broadband signals

In this section the relation governing the DOA estimation is described. Also the method used in the project to determine the DOA and the target range is explained in detail.

### 4.2.1 Equation to determine DOA

The transmitter receiver geometry for the purpose of deriving the relationship between DOA and the time difference of arrival is shown in figure 4.7. The assumption made is that the target is located far enough so that the signals arriving at the receivers $Rx_1$ and $Rx_2$ can be considered as a plane wave i.e. it is assumed that the target is located in the far-field.
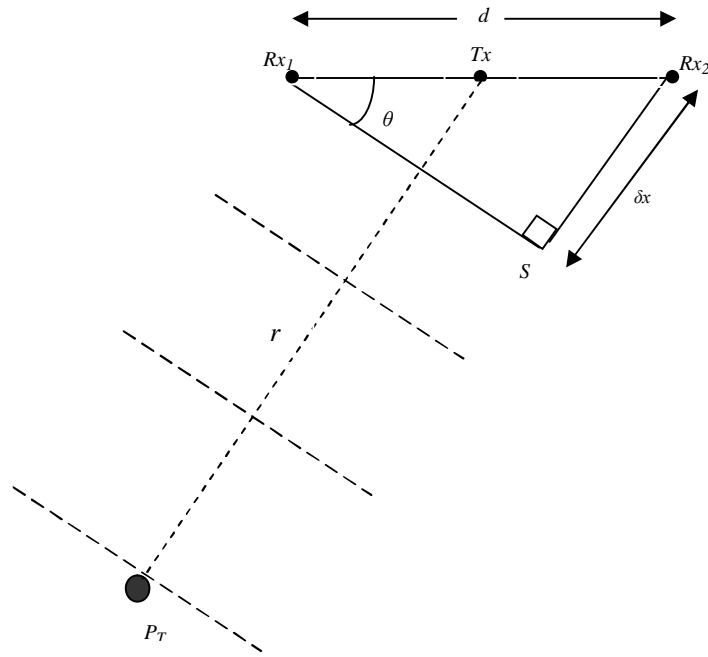
**Figure 4.7 Transmitter-Receiver geometry**

Let $P_T$ be a point target at a distance of *r metres* from the transmitter *Tx*. Let $Rx_1$ and $Rx_2$ be the two receivers which are at a distance *d* apart. The condition for far-field $(2d^2/\lambda) <<r$ is assumed making it possible to treat the signals arriving at the receiver as plane waves. $\theta$ is the DOA and is the angle made by the plane waves with the array axis. $\delta x$ is the extra distance that has to be travelled by the plane wave in order to reach the receiver $Rx_2$.

The distance $\delta x$ can be written as

$$\delta x = c \delta t \qquad\qquad 4.11$$

where $\delta t$ is the time taken to travel the extra distance of $\delta x$ and $c$ is the speed of sound in water which is 1500m/s.

In order to define $\delta t$ it is necessary to define the sampling time. Let $T$ be the sampling interval and let $n_d$ be the difference in number of samples due to $\delta x$. Thus the equation for $\delta t$ can be written as

$$\delta t = n_d (T \pm \Delta T) \qquad\qquad 4.12$$

where $\Delta T$ is the error due to finite clock accuracy. Assuming a high sampling frequency equation 4.12 can be written as

$$\delta t = n_d T \qquad\qquad 4.13$$

Substituting equation 4.13 in equation 4.11, $\delta x$ can be written as

$$\delta x = c n_d T \qquad\qquad 4.14$$

The far-field assumption makes it possible to assume the triangle $S\text{-}Rx_1\text{-}Rx_2$ in figure 4.7 to be a right triangle with the angle $S$ to be $90^0$. Thus from the right triangle $S\text{-}Rx_1\text{-}Rx_2$,

$$\sin \theta = \frac{\delta x}{d} \qquad\qquad 4.15$$

$$\sin \theta = \frac{c n_d T}{d} \qquad\qquad 4.16$$

From the above equation, it is possible to calculate the DOA of the signal. Hence

$$\theta = \sin^{-1}\left(\frac{c n_d T}{d}\right) \qquad\qquad 4.17$$

Thus, by knowing the separation between the receivers, the speed of sound in water, the sampling interval and the difference in number of samples due to the extra distance $\delta x$ traveled in order to reach the receiver $Rx_2$, it is possible to determine the DOA of the signal. In the above equation all the parameters are known except the value of $n_d$ that has to be determined. It is assumed that the sampling frequency is high so that the error in the determination of $n_d$ is low. $n_d$ is

proportional to the delay time of one signal w.r.t the other and hence its value is determined using correlation which is explained in the following paragraphs.

### 4.2.2 Correlation

Correlation can be defined as a mathematical process of comparing one signal with the other or more signals in order to establish the similarity between them [87 88]. The process of correlation involves successive shifting of signals and then finding the comparison of the signal for each shift. Thus correlation is a way to determine the presence of a signal pattern in a noisy background. If there are two signals $x_{TVG1}(t)$ and $x_{TVG2}(t)$ then the correlation process can be written mathematically using the following equation

$$R_{ss}(\tau) = \lim_{T \to \infty} \frac{1}{T} \int_0^T x_{TVG1}(t) x_{TVG2}(t + \tau) dt \qquad 4.18$$

which can be written as

$$R_{ss}(l) = \sum_{n=-\infty}^{\infty} x_{TVG1}(n) x_{TVG2}(n - l) \qquad 4.19$$

where $R_{ss}(l)$ is the correlation result. In the above equation, $l$ determines the amount of lag or lead in the signal. When the two signals are similar a peak is formed whose position is dependent on the amount of lead or lag between the signals.

The relationship between correlation and convolution can be given by using equation 4.20.

$$R_{ss}(n) = x_{TVG1}(n) * x_{TVG2}(-n) \qquad 4.20$$

The result from the correlation will have both positive and negative peaks. In order to determine the delay an absolute value function is applied to the result which is expressed as

$$R_{ss1}(l) = |R_{ss}(l)| \qquad\qquad 4.21$$

From equation 4.19 when two signals are correlated, the first signal is searched for presence of a pattern similar to that in the second signal. This can be performed by introducing delay in the second signal and sliding it over the first signal. If these signals are outputs from two hydrophone elements then the position of the peak could be used to obtain the value of the delay of one signal w.r.t the other. Thus from the above equations, the lead or lag $l$ gives the number of samples, $n_d$, by which the plane wave arriving at one hydrophone leads or lags the signal arriving at the other hydrophone.

It is possible to group the correlation result under three cases. In the first case, the signals arrive at both the receivers simultaneously. In the second case, the signal which arrives at $Rx_1$ leads the signal arriving at $Rx_2$. The third case is where the signal which arrives at $Rx_1$ lags behind the signal arriving at $Rx_2$. The following paragraphs examine each of these cases in more detail with some examples for correlation.

*Case 1: Signals arriving at both the receivers simultaneously*

When signals arrive at the receivers $Rx_1$ and $Rx_2$ at the same time they are in phase with each other. Thus the correlation peak would be formed at the center of the correlation result which corresponds to zero delay. This configuration of the target and the receivers is shown diagrammatically in figure 4.8.
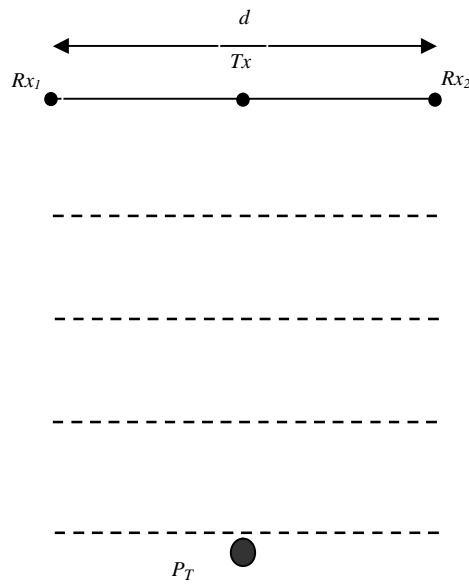
**Figure 4.8 Signals arriving at the same time**

For the purpose of demonstration, the correlation of a simulated random signal is shown in figure 4.9. A random signal is chosen as the returns from the target for a broadband signal would be more or less like that of a random signal. The number of samples assumed was 600.
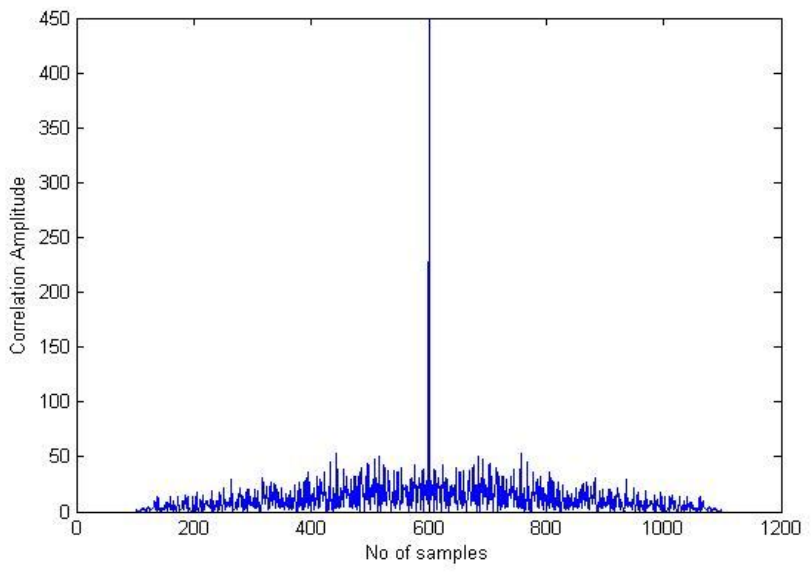


**Figure 4.9 Correlation result of the signals arriving at the same time**

The length of the correlated signal is given by

$$L = L_1 + L_2 - 1 \qquad\qquad\qquad 4.22$$

$$= 600 + 600 - 1 \qquad\qquad\qquad 4.23$$

$$= 1199 \text{ samples long} \qquad\qquad\qquad 4.24$$

where $L$ is the total length of the correlated result, $L_1$ and $L_2$ are the lengths of the signals being correlated. Since the signals arrive at the receivers at the same time, the peak would be formed at the center. It could be verified that the total length of the result is 1199 samples and the peak would be formed at $\approx 600^{th}$ sample.

*Case 2: Signal arriving at receiver $Rx_1$ before $Rx_2$*

The configuration for which the signal arriving at $Rx_1$ leads $Rx_2$ is shown diagrammatically in figure 4.10.
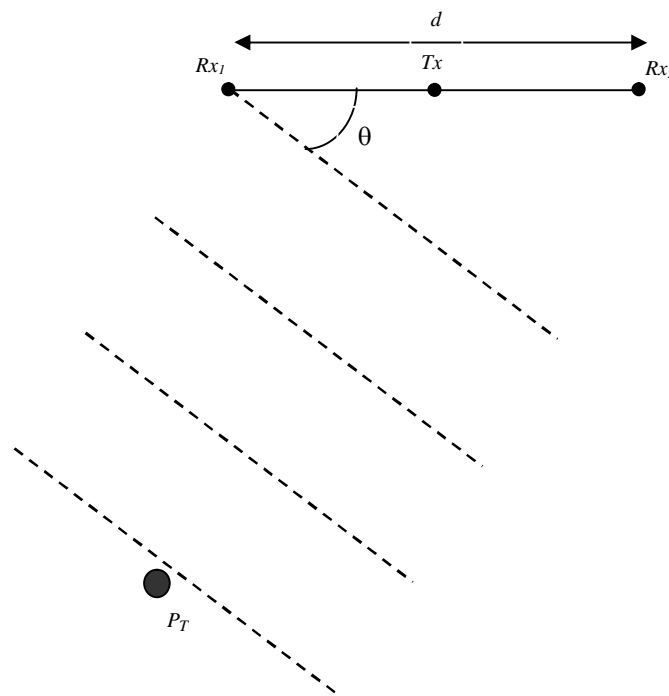


**Figure 4.10 Signals arriving at *Rx₁* before *Rx₂***

When the signals arrive at the receiver $Rx_1$ before $Rx_2$ then the signal which impinges on $Rx_1$ leads $Rx_2$ by certain amount of time which can be determined by a shift in the peak's location. Thus the peak would not be formed in the center of the result but would be moved.

In order to demonstrate this case, the same signal used in case 1 is used but the second signal which reaches receiver $Rx_2$ is given a small delay of 100 samples in order to show the movement of the peak away from the center. The result is presented in figure 4.11.
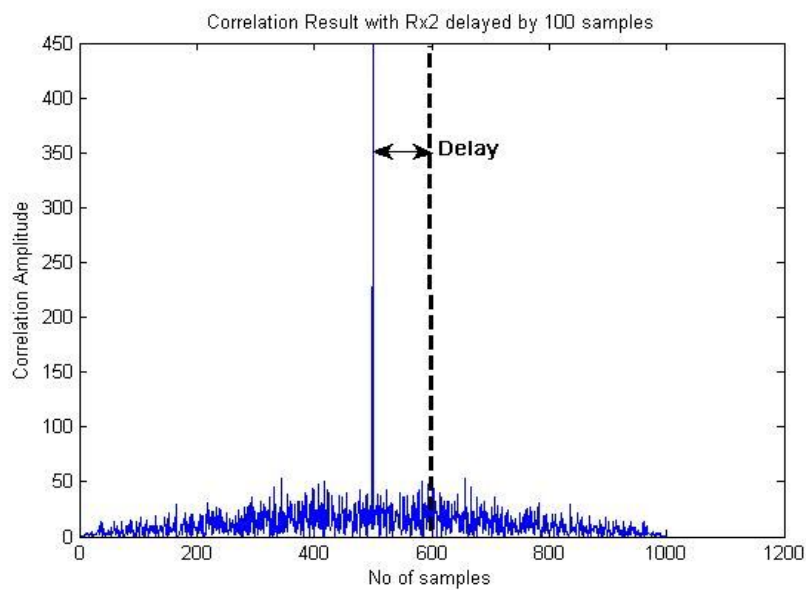


**Figure 4.11 Correlated result of the signals with the signal arriving at $Rx_1$ leading that arriving $Rx_2$ by 100 samples**

The length of the signal is 600 samples each. From equation 4.22 the length of the correlated result is

$$L = 2 \times 600 - 1 \qquad\qquad 4.25$$
$$= 1199 \ \ \text{samples long} \qquad\qquad 4.26$$

Thus if the signals had arrived at the same time the peak should have been at the center i.e. at $\approx 600^{\text{th}}$ sample but from figure 4.11 we find that the peak is located at the $500^{\text{th}}$ sample which indicates that the signal reaches $Rx_1$, 100 samples earlier

than $Rx_2$. Therefore, when the peak shifts to the left of the center it means that the receiver on the left ($Rx_1$) receives the signals sooner than the receiver on the right ($Rx_2$).

*Case 3: Signals arriving at receiver $Rx_2$ before $Rx_1$*

When the signals arrive at the receiver $Rx_2$ before $Rx_1$ the peak forms to the right of the zero lag correlation peak. In order to demonstrate this case, the signal which arrives at receiver $Rx_1$ is given a delay of 100 samples. The result is presented in figure 4.12. Both the signals have a length of 600 samples each and from the previous calculations the length of the result would be 1199 samples. Here the peak would be moved to the right by 100 samples and would be formed at $700^{th}$ sample. From figure 4.12 it is seen that since the signal arrives at $Rx_2$ before $Rx_1$ the peak is shifted to the right and that the peak is formed at $700^{th}$ sample which conforms to the calculation.
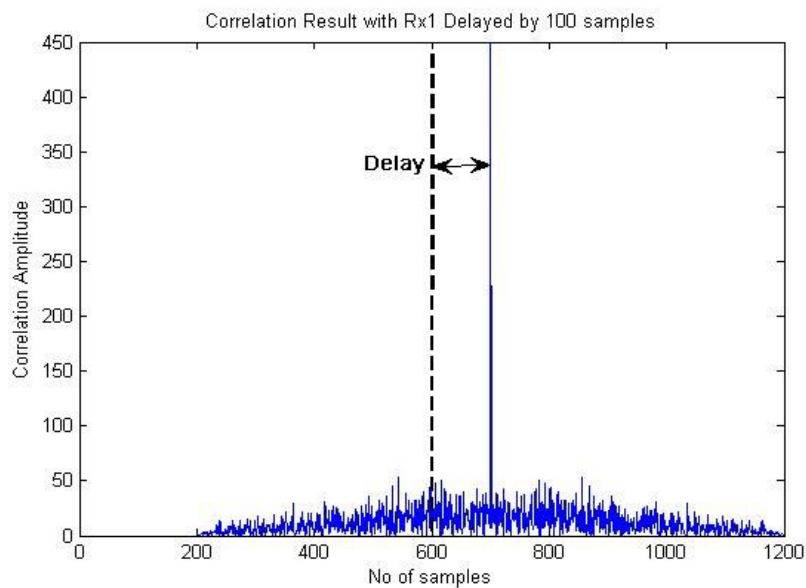


**Figure 4.12 Correlated result of the signals with the signal arriving at $Rx_2$ leading that arriving $Rx_1$ by 100 samples**

An integrator in the form of lowpass filter is applied to the output obtained after taking the absolute value of the correlated result. The lowpass filter smoothens the

results and forms distinct peaks. Consider a low pass filter with a impulse response of $h_{LP}(n)$. Mathematically the output from the lowpass filter is given by

$$R_{LP}(l) = h_{LP}(l) * R_{ss1}(l) \qquad\qquad 4.27$$

where $R_{LP}$ is the output after passing through the low pass filter. As an example a low pass filter is applied to smoothen the correlated signal in figure 4.9 and the result is given in figure 4.13. The passband of the lowpass filter applied depends on the signal bandwidth.
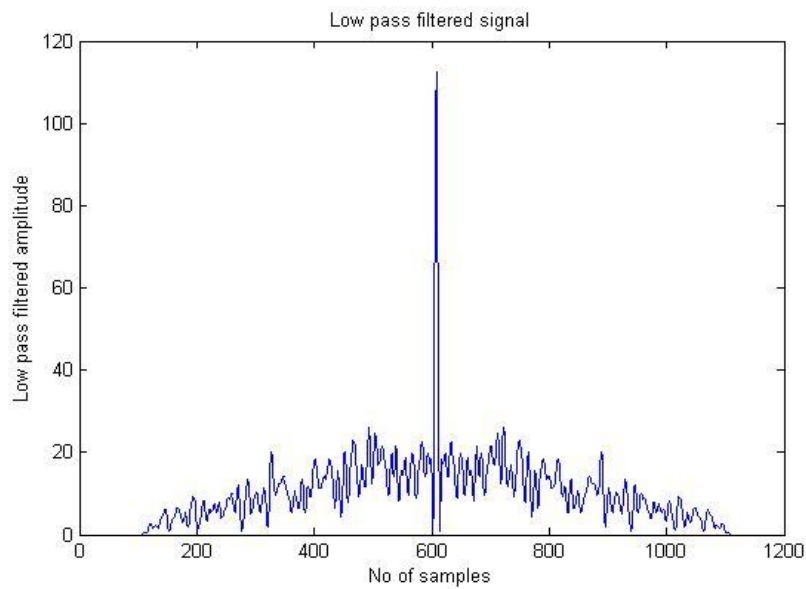


**Figure 4.13 Low Pass Filtered Output**

### 4.2.3   Determination of number of delay samples '$n_d$'

From equation 4.17 the only parameter that has to be determined is the value of $n_d$ which represents the number of delay samples. Thus knowing $n_d$ it is possible to determine the DOA. In section 4.2.2, the process of correlation was discussed. It was also shown with simulation examples that when two signals with no delay are correlated, the correlation peak is formed at the center (*zero lag*) and the peak gets shifted in case there is a delay in the signal received by either of the receivers. Thus using this method it is possible to determine the delay samples and hence the DOA of the signal from equation 4.17.

In this project it has been assumed that the complex target is made up of number of point targets. Thus each point target backscatters the signal which strikes them and the signal obtained on each of the hydrophone is a combination of all the signals from each of the point targets. Hence the signal from each of the complex target should form a signature that allows identifying the target uniquely. Since the correlation process determines the similarity between the return signals, it is considered as the suitable method to determine the similarity between the return signatures from the complex target which is received by a pair of receivers. Passing the hydrophone output through matched filter will result in a unique range profile of the target. Hence the process of determining the delay becomes that of a pattern recognition process which forms a pattern to be compared. Thus by determining the position of the peak formed due to the match in signatures from the target, it is possible to determine the delay samples.

The principle behind which the determination of DOA is based in this research can be stated as follows:

*If one transmits a signal, with bandwidth many times greater than the reciprocal of the required range resolution, then most practical targets will produce a "complex" echo, whose autocorrelation has a distinguishable peak and whose cross-correlation with other targets is reduced. This being the case, it is possible to deduce the existence of multiple, angularly separated targets from the cross-correlation of portions of the signal received on two channels.*

Figure 4.14 gives the block diagram of the beamforming that shows the procedure for determining $n_d$. In figure 4.14, the output from the hydrophones after passing through the receiver processing block produces the signals $x_{TVG1}(n)$ and $x_{TVG2}(n)$. The peak detection block in figure 4.14 is used to determine the correlation peak which gives the value of $n_d$, the number of delay samples.
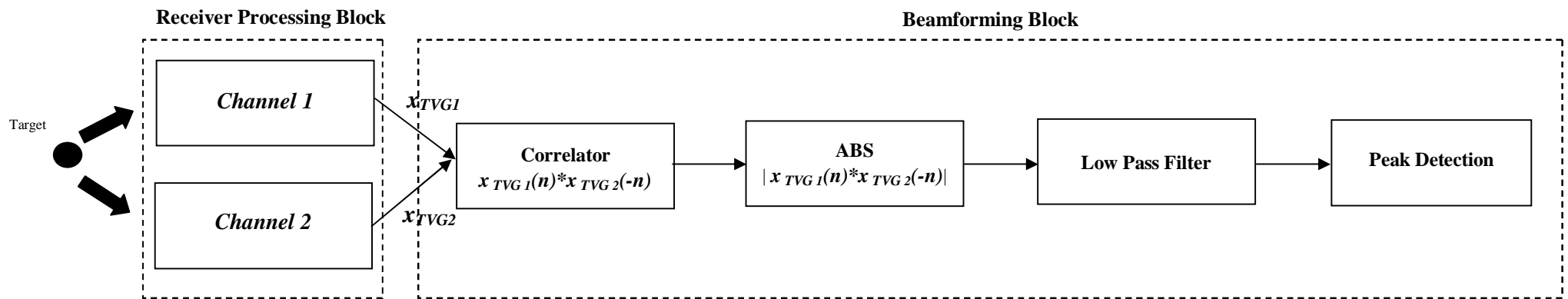
**Figure 4.14 Block diagram of the process for determining '$n_d$'**

In figure 4.14, *Channel 1* and *Channel 2* in the receiver processing block consist of the bandpass filter, matched filter and TVG amplifier. Thus by determining the delay samples $n_d$, and with the knowledge of the sampling interval $T$ it is possible to determine the delay time $\delta t$ from which it is possible to obtain the DOA.

### 4.2.4    Determination of Range 'r'

In section 4.2.3, the method for determining the number of lead or lag samples in order to determine the *DOA* was discussed. In the case where there is a single point target, it is possible to determine the range by finding the position of the peak from the matched filter output. This gives the delay between the sending out of the signal and the return signal which represents the two way travel time. Also the *DOA* can be determined using the method described.

The processing described in figure 4.14 would be suitable in the case of a single point target. Consider the case when there are number of targets in the path of the transmitted signal. All the targets in the signals path would provide a significant backscatter of the transmitted signal. Each target in the signal path forms a pattern which uniquely represents the target. Since the target is made of a collection of point targets, applying matched filter to the received signal would result in the formation of target range profile. Using the process described in figure 4.14, the matched filter outputs are correlated for determination of $n_d$. If the received signals are correlated as a whole in order to determine the direction of arrival, the range information is lost. Also correlation of the received signals as a whole would cause the formation of multiple lead and lag peaks. Hence the range and DOA information becomes ambiguous. An illustration of the same is provided in section 4.2.9.

To overcome the problem mentioned above, it would be useful to divide the signal from the receiver processing block into range cells and consider small ranges at one time. For greater accuracy in range determination it is desirable to make the range cells as small as possible. By dividing output signal into range cells it is possible to determine simultaneously the range at which the target lies with a

certain amount of accuracy and also the corresponding DOA. The process of division of signals into range cells is shown in figure 4.15.
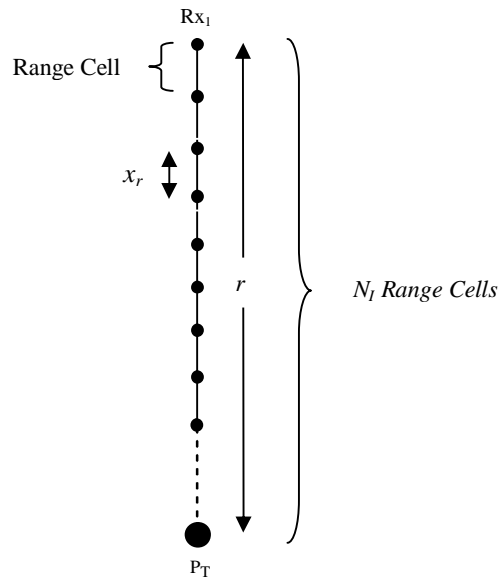


**Figure 4.15 Division into range cells**

Thus the signal is divided into small range cells which contain fewer samples. The number of samples in each range cell is calculated using the range cell size chosen. The calculation of number of samples in each range cell is given in section 4.2.5. The range cell obtained from signal of one channel is correlated with the corresponding range cell from the signal of the other channel. The correlated result gives the angular samples. The number of angular samples to be chosen is given in section 4.2.6. The lead or lag is calculated for each of the angular samples chosen. If the size of each range cells is $x_r$ meters and if there are $N_I$ range cells to the target, the range is calculated using the equation

$$r = N_I x_r \qquad\qquad 4.28$$

The process is described using figure 4.16, figure 4.17 and figure 4.18. Figure 4.16 shows the outputs of two channels $x_{TVG1}$ and $x_{TVG2}$. The numbers in each cell indicate the samples in the signal. Let $x_r$, the range cell size, corresponds to $l$ samples. Thus samples 1 to $l$ form the first range cell as indicated in figure 4.18, samples $l+1$ to $2l$ form the second range cell and so on. The samples 1 to $l$ from the first range cell of $x_{TVG1}$ and $x_{TVG2}$ are correlated. The correlated result gives the

angular cell samples. The correlated result is passed through an absolute value function and lowpass filter and stored as the first row of an array (figure 4.17 shows the correlation of $i^{th}$ range cell from signal 1 and signal 2). Similar operation is performed on subsequent range cells and stored in the corresponding rows of the array. The center column of the array corresponds to the *zero lag*. A peak in the angular cell indicates the presence of a target in the particular range cell. The position of the peak w.r.t the zero lag indicates the amount of lead or lag between the signals. The array obtained after correlation of the range cells is in the $r$-$\theta$ format. As each range cell is considered, a variable *i* is incremented by one in order to keep track of the number of range cells considered. In the figure 4.18, the array formed has $N_I$ rows thus $N_I$ range cells. The range is obtained using equation 4.28. Number of samples from the *zero lag* point of each row of the array gives the value of $n_d$. The DOA can be calculated using equation 4.17.
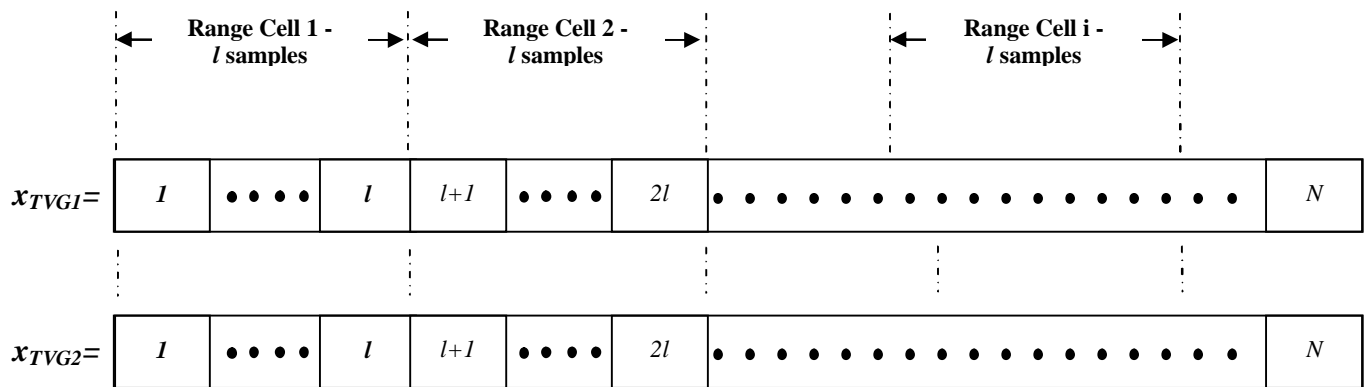


**Figure 4.16 Receiver outputs shown with cells marked**
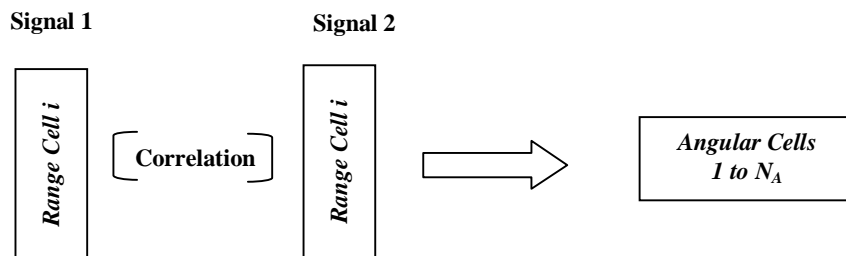


**Figure 4.17 Angular cell values from range cells**
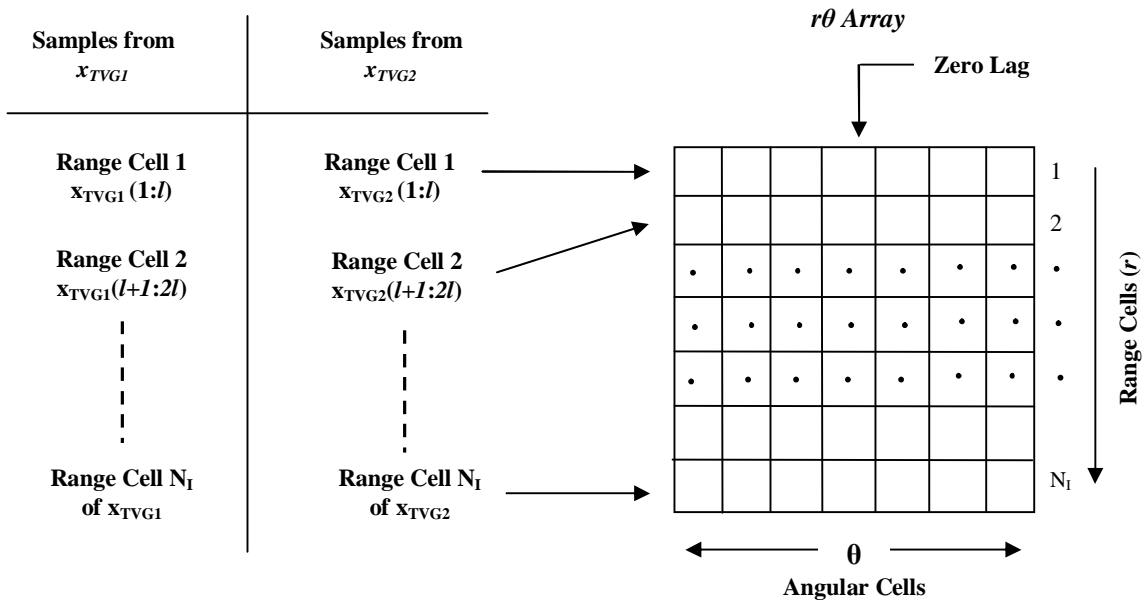
**Figure 4.18 Process of dividing into range cells and correlation (*rθ* matrix)**

Thus it is possible to determine the *DOA* from the cross-correlation procedure and the range by the division of the signals into range cell. From the process above it is seen that ***the range resolution is sacrificed in order to obtain the DOA***. The entire procedure is shown as a block diagram in figure 4.19.

When there is an overlap of *p%* between two range cells, then the equation for the determination of range is

$$r = \left(1 - \frac{p}{100}\right) \sum_{i=1}^{N_I} x_r \qquad 4.29$$

Overlapping of range cells is performed to avoid the case when a target lies in the $i^{th}$ range cell in one of the received signals whereas the same part of the target lies in the $(i+1)^{st}$ range cell of the other signal. Thus for a 50% overlap, samples 1 to *l* become the first range cell, samples *l/2+1* to *3l/2* become the second range cell, samples *l* to *2l* become the third range cell and so on. *For a monostatic system the value of* ***r*** *obtained using equation 4.28 or 4.29 is the two way travel distance.*

**Receiver Processing Block**

**Target**

*Channel 1*

*Channel 2*

*Divide into Range cells*

*Divide into Range cells*

*For each Range Cell*

**Correlator**
$x_{TVG\,1\_i}(n)*x_{TVG\,2\_i}(-n)$

**ABS**
$|\,x_{TVG\,1\_i}(n)*x_{TVG\,2\_i}(-n)|$

**Low Pass Filter**

**Peak Detection and DOA**
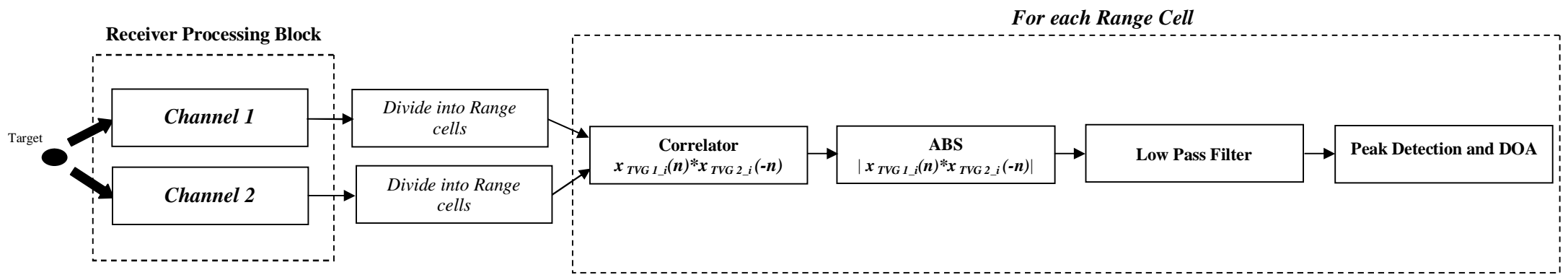
**Figure 4.19 Block diagram for determining '$n_d$' after dividing into Range cell**

### 4.2.5 Number of samples in a range cell

If the signal is divided into range cells of $x_r$ meters, the number of samples ($n_{RC}$) that constitute a range cell is given by the equation.

$$n_{RC} = \frac{x_r F}{c} \qquad \qquad 4.30$$

where $F$ is the sampling frequency in Hz. For a $p\%$ overlap, the $i^{th}$ range cell can be written as

$$x_{TVG1\_i}(m) = x_{TVG}\big((i-1)L+1:iL\big) \quad i = 1......N_I,\ m=1......n_{RC} \qquad 4.31$$

where $\quad L = round\left(\left(1 - \frac{p}{100}\right)n_{RC}\right) \qquad \qquad 4.32$

Similarly $x_{TVG2}$ can be divided into range cells using equations 4.31 and 4.32.

### 4.2.6 Number of angular cells in the $i^{th}$ range cell

The number of angular cells corresponding to the $i^{th}$ range cell chosen is another factor that has to be calculated. For a particular beam angle it is necessary that the right number of correlated data samples is considered rather than taking all the samples obtained from correlation. Consider figure 4.20.

In figure 4.20, the transmitted signal is assumed to have a beamwidth of $2\theta_b$. This means that the signal illuminates an area covered by the corresponding beam angle. Thus, while determining the DOA it is enough that the search is limited from $0^o$ to half beam angle $\theta_b$ on one side. This is repeated on the other side as well. There is no interest in looking at signals which lie outside the angle $\theta_b$ on both sides.
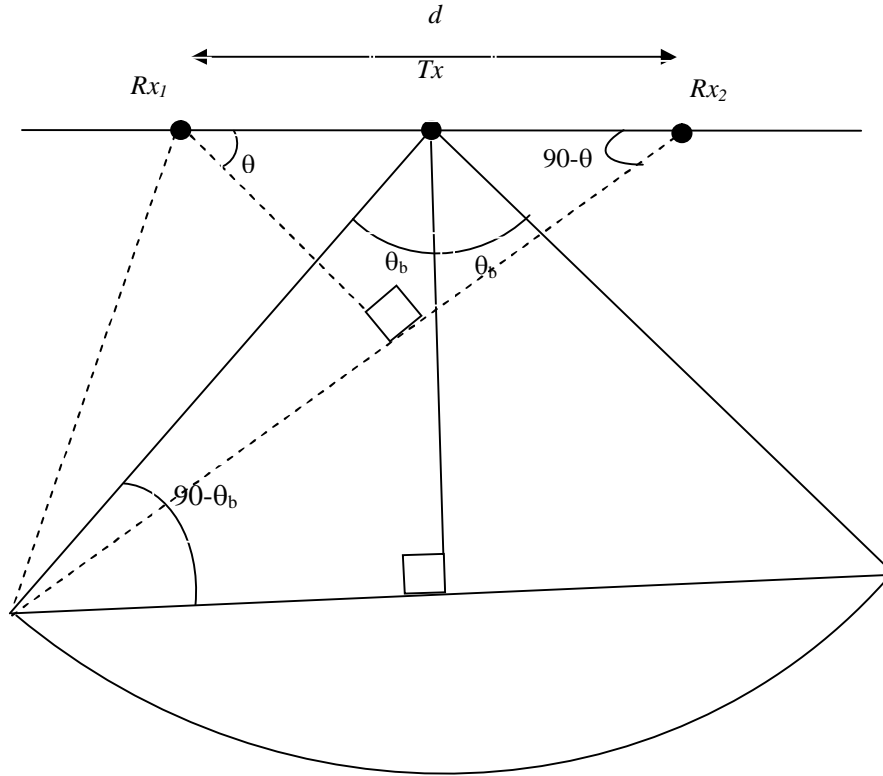
**Figure 4.20 Beam angle and receivers**

The DOA thus varies from $\theta_b$ *to 0* on one side and then from *0 to* $\theta_b$ on the other. Since the maximum angle of arrival is $\theta_b$ on each side, the maximum delay that is possible on each side would be corresponding to the angle $\theta_b$. This can be determined as follows.

Thus for half-beam angle of $\theta_b$, rearranging equation 4.16

$$n_{d\_max} = \frac{d.sin(\theta_b)}{c.T} \qquad 4.33$$

Thus after correlating each of the corresponding range cells, it is enough to consider $n_{d\_max}$ samples on each side of the correlation result from the zero lag, which corresponds to the half-beam angle. Thus the useful data for the formation of the image should lie within $2n_{d\_max}$ samples as shown in figure 4.21. Hence for all the samples which lie within the maximum limit of the samples $N_A = 2n_{d\_max}$ the DOA is calculated.
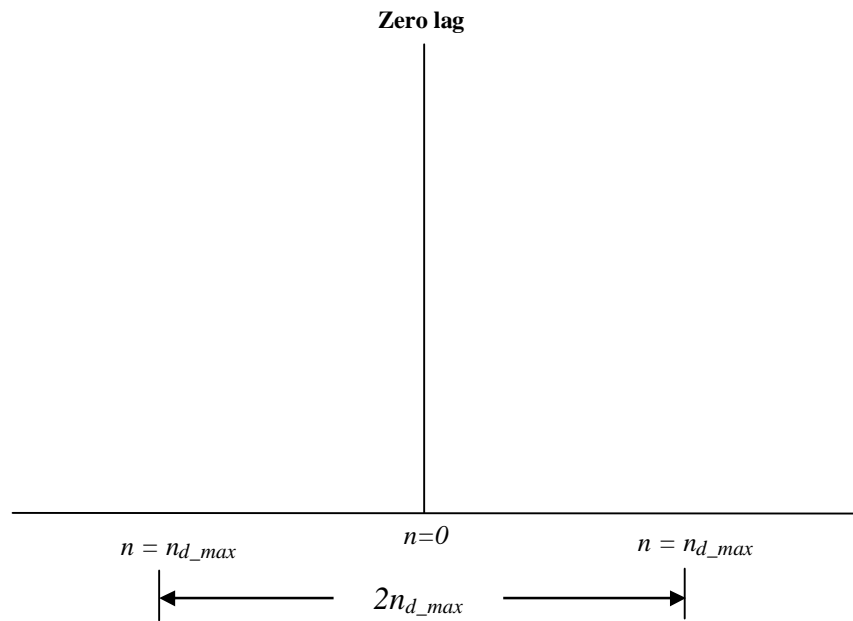
**Figure 4.21 Diagram showing the maximum number of useful samples**

## 4.2.7 Algorithm steps for determining the $r\theta$ matrix and flowchart

The steps involved in determining the **$r\theta$** matrix is presented in this section. The algorithm presented combines the procedure explained from section 4.2.4 to section 4.2.6.

*Step 1) The number of samples in each range cell is calculated using equation 4.30. Initialize a range cell counter $i = 1$.*

*Step 2) Get the $i^{th}$ range cell from the signals obtained from the Channel 1 and Channel 2.*

*Step 3) Correlate the $i^{th}$ range cell of the signal from Channel 1 with the corresponding range cell of signal from Channel 2. Increment the counter $i$.*

*Step 4) Calculate the number of angular cell samples using equation 4.33 and store them into an $i^{th}$ row of the array.*

*Step 5) If all the samples from the signals have been considered then **Stop** otherwise go to Step 2.*
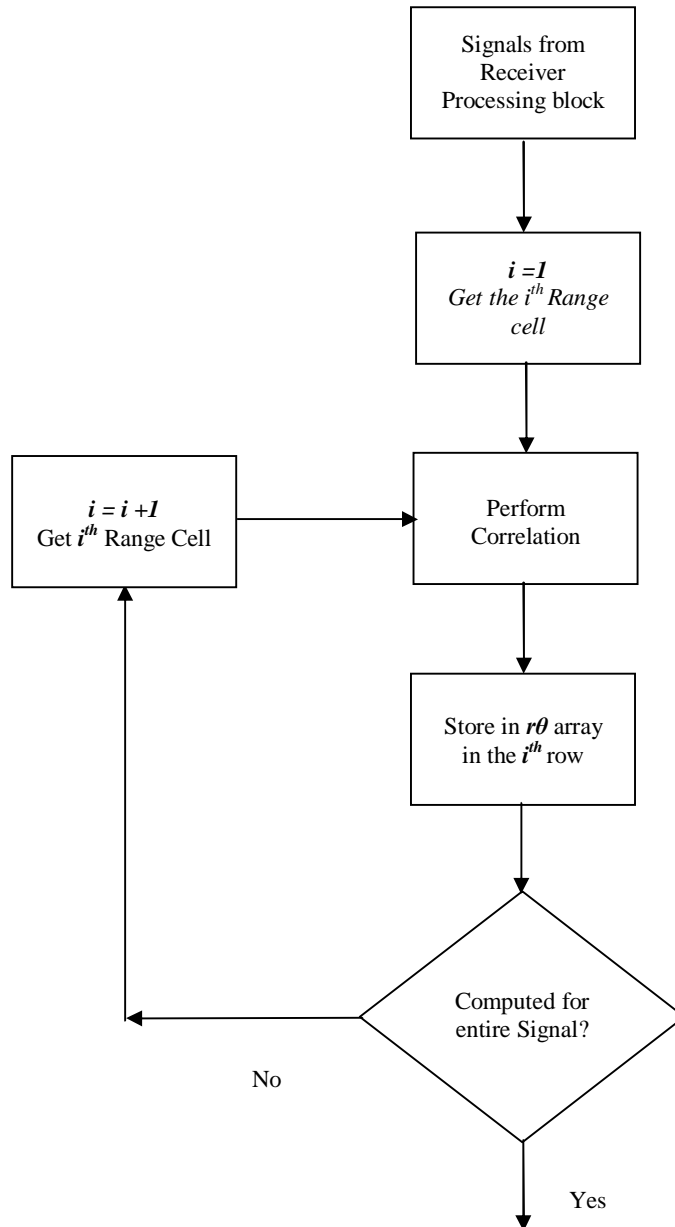
**Figure 4.22 Flowchart of the algorithm**

An illustration of the process of determining the range and DOA is presented in section 4.2.9.

### 4.2.8 Mathematical explanation of the entire procedure

When a received signal is matched filtered, a peak is formed at the range where the target occurs. Since the target is modeled as a collection of point targets, each of the point target whose dimension is greater than the signal wavelength $\lambda$ backscatters the incident signal. The signals received would be a collection of all

the signals from each point on the target. When a matched filter is applied to the received signal, a collection of peaks are formed. Since the matched filter peaks are formed at the range where the point targets are located, these peaks form a distinct target profile of the target being imaged. When correlation is performed, these target profiles are matched. Depending on the shift of the samples from the zero lag point, DOA is determined. Thus the determination of DOA is narrowed to pattern matching technique. Hence $i^{th}$ row of the $r\theta$ matrix can be mathematically written as

$$r\theta_i = \left\{ h_{LP}(m) * \left| x_{TVG1\_i}(m) \otimes x_{TVG2\_i}(m) \right| \right\}$$  4.34



Figure 4.23 Explanation of the equation 4.34 in parts

where $x_{TVG1\_i}$ and $x_{TVG2\_i}$ are the $i^{th}$ range cells obtained using signals from *Channel1* and *Channel2*. The symbol $\otimes$ is used to indicate correlation. Figure 4.23 shows the entire procedure followed in obtaining the $i^{th}$ row of $r\theta$ matrix. $x_{TVG1\_i}$ and $x_{TVG2\_i}$ contain target profiles which are obtained after matched filtering of received signal. The correlation between them gives the lead or lag in the signatures. The correlation is performed using *fft* operation.

## 4.2.9 Illustrating range and delay determination procedures

A chirp signal with frequency varying from 325 kHz to 425 kHz is transmitted. The signal is sampled with a sampling frequency of 1 MHz. Two hydrophone elements $Rx_1$ and $Rx_2$ separated by a distance of 0.4m receive the backscattered

signal. The signals at the receivers outputs are shown in figure 4.24 and figure 4.25.
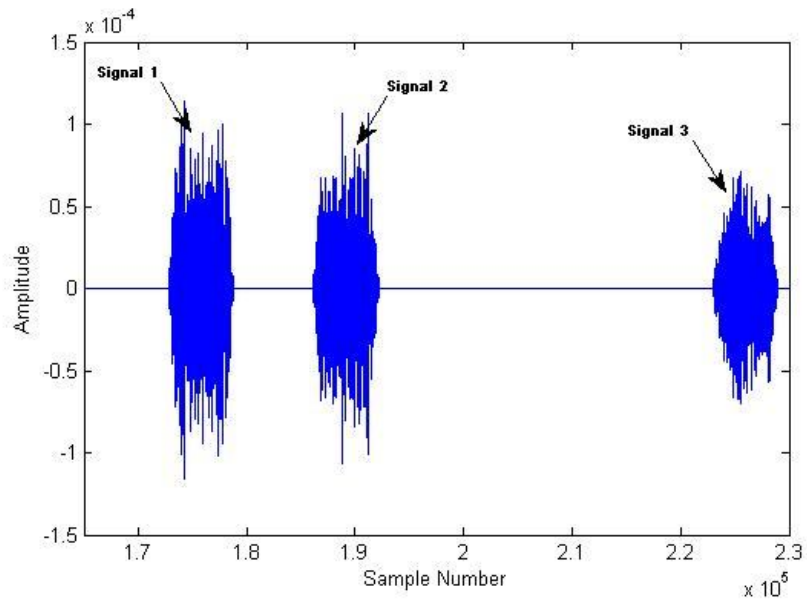


**Figure 4.24 Receiver output *Rx₁***
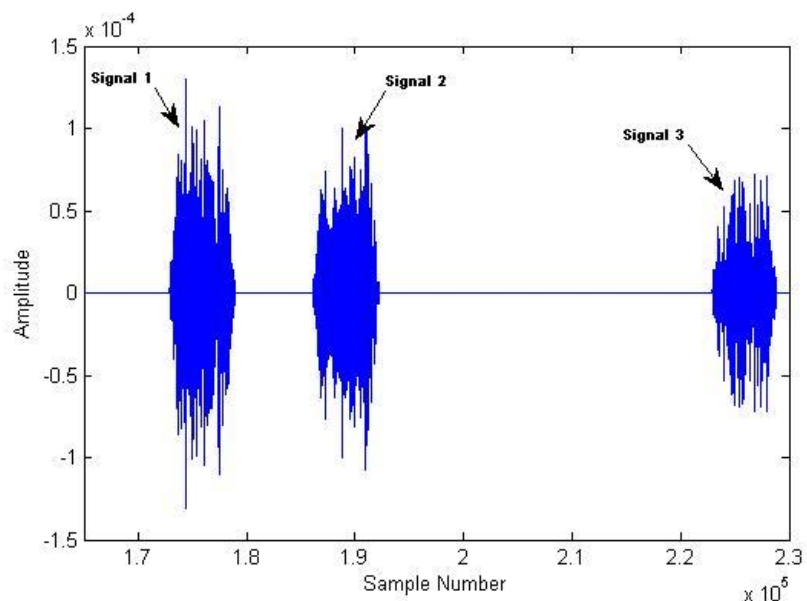


**Figure 4.25 Receiver output *Rx₂***

In figure 4.24 and figure 4.25, signal 2 arrives at the receivers $Rx_1$ and $Rx_2$ at the same time. Signal 1 arrives at $Rx_1$ before $Rx_2$ by 102 samples. Similarly signal 3 arrives at $Rx_2$ before $Rx_1$ by 80 samples. The output after applying matched filter and TVG to the receiver $Rx_1$ and $Rx_2$ outputs are shown in figure 4.26 and figure 4.27.
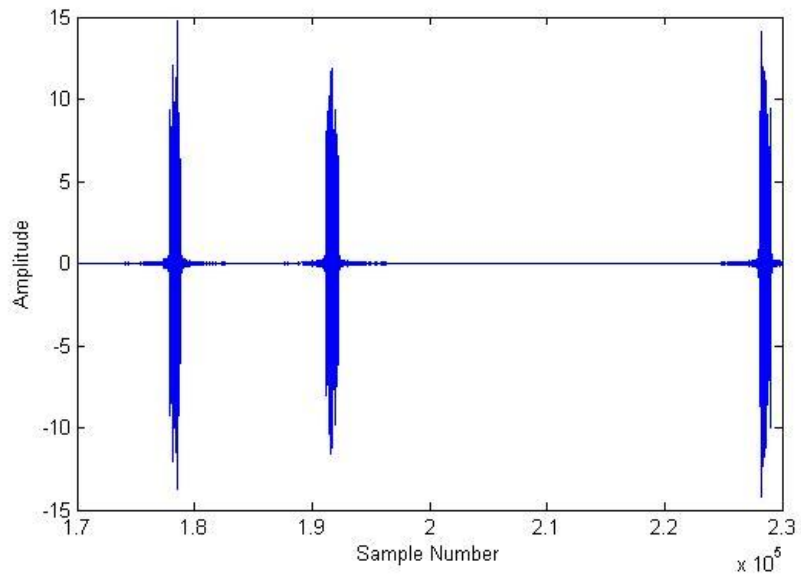
**Figure 4.26 Matched filter output from $Rx_1$**
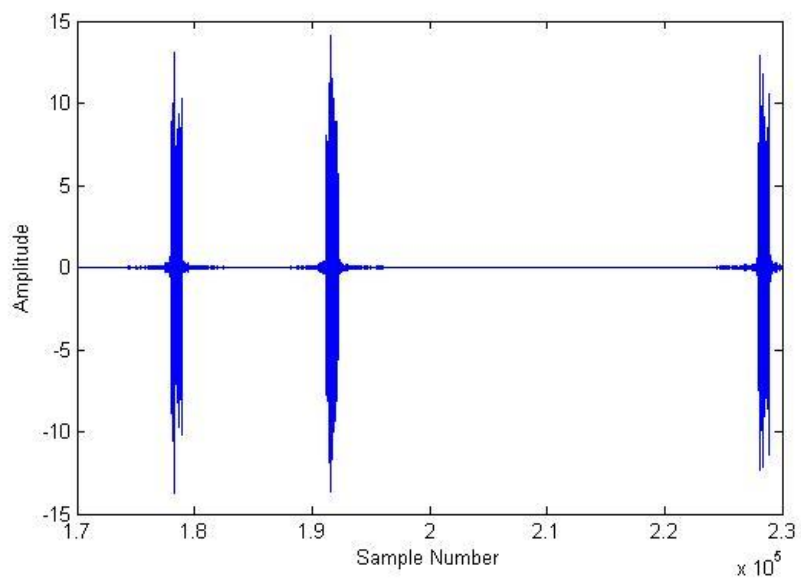


**Figure 4.27 Matched Filter output from $Rx_2$**

The output obtained by correlating the signals in figure 4.26 and figure 4.27 without dividing it into range cells is given in figure 4.28.
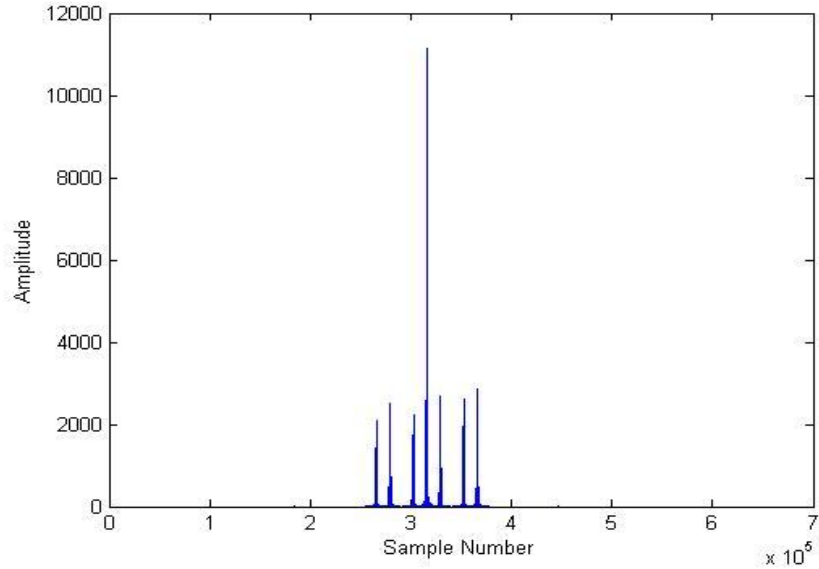
**Figure 4.28 Correlation between *Rx₁* and *Rx₂* without dividing into range cells**

Here similar target clusters (explained further in Chapter 5) are placed at different distances. Thus the signals while correlating matches with itself and the other arriving signals. Hence a number of peaks are formed in the correlated output. Determining the delay and hence the DOA is difficult from this correlated output. There are only three target clusters but in figure 4.28 seven peaks are seen. This is using the receiver model in figure 4.14.

The signals are now divided into range cells and then correlated. The signals from the matched filter output of *Rx₁* and *Rx₂* are divided into range cells of 0.75m. Hence

$$n_{RC} = \frac{x_r F}{c} = \frac{0.75 \times 10^6}{1500} = 500 \, samples \qquad\qquad 4.35$$

Therefore each range cell will have 500 samples. Each range cell of *Rx₁* is correlated with the corresponding range cell of *Rx₂* i.e. first range cell of *Rx₁* is correlated with the first range cell of *Rx₂* and so on. If there is a match then a peak is formed. The position of the peak from the zero lag (in this case 500th sample) gives the number of delay samples and hence the DOA can be calculated from the

delay samples. From the matched filter outputs in figure 4.26 and 4.27, the first signal arrives at 347th range cell. Thus correlating between the 347th range cell of receivers $Rx_1$ and $Rx_2$ the following result is obtained.
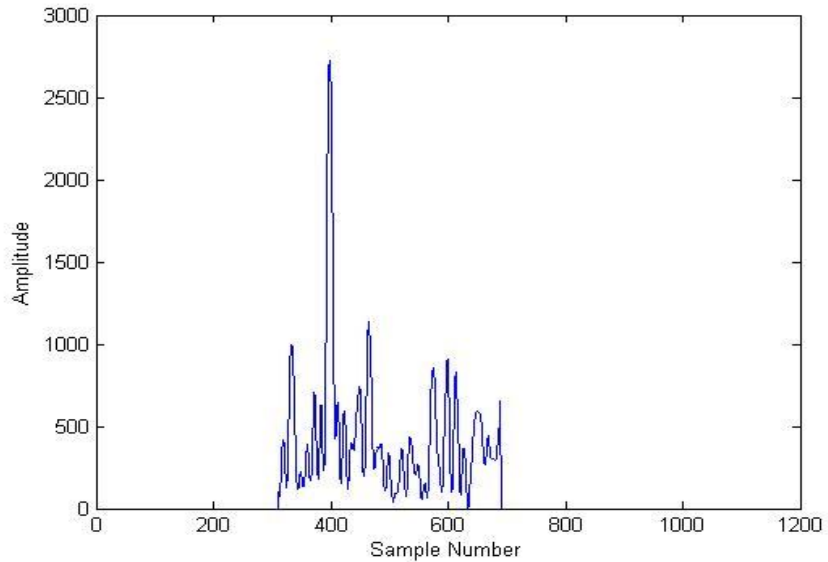


**Figure 4.29 Correlation between 347th range cell of $Rx_1$ and $Rx_2$**
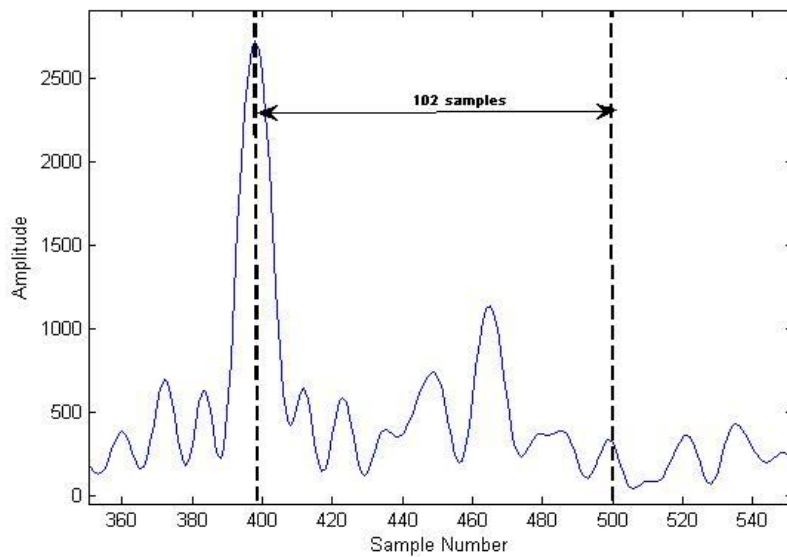


**Figure 4.30 Correlation between 347th range cell of $Rx_1$ and $Rx_2$ magnified around the correlation peak**

Figure 4.29 and figure 4.30 shows the same plot but figure 4.30 is magnified around the area where the peak is formed. The length of the correlation result should be 999 samples. Since the signal 1 arrives at the receiver $Rx_1$ earlier than $Rx_2$ by 102 samples, the peak would be formed at 398th sample position. It is

found from figure 4.30 that the peak is formed at the ≈398th sample. This means that $Rx_1$ leads $Rx_2$ by 102 and hence the DOA is 22.48°. Using equation 4.28, the range is given by

$$r = N_I x_r = 347 \times 0.75 \approx 260.25m \qquad\qquad 4.36$$

This was verified from the knowledge of target coordinates which gave 260m. This gives the two way travel distance as the system considered is monostatic.

Signal 2 occurs in the 374th range cell. The result of correlation between the 374th range cell of $Rx_1$ and $Rx_2$ is shown in figure 4.31 and figure 4.32.
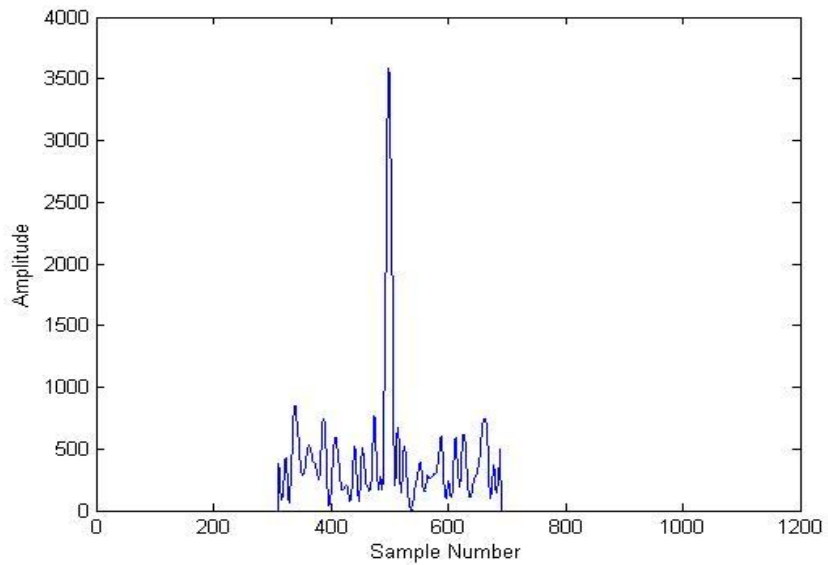


**Figure 4.31 Correlation between 374th range cell of $Rx_1$ and $Rx_2$**
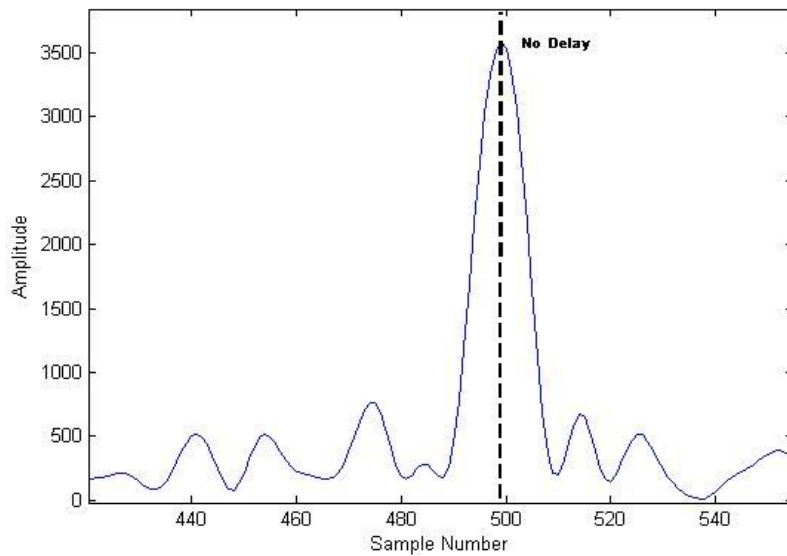
**Figure 4.32 Correlation between 374th range cell of *Rx₁* and *Rx₂* magnified around the correlation peak**

From figure 4.32 it is seen that the peak is formed at $\approx 500^{th}$ sample which is the zero lag position. This indicates that the signal arrives at $Rx_1$ and $Rx_2$ at the same time. The range can be calculated in the same way as in equation 4.36 which was then verified using the target coordinates.

Similarly figure 4.33 and figure 4.34 shows the result of correlating the 447th range cell where signal 3 occurs.
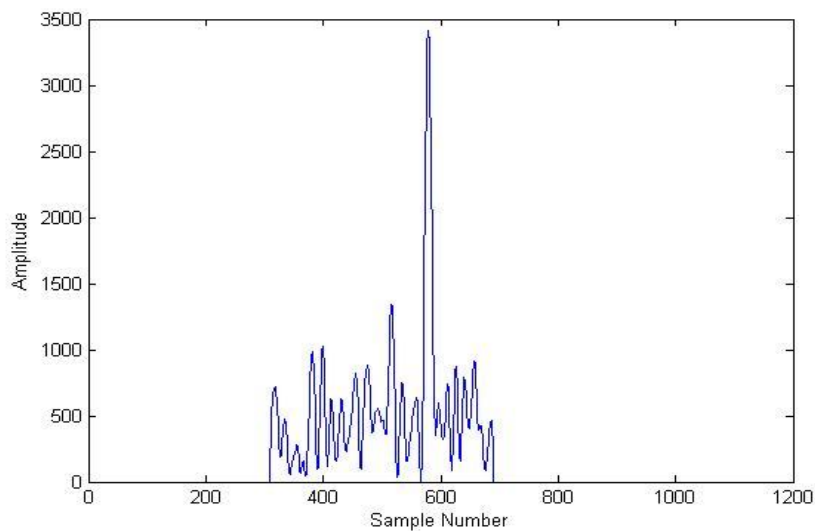


**Figure 4.33 Correlation between 447th range cell of *Rx₁* and *Rx₂***
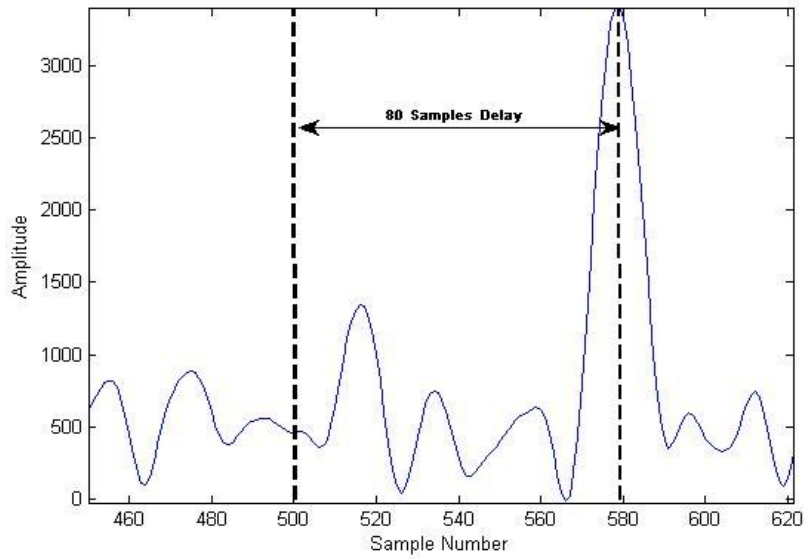
**Figure 4.34 Correlation between 447<sup>th</sup> range cell of *Rx₁* and *Rx₂* magnified around the correlation peak**

Correlating the 447<sup>th</sup> range cell of $Rx_1$ and $Rx_2$ a delay of 80 samples is obtained. Since the correlation peak is formed on the right side of the zero lag, the signal arriving at $Rx_2$ leads that arriving at $Rx_1$.

### 4.2.10  Resolution in the calculation of range

The algorithm divides the returns into range cells of $x_r$ meters. Objects that lie within the range cell are taken to be at the distance where the range cell is located. Thus, there is a maximum error in the measurement of range equal to $x_r$ meters. Let $r_M$ and $r_A$ be the measured and actual range at which the target is present. The measured range can be given as

$$r_M = x_r N_I \qquad\qquad 4.37$$

where $N_I$ is the total number of range cells to the target when there is no overlap. Consider figure 4.35.
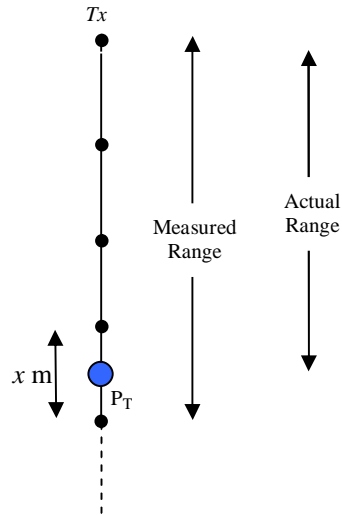
**Figure 4.35 Diagram showing actual and measured ranges**

Thus the error $e$ between the measured and actual range is

$$e = r_M - r_A \qquad\qquad 4.38$$

$$e = x_r N_I - \left[ (x_r N_I - x_r) + x_{r1} \right] \qquad\qquad 4.39$$

where $x_{r1}$ is the distance from the edge of previous range cell to the target. Thus

$$e = x_r - x_{r1} \qquad\qquad 4.40$$

Thus from the above equation it is possible to write

$$\lim_{x_r \to x_{r1}} (e) \Rightarrow 0 \qquad\qquad 4.41$$

and hence $\quad r_M \Rightarrow r_A$

The above equation states that smaller the range cell size more closer the calculated range would be to the actual range. When there is an overlap of $p\%$

between the range cells, the error $e$ in range determined is reduced. This can be shown as follows.

$$r_M = \left(1 - \frac{p}{100}\right) x_r N_I \qquad 4.42$$

Let $e_I$ be the error obtained when the range cells are overlapped.

$$e_I = \left(1 - \frac{p}{100}\right) x_r N_I - \left[\left[\left(1 - \frac{p}{100}\right) x_r N_I\right] - x_r + x_{rI}\right] \qquad 4.43$$

where $\lceil m \rceil$ is the smallest distance greater than $m$ and obtained with same range cell and without overlap.

$$e_I = \left(1 - \frac{p}{100}\right) x_r N_I - \left[\left(1 - \frac{p}{100}\right) x_r N_I\right] + x_r - x_{rI} \qquad 4.44$$

$$e_I = \left[(x_r - x_{rI}) + \left[\left(1 - \frac{p}{100}\right) x_r N_I - \left[\left(1 - \frac{p}{100}\right) x_r N_I\right]\right]\right] \qquad 4.45$$

Let

$$e_R = \left(1 - \frac{p}{100}\right) x_r N_I - \left[\left(1 - \frac{p}{100}\right) x_r N_I\right] \qquad 4.46$$

From equation 4.40 and 4.46, equation 4.45 can be written as

$$e_1 = \left[e + (-e_R)\right] = \left[e - e_R\right] \qquad 4.47$$

From equation 4.46 it can be found that the error $e_R$ is always negative. Thus equation 4.47 states that overlapping the range cells would reduce the error in range and would provide a better estimation of the target range.

## 4.3    Image formation

The DOA and the range at which the target lies are determined by obtaining the time difference of arrival of the signals at each of the hydrophones. By knowing the range and the DOA, the position of individual pixels in the image can be obtained using the basic trigonometric formulas. The method of image formation is described in the following paragraphs.

### 4.3.1    Digital image

This section defines the structure of a digital image. A digital image can be represented by a function $f(x,y)$ which is a two-dimensional matrix. The value at the location $(x, y)$ provides the intensity of the pixel at that particular location [89]. The image is represented in the matrix form using the following equation [89]

$$f(x,y) = \begin{bmatrix} f(1,1) & f(1,2) & . & . & f(1,N) \\ f(2,1) & f(2,2) & . & . & f(2,N) \\ . & . & . & . & . \\ . & . & . & . & . \\ f(M,1) & f(M,2) & . & . & f(M,N) \end{bmatrix} \qquad 4.48$$

Thus in equation 4.48, the continuous image is written in the discrete form as a *MxN* array where each array element represents a discrete sampled value from the continuous image.

### 4.3.2    Equation for image formation

This section deals with equations involved in image formation i.e. determination of the position of the pixel in *f(x,y)*.   The process of formation of *rθ* matrix requires two hydrophone elements. Thus for image formation, response from a pair of hydrophones is required.
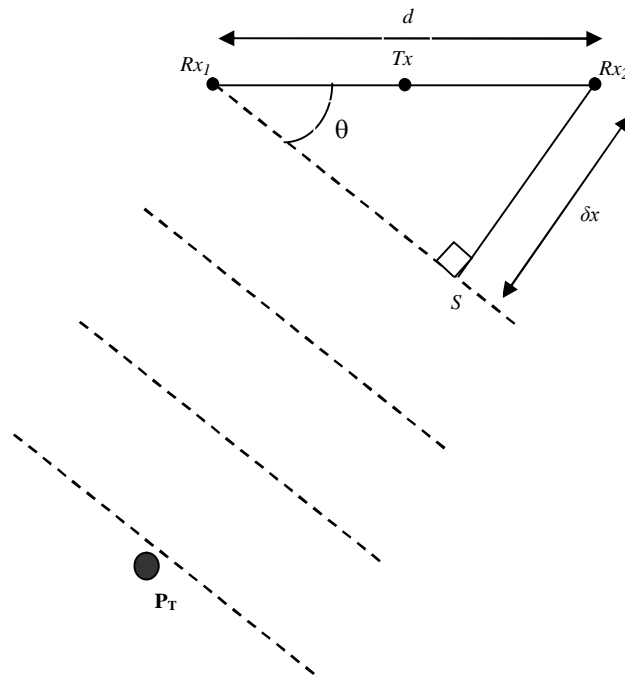
**Figure 4.36 Diagram showing two receivers and the DOA**

Consider figure 4.36. The figure shows the receiver geometry for the received signal along with the DOA marked. The DOA is determined by the process described in section 4.2. The triangle $Rx_1$-$S$-$Rx_2$ is a right angled triangle at $S$ and hence

$$\angle Rx_1 Rx_2 S = 90^0 - \theta \qquad\qquad 4.49$$

The image coordinates have to be obtained with reference to $Rx_2$ in the above case. Figure 4.36 is simplified and redrawn with the axis located at $Rx_2$ in figure 4.37. The value of range $r$ can be determined from the number of range cells to the target.

From figure 4.37 the $X$ and $Y$ coordinates of the image can be deduced by considering $Rx_2$-$P_T$, which represents the range $r$, as the resultant. Using the basic trigonometric relation it is possible to split $Rx_2$-$P_T$ into its x and y components. From figure 4.37
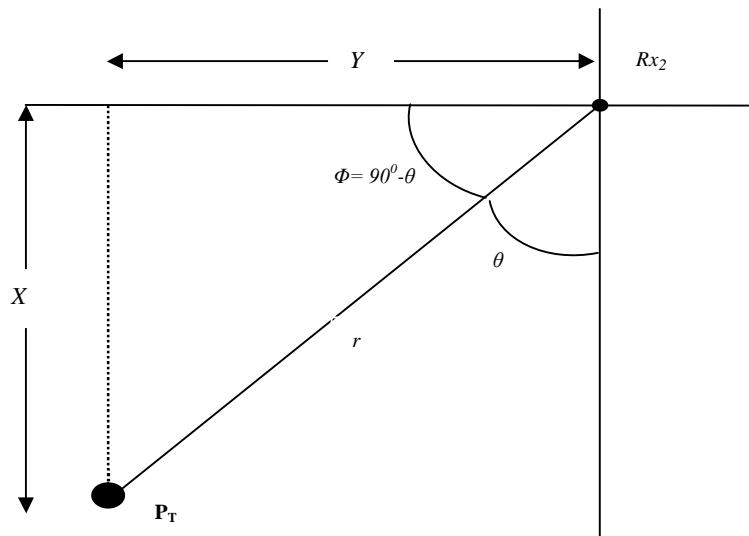
**Figure 4.37 Simplified figure showing the resolving of the image coordinates**

$$\phi = 90^0 - \theta \qquad\qquad 4.50$$

Therefore

$$Y = r.\cos\phi \qquad\qquad 4.51$$
$$X = r.\sin\phi \qquad\qquad 4.52$$

The $X$ and $Y$ components are reversed when compared to the normal Cartesian coordinate system because in the case of the image the rows correspond to the $X$ values and the columns correspond to the $Y$ values considering the image as a two dimensional matrix.

### 4.3.3  Determination of pixel intensity

In section 4.3.2 the scheme to determine the image from the coordinate obtained was described. The location of the pixel is not the only desired value for the formation of the image. Apart from the coordinate values it is necessary to decide on the value of the pixel intensity at a particular coordinate.

In this section, determination of pixel intensity at the coordinates chosen is described. A brief explanation of the process in the form of a block diagram is shown in figure 4.38. It is known that the received signal is matched filtered in order to detect the positions of the returns. The output of the matched filter would give the signal energy. Then the matched filtered signal passes through the TVG amplifier block in order to compensate for the spreading losses. In figure 4.38 the blocks named *Channel 1* and *Channel 2* includes these operations. In the beamforming process, the matched filtered signals from two channel blocks are divided into range cells and cross-correlation is performed in order to determine range and *DOA*. The result obtained would thus be square of energy as can be shown from the following equations and the pixel intensity is taken to be the square root of that result. Thus if

$$x_{TVG1\_i}(m) = E_1(m) \qquad m = 1......n_{RC} \qquad\qquad 4.53$$

$$x_{TVG2\_i}(m) = E_2(m) \qquad m = 1......n_{RC} \qquad\qquad 4.54$$

where $x_{TVG1\_i}$ and $x_{TVG2\_i}$ are $i^{th}$ range cells of the match filtered signals from *Channel 1* and *Channel 2*. Since matched filtering involves correlation of the signal with itself, the TVG amplifier output would be energy signal as indicated by equations 4.53 and 4.54. Correlating equation 4.53 and equation 4.54 would give squared of energy signal. Thus,

$$E_T(k) = |E_1(m) \otimes E_2(m)| \qquad k = 1......N_A \qquad\qquad 4.55$$

$$r\theta_i(k) = \sqrt{E_T(k)} \qquad\qquad 4.56$$

where $r\theta_i$ are the values in the $i^{th}$ row of the $r\theta$ matrix.
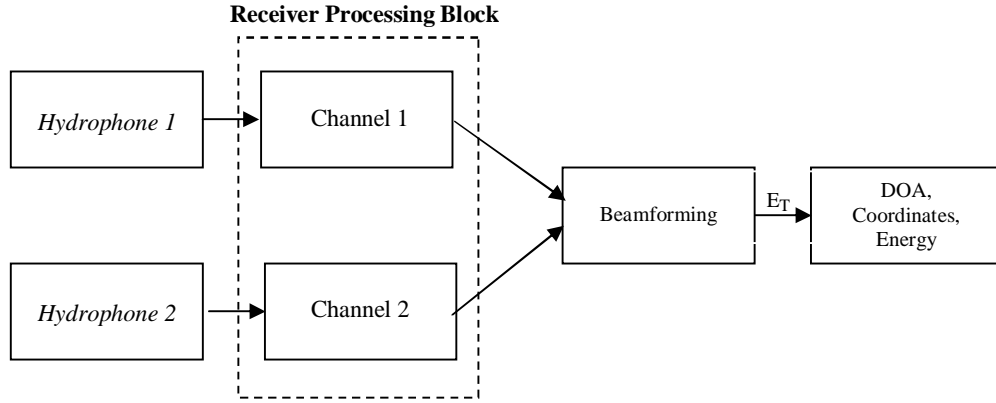
**Figure 4.38 Determination of pixel intensity**

### 4.3.4 Forming image from the coordinate values

The image mapping process is described below. Let *V* be a pixel value in the **rθ** matrix. This pixel value has to be mapped on to the image matrix. Knowing the row and column in which the chosen pixel is located in the **rθ** matrix, the range and DOA can be calculated. The image coordinates can be obtained using equation 4.51 and equation 4.52. The *X* value determines the row in which the pixel to be mapped is located in the image matrix. The *Y* value determines the column in which the pixel is located from the center column of the image matrix. The exact positions of the pixel i.e. the coordinates of the pixel on the image is obtained using the formula which is given under three cases.

*Case 1: Correlation peak on the left of the center point in **rθ** matrix*

Let $X_{PT}$ and $Y_{PT}$ be the image coordinates for the pixel obtained using equation 4.51 and equation 4.52. Let $X_c$ and $Y_c$ be the center row and column of the image array.

$$Y_{PT} = Y_c - Y \qquad\qquad 4.57$$

$$X_{PT} = X \qquad\qquad 4.58$$

In a matrix form, it can be described as follows in the form of the following equation.

$$f(X_{PT}, Y_{PT}) = \begin{bmatrix} 0 & 0 & 0 & . & . & 0 \\ 0 & 0 & 0 & . & . & 0 \\ 0 & 0 & 0 & . & . & 0 \\ 0 & 0 & 0 & . & . & 0 \\ 0 & V & 0 & . & . & 0 \\ 0 & 0 & 0 & . & . & 0 \end{bmatrix} \qquad 4.59$$

where *V* is pixel intensity at the pixel position. The determination of this value is explained in section 4.3.3.

*Case 2: Correlation peak on the right of the center point in **rθ** matrix*

$$Y_{PT} = Y_c + Y \qquad 4.60$$

$$X_{PT} = X \qquad 4.61$$

As in equation 4.59, after determining the *X* and *Y* coordinates, the value at these coordinates are placed in the appropriate position in the image matrix.

*Case 3: Correlation peak at the center point in **rθ** matrix*

$$Y_{PT} = Y_c \qquad 4.62$$

$$X_{PT} = X \qquad 4.63$$

The image matrix can be obtained in the same way as the above two cases.

**4.3.5   Modified flowchart of the process**

In this section the flowchart in figure 4.22 is modified based on the new additions to the processing explained in sections 4.3.2 to 4.3.4. The modified flowchart is shown in figure 4.39.
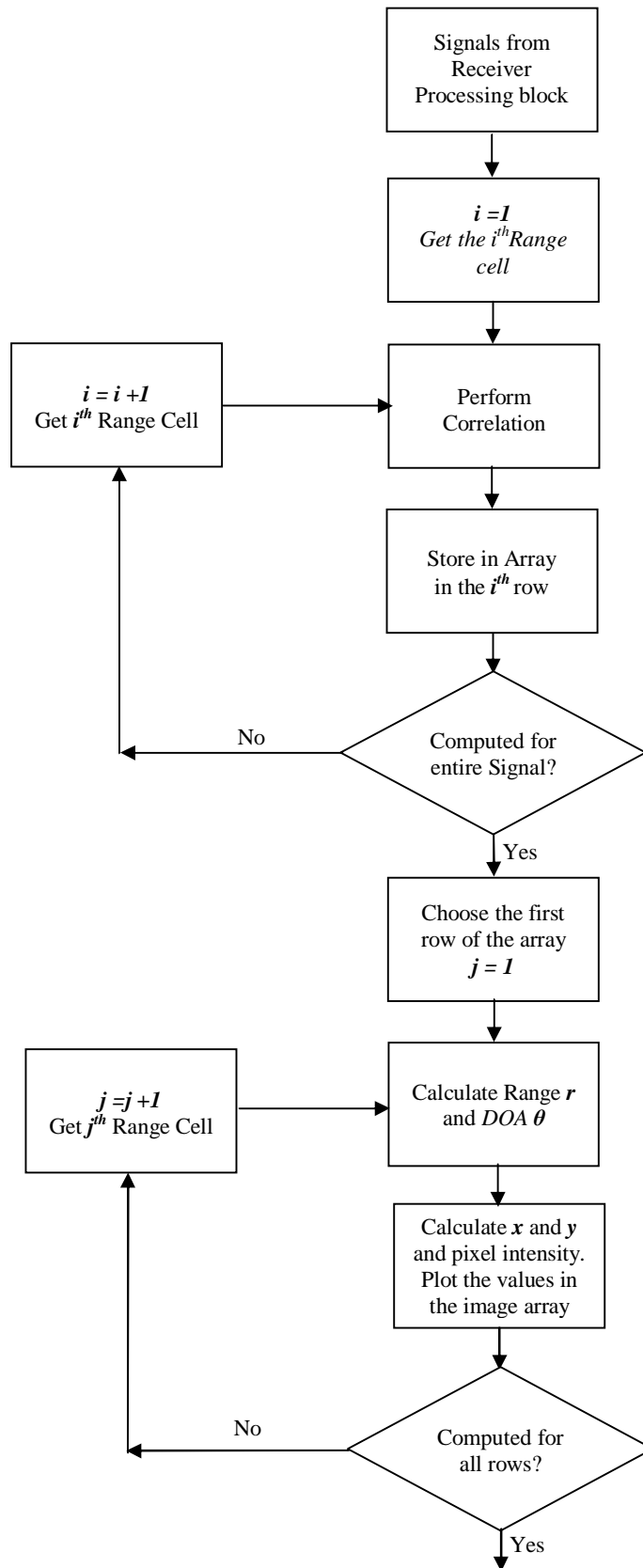
**Figure 4.39 Modified flowchart with additional processing features**

## 4.4 Multiple Direction of Arrival Estimation using Sparse Arrays

The previous sections dealt with theory for forming an image of the target scene using an array with two hydrophone elements. A summary of the steps involved in the image formation using two hydrophone elements are as follow:

1)    Divide signals into range cells.
2)    Determine the $r\theta$ matrix by cross-correlating between the range cells.
3)    Map the elements of the $r\theta$ matrix into an image array.

### 4.4.1 Shortcomings of using two element array

The steps above show that the $r\theta$ matrix, obtained from the cross-correlation of range cells, is mapped without any additional processing to form the image matrix. However the cross-correlation between the signals is not ideal. Also since the target returns not being orthogonal, cross-correlation gives rise to unwanted artifacts in the form of correlation sidelobes. As a result, when the $r\theta$ matrix is mapped to form the image, these cross-correlation artifacts are also mapped into the image array. This would result in the inability to distinguish between true targets and artifacts. Thus if there are multiple targets in the same range cell but at different angular direction it would be impossible to distinguish between them and they might look as a single target spread across the corresponding range cell.

### 4.4.2 Alternative signal processing techniques to determine DOA and their shortcomings

One way to avoid the problem of artifacts is to use modern beamforming methods. But as discussed and described in Chapter 3, these are not suitable as the array under investigation is a very sparse whose array elements are separated by many times the signal wavelength. Another problem is that for these beamformers to work effectively, they require a large number of array elements and hence a large

number of channels which nullifies the very purpose of this research. As a result of this modern beamformers were not used in this research.

Another method that could be used and has been the hot topic of research in recent days is the *independent component analysis (ICA)*. ICA is a blind signal deconvolution technique. Blind signal deconvolution is a process by which a set of signals are separated from its mixture without any knowledge of the signal statistics or the mixing process [90]. Thus if there are two or more returns in a signal, ICA would be able to separate these returns. Thus by finding the time delay between these components, the DOA can be estimated. The major problem here is that ICA is dependant on the signal statistics. The signals from different sources are assumed to be independent which might not be the case. In the case of underwater imaging, it is impossible to determine the statistics of the target returns. ICA requires the knowledge of number of targets in order to separate the signal mixture into independent components. Another problem that is encountered is that ICA requires the number of array elements to be greater than or equal to the number of targets. For these reasons it was decided not to use ICA.

This section investigates processing techniques to minimize the artifacts in the image formed; to make the image formed less ambiguous and to allow recognition of genuine targets. There are numerous signal processing or mathematical methods available in the literature. But keeping in view the objectives of the research, the processing methods that have been investigated here are such that they could be implemented with minimal hardware channels thereby reducing the system cost.

An image of the target scene is formed by combining the information from a couple of hydrophone elements. In the parlance of this research, one-look of the target scene is obtained using a couple of hydrophone elements. Thus, *multi-look processing* involves forming a processed image by fusing data obtained using more than two hydrophone elements. This section begins with determining the number of looks that can be obtained for number of hydrophone greater than two.

### 4.4.3  Number of images formed from *K* hydrophone elements

In this section, the number of images that can be formed from *K* hydrophone elements is calculated. From the image formation algorithm that was described in previous sections, it is known that an image is formed by combining the output of 2 hydrophone elements. The number of images that can be formed from 3 hydrophone elements is shown diagrammatically in figure 4.40.
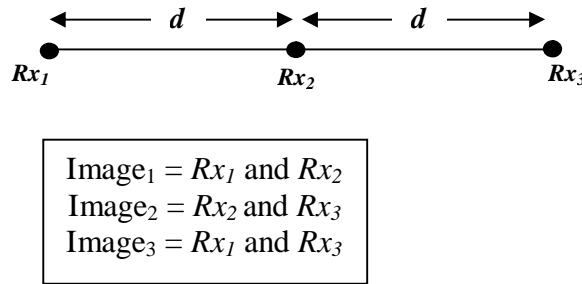


**Figure 4.40 Number of images formed from 3 elements**

In figure 4.40, three hydrophone elements $Rx_1$, $Rx_2$ and $Rx_3$ form an array. The distance between two successive elements is *d* meters. An image is formed by suitably combining the outputs of 2 hydrophone elements which form a sub-array. From figure 4.40 it is seen that with 3 hydrophone elements, there are 3 sub-arrays that can be formed and hence 3 images can be obtained. Image$_1$ is formed by combining $Rx_1$ and $Rx_2$ which forms the first sub-array in which the elements are separated by a distance *d* meters. Image$_2$ is formed by combining $Rx_2$ and $Rx_3$ which forms the second sub-array in which the elements are separated by a distance *d* meters. Finally Image$_3$ is formed by combining $Rx_1$ and $Rx_3$ which is the third sub-array in which the elements are separated by a distance of *2d* meters. Thus if there are *K* hydrophone elements then the number of sub-arrays and hence the number of images that can be obtained is given by

$$N_{IMG} = \frac{K!}{(K-2)!2!} = {}^{K}C_2 \qquad\qquad 4.64$$

From equation 4.64 it can be verified that for 3 elements, the number of images that can be formed is 3, for 4 elements that number of images that can be formed is 6 etc.

### 4.4.4  Principle of multi-look processing

The multi-look processing technique makes use of the spatial diversity principle. Spatial diversity principle exploits the fact that the signals received on different hydrophone elements are different as a result of spatial separation of the hydrophones. The signal from the hydrophone elements would be similar only at the locations where target signatures are present. Figure 4.41 explains the spatial diversity principle.
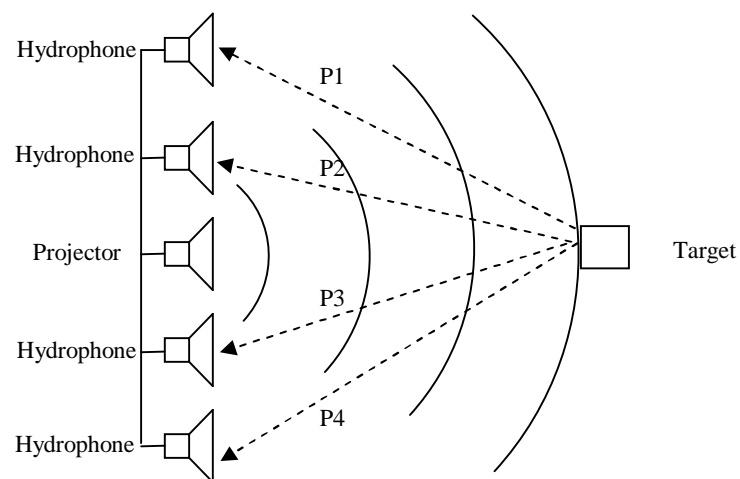


**Figure 4.41 Spatial diversity principle**

Figure 4.41 shows the acoustic waves emitted by the projector being backscattered after impinging on the target. Assume that four hydrophones are used. Since the hydrophones are spatially separated, the backscattered signals follow the path P1, P2, P3 and P4 to arrive at the hydrophones. Multi-look processing involves combining these signals in such a way so as to improve the SNR.  As the target returns follow different paths to each hydrophone elements, the noise signals would not correlate. However the target signature resulting from the interaction of the acoustic waves with the target remains unchanged. Thus the

cross-correlation between the noise present in the signal return would be minimal whereas that between the target signatures would be maximum. Increasing the receiver spacing can further decrease the noise cross-correlation.

The elements of each sub-array formed from the main array views the target at a slightly different angle. This causes the correlation artifacts to be independent at the output of each sub-array. By combining the outputs of the multiple sub-arrays suitably it is possible to reduce the correlation artifacts which are caused due to the non-orthogonality of the signals arriving at different hydrophone elements.

The concept of multi-look processing can be summarized as follows: the gain obtained by the multi-look processing is maximal when the cross-correlation between the noise artifacts is minimal and the auto-correlation between the target signatures is maximal.

### 4.4.5  Receiver structure modification to include multi-looks

The receiver structure in figure 4.1 is for two channels. The structure has to be modified for multi-look processing with the inclusion of a block for *data fusion* of the data formed using pairs of hydrophone elements. The modified receiver structure is shown in figure 4.42. Each channel in the receiver processing block contains a bandpass filter, a matched filter and TVG amplifier.

Figure 4.42 shows the receiver structure with $K$ hydrophone channels. With $K$ hydrophones it is possible to form $K-1$ $r\theta$ matrices with the hydrophones having same array element separation. Here processing is applied on the $r\theta$ matrices formed using equal elemental spacing. This is extended to all element combination and the process is explained in Chapter 6. The fusion process is performed by assuming that the target is located in the far-field.
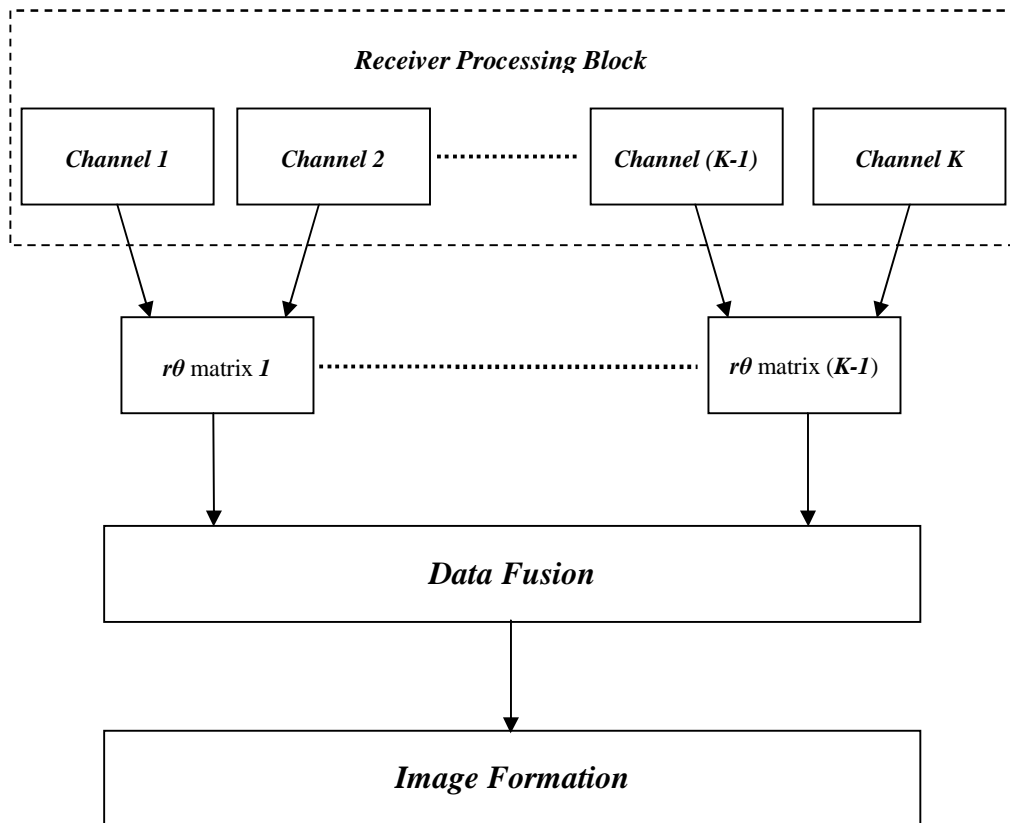
**Figure 4.42 Receiver structure modified**

### 4.4.6  Data Fusion

This section discusses few data fusion methods that have been tested in this research. The results for the methods discussed are presented in Chapter 6 after describing the sonar simulation model. The data fusion is performed by keeping spatial diversity in mind.

#### 4.4.6.1 Averaging

Mean or averaging is the first mathematical operation that is applied when looking for a processing technique that makes use of spatial diversity. This is also the first technique that was tried in order to remove the artifacts from the image. The averaging process is shown in figure 4.43.
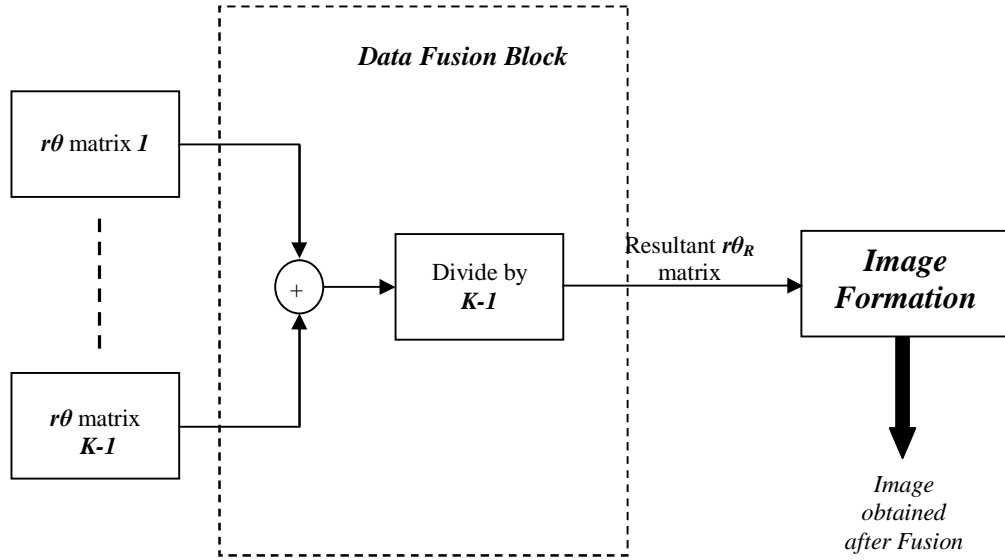
**Figure 4.43 Averaging process**

In figure 4.43 *K-1* *rθ* matrices obtained using *K* hydrophone elements with an array spacing of *d* meters are combined. The resultant *rθ*$_{\mathbf{R}}$ matrix is obtained by averaging each element in *K-1* *rθ* matrices. Mathematically this can be written as

$$r\theta_R(x,y) = \frac{r\theta_1(x,y) + ..... + r\theta_{K-1}(x,y)}{K-1} \qquad 4.65$$

Thus equation 4.65 shows that the averaging process performs a linear combination of the *rθ* matrices to obtain the resultant *rθ*$_{\mathbf{R}}$ matrix.

### 4.4.6.2 Non-Linear Combining

For the purpose of reducing clutter or artifacts which occur due to cross-correlation, a novel combining algorithm was implemented. The algorithm works on the *rθ* matrix. Each row in the *rθ* matrix corresponds to a particular range cell and hence this algorithm is designed to fuse each row of the matrix into a single row of the resultant *rθ*$_{\mathbf{R}}$ matrix. *rθ* matrices formed by equally spaced elements are considered. Thus if there are *K* hydrophone elements then it is necessary to fuse *K-1* *rθ* matrices obtained into a resultant *rθ*$_{\mathbf{R}}$ matrix which can be mapped into an image of the target scene.

The algorithm is based on the premise that the correlation artifacts in each range cell correlate poorly between the $r\theta$ matrices. This is because the hydrophone elements being spaced by several wavelengths apart each look of the sub-array forms a slightly different correlation sidelobe in corresponding range cells of the $r\theta$ matrices. The idea that each corresponding range cell of $r\theta$ matrices has different sidelobe is used to reduce the correlation sidelobes and obtain the resultant $r\theta_R$ matrix thus applying the principle of spatial diversity. In order to enhance gain it is necessary to combine the corresponding rows from the $r\theta$ matrix so as to bring down the unwanted artifacts to a minimum value. Thus instead of a linear combination of the array outputs to form an image, a non-linear approach is used to obtain a maximum gain in the image quality. The non-linear combining processing method developed is shown in figure 4.44.

For the purpose of explanation it is assumed that there are *K-1* $r\theta$ matrices available. In figure 4.44, the $i^{th}$ row of the $r\theta$ matrices is considered. The mean of the elements of the $i^{th}$ row of each $r\theta$ matrix is determined. In figure 4.44, $\mu_1$, $\mu_2$, ...., $\mu_{K-1}$ be the mean obtained using $i^{th}$ row of the $r\theta$ matrices. Then the initial threshold $\beta$ is determined by finding the average of all the means. Thus

$$\beta = \frac{\xi}{K-1} = \frac{\mu_1 + \mu_2 + .... + \mu_{K-1}}{K-1} \qquad 4.66$$

where $\xi$ is the sum of the means from $i^{th}$ row of the $r\theta$ matrices. This threshold calculated is subtracted from the $i^{th}$ row of the $r\theta$ matrices and any value which is less than *0* is replaced by zero. Thus the following operation is performed

$$U_j = \max\left(r\theta_{ij} - \beta, 0\right) \qquad 4.67$$

where *j=1......K-1* and *i* is equal to the number of rows in the $r\theta$ matrix which depends on the number of range cells. The $i^{th}$ row is modified according to equation 4.67. After modifying the $i^{th}$ row of the array, the standard deviation of the modified row is determined.
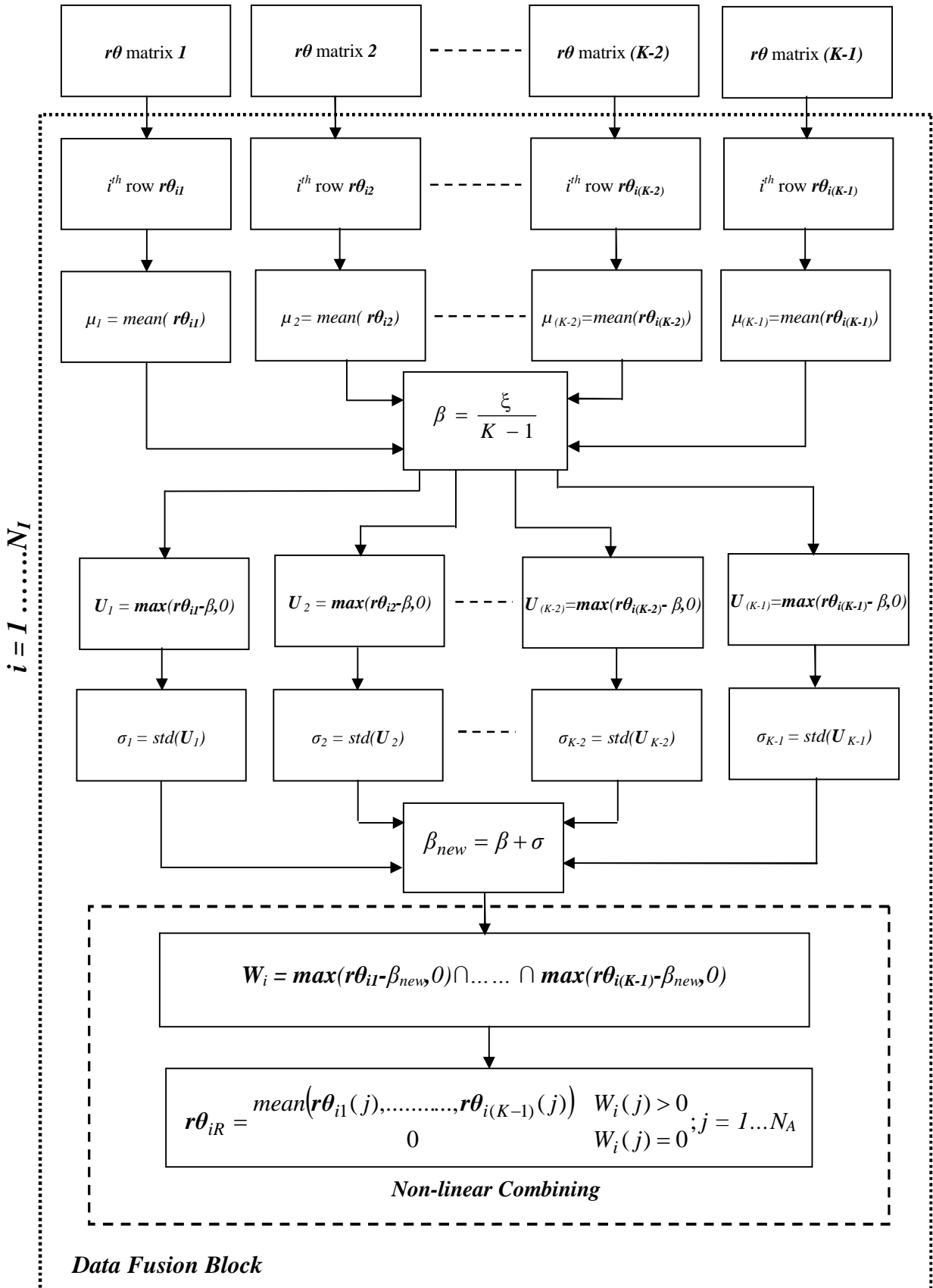
**Figure 4.44 Data fusion using non-linear combining**

Thus

$$\sigma_j = std(U_j) \tag{4.68}$$

where $j = 1......K-1$. The threshold is modified by the addition of the factor $\sigma$ which is given as

$$\sigma = \frac{\sigma_1 + \sigma_2 + ..... + \sigma_{K-1}}{K-1} \tag{4.69}$$

Thus,

$$\beta_{new} = \beta + \sigma \tag{4.70}$$

The non-linear combining is performed on the $r\theta$ matrices using the following condition

$$\boldsymbol{W_i} = \boldsymbol{max(r\theta_{i1}\text{-}\beta_{new},0)} \cap \boldsymbol{max(r\theta_{i2}\text{-}\beta_{new},0)} \cap ...... \cap \boldsymbol{max(r\theta_{i(K-1)}\text{-}\beta_{new},0)} \tag{4.71}$$

$$\boldsymbol{r\theta_{iR}} = \begin{matrix} mean\big(\boldsymbol{r\theta_{i1}}(j),.....,\boldsymbol{r\theta_{i(K-1)}}(j)\big) & W_i(j) > 0 \\ 0 & W_i(j) = 0 \end{matrix}, j = 1...N_A \tag{4.72}$$

where $\boldsymbol{r\theta_{iR}}$ is the resultant row of the final $r\theta$ matrix and $N_A = 2n_{d\_max}$ from equation 4.33. The $\cap$ operator in equation 4.71 is the *and* operation. $\boldsymbol{W_i}$ is a row vector. A column of $\boldsymbol{W_i}$ i.e. $W_i$(j) contains a value of '$1$' if the corresponding column of $i^{th}$ row of all the $r\theta$ matrices is greater than the threshold. If the condition is false then the value of $W_i$(j) is '$0$'. Thus values in matrix $\boldsymbol{W_i}$ is true or false. Hence the value at a pixel location of the resultant matrix depends on whether all the pixels at the corresponding pixel location are greater than the threshold in all the $r\theta$ matrices to be combined. If there is a target in the corresponding pixel location, it means that the target should be present in each of the considered pixel locations in all the matrices. If there is a high pixel in one of the matrix and the other matrices have a value less than the threshold in the

109

corresponding location, it would mean that the high pixel is due to the noise and not due to the target and hence a zero would be placed.

The demonstration of the non-linear combining process is done by taking the result obtained from one range cell. Figure 4.45 shows the output of $250^{th}$ range cell of three $r\theta$ matrices obtained using a four element array. Figure 4.45 is obtained without the application of the non-linear combining process.
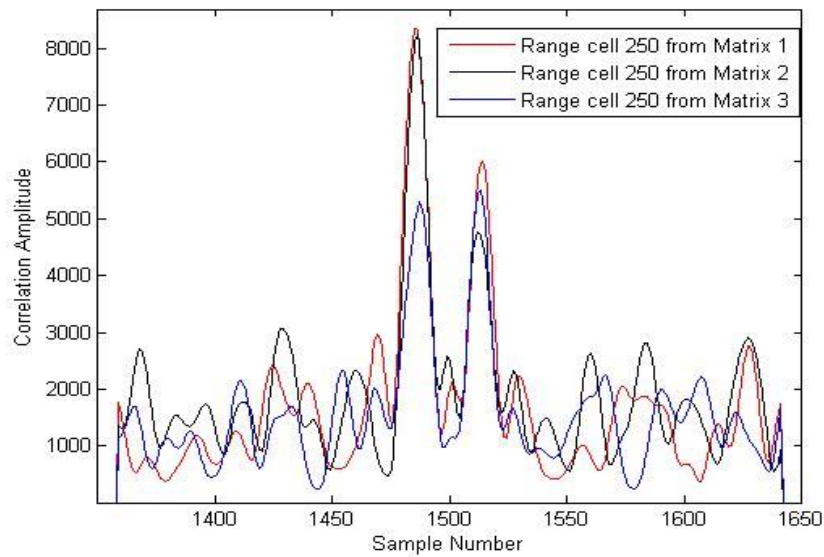


**Figure 4.45 Result obtained for one range cell of a distributed target profile before the application of non-linear combining process to the *rθ* matrices**

It is seen from figure 4.45 that there are two target peaks in all the three *rθ* matrices while the rest are artifacts which are random. The result obtained after applying the non-linear combining process is shown in figure 4.46. From figure 4.46, it can be found that the artifacts are removed and the peaks remain. This shows that the non-linear combining process works.
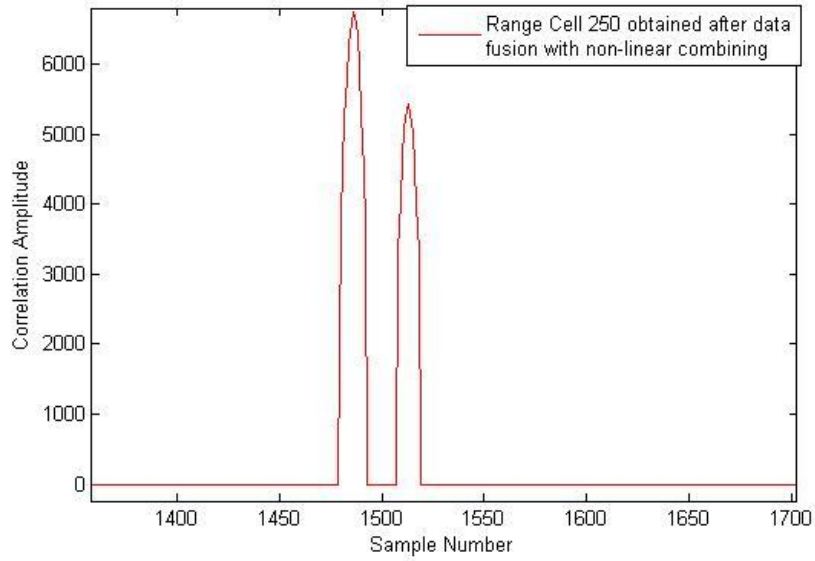
**Figure 4.46 Result obtained for one range cell of a distributed target profile after the application of non-linear combining process to the *rθ* matrices**

## 4.5    Summary

This chapter describes the receiver structure used in the project. On deriving the DOA equation it was found that the equation contained only one unknown parameter which was the delay between the signals received by the two receivers. Correlation, which is the process of determining the lead or lag of between two signals, is explained and used to determine the value of the delay. The received signals were divided into range cells in order to determine the range. The divided range cells were correlated whose absolute value were passed through a lowpass filter and stored in an array. This array forms the *rθ* matrix. The center column of the *rθ* matrix corresponds to the zero lead or lag point. In the *rθ* matrix, the number of columns to the left of the zero lag point corresponds to the number of delay samples of the signal arriving at $Rx_2$ w.r.t the signals arriving at $Rx_1$. Similarly the number of columns to the right of zero lag point corresponds to the number of delay samples of the signal arriving at $Rx_1$ w.r.t $Rx_2$. The process of determining the range and DOA was demonstrated for a point target cluster arranged in a way that each of the three cases i.e. signals arriving at the same time, signal arriving at $Rx_1$ earlier than $Rx_2$ and vice-versa was satisfied. The result from

111

the demonstration showed that the process can be used for the determination of range and DOA.

The $r\theta$ matrix is then converted into an image by plotting on an $XY$ grid after determining the corresponding $X$ and $Y$ locations in an array. The value of the pixel intensity at the location determined is based on the amplitude of the cross-correlation result in the $r\theta$ matrix. The output of matched filtering of the received signals would be an energy signal as matched filtering is the cross-correlation of the signal with itself. Further cross-correlation between the two signals after dividing into range cells to determine the delay would provide a result which is squared of the signal energy. Thus the pixel intensity at a particular pixel location is the square root of the cross-correlated value. Thus in this chapter it is shown that using a broadband signal an image can be formed by dividing the return signal into range cells and determining the delay.

After describing the theory for the image formation using two hydrophone elements, the receiver structure introduced for two element array was modified by the addition of a data fusion block. This block was added to reduce the correlation artifacts which would be obtained when the $r\theta$ matrix obtained using the two element array is mapped onto the image coordinates. The main aim of data fusion method is to use the $r\theta$ matrices obtained using multiple elements to form an image which has reduced artifacts. This chapter concludes after the presentation of two different types of data fusion methods whose performance has to be analysed.

# Chapter 5
# Sonar Simulation Model

In Chapter 4 the procedure to determine the range and DOA was described. The process of forming the image was developed and explained. The method to determine the intensity of each pixel in the image was also explained.

Chapter 5 describes the simulation model used in this research. The simulation model is used to evaluate the theory. The simulation model would help to understand the flaws in the proposed theory and also provide ways to improve the theory to obtain better results. Performing simulation would help in checking the theory before building the hardware. The simulation model is built using MATLAB.

## 5.1    Simulation model and parameters

The basic objective is to build an *Imaging Sonar Simulation Model* and test the theory developed. Figure 5.1 shows the entire *Imaging Sonar Simulation Model* which consists of the Sonar Transmission Block added to the receiver structure developed in Chapter 4. Thus the *Imaging Sonar Simulation Model* is divided into the following blocks

i)      Sonar Transmission Block
ii)     Receiver Processing Block
iii)    Beamforming Block
iv)     Signal Processing Block
v)      Image Formation Block

The functions of receiver processing block, beamforming block and the image formation block were described in detail in Chapter 4. The processing block which has the data fusion block is developed in Chapter 4, section 4.4. In this chapter the components of sonar transmission block is described.  This block together with the other blocks described in Chapter 4 form the entire *Image Sonar Simulation Model*.
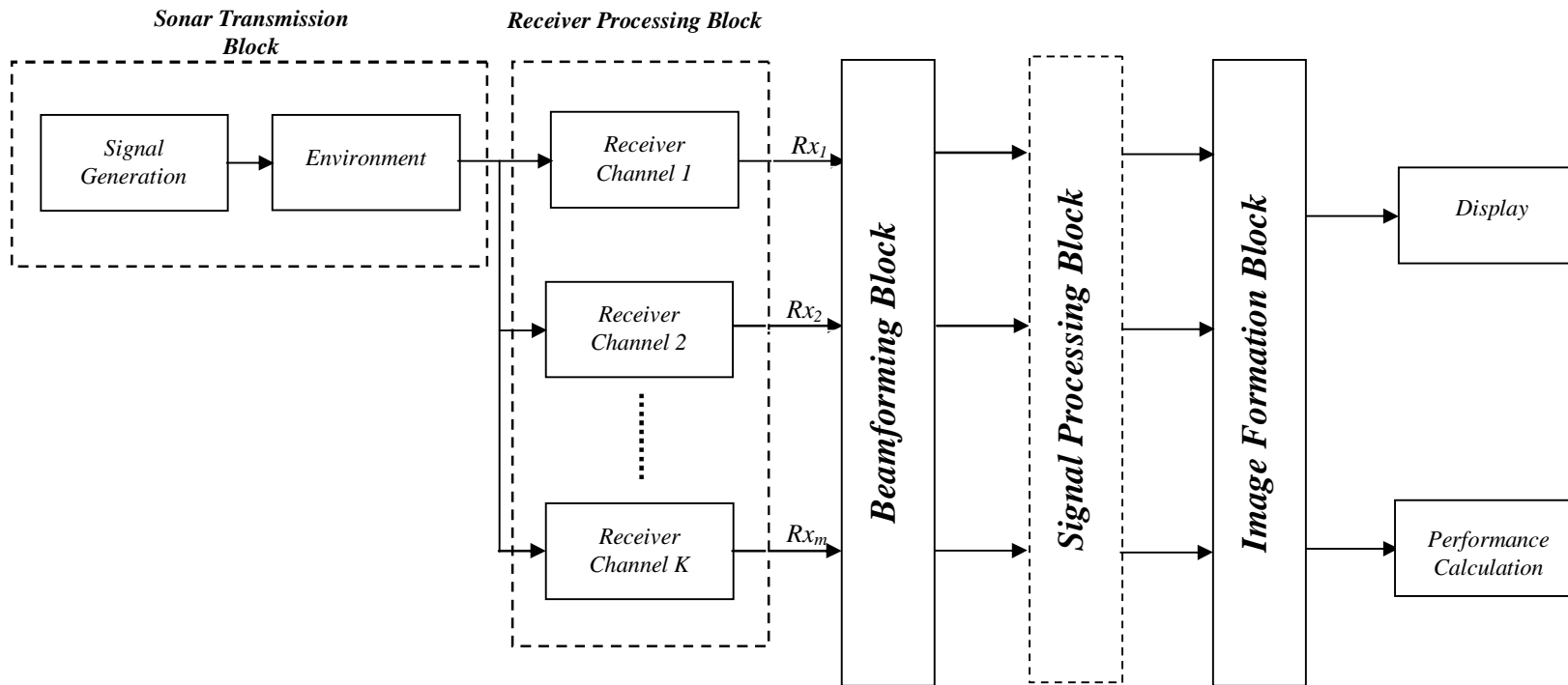
**Figure 5.1 Imaging sonar simulation model**

## 5.2    Sonar transmission block

The *sonar transmission block* is divided into two blocks. They are

i)    *Signal Generation Block*

ii)    *Environment Block*

### 5.2.1    Signal generation block

For the purpose of signal generation it is necessary to decide on various parameters like the source level of the signal, the type of signal to be used for the application, frequency and time duration of the signal and the sampling frequency. The simulation model was developed in a way that the signal parameters can be adjusted. The parameters used for simulation are tabulated in table 5.1

| | |
|---|---|
| *Source Level* | *194 db re 1µPa@1m* |
| *Signal Type* | *Linear Frequency Modulated Chirp* |
| *Start Frequency* | *200kHz* |
| *Stop Frequency* | *300kHz* |
| *Pulse Duration* | *5ms* |
| *Sampling Frequency* | *1MHz* |

**Table 5.1 Signal parameters**

A source level of 194 dB re 1 µPa @ 1m was chosen to match the characteristics of the transmit transducer and electronics available. The value is defined in *dB* for ease of calculation. The minimum sampling frequency required (Nyquist frequency) should be at least two times the highest frequency of the signal. Simulation was performed using a sampling frequency of 1 MHz which is about 3 times the highest frequency of the chirp signal and hence satisfies the Nyquist criterion. The simulated received signals were not basebanded as the center

frequency is comparable to the bandwidth of the signal. Converting the signals to baseband would be useful only if the fractional bandwidth is very small and hence saving in terms of computation would be obtained. The computational savings obtained here by converting the signals to baseband would be small and hence the signals were not converted to baseband.

### 5.2.1.1    Range resolution

Range resolution is defined as the ability to distinguish between two objects that are separated in range. The purpose of using a chirp signal was to obtain a good range resolution which is dependant on the bandwidth of the signal and is defined by the formula [44]

$$\Delta r = \frac{c}{2B}$$

5.1

where $B$ is the bandwidth of the LFM signal and $\Delta r$ is the range resolution. Thus from the above equation it is seen that range resolution is better for large bandwidth signals. Thus from the above equation the range resolution for a chirp having a frequency sweep of 200-300 kHz is calculated to be

$$\Delta r = \frac{1500}{2 \times 100 \times 10^3} = 0.0075m$$

5.2

The result shows that by using a chirp signal the system should be able to distinguish between targets which are separated by 0.0075m in range.

In this project as the received signals are divided into range cells, the range resolution would be less than the theoretical value given in equation 5.2. When there is no overlap between the range cells, two targets in the same range direction can be distinguished only if they fall in different range cells. Thus when there is no overlap, the range resolution is equal to the size of the range cell. When there is a $p\%$ overlap between range cells of size $x_r$ meters, then the range resolution will be equal to

$$\Delta r = \left(1 - \frac{p}{100}\right) x_r \qquad\qquad 5.3$$

*5.2.1.2    Angular resolution*

Angular resolution is defined as the minimum angular separation that is required between the targets so that they can be resolved. If the angular separation between the targets is less than the value given by angular resolution then the targets would appear as one.
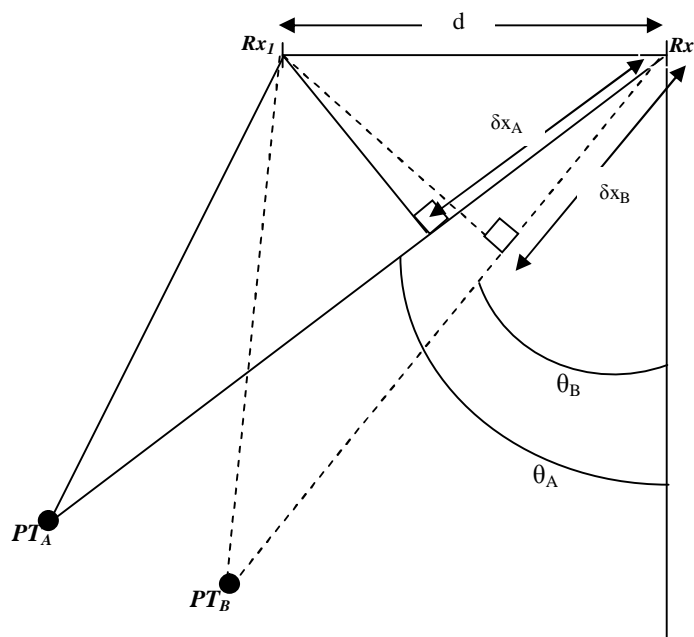


**Figure 5.2 Receiver geometry for determining angular resolution**

In figure 5.2, $PT_A$ and $PT_B$ are two targets which are at angles $\theta_A$ and $\theta_B$ respectively. $\delta x_A$ and $\delta x_B$ are the extra distances traveled by the plane waves scattered by targets $PT_A$ and $PT_B$ respectively to arrive at receiver $Rx_2$. Receivers $Rx_1$ and $Rx_2$ are separated by a distance $d$. From Chapter 4, section 4.2.1, equation 4.15

$$\sin\theta_A = \frac{\delta x_A}{d} \qquad\qquad 5.4$$

$$\sin \theta_B = \frac{\delta x_B}{d} \qquad\qquad 5.5$$

Subtracting equation 5.4 from 5.5,

$$\sin \theta_A - \sin \theta_B = \frac{\delta x_A}{d} - \frac{\delta x_B}{d} \qquad\qquad 5.6$$

By using the trigonometric relation,

$$\sin \theta_A - \sin \theta_B = 2\cos\left(\frac{\theta_A + \theta_B}{2}\right)\sin\left(\frac{\theta_A - \theta_B}{2}\right) \qquad\qquad 5.7$$

Substituting equation 5.7 in equation 5.6

$$2\cos\left(\frac{\theta_A + \theta_B}{2}\right)\sin\left(\frac{\theta_A - \theta_B}{2}\right) = \frac{\delta x_A}{d} - \frac{\delta x_B}{d} \qquad\qquad 5.8$$

$(\theta_A\text{-}\theta_B)$ is very small as the angular resolution is the smallest angular separation required to distinguish between two targets. Thus using the small angle approximation,

$$\sin\left(\frac{\theta_A - \theta_B}{2}\right) \cong \left(\frac{\theta_A - \theta_B}{2}\right) = \frac{\Delta\theta}{2} \qquad\qquad 5.9$$

where $\Delta\theta$ is the angular resolution. Substituting equation 5.9 in equation 5.8,

$$\Delta\theta \cos(\theta_s) = \frac{\delta x_A}{d} - \frac{\delta x_B}{d} = \frac{\delta x_A - \delta x_B}{d} \qquad\qquad 5.10$$

where $\theta_s = \left(\frac{\theta_A + \theta_B}{2}\right)$ is the look angle of the array. Hence,

$$\Delta\theta = \left| \frac{\delta x_A - \delta x_B}{d\cos\theta_s} \right| \qquad 5.11$$

$$\Delta\theta = \left| \frac{cn_{d\_A}T - cn_{d\_B}T}{d\cos\theta_s} \right| \qquad 5.12$$

where $T$ is the sampling interval. $n_{d\_A}$ and $n_{d\_B}$ are the difference samples due to $\delta x_A$ and $\delta x_B$ respectively. Thus equation 5.12 can be written as

$$\Delta\theta = \left| \frac{c(n_{d\_A} - n_{d\_B})}{Fd\cos\theta_s} \right| = \left| \frac{c(\Delta n_d)}{Fd\cos\theta_s} \right| \qquad 5.13$$

where $F$ is the sampling frequency. Since the considered waveform is a wide bandwidth signal and since the bandwidth is comparable to the frequencies used, the sampling frequency $F$ can be written in terms of the bandwidth as

$$F = N_{samp}B \qquad 5.14$$

where $N_{samp}$ is chosen suitably in order to avoid aliasing. Thus

$$\Delta\theta = \left| \frac{c(\Delta n_d)}{N_{samp}B.d\cos\theta_s} \right| \qquad 5.15$$

$$\Delta\theta = \left| \frac{kc}{B.d\cos\theta_s} \right| \qquad 5.16$$

where $k = \dfrac{\Delta n_d}{N_{samp}}$. The value of $\Delta\theta$ is approximated to

$$\Delta\theta \approx \left| \frac{c}{Bd\cos\theta_s} \right| \qquad 5.17$$

where $B$ is the bandwidth of the signal and $d$ is the receiver spacing. The above equation shows that the angular resolution is a function of the array spacing $d$ and the bandwidth $B$. Larger the values of $B$ and $d$, smaller will be the value of angular resolution and hence better chances for the targets which are close together to be resolved. Also seen from equation 5.17 is that the angular resolution is dependant on the look angle of the array. Assume a receiver spacing of 0.3 m, bandwidth of 100 kHz, and let $\theta_s$ be $30^0$, angular resolution is given by

$$\Delta\theta \approx \frac{1500}{100 \times 10^3 \times 0.3 \times \cos(30^o)} \qquad 5.18$$

$$\Delta\theta \approx \frac{1500}{100 \times 10^3 \times 0.3 \times \cos(30^o)} \qquad 5.19$$

$$\Delta\theta \approx \frac{1500}{100 \times 10^3 \times 0.3 \times 0.866} = 3.3^o \qquad 5.20$$

Thus in order for the two targets to be resolved they have to be separated approximately by $3.3^o$.

### 5.2.2 Environment block

The ocean environment model is divided into targets block, spreading losses block and noise block. The environment block is shown in figure 5.3 and the implementation is described in the following paragraphs.
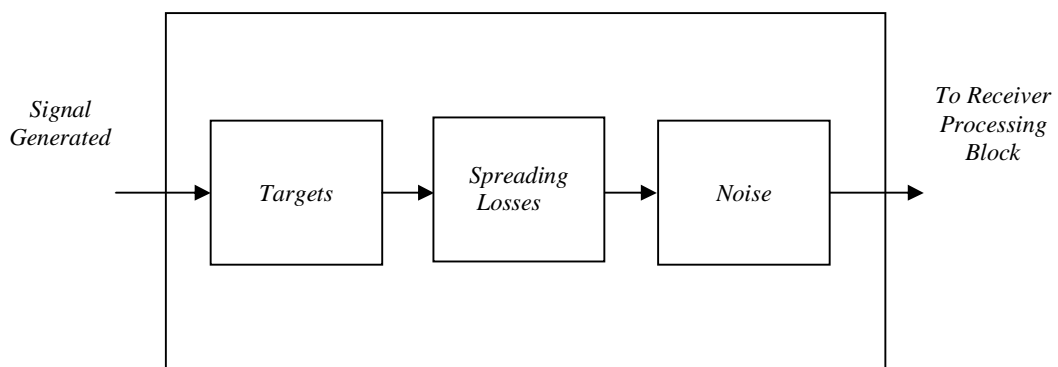


**Figure 5.3 Model of environment**

The chirp (LFM) signal generated interacts with each of these blocks. From the sonar equation in Chapter 2 it is seen that spreading loss occurs as the signal travels to the target and is backscattered from it. The system is monostatic and hence the spreading loss is assumed to be the same in both the directions as spreading depends on range. Spreading is assumed to be spherical and is proportional to the square of the distance travelled. Since the calculations are in *dB* the spreading loss is given by equation 2.13 in section 2.1.2.1.

In this project a practical target is considered to be a collection of clusters of point targets. Each cluster is assumed vary randomly with a maximum radius of $r_{c1}$ meters. Each point target in the cluster is assumed to be spherical. The point targets which make up the cluster are assumed to be uniformly distributed within the cluster. The radius of each point target in the cluster is assumed to vary randomly (uniformly) with a maximum value of $r_{c2}$ meters. When the position of a point target is defined within the cluster, a check is performed to make sure that the distance between the defined point target with the other point targets defined within the cluster is greater than or equal to the sum of their radii. If this condition is not satisfied it would mean that the two point targets under comparison are overlapping which is not possible. Hence if the condition fails a new position is defined and then the condition is checked again. The procedure is continued until a new position for the point target is obtained where the condition is satisfied. The procedure of forming the cluster is shown in flowchart in figure 5.4.

In the flowchart, $D_{pj}$ is the distance between the centers of the recently defined point target and $j^{th}$ point target already defined. $C_p$ is the radius of the present point target defined and $C_j$ is the radius of the $j^{th}$ point target. The number of point targets in a cluster is assumed to be $K_{pt}$.

The point target clusters were distributed in a straight line pattern or a sine wave pattern in order to represent the straight surface or a surface in the form of a sine wave. In order to obtain such surface patterns, the positions of center points of these profiles are determined. The center point act as the center of the cluster and the point targets are distributed around this center. Since each point target within

the cluster is spherical, target strength (TS) is calculated using the following formula [36].

$$TS = 20\log_{10}\left(\frac{r_{c2}}{2}\right) dB \qquad\qquad 5.21$$

where $r_{c2}$ *meters* is the radius of the point target. A single cluster which is made up of many point targets is shown in figure 5.5. The four different profiles that are generated are shown in figure 5.6, figure 5.8, figure 5.10 and figure 5.12.

In order to calculate the signal backscattered from the cluster, consider the equation 2.18. The equation can be modified and written as

$$RL_i = SL + RS + TS_i - TL_i \qquad\qquad 5.22$$

where *RS* is the receiver sensitivity and $RL_i$ (in *dB*) is the received signal level from the $i^{th}$ point target. Thus the root mean square (rms) value of the signal amplitude ($V_{rms\_i}$) received from a point target is

$$V_{rms\_i} = 10^{\frac{RL_i}{20}} \qquad\qquad 5.23$$

From equation 5.23, the peak value of the received signal from a point target is

$$V_{A\_i} = 1.414 V_{rms\_i} \qquad\qquad 5.24$$

The signal amplitude given by equation 5.24 is for a signal received from a single point target. The return signal is obtained by multiplying the amplitude $V_{A\_i}$ with the equation of the signal (in this case a chirp signal). Depending on the distance to and from the point target, appropriate delay is inserted to the signal. Let $y_i(t)$ be the received signal due to $i^{th}$ point target in a cluster. Thus
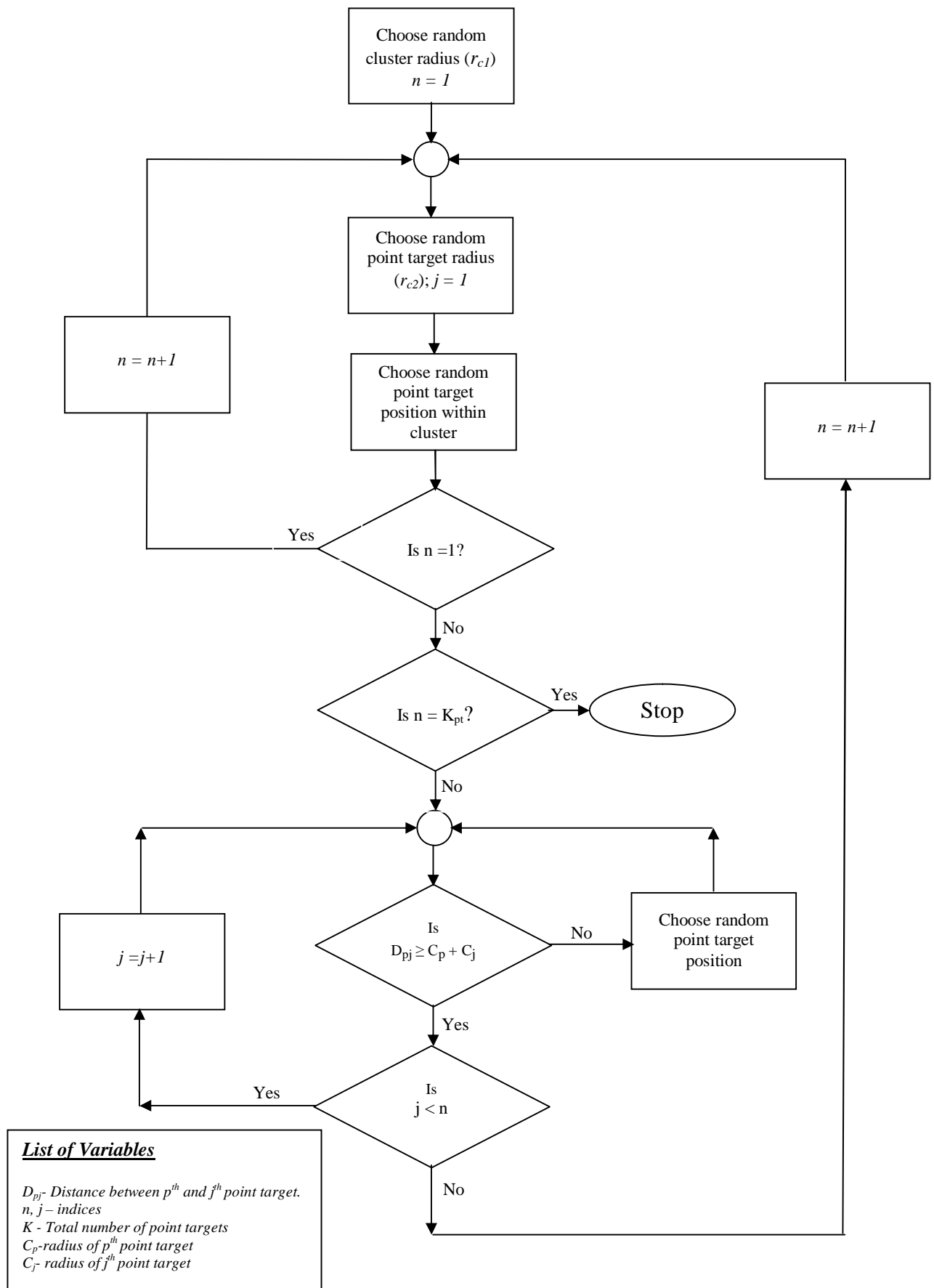
**Figure 5.4 Flowchart describing the formation of a cluster**

Choose random cluster radius ($r_{c1}$)
$n = 1$

Choose random point target radius ($r_{c2}$); $j = 1$

$n = n+1$

Choose random point target position within cluster

Is n =1?

Yes

No

Is n = $K_{pt}$?

Yes

Stop

No

$n = n+1$

$j = j+1$

Is $D_{pj} \geq C_p + C_j$

No

Choose random point target position

Yes

Is $j < n$

Yes

No

**List of Variables**

$D_{pj}$- Distance between $p^{th}$ and $j^{th}$ point target.
$n, j$ – indices
$K$ - Total number of point targets
$C_p$-radius of $p^{th}$ point target
$C_j$- radius of $j^{th}$ point target

**Figure 5.5 Diagram showing a single cluster**

$$y_i(t) = V_{A\_i} \times Chirp(t - t_i)$$  5.25

$y_i(t)$ is the return due to single point target and $t_i$ is obtained using the distance travelled. If there are $K_{pt}$ point targets in the cluster and if there are $K_c$ clusters then the total number of point targets ($K_{tot}$) in the entire target is

$$K_{tot} = K_{pt} \times K_c$$  5.26

$$y_{tot}(t) = \sum_{i=1}^{K_{tot}} y_i(t)$$  5.27

where $y_{tot}(t)$ is the return from all the point targets and hence the return signal. This procedure is repeated for all available hydrophones. Thus by knowing the source level, the target strength and the spreading losses, it is possible to calculate the received signal strength and hence the received signal using the sonar equation.

The coordinates of the point targets generated are stored in a file along with the radius of the point targets. From the generated coordinates, spreading loss and delays that have to be applied to the return signal can be calculated. The target strength of the target is calculated using equation 5.21 from the knowledge of the radius. This provides all the parameters for the generation of the received signal.

Next described is the addition of noise. Noise in the ocean environment depends on various factors like the wind speed, shipping density, frequency of the signal used. There are many formulas that have been put forward from which the noise spectral level (*NSL*) is calculated. The *NSL* is calculated using the following formulas [40 91 92]

$$NSL1 = 17 - 30\log_{10}(f_c)$$  5.28

$$NSL2 = 40 + 20(D_s - 0.5) + 26\log_{10}(f_c) - 60\log_{10}(f_c + 0.03)$$  5.29

$$NSL3 = 50 + 7.5W^{\frac{1}{2}} + 20\log_{10}(f_c) - 40\log_{10}(f_c + 0.4)$$  5.30

$$NSL4 = -15 + 20\log_{10}(f_c)$$  5.31

where $f_c$ is the center frequency in kHz. Equation 5.28 is the noise spectral density due to turbulence (<10 Hz), equation 5.29 is the noise spectral density due to shipping (10 – 100 Hz), equation 5.30 is noise spectral density due to surface agitation (100 Hz – 100 kHz) and equation 5.31 is the noise spectral density due to thermal noise (>100kHz) [40 91 92]. The total *NSL* can be calculated using the equation [40]

$$NSL = 10\log_{10}\left(10^{\frac{NSL1}{10}} + 10^{\frac{NSL2}{10}} + 10^{\frac{NSL3}{10}} + 10^{\frac{NSL4}{10}}\right)$$  5.32

The noise level is calculated using Chapter 2, equation 2.22 [40]. From the noise level obtained the noise power is calculated. Then using random numbers it is

possible to synthesize the Additive White Gaussian (AWGN) noise which is added to each of the hydrophone signals. Since the noise is random and independent for each of the hydrophones this procedure has to be repeated for each of the hydrophones. Thus the output of the receiver will become

$$y_T(t) = y_{tot}(t) + v(t) \qquad\qquad 5.33$$

where $y_T(t)$ is the signal obtained after the addition of noise and $v(t)$ is the noise generated.

## 5.3  Receiver processing blocks

The outputs obtained from the environment block are passed on to the receiver processing block. The receiver processing block was explained in Chapter 4, section 4.1.  Each channel in the receiver processing block involves the functions as shown in the figure 4.1. The filtering operation involves the implementation of a bandpass filter with a passband of 200 kHz-300 kHz which lies in the same range as that of the signal frequency used. Suitable finite impulse response (FIR) filter coefficients are designed using the in built *sptool* function in Matlab. The signal from the bandpass filter passes on to the matched filter. The operation of the matched filter and the pulse compression technique was described in Chapter 4, section 4.1.1. TVG is explained in detail in Chapter 4, section 4.1.2.

The output from the receiver processing block is applied to the beamforming block which is described in Chapter 4, section 4.2. The output from the beamforming block is applied to the image formation block whose implementation is described in detail in Chapter 4, section 4.3. The processing block which is in between the beamforming and image formation blocks is explained in Chapter 4, section 4.4 where multi-look processing is performed in order to fuse the outputs of multiple elements for obtaining a better output image.

## 5.4 Forming reference binary image

The image formed using the procedure described in Chapter 4 has to be verified in order to determine whether the image formed by the algorithm is representative of the target defined by the coordinates. It is also a desirable factor to check how much noise in the form of artifacts is present in the image formed. Hence a reference binary image is formed using the target coordinates which is of the same size as the final image formed using the image formation algorithm. The binary image is formed by switching the pixels *on* at the locations where the target is present whereas the other pixels are switched *off*. A binary image is formed because from the target coordinates as it is impossible to determine the true value of the pixels at a particular pixel location. The intensity of each pixel is a function of correlation of number of signals from various point targets. Thus a binary image which closely represents the true image is formed.

| Images formed from coordinates | Binary Images |
|---|---|
|  |  |
| **Figure 5.6 Simulated Point target from Coordinates** | **Figure 5.7 Binary Image of Simulated Point target** |
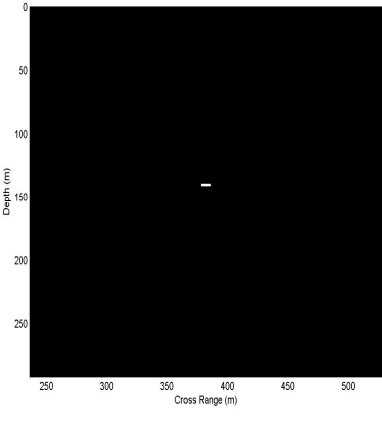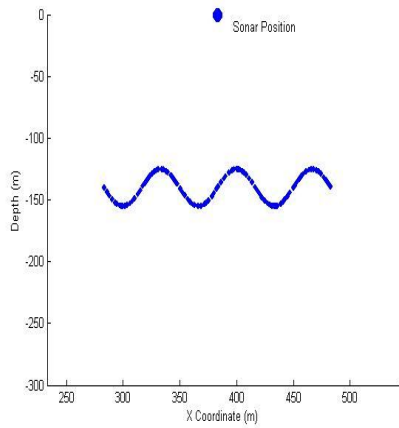
**Figure 5.8 Sine Profile from coordinates**
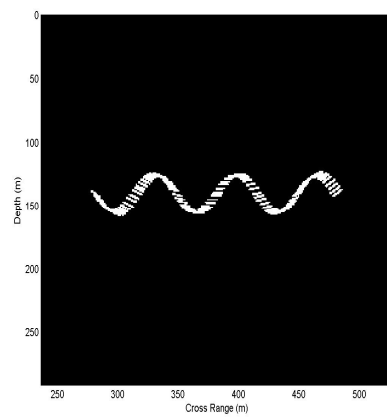


**Figure 5.9 Binary Image of Sine Profile**
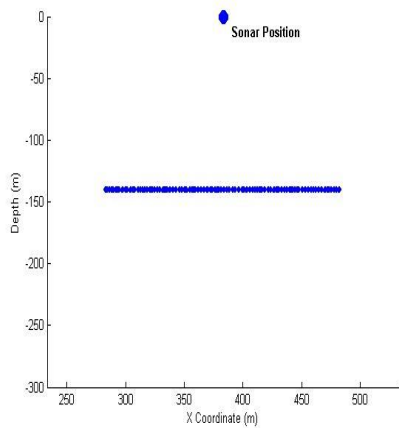


**Figure 5.10 Straight line profile from coordinates**
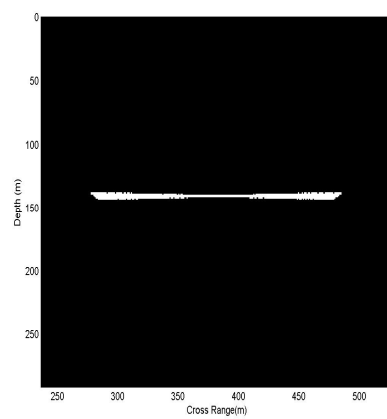


**Figure 5.11 Binary Image of Straight line profile**
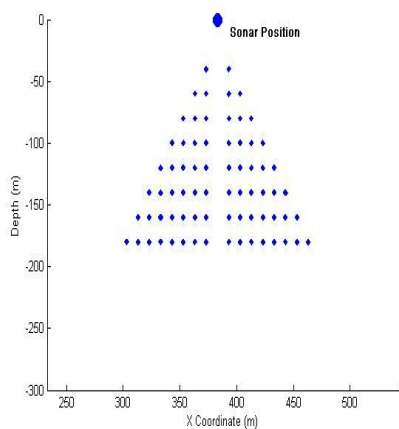


**Figure 5.12 Distributed Target Profile from coordinates**
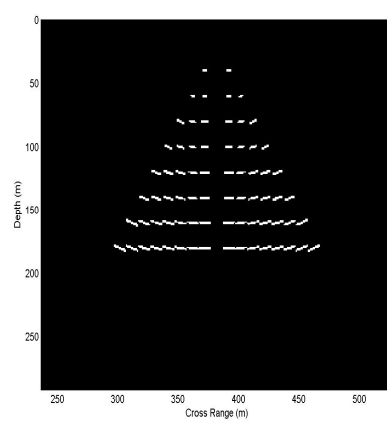


**Figure 5.13 Binary Image of Distributed target profile**

Figure 5.7, figure 5.9, figure 5.11 and figure 5.13 are the binary images formed for the target profiles considered, using the angular resolution of typical multibeam sonar. In order to form the reference images an angular resolution of $1.5^o$ is considered. A few examples of multibeam sonar along with their specifications are given in Table 1.1. The spreading of the targets away from the axis of the sonar array is the effect of angular resolution.

## 5.4.1   Measurement Metrics

Measurement metrics are required to quantify the performance of the algorithm developed. The image obtained using the algorithm developed has to be verified in order to check whether the simulated target and the target formed in the image by the imaging algorithm are in the same location. The amount of noise or any imaging artifacts that are present in the image formed using the imaging algorithm should also be measured.

There are many techniques available in literature to determine the image quality. They can be broadly classified under subjective and objective measures. Subjective measures try to determine the image quality in a way the humans classify the image. The subjective measures can be further classified depending on how the image quality is determined [89]. They are i) Full Reference (FR) ii) No Reference (NR) iii) Reduced Reference (RR) methods [93]. In the FR and RR methods, full knowledge or partial knowledge of the original image is required for the calculation of the image quality measure [93]. NR models do not require the knowledge of the original image [93]. The NR models are application specific and are developed to measure the artifacts arising due to specific image processing application [93]. The subjective measures developed in order to determine the image quality are suitable for natural images. Thus if there is a set called images which contains all the images, then natural images form a subset of images. Images formed using the principles of radar, sonar etc do not come under this category [94]. The determination of subjective image quality measure is by itself a separate field of research [94].

The second type of image quality measure is the objective measure. The objective measure determines the image quality using techniques like signal-to-noise (SNR) ratio, Peak Signal to Noise ratio (PSNR) etc. The SNR, PSNR etc are full reference methods in that it requires the knowledge of the original image. In this project we have tried to use one full reference subjective measure and the objective measures. The measures used are described in the following paragraphs.

### 5.4.1.1    *Signal-to-noise ratio (SNR)*

Signal-to-Noise ratio is defined as the ratio of the total signal power to the noise power. In this research it is taken as the ratio of sum squared intensity of the signal area in the image to the sum squared intensity of noise area in the image. This measure gives an indication of the gain obtained as a result of the algorithm. The procedure to extract the intensities from the signal area and noise area is given below.

The reference binary image formed contains zeros and ones. The binary images are formed by assuming an angular resolution of $1.5^{o}$. Thus in the binary image, ones are placed in the position where the target should appear and zeros are placed in other places. When the binary image is multiplied pixel by pixel with the image formed from the sonar simulation model, the resultant image would contain just the target. The signal power is calculated by squaring and summing the intensities of the pixels formed by the target. In order to determine the noise power, a complimentary image is formed by subtracting the binary image from unity. Thus in the complimentary image ones are placed in the position where there is a possibility of noise. The complimentary image would contain zeros in the position where the target was present. Multiplying this complimentary image pixel by pixel with the image from the simulation model would extract the noise. The noise power is determined in the same way as before. Let the reference binary image formed be represented as $I_{ref}$, the complimentary image as $I_C$ and the image formed by the simulation model as $I_{Sim}$. The procedure described can be given as follows

130

$$S = \sum_{r=1}^{N_I} \sum_{c=1}^{N_A} \left( I_{ref}(r,c) \times I_{Sim}(r,c) \right)^2 \qquad\qquad 5.34$$

$$I_C = 1 - I_{ref}(r,c); \; r = 1....N_I, \, c = 1...N_A \qquad\qquad 5.35$$

$$N = \sum_{r=1}^{N_I} \sum_{c=1}^{N_A} \left( I_{ref}(r,c) \times I_C(r,c) \right)^2 \qquad\qquad 5.36$$

$$SNR = 10\log_{10}\left(\frac{S}{N}\right) \qquad\qquad 5.37$$

### 5.4.1.2    *Peak Signal-to-noise ratio (PSNR)*

PSNR of an image can be defined as the ratio of the squared of maximum possible value a pixel can take to the mean squared error between the reference and binary image. PSNR can be obtained using the following equation [95]

$$PSNR = 10\log_{10}\left(\frac{IMax^2}{MSE}\right) \qquad\qquad 5.38$$

$$MSE = \frac{1}{N_I \times N_A} \sum_{r=1}^{N_I} \sum_{c=1}^{N_A} \left( I_{ref}(r,c) - I_{Sim}(r,c) \right)^2 \qquad\qquad 5.39$$

where *IMax* is the maximum possible value of pixel intensity in the image and *MSE* is the mean squared error. The *PSNR* is the common image quality metric that is used due to the ease of computation and tries to quantify the quality of image obtained [96 97 98].

### 5.4.1.3    *Structural similarity index (SSIM)*

SSIM is a subjective measure which tries to evaluate the image formed subjectively. SSIM has grown in popularity due to its simplicity and numerous researches are taking place [99]. SSIM was chosen because of these factors. SSIM

is a full reference technique. Although the subjective measures available are suitable only for natural images, in this research we have tried to determine the image quality subjectively.

SSIM assumes that the Human Visual System (HVS) assesses the image using three parameters [100 101]. They are luminance, contrast and structure in the image [92 93]. Thus each parameter is calculated and the index obtained is the product of these three parameters [100 101]. Thus [100 101]

$$l(A,B) = \frac{2\mu_A\mu_B + \varepsilon_1}{\mu_A^2 + \mu_B^2 + \varepsilon_1} \qquad\qquad 5.40$$

$$Ct(A,B) = \frac{2\sigma_A\sigma_B + \varepsilon_2}{\sigma_A^2 + \sigma_B^2 + \varepsilon_2} \qquad\qquad 5.41$$

$$st(A,B) = \frac{2\sigma_{AB} + \varepsilon_3}{\sigma_A\sigma_B + \varepsilon_3} \qquad\qquad 5.42$$

$$\varepsilon_1 = \left(k_1 D_y\right)^2 \qquad\qquad 5.43$$

$$\varepsilon_2 = \left(k_2 D_y\right)^2 \qquad\qquad 5.44$$

$$\varepsilon_3 = \frac{\varepsilon_2}{2} \qquad\qquad 5.45$$

where $l(A,B)$ is the measure of luminance, $Ct(A,B)$ is the measure of contrast and $st(A,B)$ is the structural measure. $\mu_A$ and $\mu_B$ are the mean of images A and B respectively. $\sigma_A$ and $\sigma_B$ are the variances of images A and B and $\sigma_{AB}$ is the covariance between images A and B [100 101]. $D_y$ is the dynamic range of the image, $k_1$ and $k_2$ are constants which are chosen by trial and error [100 101]. $\varepsilon_1$, $\varepsilon_2$ and $\varepsilon_3$ are very small constant values introduced in order to make the system of equation stable. The SSIM is obtained by multiplying equation 5.40, equation 5.41 and equation 5.42

## 5.5 Computational Complexity

This section contains an estimate of the computational complexity of the developed algorithm in order to show that the implementation of the algorithm is feasible on a digital signal processing (DSP) processor. The total computational complexity of the algorithm developed is calculated in this section. Fast Fourier Transform (FFT) is used to determine the correlation. It is assumed that FFT performed is a radix-2 FFT. Since the return signals are not converted to baseband, the FFT operation is performed on a real signal. The complexity of the algorithm would vary depending on the type of FFT algorithm that is implemented.

### 5.5.1 Computational complexity of forming $r\theta$ matrices

The complexity of an algorithm is the total number of multiplications and additions in the entire process. In forming **$r\theta$** matrices since correlation is involved between the range cell data, the complexity of the process can be calculated by determining the complexity of correlation. Let $d_1(t)$ and $d_2(t)$ be the data to be correlated.

The correlation process involves the following steps

1) Determine the FFT of the data to be correlated. Thus

$$D_1(f) = fft(d_1(t)) \qquad\qquad 5.46$$

$$D_2(f) = fft(d_2(t)) \qquad\qquad 5.47$$

It is assumed that a M point fft is determined.

2) Find the resultant by multiplying each element of $D_1(f)$ and $D_2(f)$. Thus

$$D(f) = D_1(f).D_2(f) \qquad\qquad 5.48$$

3) Find the inverse of $D(f)$ to determine the correlated result:

$$d(f) = ifft(D(f))$$ 5.49

Step 1 involves determining the fft of each data sequence. The number of multiplications and additions for one $M$ point radix 2 fft is

$$Number\_of\_Multi = \frac{M}{2}\log_2 M$$ 5.50

$$Number\_of\_Add = M \log_2 M$$ 5.51

Step 1 involves taking fft of two data sequences. Thus the total number of operations in step 1 is

$$C_1 = 2\left(\frac{M}{2}\log_2 M + M \log_2 M\right)$$ 5.52

$C_1$ is the complexity in step 1. Step 2 involves performing $M$ complex multiplications as $D_1(f)$ and $D_2(f)$ are complex numbers. Thus the complexity in step 2 is

$$C_2 = 2M$$ 5.53

$C_2$ is the complexity in step 2. Step 3 involves taking inverse fft of $D(f)$ and hence one inverse fft operation. The number of multiplications and additions is same as performing a forward fft. Thus

$$C_3 = \left(\frac{M}{2}\log_2 M + M \log_2 M\right)$$ 5.54

$C_3$ is the complexity in step 3. Thus the total complexity of *one* correlation process is

$$C_{r\theta} = C_1 + C_2 + C_3 \qquad\qquad 5.55$$

$$C_{r\theta} = 3\left(\frac{M}{2}\log_2 M + M\log_2 M\right) + 2M \qquad\qquad 5.56$$

$C_{r\theta}$ in equation 5.57 is the complexity of forming one range cell in **r$\theta$** matrix. Suppose the return signal is divided into $N_I$ range cells then equation 5.56 is written as

$$C_{r\theta} = N_I\left(3\left(\frac{M}{2}\log_2 M + M\log_2 M\right) + 2M\right) \qquad\qquad 5.57$$

This above complexity is for 2 element array. Thus for *K* elements *K-1* such operations have to be performed. Hence equation 5.57 can be modified as

$$C_{r\theta} = N_I(K-1)\left(3\left(\frac{M}{2}\log_2 M + M\log_2 M\right) + 2M\right) \qquad\qquad 5.58$$

Thus equation 5.58 gives the total complexity for forming *K-1* **r$\theta$** matrices.

### 5.5.2 Computational complexity of the image formation process

The image formation process involves the calculation of the angle and placing the co-ordinate calculated at the correct pixel position. Assume that $K_n$ samples are contained in the correlation result. Let the number of range cells be $N_I$. Each operation has to be performed for $K_n$ samples and $N_I$ range cells. The calculation of delay involves *one* multiplication and the calculation of DOA involves *two* multiplications. The decomposition to image coordinates involves multiplication of the range with the *sine* and *cosine* terms and hence involves 2 multiplications. The total number of addition would be *one* which is for the calculation of pixel position. Thus

$$C_{IM} = 6K_n N_I \qquad\qquad 5.59$$

where $C_{IM}$ is the total complexity of the image formation process. There would be one addition for the calculation of range from the range cells and hence a total of $N_I$-1 additions. If there are $K$ receiver elements then there would be $K$-1 such computations. Thus

$$C_{IM} = (6K_n N_I + N_I - 1)(K - 1) \qquad\qquad 5.60$$

### 5.5.3 Computational complexity of the signal processing algorithm

The result obtained by correlating the signals from range cell is further processed. If there are $N_I$ range cells then the processing algorithm would be called $N_I$ times. Initially the complexity of the algorithm for one range cell is calculated.

Suppose there are $K_n$ correlation samples then there would be $K_n$-1 additions and *one* multiplication for the determination of the mean value for a pair of receivers. Initial threshold calculation involves $K$-2 additions and *one* multiplication, $K$ being the number of receiver elements. Thus for *one* range cell

$$C_{S1} = (K_n + 1)(K - 1) \qquad\qquad 5.61$$

where $C_{S1}$ is the complexity of determining the mean.

The comparing operation would involve $K_n$ additions and $K_n$ comparisons thus forming $2K_n$ operations. For *one* range cell of *(K-1) r$\theta$* matrices,

$$C_{S2} = 2K_n(K - 1) \qquad\qquad 5.62$$

The determination of standard deviation of one range cell would involve *4$K_n$+2* operations. In order to determine *(K-1)* standard deviations it is *(K-1)(4$K_n$+2)* operations. Adding the standard deviations obtained and determining the mean of

standard deviations for all the **rθ** matrices involves *(K-1)* operations. Determining the new threshold would involve one addition operation. Thus for *one* range cell,

$$C_{S3} = (K-1)(4K_n + 2) + K \qquad 5.63$$

After this there are same number of addition and comparison operations as equation 5.62 and $K_n(K-1)$ *'and'* operations. Thus in the final stage and for *one* range cell there are

$$C_{S4} = 2K_n(K-1) + K_n(K-1) = (3K-3)K_n \qquad 5.64$$

Thus the complexity of the signal processing algorithm for *one* range cell is

$$C_S = C_{S1} + C_{S2} + C_{S3} + C_{S4} = (K-1)(10K_n + 3) + K \qquad 5.65$$

For $N_I$ range cells, equation 5.65 can be written as

$$C_S = N_I(K-1)(10K_n + 3) + KN_I \qquad 5.66$$

$C_s$ is the total complexity of the processing algorithm developed.

### 5.5.4 Complexity of Matched filtering

No of taps per sample $\qquad\qquad = Ft$ taps/sample $\qquad 5.67$

Let the number of samples in the return signal be $K_T$

Total number of operations $C_{Mt} \qquad\qquad = K_T FtK \qquad 5.68$

### 5.5.5 An example of time taken by a SHARC ADSP 21261 processor

The number of flops for a SHARC ADSP 21261 processor at 150 MHz is 900MFLOPS. The calculations are preformed by assuming a 1.5 *meter* range cell with no overlap.

| | |
|---|---|
| Depth | $= 200$ meters |
| Number of samples | $= \dfrac{2 \times 200 \times 10^6}{1500} = 266667\,samples$ |
| Number of hydrophones $K$ | $= 4$ |
| Number of samples in a 1.5m range cell | $= \dfrac{1.5 \times 10^6}{1500} = 1000\,samples$ |
| Number of points for fft $M$ | $= 1024$ |
| Number of range cells $N_I$ | $\approx \dfrac{Depthsamples}{Rangecellsamples} = \dfrac{266667}{1000}$ |
| | $\approx 270\ Range\ cells$ |
| Number of correlation samples $K_n$ | $= 2048$ samples |

Thus using equation 5.58, 5.60 and 5.66

| | |
|---|---|
| $C_{r\theta}$ | $= 38983680$ operations |
| $C_{IM}$ | $= 9954087$ operations |
| $C_s$ | $= 1659230$ operations |
| Total | $= 65530077$ operations |

$$\text{Time taken} = \frac{65530077}{900 \times 10^6} = 0.0729\,\sec$$

In case of an overlap by *50%* then the time taken would be double.

Total number of matched filter operations $\approx 6 \times 10^9$ operations

$$\text{Time taken for matched filtering operation} = \frac{6 \times 10^9}{900 \times 10^6} = 6.67\,\sec$$

It can be seen that the time taken for matched filtering operation is much more than that required for processing. Matched filtering has been efficiently implemented using DSP processor. Since the number of operations required for the total signal processing operation is much less than that of matched filtering operation the developed algorithm can be implemented using DSP processor. This can also be implemented using a PC loaded with a accelerated library containing optimized function which would take the same amount of time or would be faster. This shows that these operations are feasible to be performed using a DSP processor.

## 5.6  Summary

In this chapter various blocks which make up the *Imaging Sonar Simulation Model* is presented. The signal parameters are chosen to have a value to correspond to existing sonar. The signal was not converted to baseband because the saving would be less as the fractional bandwidth is large. The range resolution was shown to depend on the amount of overlap between the range cell and the range cell size. The angular resolution was seen to depend on the bandwidth, elemental separation and the look angle of the array. Greater the bandwidth and array element separation better would be the angular resolution. Smaller the look angle of the array better the angular resolution as *cosine* of smaller angles would tend towards 1. As the look angle of the array increases, *cosine* of the angle would be smaller than 1 and hence the angular resolution would be worse.

The environment block consists of the targets, the spreading loss block and noise block. The targets here are considered to be a cluster of point targets. Different profiles like the sine profile, straight line profile and distributed target profile were generated. A point target cluster was also generated. The spreading loss which the signal undergoes was assumed to be spherical and hence loss varies as the square of the distance travelled. It was also found that in different ranges different kinds of noise exist whose spectrum level was given. From the spectrum level the noise level is calculated and the noise is added.

Various measurement metrics were discussed. SNR and PSNR both of which are objective metrics and SSIM which is a subjective metric was decided to be used. One reason for its choice is the simplicity in calculation and implementation. SSIM is chosen because it is a widely used and researched subjective metric and is supposed to judge the image quality close to that of a human visual system.

The complexity of the algorithm developed was calculated in section 5.5. It is found that the algorithm is computationally very intensive. Thus by reducing the number of receiver channels, the algorithm tries to shift most of the computational load to the processor. The complexity of the developed signal processing algorithm and the matched filtering operation was calculated. It was seen that the complexity of signal processing algorithm was less than the complexity of matched filtering operation. The time taken to perform these operations on a SHARC ADSP 21261 processor was calculated. The calculations showed that the operations are feasible on a DSP processor.

`

# Chapter 6

# Simulation and Results

In Chapter 5, the sonar simulation model was described. The metrics to be used in order to determine the algorithm performance and image quality are

1)      Signal-to-Noise ratio (SNR)

2)      Peak Signal-to-Noise ratio (PSNR)

3)      Structural Similarity Index (SSIM)

The metrics 1 and 2 are objective metrics. SNR is used to measure the gain obtained using the algorithm. PSNR is a measure of the image quality. The third metric is a subjective image quality metric. It should be noted that the subjective measures developed in order to judge the image quality are only suitable for images of natural scenes which is only a small subset of the set images. There has never been an attempt to use subjective metrics for evaluating images other than that obtained using normal photographic cameras. The simulations are performed without any addition of noise as at the frequencies used only thermal noise dominates.

## 6.1      Image formed using two elements

The images are formed using two hydrophone elements. There is no additional processing applied except the formation of $r\theta$ matrix and conversion of the matrix into an image. The following parameters are used for the simulation

| Signal | Chirp Signal<br>**Duration    : 0.005 s**<br>**Frequency  : 200 – 300 kHz** |
|---|---|
| Number of hydrophone elements | **2** |
| Number of Sub Arrays | **1** |
| Bandwidth | **100 kHz** |
| Sampling Frequency (*F*) | **1 MHz** |
| Processing | **No Processing** |
| Range cell (m) | **0.375m, 0.75m, 1.5m, 2.25m** |
| Array Spacing (m) | **0.1 m - 0.5 m** |
| Windowing | **No Windowing** |
| Beamangle | **90$^0$** |

**Table 6.1 Simulation parameters 1**

The simulation is performed for a point target, sine profile, straight line profile and distributed point target profile. The simulation was performed for four different range cell sizes 0.375m 0.75m, 1.5m and 2.25m.
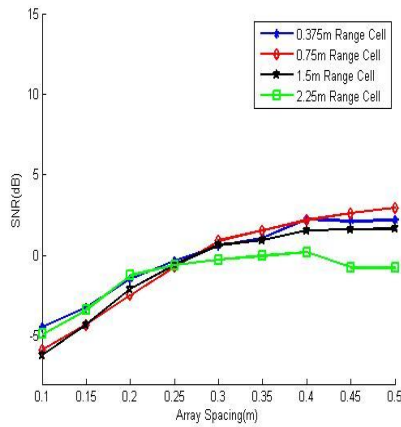


**Figure 6.1 SNR of point target using simulation parameters 1**
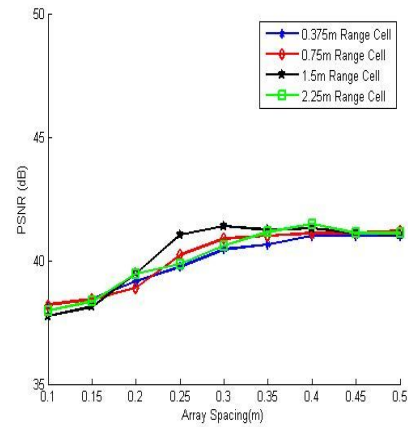


**Figure 6.2 PSNR of point target using simulation parameters 1**
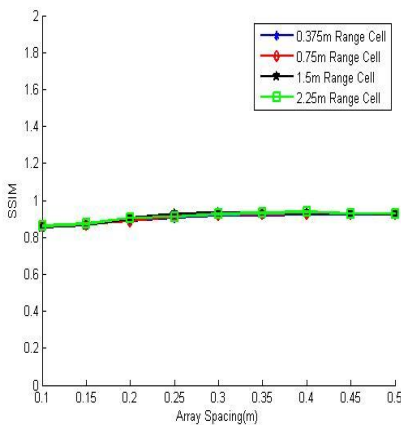


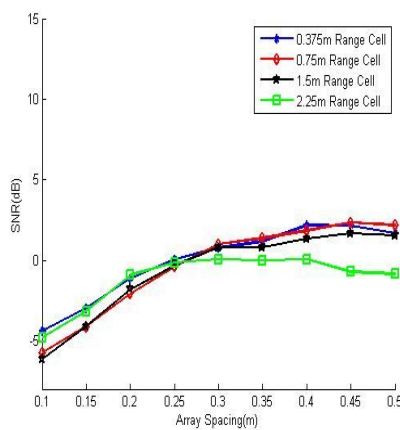**Figure 6.3 SSIM of point target using simulation parameters 1**
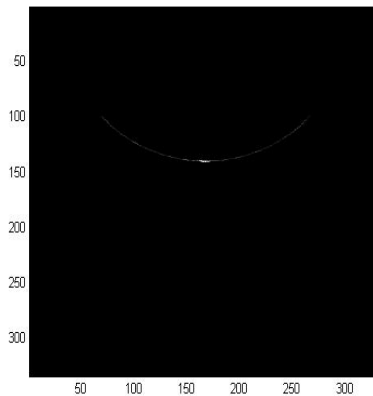


**Figure 6.4 Image formed – point target (0.3m array spacing, 2.25m range cell )**

The results obtained for a point target using the simulation parameters in table 6.1 are given in figure 6.1, figure 6.2 and figure 6.3. Figure 6.4 gives the image of the point target formed using an array spacing of 0.3m. A small rise is seen in SNR curve in figure 6.1 initially and then after 0.3m array spacing the rise is very small. This is because for smaller array spacing the target spread is greater and as the array spacing increases this spread decreases giving high energy. The PSNR

curve in figure 6.2 shows a small peak at 0.3m array spacing indicating that the image quality of the point target image is better than the rest of the spacing at an array spacing of 0.3m. The SSIM curve in figure 6.3 indicates that the subjective quality is constant for all the range cells i.e. for the human eyes there is no change or little change in the image quality. The SSIM is always between 0 and 1 with *zero* indicating bad quality image and *one* indicating a very good quality. The SSIM index for a point target is very close to one because for a point target the amount of correlation artifacts is very little as seen from figure 6.4.
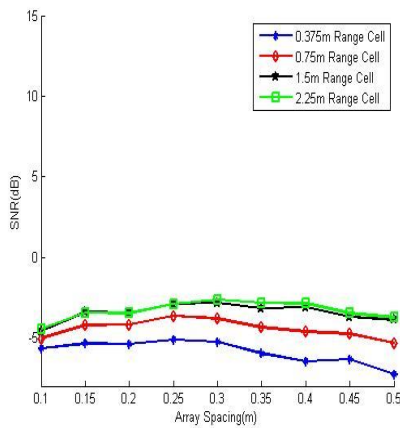


**Figure 6.5 SNR of sine profile using simulation parameters 1**
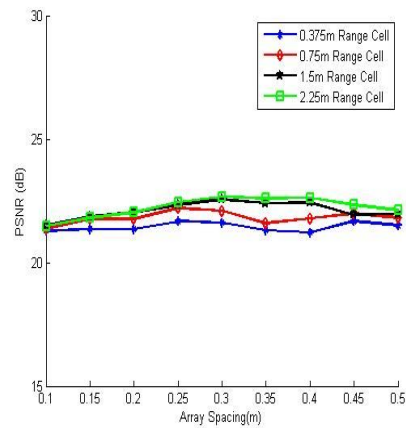


**Figure 6.6 PSNR of sine profile using simulation parameters 1**
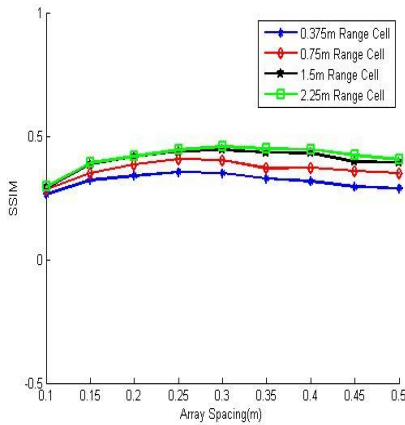


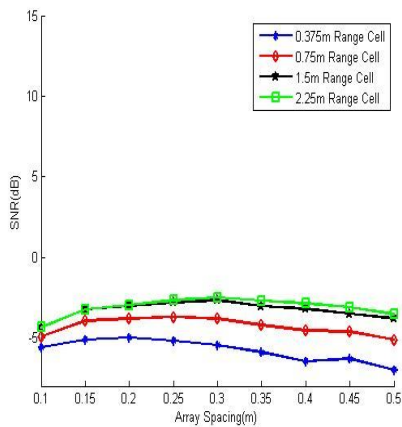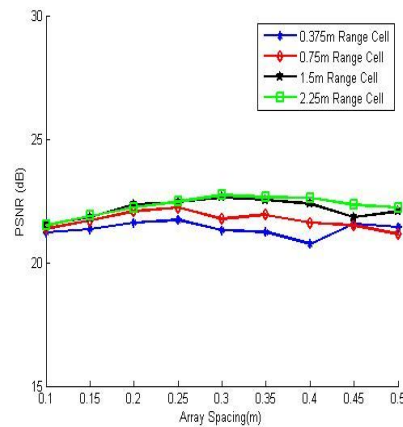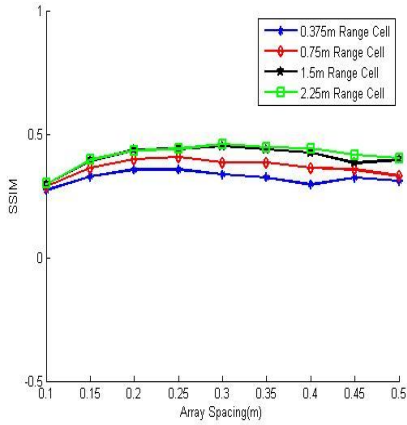**Figure 6.7 SSIM of sine profile using simulation parameters 1**
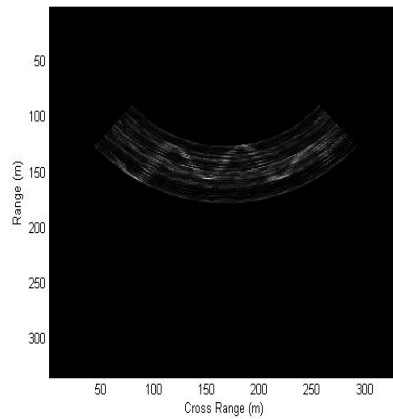


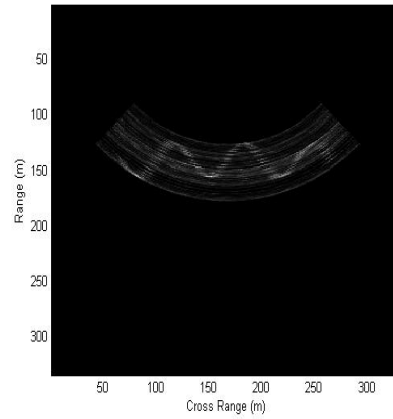**Figure 6.8 Image formed – sine profile (0.3m array spacing, 2.25m range cell)**

Figure 6.5 shows the SNR of a sine profile. The curves indicate that SNR is better using a 2.25m range cell and the worst SNR is obtained for 0.375m range cell.

143

This is because when the range cell size is large, there is increased amount of profile signature in each range cell that can be compared. It is seen from figure 6.6 and figure 6.7 of PSNR and SSIM that 2.25m range cell forms a better quality image. Figure 6.8 shows the image of the sine profile formed using a two element array. It can be seen from figure 6.8 that the correlation sidelobes distort the image. These sidelobes are formed because the return signals in the range cells compared are not orthogonal. All the curves show a slight peak at 0.3 m array spacing.
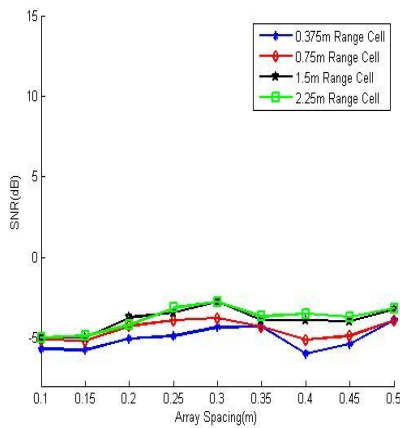


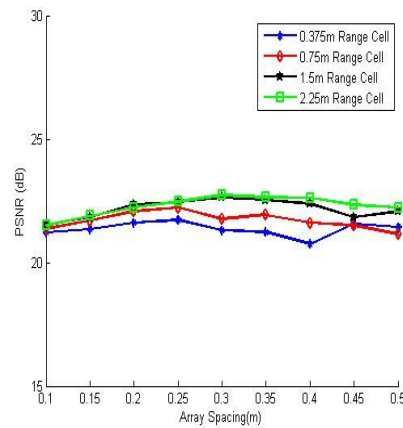**Figure 6.9 SNR of straight line profile using simulation parameters 1**
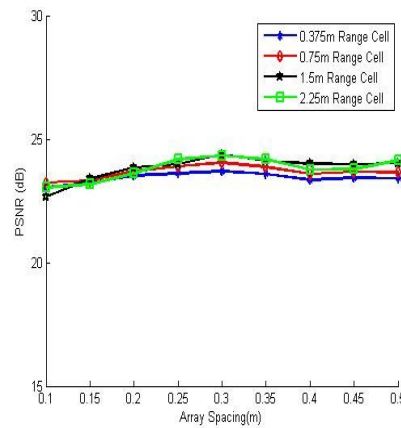
**Figure 6.10 PSNR of straight line profile using simulation parameters 1**
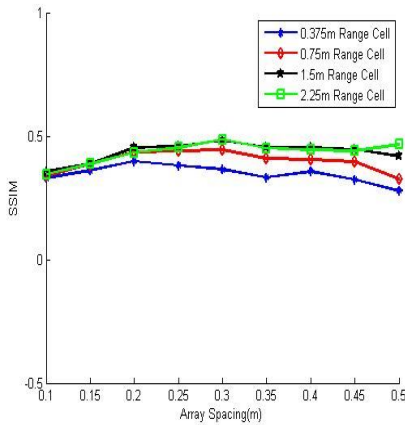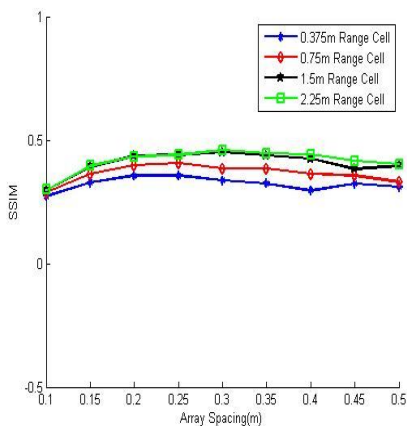


**Figure 6.11 SSIM of straight line profile using simulation parameters 1**
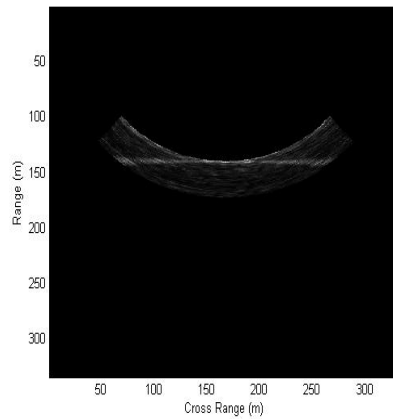
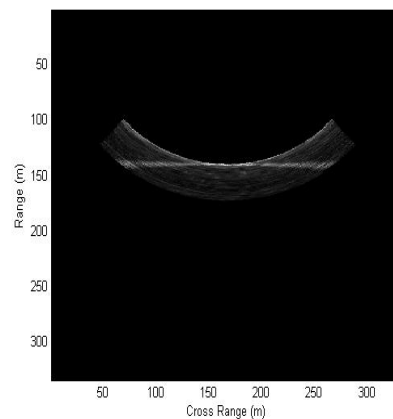**Figure 6.12 Image formed – straight line profile (0.3m array spacing, 2.25m range cell)**

The metric measures in figure 6.9, figure 6.10 and figure 6.11 obtained for straight line profile shows the same trend as the sine profile. All range cells except

0.375m range cell show a peak at 0.3m array spacing. The 0.375 m range cell shows a peak at 0.35m array spacing and then a fall and rise upto 0.5m array spacing. This could be due to two reasons 1) Profile characteristic or 2) the number of samples in the range cell is not enough to distinguish the targets at the profile ends and hence oscillates. Figure 6.12 shows the image formed for a straight line profile. From the image it seems that this could be the worst case condition as the profile cannot be distinguished from its artifacts. The PSNR and SSIM in figure 6.10 and figure 6.11 shows that the best image formed is using 0.3m array spacing.
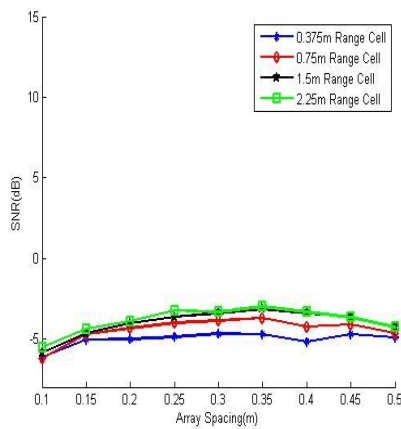


**Figure 6.13 SNR of distributed target profile using simulation parameters 1**
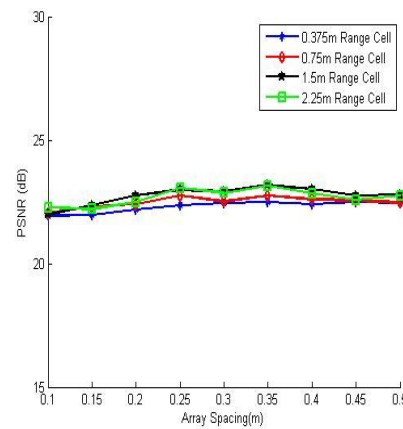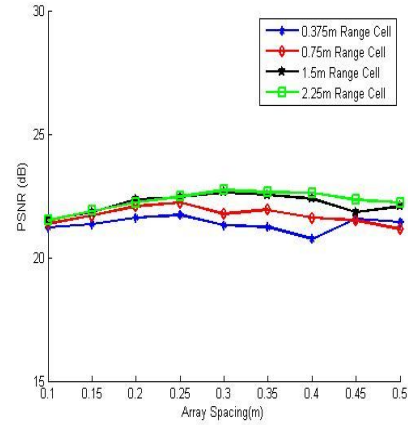
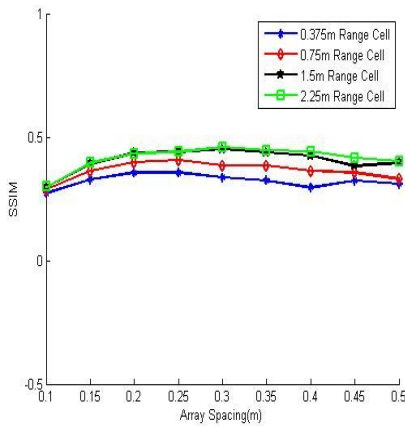**Figure 6.14 PSNR of distributed target profile using simulation parameters 1**
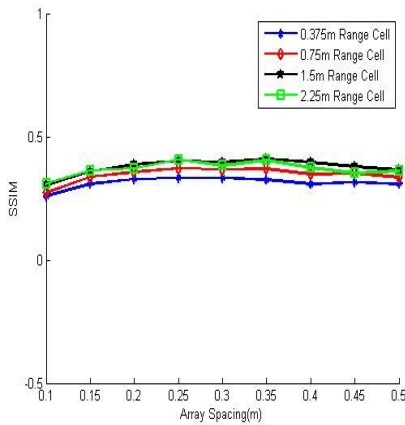


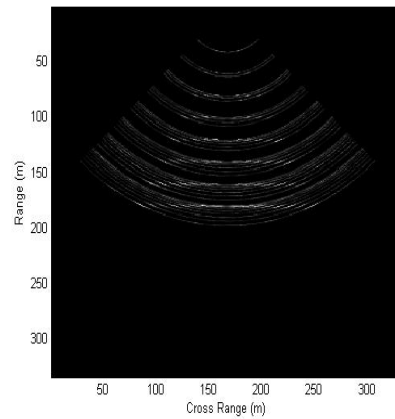**Figure 6.15 SSIM of distributed target profile using simulation parameters 1**
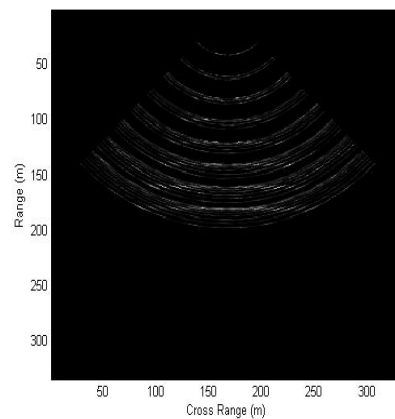
**Figure 6.16 Image formed – distributed target profile (0.3m array spacing, 2.25m range cell)**

145

The metric curves in figure 6.13, figure 6.14 and figure 6.15 show a small peak at 0.25m array spacing. The SNR graphs of the profiles indicates that using a two element array there is not much gain obtained by increasing the array spacing. The correlation artifacts which is a matter of concern distorts the image formed. The PSNR and SSIM measures indicate that the image quality is the same for all the array spacing.

## 6.2    Averaging

In this section, simulation results obtained by combining multiple elements are presented. The averaging operation is performed on $r\theta$ matrices. Simulation parameters are presented in table 6.2.

| Signal | **Chirp Signal**<br>***Duration    : 0.005 s***<br>***Frequency  : 200 – 300 kHz*** |
|---|---|
| Number of hydrophone elements | **4** |
| Number of Sub Arrays | **3** |
| Bandwidth | **100 kHz** |
| Sampling Frequency (**F**) | **1 MHz** |
| Processing | **Averaging** |
| Range cell (m) | **0.375m, 0.75m, 1.5m, 2.25m** |
| Array Spacing (m) | **0.1 m - 0.5 m** |
| Windowing | **No Windowing** |
| Beamangle | **90$^0$** |

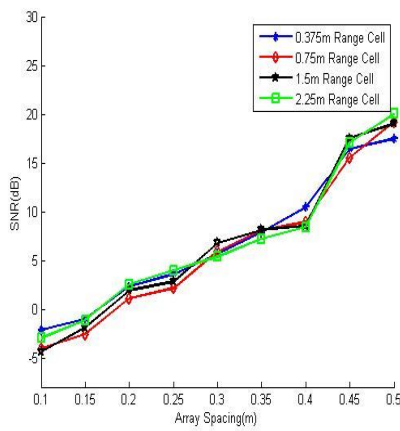**Table 6.2 Simulation parameters 2**



**Figure 6.17 SNR of point target using simulation parameters 2**
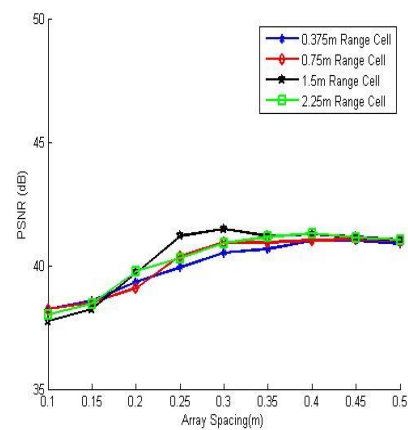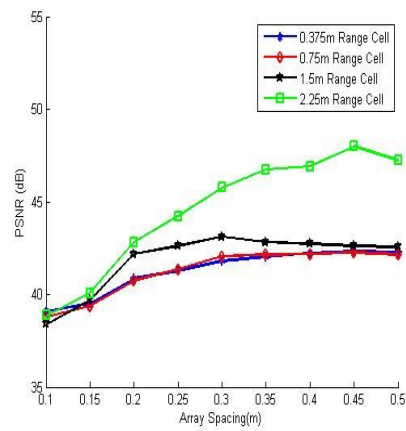
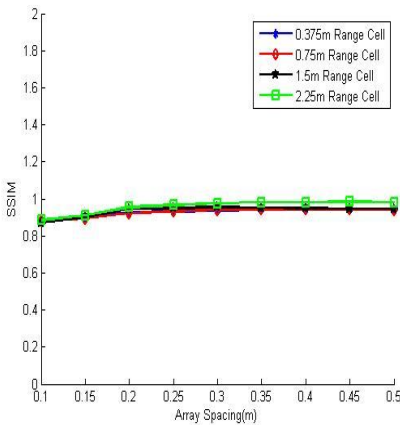**Figure 6.18 PSNR of point target using simulation parameters 2**

146
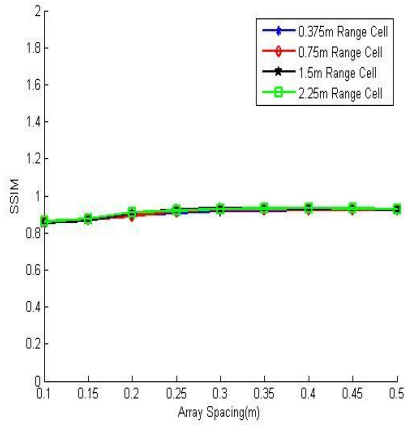
**Figure 6.19 SSIM of point target using simulation parameters 2**
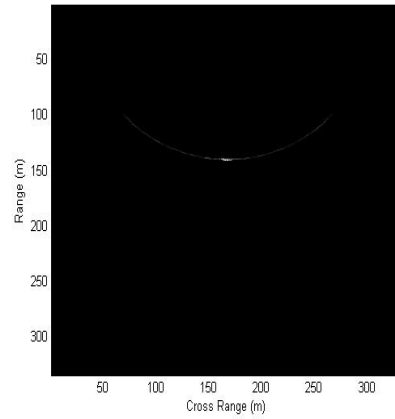


**Figure 6.20 Image formed – point target (0.3m array spacing, 2.25m range cell)**

The measurement metrics in figures 6.17, figure 6.18 and figure 6.19 show no change in comparison to the metric values obtained using 2 hydrophone elements. The correlation artifacts still exist. This can be seen from the graphs of the metric values for sine profile (figures 6.21, 6.22, 6.23), straight line profile (figures 6.25, 6.26, 6.27) and distributed target profile (figures 6.29, 6.30, 6.31).



**Figure 6.21 SNR of sine profile using simulation parameters 2**



**Figure 6.22 PSNR of sine profile using simulation parameters 2**

**Figure 6.23 SSIM of sine profile using simulation parameters 2**



**Figure 6.24 Image formed – sine profile (0.3m array spacing, 2.25m range cell)**
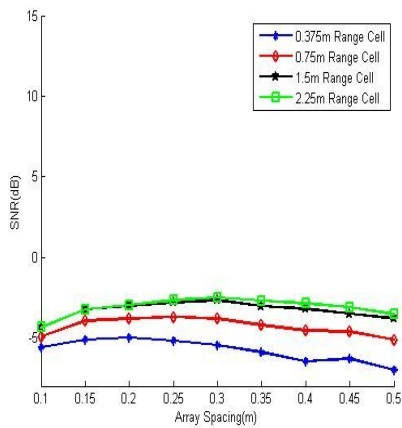


**Figure 6.25 SNR of straight line profile using simulation parameters 2**



**Figure 6.26 PSNR of straight line profile using simulation parameters 2**



**Figure 6.27 SSIM of straight line profile using simulation parameters 2**



**Figure 6.28 Image formed – straight line profile (0.3m array spacing, 2.25m range cell)**
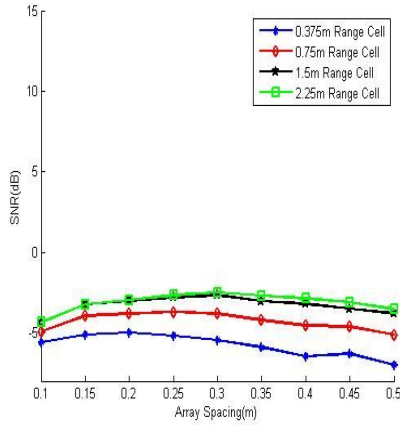
**Figure 6.29 SNR of distributed target profile using simulation parameters 2**



**Figure 6.30 PSNR of distributed target profile using simulation parameters 2**



**Figure 6.31 SSIM of distributed target profile using simulation parameters 2**



**Figure 6.32 Image formed – distributed target profile (0.3m array spacing, 2.25m range cell)**

It is also from the images of the profiles that the artifacts still exist. The averaging operation only performs smoothening in this case. This indicates that simple linear process like averaging is not enough to remove the artifacts formed.

## 6.3    Non-Linear Combining

In this section, the results obtained by combining the *rθ* matrices non-linearly using multiple direction of arrival process developed in Chapter 4, section 4.4.6.2 is presented. The simulation parameters are given in table 6.3.

| Signal | Chirp Signal<br>*Duration    : 0.005 s*<br>*Frequency  : 200 – 300 kHz* |
|---|---|
| Number of hydrophone elements | **4** |
| Number of Sub Arrays | **3** |
| Bandwidth | **100 kHz** |
| Sampling Frequency (*F*) | **1 MHz** |
| Processing | **Non-Linear Combining** |
| Range cell (m) | **0.375m, 0.75m, 1.5m, 2.25m** |
| Array Spacing (m) | **0.1 m - 0.5 m** |
| Windowing | **No Windowing** |
| Beamangle | **$90^0$** |

**Table 6.3 Simulation parameters 3**

**Figure 6.33 SNR of point target using simulation parameters 3**

**Figure 6.34 PSNR of point target using simulation parameters 3**

**Figure 6.35 SSIM of point target using simulation parameters 3**
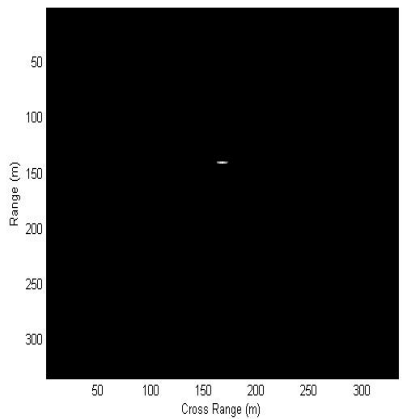
**Figure 6.36 Image formed – point target (0.3m array spacing, 2.25m range cell)**

150

Figure 6.33 shows the gain obtained using the non-linear combining algorithm. The figure shows that the gain increases as the array spacing increases. The PSNR graph in figure 6.34 shows that the image quality increases until 0.25m spacing and then the increase in quality almost remains a constant. The SSIM index in figure 6.35 also shows a slight increase in the image quality till 0.2m array spacing and it remains a constant after that. Since these two measures the image quality, it becomes a constant because after 0.2m spacing the increase in image quality is not sensed by the human eye. These measures show that the algorithm has certainly improved the image.
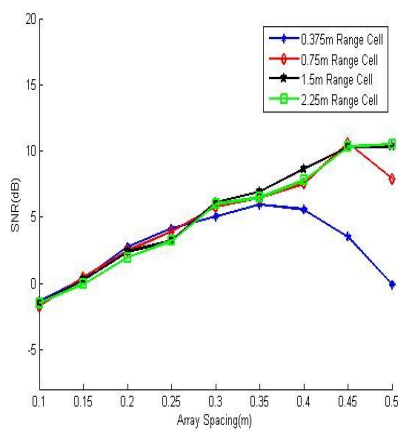


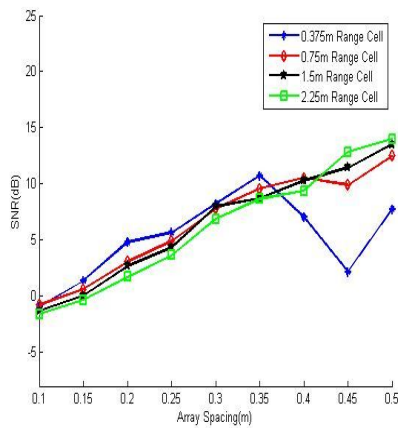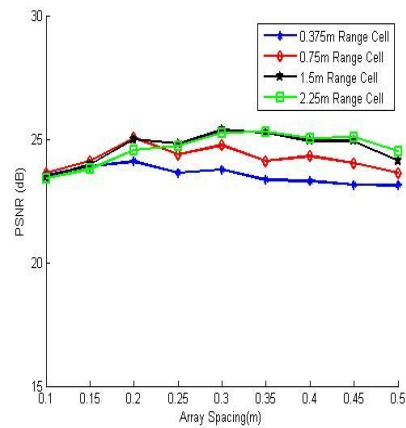**Figure 6.37 SNR of sine profile using simulation parameters 3**
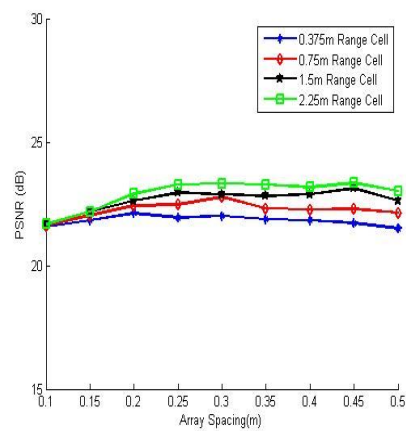


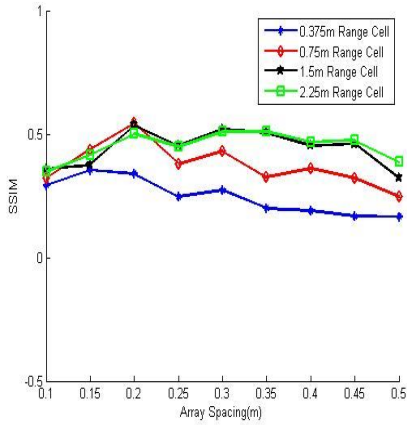**Figure 6.38 PSNR of sine profile using simulation parameters 3**
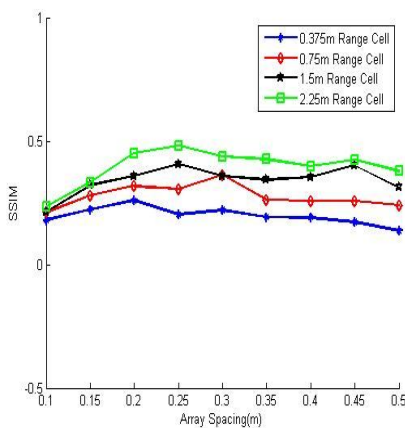


**Figure 6.39 SSIM of sine profile using simulation parameters 3**
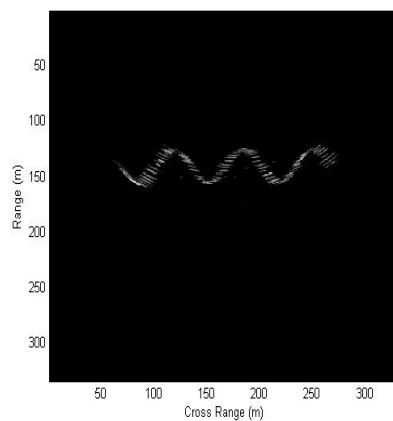

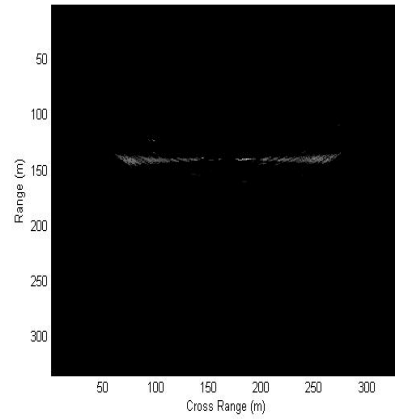
**Figure 6.40 Image formed – sine profile (0.25m array spacing, 2.25m range cell)**

The SNR curves in figure 6.37 for a sine profile shows that the gain increases for the various array spacing except for 0.375m range cell where the gain starts to decrease after 0.4m spacing. As indicated in section 6.1, a similar decrease in the gain was seen in the case of straight line profile. If this decrease was due to the nature of the profile then it should have been seen in the case of all range cells. But this is seen only for 0.375m range cell. Thus this would indicate the case where the number of samples in the range cell is less in order to obtain good correlation and hence oscillates. The number of samples in a 0.375m range cell is 250 samples. The maximum delay for a half beam angle of $45^{o}$ for an array spacing of 0.4m is $0.4\cos45 \approx 0.282m \approx 189$ samples. The profile is well correlated if it is less than 189 samples but for the number of samples greater than 189 the correlation decreases. Thus the range cell size should be chosen large enough to have sufficient samples for correlation. The PSNR and SSIM image quality metric in figure 6.38 and figure 6.39 for a sine profile shows that image quality increase until 0.25m array spacing and then there is a very slow decrease. The slow decrease indicates that there is not much difference in the image quality for array spacing greater than 0.25m.



**Figure 6.41 SNR of straight line profile using simulation parameters 3**

**Figure 6.42 PSNR of straight line profile using simulation parameters 3**

152

**Figure 6.43 SSIM of straight line profile using simulation parameters 3**



**Figure 6.44 Image formed – straight line profile (0.2m array spacing, 2.25m range cell)**

The SNR of the straight line profile in figure 6.41 shows an increasing SNR trend except for 0.375m range cell size where oscillation due to lack of correlation is seen after an array spacing of 0.4m. The PSNR and SSIM image quality index in figure 6.42 and figure 6.43 shows that after increasing to a maximum at 0.2m array spacing, there is a decrease in image quality.
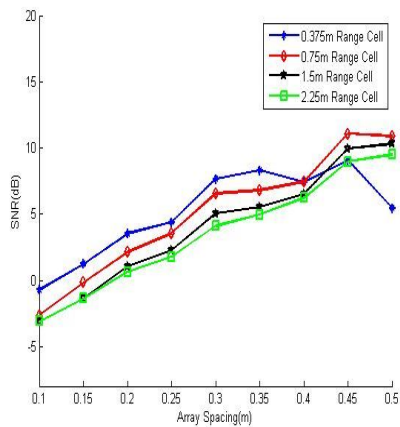


**Figure 6.45 SNR of distributed target profile using simulation parameters 3**
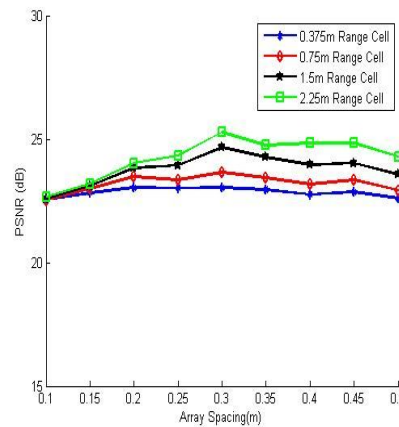


**Figure 6.46 PSNR of distributed target profile using simulation parameters 3**
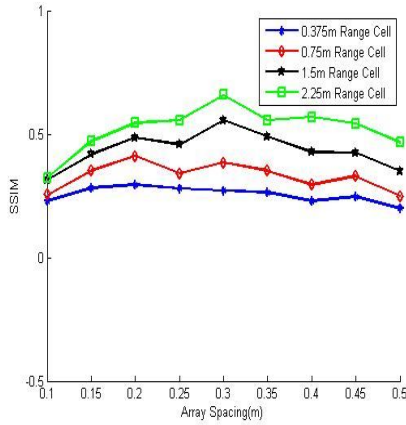
**Figure 6.47 SSIM of distributed target profile using simulation parameters 3**
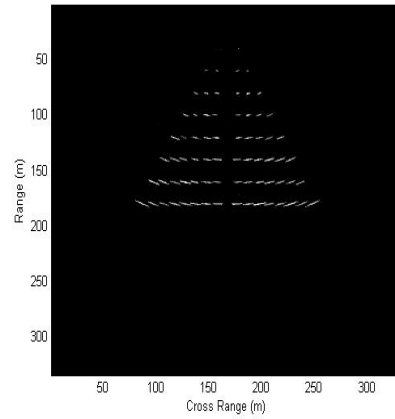
**Figure 6.48 Image formed – distributed target profile (0.3m array spacing, 2.25m range cell)**

The SNR curve for distributed target profile in figure 6.45 shows a similar oscillation in the case of 0.375m range cell with the gain decreasing from 0.4m array spacing. The PSNR and SSIM index for the distributed target profile in figure 6.46 and figure 6.47 indicates that the maximum occurs at 0.3m array spacing.

It is seen that each profile gives a good image quality at different array spacing. Thus the choice of array spacing is profile dependant. Also in the case of the range cells, the image quality formed by 2.25m range cell gives the best result. As indicated, this should be because there is more signature of the profile when larger range cell is considered. But larger range cell would result in low range resolution. Thus it is a compromise between image quality and range resolution.

## 6.4    Comparison of measurement metric for different number of hydrophone elements

In this section, the measurement metrics obtained for different hydrophone elements are compared. Since the measurement metrics indicate best results for 2.25m range cell, the comparison of metrics is performed for 2.25m range cell.
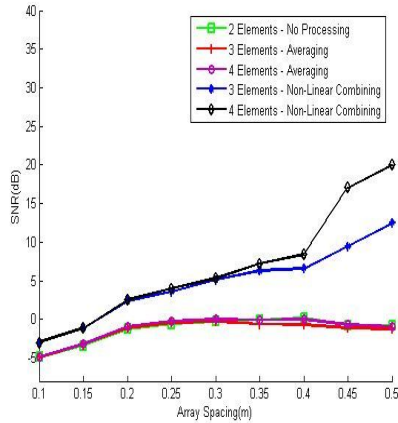
154

**Figure 6.49 Comparison of SNR of point target**
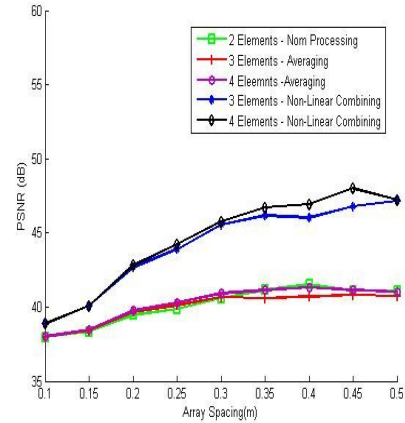


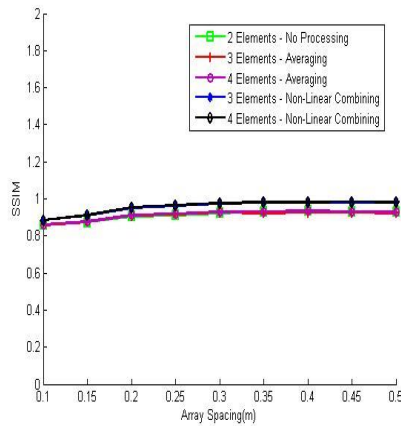**Figure 6.50 Comparison of PSNR of point target**



**Figure 6.51 Comparison of SSIM of point target**

Figure 6.49, figure 6.50 and figure 6.51 provides a comparison of the algorithms used and using different number of elements for a point target. SNR curves in figure 6.49 shows that the algorithm developed does provide a gain over the other methods. The averaging process is found to have the same response as with no processing. SNR curves for a 3 element array and 4 element array do not show much difference except for higher spacing elements. The PSNR and SSIM index image metric in figure 6.50 and figure 6.51 indicates that the gain obtained is small that it is least discernable to human eye.
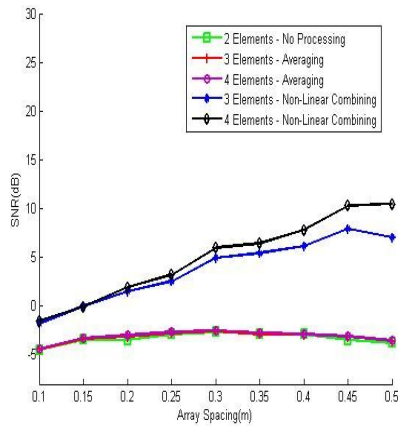
**Figure 6.52 Comparison of SNR of sine profile**
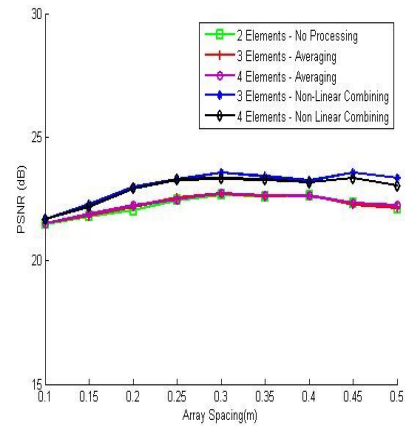


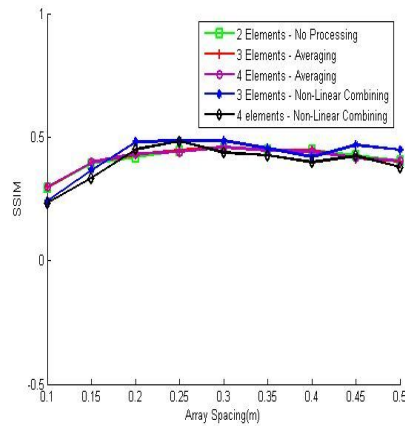**Figure 6.53 Comparison of PSNR of sine profile**



**Figure 6.54 Comparison of SSIM of sine profile**

Figure 6.52, figure 6.53 and figure 6.54 provide a comparison for a sine profile. SNR curves in figure 6.52 show very little change in the gain at lower array spacing where as at higher array spacing the gain increases. The PSNR and SSIM index in figure 6.53 and figure 6.54 shows that the best image is obtained for 0.25m array spacing. Though the gain obtained for a 0.5m array spacing is greater than that of 0.25m spacing PSNR and SSIM metric confirms that the image formed by 0.25m spacing would look much better and hence the peak at 0.25m spacing. The PSNR and SSIM index shows a very small improvement in image quality because while applying the final threshold given by equation 4.70 there might be a loss of targets because the threshold is very high. This is further investigated in section 6.10.
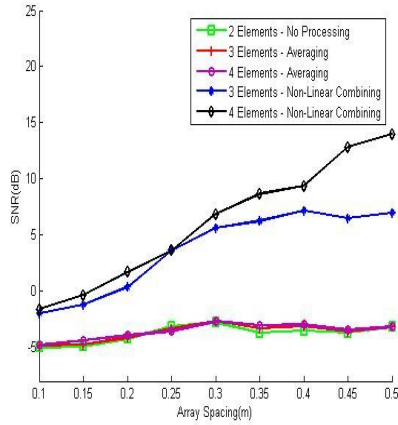
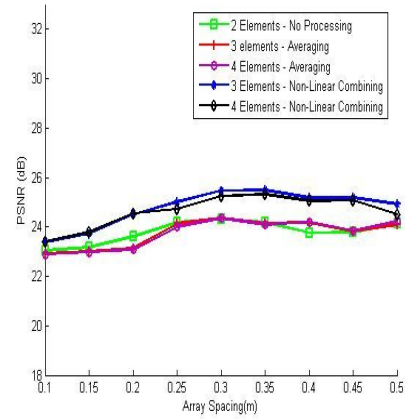**Figure 6.55 Comparison of SNR of straight line profile**



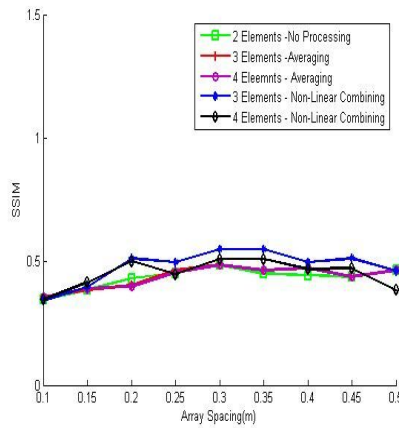**Figure 6.56 Comparison of PSNR of straight line profile**



**Figure 6.57 Comparison of SSIM of straight line profile**

Figure 6.55, figure 6.56 and figure 6.57 provide a comparison of the metrics obtained for a straight line profile. It is seen in figure 6.55 that the gain increases after 0.3m spacing. Though the SNR curves shows a gain at higher array spacing the SSIM index shows that the image of straight line obtained for spacing higher than 0.4m is poorer than the averaging process. This is because the threshold which is automatically decided by the algorithm is too high and the targets might be missed due to this high level. But since the artifacts are reduced, the SNR curve in figure 6.55 shows an improvement in gain although there is a loss of image quality as indicated by figures 6.56 and figure 6.57.
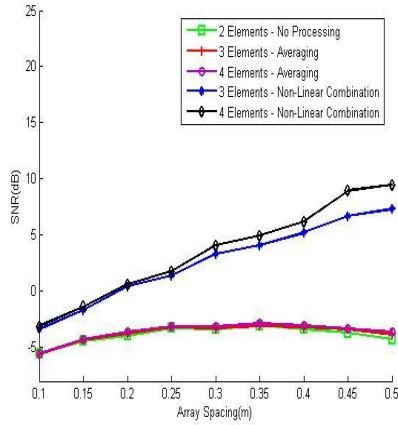
157

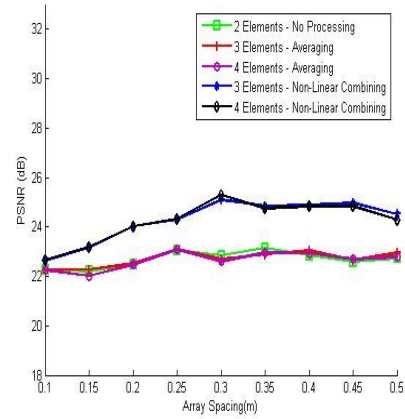**Figure 6.58 Comparison of SNR of distributed target profile**



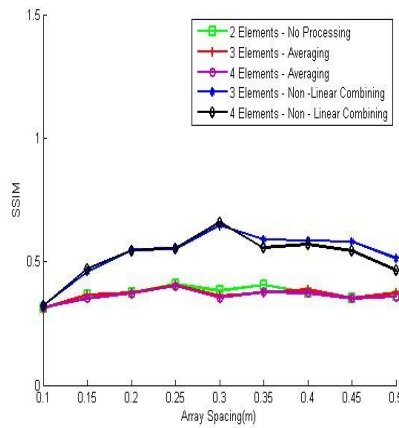**Figure 6.59 Comparison of PSNR of distributed target profile**



**Figure 6.60 Comparison of SSIM of distributed target profile**

Figure 6.58, figure 6.59 and figure 6.60 provide a comparison for a distributed target profile. SNR curve in figure 6.58 has the same trend with the gain increasing at higher array spacing. The PSNR and SSIM index in figure 6.59 and figure 6.60 indicates that the best image is obtained using 0.3m array spacing.

## 6.5    Windowing

Windows are used to reduce the sidelobes. Here windows are applied to check whether there is any improvement in the image quality as correlation process is involved. A window is applied to the data in each range cell before the correlation of the range cell from the signal on one hydrophone with the corresponding range cell of the signal from the other hydrophone. A hamming window was chosen

158

because they have low first sidelobe. The window was applied to all the profiles and the result obtained with 2.25m range cell is compared with when no window is applied. The simulation parameters are given in table 6.4.

| Signal | **Chirp Signal**<br>*Duration    : 0.005 s*<br>*Frequency  : 200 – 300 kHz* |
|---|---|
| Number of hydrophone elements | **4** |
| Number of Sub Arrays | **3** |
| Bandwidth | **100 kHz** |
| Sampling Frequency (*F*) | **1 MHz** |
| Processing | **Non-Linear Combining** |
| Range cell (m) | **2.25m** |
| Array Spacing (m) | **0.1 m - 0.5 m** |
| Windowing | **Hamming Window & No Window (Comparison)** |
| Beamangle | **$90^0$** |

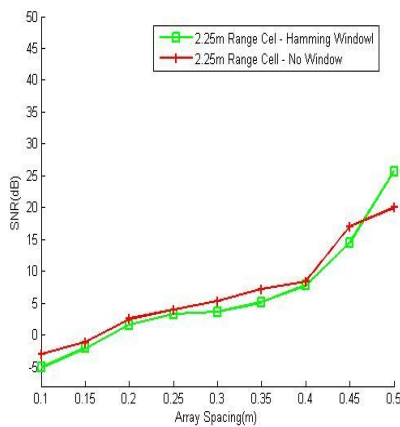**Table 6.4 Simulation parameters 4**



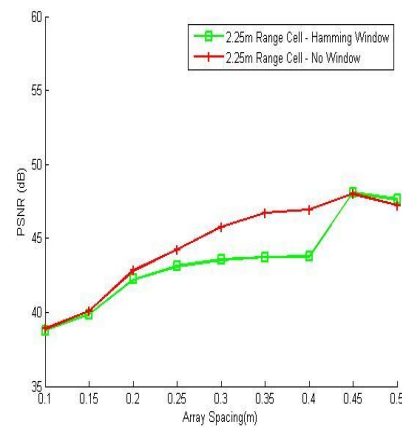**Figure 6.61 SNR of point target using simulation parameters 4**

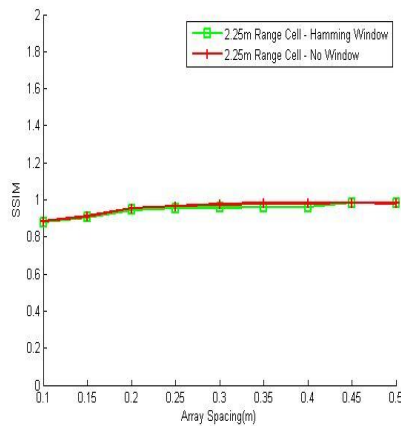**Figure 6.62 PSNR of point target using simulation parameters 4**



**Figure 6.63 SSIM of point target using simulation parameters 4**
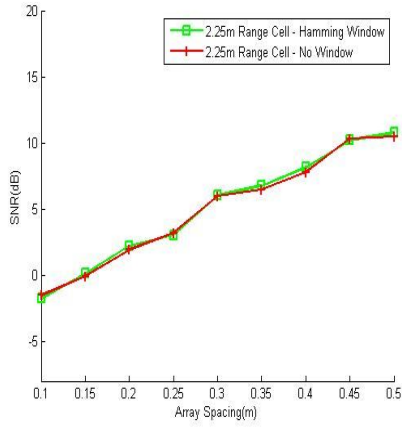
159

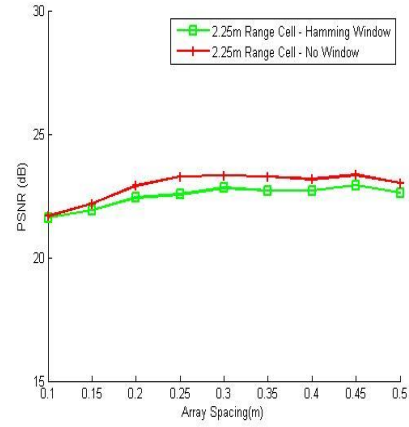**Figure 6.64 SNR of sine profile using simulation parameters 4**



**Figure 6.65 PSNR of sine profile using simulation parameters 4**
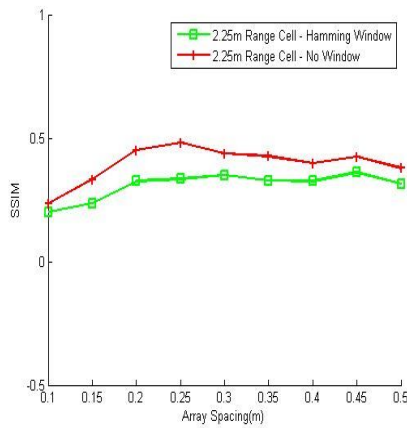


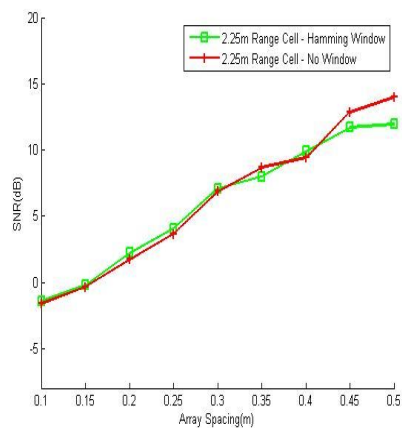**Figure 6.66 SSIM of sine profile using simulation parameters 4**



**Figure 6.67 SNR of straight line profile using simulation parameters 4**



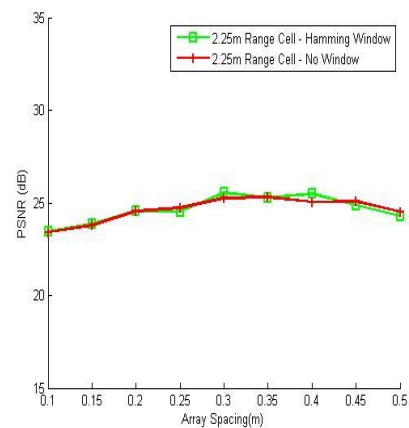**Figure 6.68 PSNR of straight line profile using simulation parameters 4**
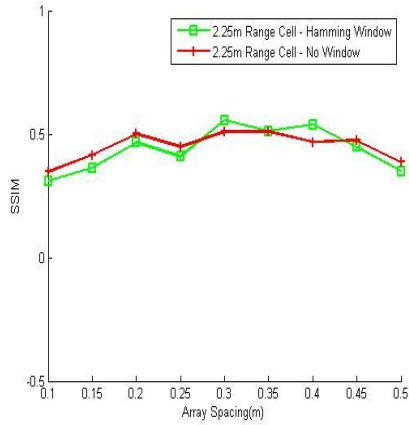
**Figure 6.69 SSIM of straight line profile using simulation parameters 4**
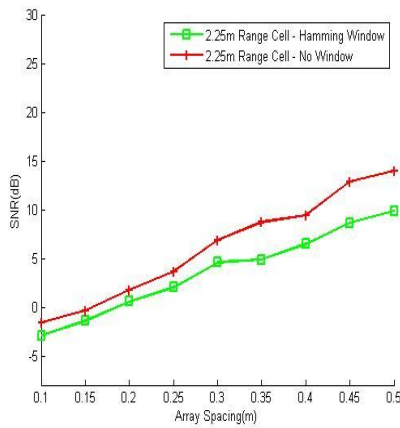


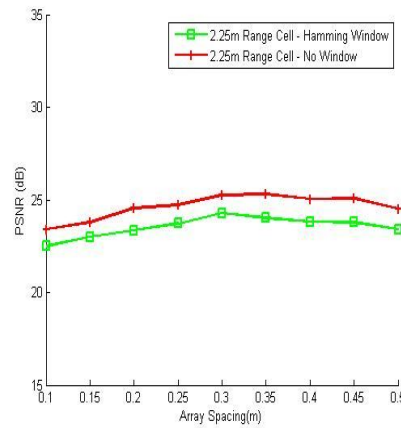**Figure 6.70 SNR of distributed target profile using simulation parameters 4**



**Figure 6.71 PSNR of distributed target profile using simulation parameters 4**
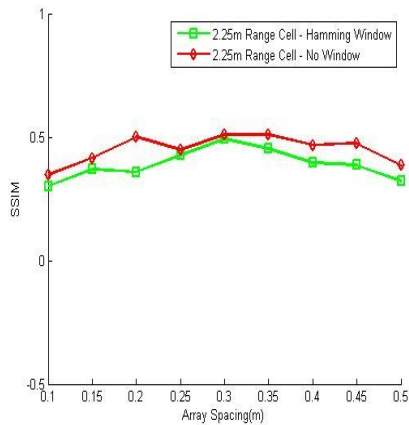


**Figure 6.72 SSIM of distributed target profile using simulation parameters 4**

161

The graphs for the measurement metrics for the point target (figures 6.61, 6.62, 6.63), sine profile (figures 6.64, 6.65, 6.66), straight line profile (figures 6.67, 6.68, 6.69) and distributed target profile (figures 6.70, 6.71, 6.72) does not show any improvement after the hamming window is applied. The values obtained for all the metrics for all target profiles either have the same value as when no widow is applied or are worse. This is because each cluster consists of very closely spaced point targets and applying a window to the data in the range cell would only suppress certain areas of the profile signature. As a result it is concluded that applying window degrades the image quality.

## 6.6    Comparison by increasing signal bandwidth

In this section the bandwidth of the chirp signal is increased from 100 kHz to 200 kHz in order to check whether there is any improvement in the image quality. The simulation parameters are given in table 6.5. The simulation results are presented for 2.25m range cell and compared against the result obtained for a 100 kHz bandwidth signal for the same size range cell. Thus using a signal of bandwidth 200 kHz the compression ratio of the matched filter is increased two fold.

| Signal | **Chirp Signal**<br>*Duration    : 0.005 s*<br>*Frequency  : 200 – 300 kHz, 200 – 400 kHz* |
|---|---|
| Number of hydrophone elements | **4** |
| Number of Sub Arrays | **3** |
| Bandwidth | **100 kHz and 200 kHz (*Comparison*)** |
| Sampling Frequency (*F*) | **1 MHz** |
| Processing | **Non-Linear Combining** |
| Range cell (m) | **2.25m** |
| Array Spacing (m) | **0.1 m - 0.5 m** |
| Windowing | **No Window** |
| Beamangle | **$90^0$** |

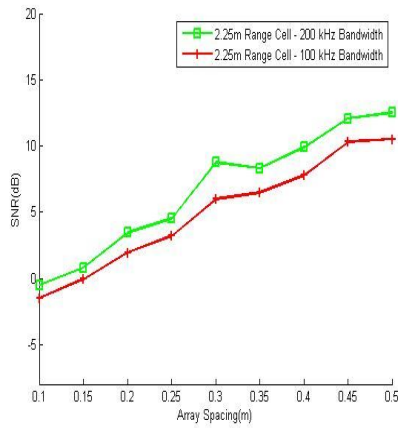**Table 6.5 Simulation parameters 5**

**Figure 6.73 SNR of sine profile using simulation parameters 5**
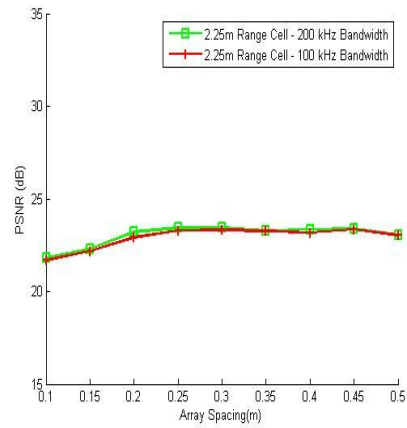


**Figure 6.74 PSNR of sine profile using simulation parameters 5**
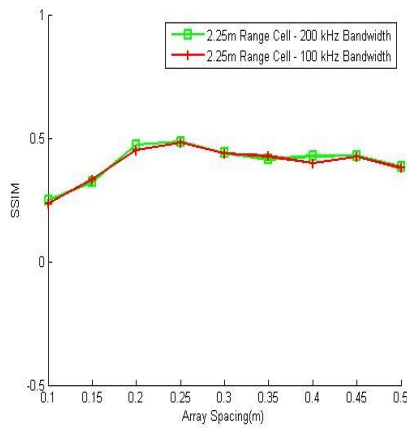


**Figure 6.75 SSIM of sine profile using simulation parameters 5**
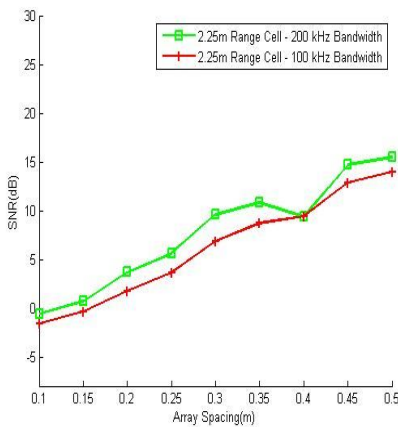


**Figure 6.76 SNR of straight line profile using simulation parameters 5**
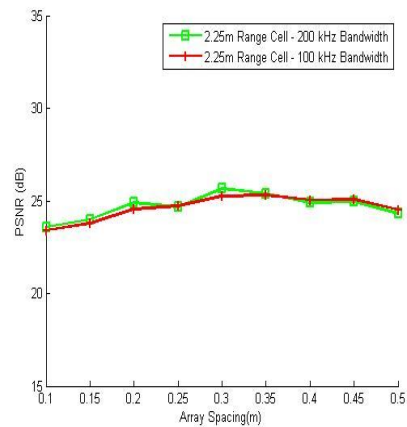


**Figure 6.77 PSNR of straight line profile using simulation parameters 5**

163

**Figure 6.78 SSIM of straight line profile using simulation parameters 5**



**Figure 6.79 SNR of distributed target profile using simulation parameters 5**
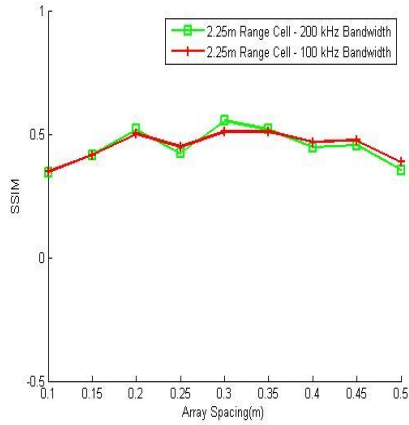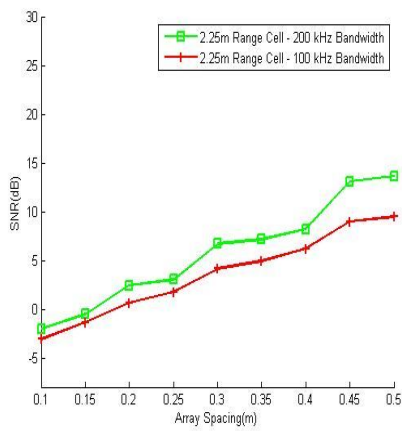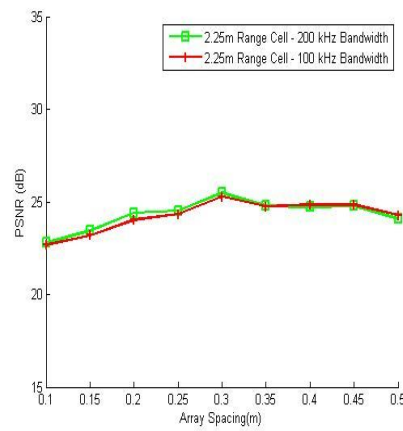
**Figure 6.80 PSNR of distributed target profile using simulation parameters 5**
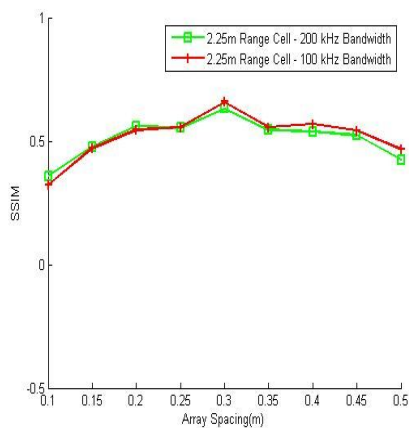


**Figure 6.81 SSIM of distributed target profile using simulation parameters 5**

The metric plots for sine profile (figures 6.73, 6.74, 6.75), straight line profile (figures 6.76, 6.77, 6.78) and distributed target profiles (figures 6.79, 6.80, 6.81)

presented compares the various measurement metrics obtained for a chirp signal of bandwidth 200 kHz with that obtained for 100 kHz. The comparison is performed for a 2.25m range cell. PSNR and SSIM index curves show a slight improvement or in some cases no improvement in the image quality. Equation 5.15 for angular resolution,

$$\Delta\theta = \left| \frac{c(\Delta n_d)}{N_{samp}B.d\cos(\theta_s)} \right|$$

6.1

The equation shows that angular resolution depends not only on the bandwidth and array spacing but also on $N_{samp}$, which is the factor by which the bandwidth has to be multiplied for a suitable sampling rate. The angular resolution also depends on $\Delta n_d$ which is the difference in the difference samples from two targets. The simulation parameters show that the bandwidth is increased but the sampling frequency is kept constant. This causes $N_{samp}$ to be reduced thus keeping the factor $\dfrac{\Delta n_d}{N_{samp}B}$ same as when the bandwidth was 100 kHz and hence there is no improvement seen in the image quality. The SNR curves shows an increase in gain and this would be due to the matched filter processing gain obtained by using signal of bandwidth 200 kHz. This indicates that in order to have a gain in image quality the factor $\dfrac{\Delta n_d}{N_{samp}}$ should be kept constant.

## 6.7    Comparison by increasing the sampling frequency

In this section the sampling frequency is increased from 1 MHz to 5 MHz. Thus the sampling frequency is approximately 17 times the highest signal frequency available. By increasing the sampling frequency any small changes can be studied. The simulation is performed on the profiles considered and the comparison graphs are plotted for a 2.25m range cell using 1 MHz and 5 MHz sampling frequencies. The simulation parameters are given in table 6.6.

| Signal | Chirp Signal<br>*Duration   : 0.005 s*<br>*Frequency  : 200 – 300 kHz* |
|---|---|
| Number of hydrophone elements | **4** |
| Number of Sub Arrays | **3** |
| Bandwidth | **100 kHz** |
| Sampling Frequency (*F*) | **1 MHz and 5 MHz (*Comparison*)** |
| Processing | **Non-Linear Combining** |
| Range cell (m) | **2.25m** |
| Array Spacing (m) | **0.1 m - 0.5 m** |
| Windowing | **No Window** |
| Beamangle | **$90^0$** |

**Table 6.6 Simulation parameters 6**



**Figure 6.82 SNR of sine profile using simulation parameters 6**
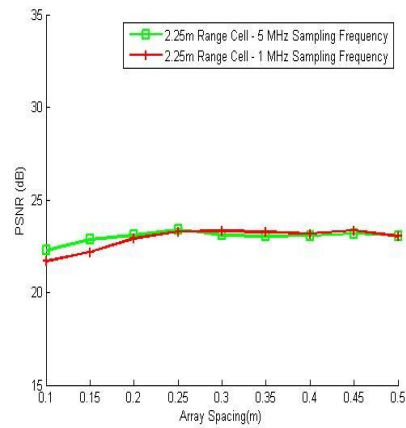


**Figure 6.83 PSNR of sine profile using simulation parameters 6**
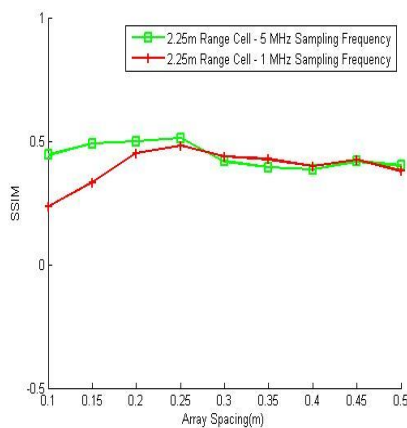


**Figure 6.84 SSIM of sine profile using simulation parameters 6**

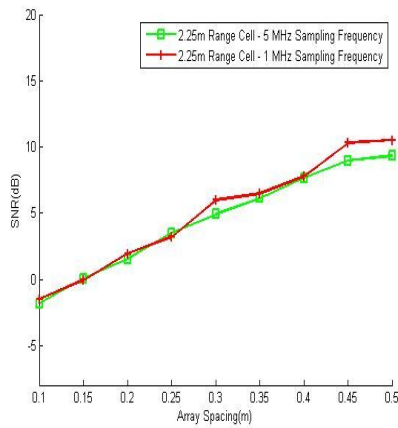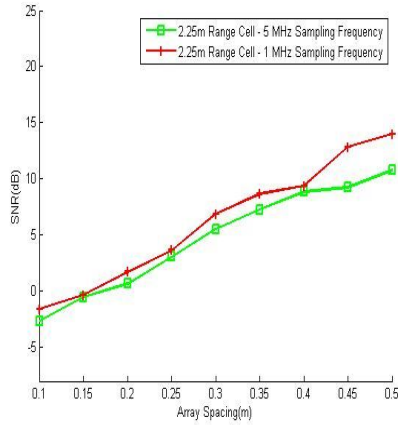**Figure 6.85 SNR of straight line profile using simulation parameters 6**
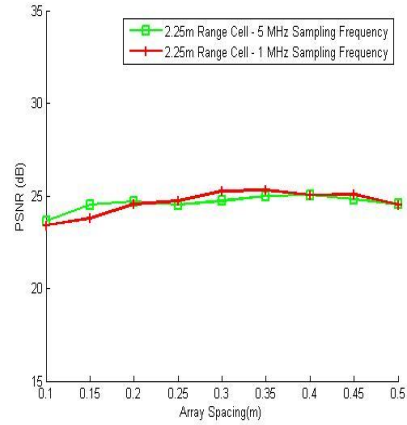
**Figure 6.86 PSNR of straight line profile using simulation parameters 6**
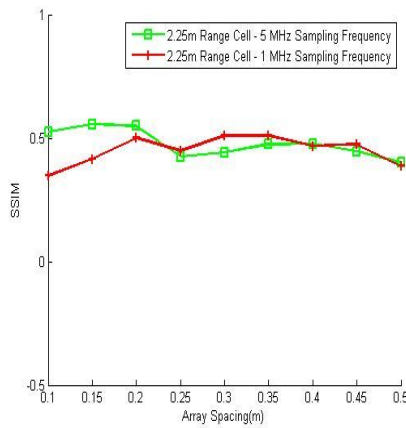


**Figure 6.87 SSIM of straight line profile using simulation parameters 6**
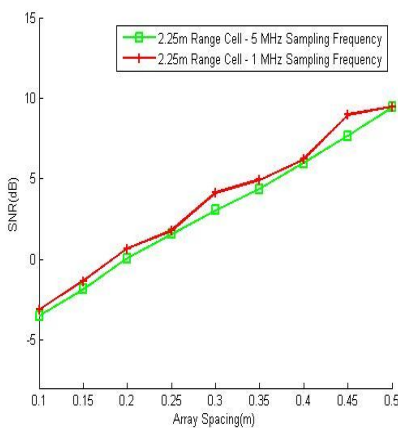




**Figure 6.88 SNR of distributed target profile using simulation parameters 6**
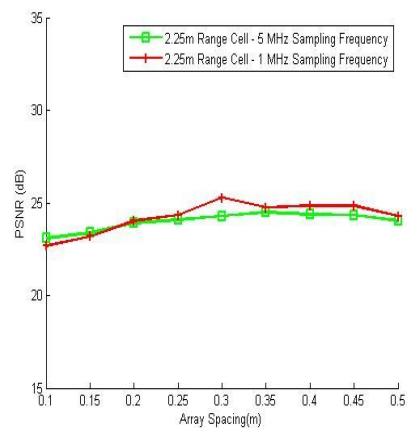
**Figure 6.89 PSNR of distributed target profile using simulation parameters 6**
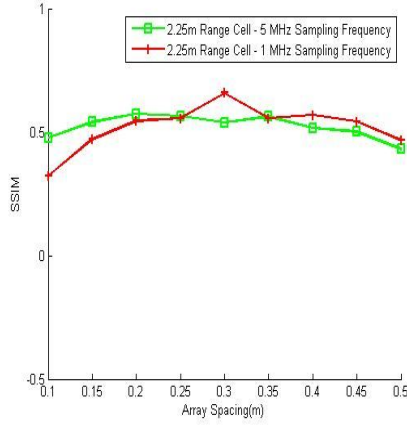
**Figure 6.90 SSIM of distributed target profile using simulation parameters 6**

The measurement metric graphs for the profile show that for higher sampling frequency of 5 MHz the curves have become much smoother than the one using 1 MHz. The SNR and PSNR graphs do not indicate much change. The SSIM index shows an improvement at the lower array spacing. This is because the visual quality at low array spacing is improved at higher sampling frequency while at higher array spacing there is no significant improvement. The nature of the curves obtained using 5 MHz sampling frequency confirms the result obtained using lower sampling frequency of 1MHz. As there is no out of frequency noise added to the signal there is no chance of aliasing to occur. Thus sampling at higher frequency here only increases the accuracy in the determination of the angular position of the target. This can be explained using equation 6.1. Increasing the sampling frequency increases $\varDelta n_d$ and $N_{samp}$. This indicates that the ratio $\dfrac{\varDelta n_d}{N_{samp}}$ remains a constant. With all the other parameters in the equation 6.1 constant, the image quality remains the same.

## 6.8 Using all array combinations

In all the simulations performed the number of subarrays formed using *K* hydrophone elements were *K-1*. Equation 4.64 in Chapter 4, section 4.4.3 gives the total number of subarrays that can be formed using *K* hydrophone elements. In this section, the non-linear combining process developed is applied to all the subarray combination and the result is investigated.

168

The DOA determination and processing algorithm assumes that the target is located in the far-field. Using this assumption, the look angle of each subarray remains the same. It has been shown in Chapter 5, section 5.2.1.2 that increasing the array spacing increases the angular resolution. Thus larger array spacing can be considered a higher sampled version of the smaller array spacing. Thus in order to combine $r\theta$ matrix obtained by two different array spacing, the smaller array spacing has to be interpolated to the larger array spacing. This can be performed as long as the far-field condition holds. But once when this assumption breaks down, the subarrays would be looking at the targets at different angles and hence the quality of image formed would be worse. The process of converting the result obtained using smaller spacing to that of a larger spacing is given in the block diagram in figure 6.91.
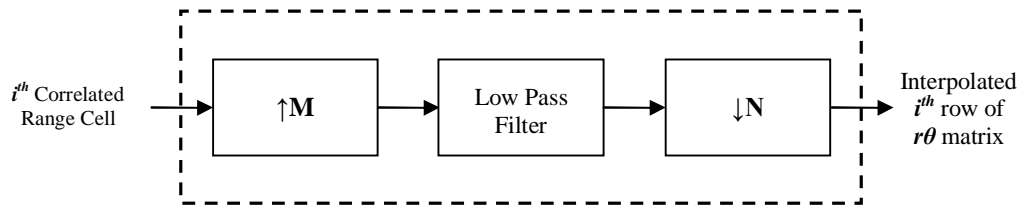


**Figure 6.91 Interpolating procedure**

Thus each row of the $r\theta$ matrix is upsampled by a factor of **M** then passed through a low pass filter. If the interpolation is not a exact factor then the process is performed by first interpolating and then decimation to obtain the correct factor. The interpolating factor is decided by the ratio of the effective array spacing to the array spacing under consideration. The effective array spacing is the distance between the first and the last element of the array. Thus if the effective array spacing is 0.6m and the array spacing under consideration is 0.4m then the interpolating factor is $\frac{0.6}{0.4} = \frac{3}{2}$. Thus to obtain a result equivalent to that of a 0.6m spacing with a 0.4m spacing array, it is required to interpolate by a factor of 3 and decimate by a factor of 2. The low pass filter will have a pass band which is equivalent to the signal bandwidth but the sampling frequency used for 0.4m spacing would be 3 times that used to filter each row of 0.6m array spacing. Using all array combinations, the receiver structure in figure 4.19 is modified by adding an interpolation block before the lowpass filter and a decimation block after the

lowpass filter. The $r\theta$ matrix thus formed will be equivalent to that obtained with the effective array spacing. The simulation parameters are given in table 6.7.

| Signal | Chirp Signal<br>*Duration     : 0.005 s*<br>*Frequency  : 200 – 300 kHz* |
|---|---|
| Number of hydrophone elements | 4 |
| Number of Sub Arrays | 6 |
| Bandwidth | 100 kHz |
| Sampling Frequency (**F**) | 1 MHz |
| Processing | Non-Linear Combining |
| Range cell (m) | 1.5m, 2.25m |
| Array Spacing (m) | 0.1 m - 0.5 m |
| Windowing | No Window |
| Beamangle | $90^0$ |

**Table 6.7 Simulation parameters 7**



**Figure 6.92 SNR of sine profile using simulation parameters 7**



**Figure 6.93 PSNR of sine profile using simulation parameters 7**
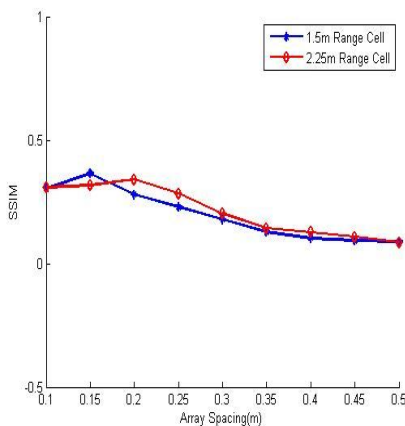


**Figure 6.94 SSIM of sine profile using simulation parameters 7**
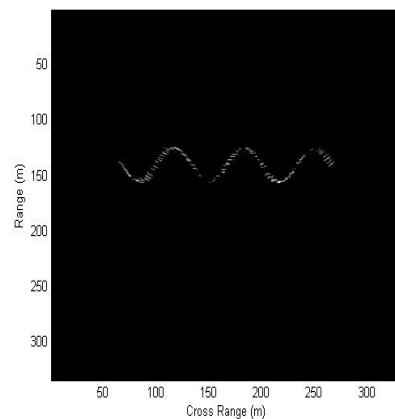


**Figure 6.95 Image formed -sine profile (0.2m array spacing, 2.25m range cell)**

170

Figure 6.92, figure 6.93 and figure 6.94 show the measurement metrics for a sine profile obtained by combining all the elements. PSNR and SSIM index in figure 6.93 and figure 6.94 shows that the best image formed is for 0.2m spacing for a 2.25m range cell and 0.15m spacing for a 1.5m range cell. After that the image quality index curve shows image degradation. The SNR graph in figure 6.92 show that the gain is increased until 0.3m array spacing and then there are oscillations. This is because in the case of array spacing greater than 0.35m the far field condition fails. Thus the SNR curve would indicate good result until about 0.3m spacing and after that it fails to reflect the true gain. This phenomenon can be seen in the rest of the profiles.
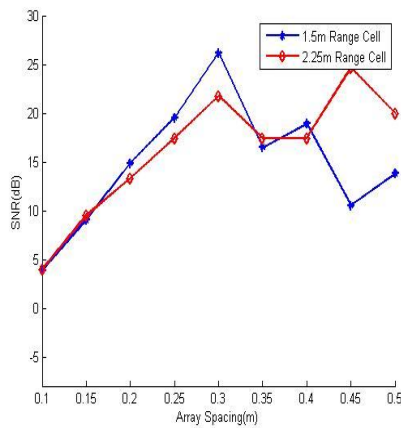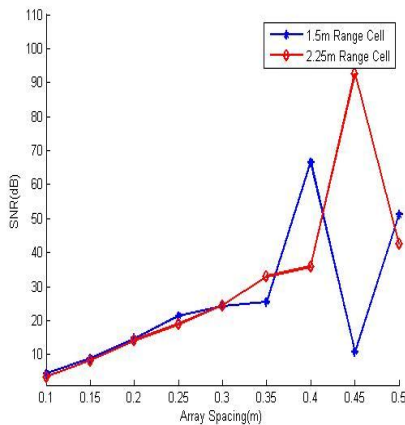


**Figure 6.96 SNR of straight line profile using simulation parameters 7**
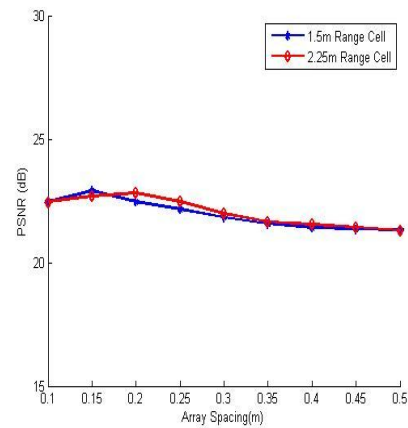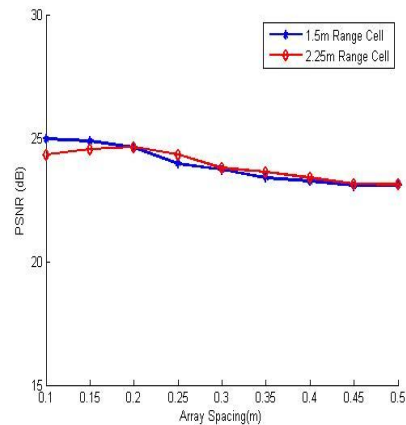


**Figure 6.97 PSNR of straight line profile using simulation parameters 7**
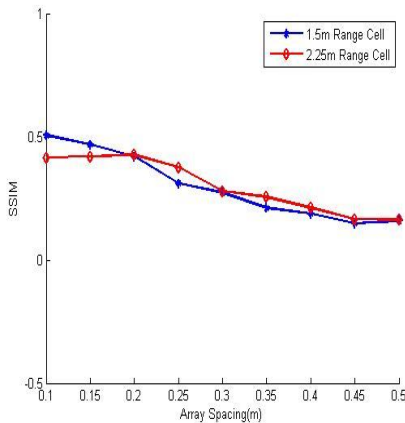


**Figure 6.98 SSIM of straight line profile using simulation parameters 7**
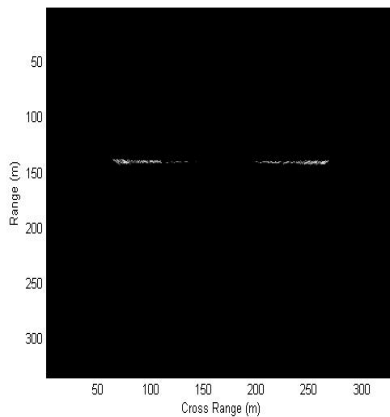


**Figure 6.99 Image formed-straight line profile (0.2m spacing, 2.25m range cell)**

The phenomenon seen in the SNR curve of sine profile is also seen in the straight line profile in figure 6.96. PSNR and SSIM index in figure 6.97 and figure 6.98 indicate the best image obtained for a straight line profile considering all array combination is by using an array spacing of 0.2m and a range cell size of 2.25m. The image formed in figure 6.99 for a straight line profile shows the loss of useful information.
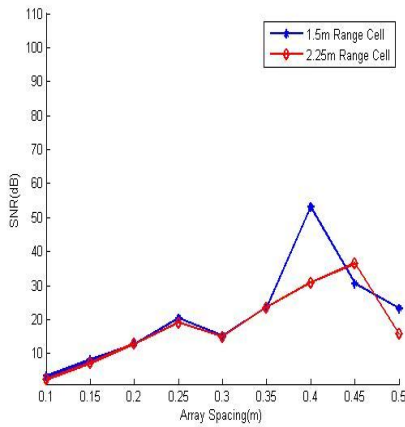


**Figure 6.100 SNR of distributed target profile using simulation parameters 7**
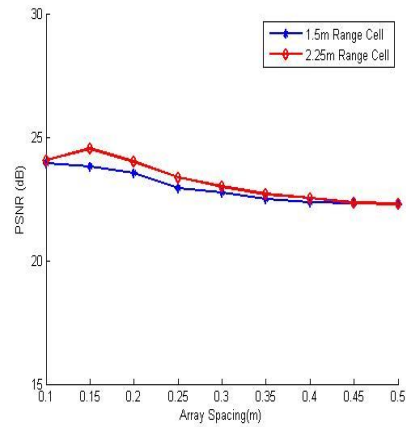


**Figure 6.101 PSNR of distributed target profile using simulation parameters 7**
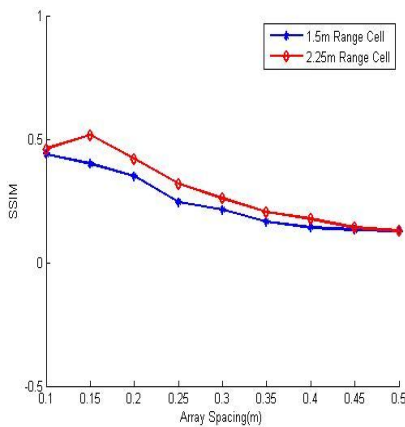


**Figure 6.102 SSIM of distributed target profile using simulation parameters 7**
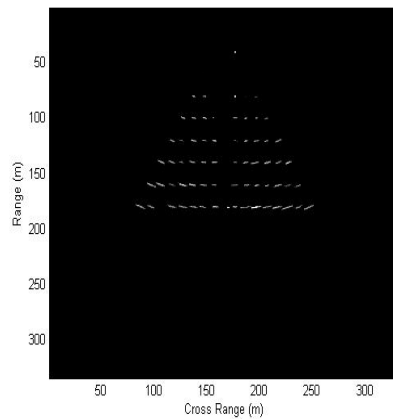


**Figure 6.103 Image formed - distributed target profile – (0.15m array spacing, 2.25m range cell)**

The metric curves for a distributed target profile in figure 6.100, figure 6.101 and figure 6.102 shows the same trend as shown by sine profile and straight line profile.

The PSNR and SSIM index of all profiles is seen to peak at lower array spacing. This is because the lower array spacing tries to achieve the angular resolution of higher array spacing. Here the higher array spacing would be the separation between the first and the last element of the array. It was seen previously that after a certain array spacing the image quality begins to degrade. This reason can be attributed to the lack of correlation in the range cells. This is because for large array spacing only a small part of the target lies in the same range cell and hence the strength of correlation decreases. When the received signals are divided into range cells there is also possibility that the target is not lying in the same range cell when the array spacing is large. The different peaks obtained for different range cells as seen in PSNR and SSIM index graphs gives this indication.

The comparison of performance of a 4 element array with that of a 3 element array is for a 2.25m range cell for the profiles considered is given. Only the SSIM index and PSNR are compared.
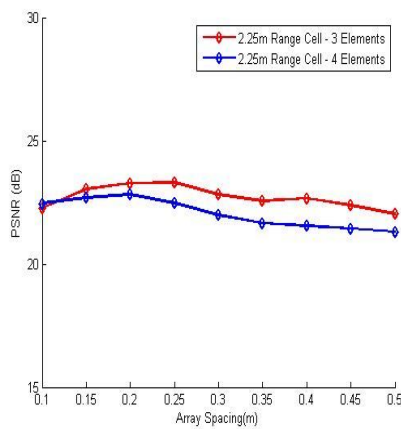


**Figure 6.104 Comparison of PSNR of sine profile for all combinations**
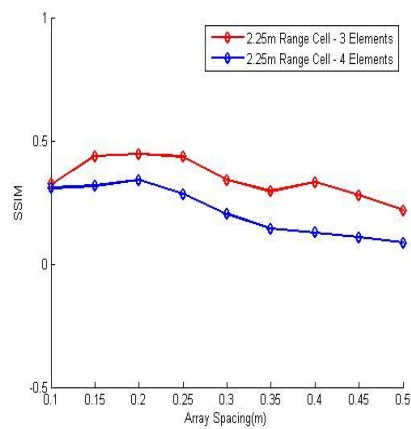
**Figure 6.105 Comparison of SSIM of sine profile for all combinations**
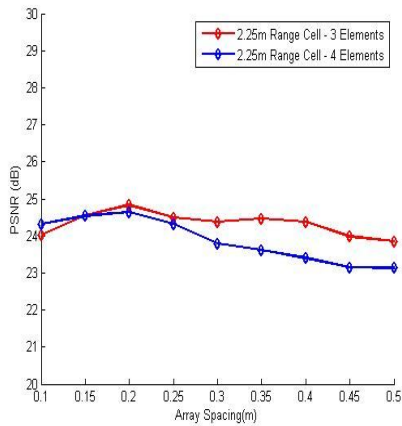
**Figure 6.106 Comparison of PSNR of straight line profile for all combinations**
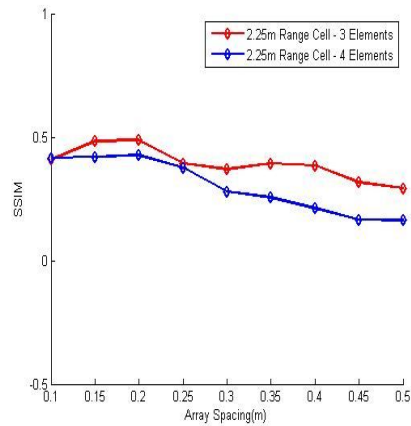


**Figure 6.107 Comparison of SSIM of straight line profile for all combinations**
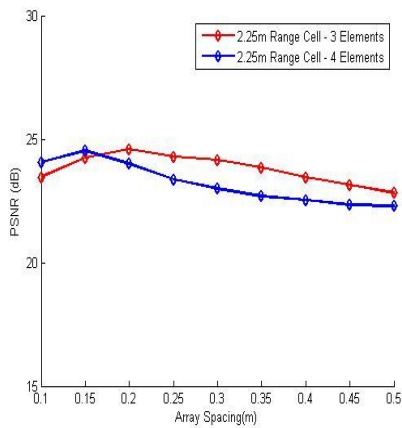


**Figure 6.108 Comparison of PSNR of distributed target profile for all combinations**
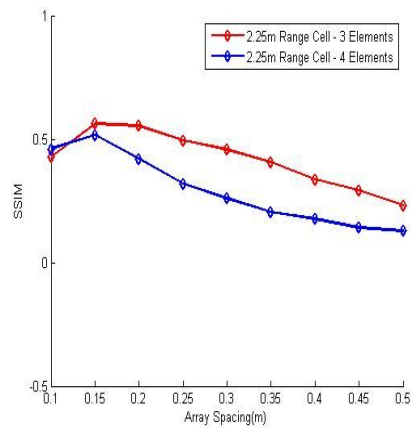


**Figure 6.109 Comparison of SSIM of distributed target profile for all combinations**

The PSNR and SSIM index of the profiles for all array element combination shows that the image obtained using 3 elements is much better than that obtained using 4 element array. This is expected as before as for 4 element array the effective array spacing is greater than 3 element array. This shows that correlation decreases as the array spacing increases. This is because the time delay of arrival between the two elements is large. Thus when the signals are divided into range cells, the target would lie in one range cell of one signal whereas in the other signal the same target would be in a different range cell. When the array spacing

is small, the time delays between the elements are small and hence the two range cell compared will have the same target.

## 6.9 Comparison between equal element spacing combination and all combination

In this section, PSNR and SSIM index curves obtained by combining equal array spacing and that obtained by using all combinations are compared. A 3 element array using all possible subarray combinations is compared against a 4 element array. The comparison is given for sine profile, straight line profile and a distributed target profile. Another reason for the comparison of 3 element array with that of 4 element array is because the number of subarrays for all combinations of a 3 element array is 3 which is the same number of subarrays that is considered when only equally spaced elements are considered.
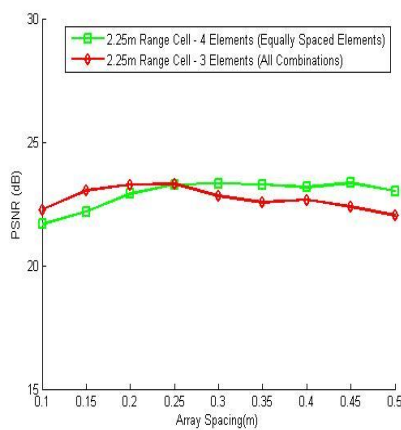


**Figure 6.110 Comparison of PSNR of sine profile with equally spaced elements and all combinations**
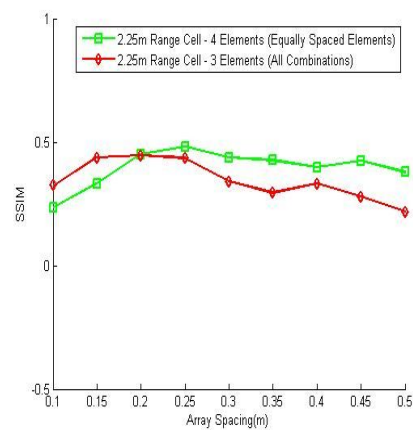
**Figure 6.111 Comparison of SSIM of sine profile with equally spaced elements and all combinations**
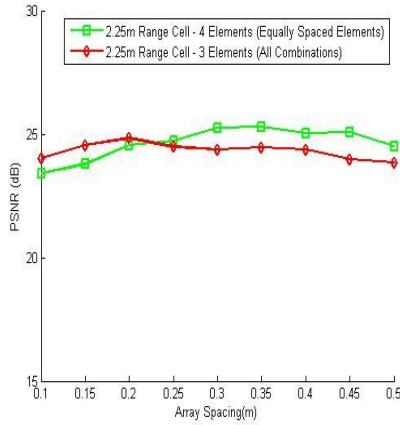
**Figure 6.112 Comparison PSNR of straight line profile with equally spaced elements and all combinations**
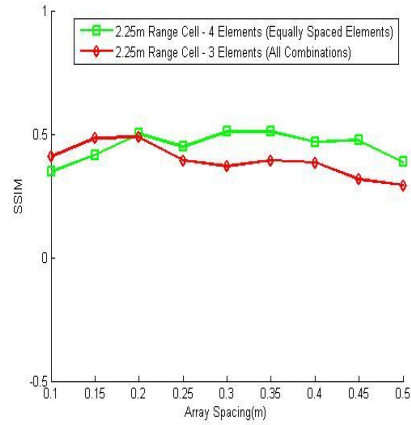


**Figure 6.113 Comparison of SSIM of straight line profile with equally spaced elements and all combinations**
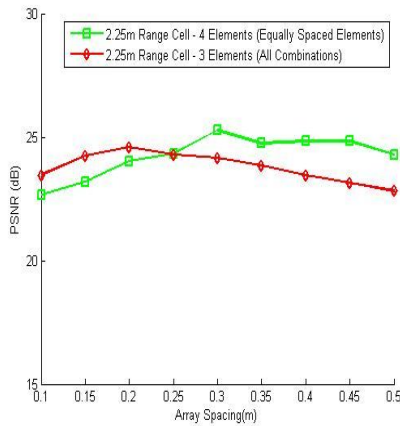


**Figure 6.114 Comparison of PSNR of distributed target profile with equally spaced elements and all combinations**
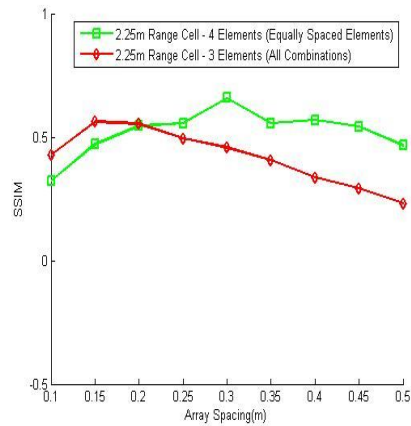


**Figure 6.115 Comparison of SSIM of distributed target profile with equally spaced elements and all combinations**

From the metric graphs presented it can be seen that when the array spacing is greater than 0.25m the quality of images obtained using all combinations start to decrease. An array spacing of 0.25m indicates an effective array spacing of 0.5m in case when all the array combinations are taken into consideration. Thus the metric indicates that the image quality would start getting worse for an array spacing greater than 0.5m and with 2.25m range cell. It is also seen from the graphs that using all array spacing combinations, the image quality of 0.1m spacing is improved and is similar to image quality obtained using 0.2m array

176

spacing. This shows that lower array spacing tries to achieve the resolution of array spacing which is equivalent to the effective length of the array.

## 6.10    Adjusting the threshold to improve image quality

In all the above cases considered, the threshold was chosen according to the equation 4.66 and equation 4.70. It has been seen from the simulation results that the improvement in image quality is negligible. This factor was attributed to the high value of the threshold. In all the above cases the threshold was not controlled. In order to get better results equation 4.66 and 4.70 can be rewritten as

$$\beta = \frac{k_1 \xi}{K - 1} \qquad\qquad 6.2$$

$$\beta_{new} = k_1 \beta + k_2 \sigma \qquad\qquad 6.3$$

where $k_1$ and $k_2$ are constants. The values of these constants are determined by manual tuning. The simulations presented in the previous section assumed $k_1 = 1$ and $k_2 = 1$. The PSNR and SSIM index for a sine profile and distributed target profile is presented. The value of $k_1$ is increased from 0 to 1 in steps of 0.2 and the value of $k_2$ is increased from 0 to 3 and the graphs are plotted. The simulation parameters are given in table 6.8.

| Signal | **Chirp Signal** <br> *Duration    : 0.005 s* <br> *Frequency  : 200 – 300 kHz* |
|---|---|
| Number of hydrophone elements | **4** |
| Number of Sub Arrays | **3** |
| Bandwidth | **100 kHz** |
| Sampling Frequency (*F*) | **1 MHz** |
| Processing | **Non-Linear Combining** |
| Range cell (m) | **2.25m** |
| Array Spacing (m) | **0.3 m** |
| Windowing | **No Window** |
| Beamangle | **$90^0$** |

**Table 6.8 Simulation parameters 8**

Only subarrays with equal spacing are considered.
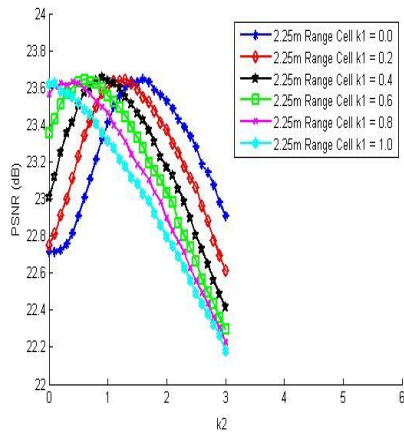


**Figure 6.116 PSNR of sine profile using simulation parameters 8**
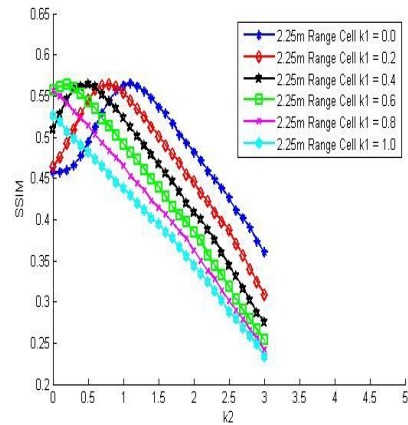


**Figure 6.117 SSIM of sine profile using simulation parameters 8**
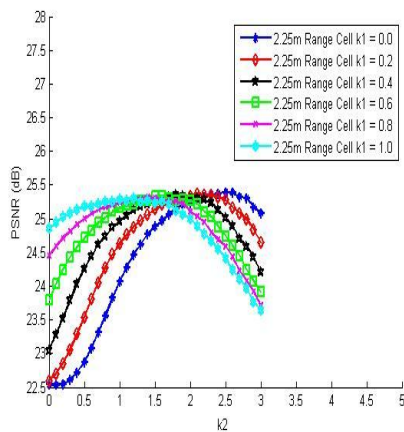


**Figure 6.118 PSNR of distributed target profile using simulation parameters 8**
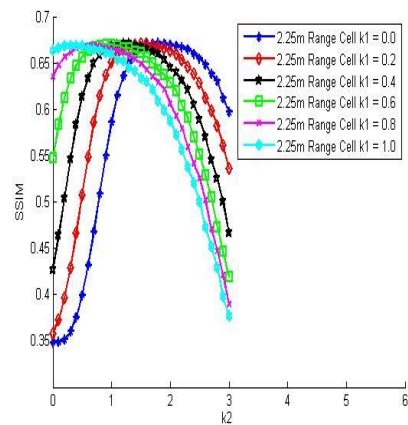


**Figure 6.119 SSIM of distributed target profile using simulation parameters 8**

The PSNR and SSIM graphs in figure 6.116 and 6.117 for a sine profile show that the maximum image quality that can be obtained by this method. For $k_1 = 1$ and $k_2 = 1$ the image quality obtained for a sine profile is found to be less than the highest image quality that can be attained. The best image quality for a sine profile is attained with $k_1 = 0.6$ and $k_2 = 1$ which is one of the combinations of values. It can be seen from the graph that as $k_2$ increases, $k_1$ decreases and for any value of $k_1$ and $k_2$, the maximum image quality attained is the same. This is the reason that

178

the curves show a very small improvement in image quality. The PSNR and SSIM index curves follow the same trend.

For a distributed target profile, it can be seen from the PSNR and SSIM index curves in figure 6.118 and figure 6.119 that the value of the threshold chosen is close to the value which gives the best image quality. Thus the PSNR and SSIM curves in the simulations presented in the previous sections show a considerable improvement in the image quality. The images of the sine profile and distributed target profile formed by considering one of the best values of $k_1$ and $k_2$ is shown in figure 6.120 and figure 6.121.
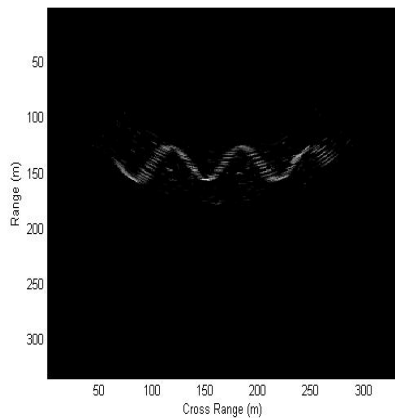


**Figure 6.120 Image of sine profile by using $k_1 = 0.6$ and $k_2 = 1$**
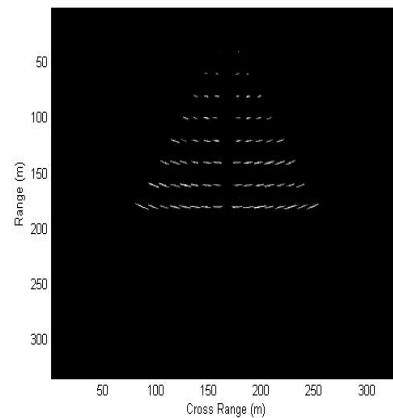
**Figure 6.121 Image of distributed target profile using $k_1 = 0.6$ and $k_2 = 1.5$**

## 6.11   Summary

This chapter presents the simulation results and tests the theory developed in Chapter 4. Three measures 1) SNR 2) PSNR and 3) SSIM was used.  The image quality of the images formed using two elements was found to be poor due to the presence of correlation artifacts. Hence to improve the image quality, the number of array elements was increased to four and averaging was applied. It was found that even by averaging the correlation artifacts did not reduce. Thus it was confirmed that linear operation was not suitable in removing the correlation artifacts.

The non-linear combining process was applied to all the target profiles considered. Applying the non-linear combining process found to improve the image. In order to improve the flexibility and to fine tune the non-linear combining process two variables were introduced into the equation which calculates the threshold. By adjusting these variables and fine tuning the algorithm the results were seen to improve. The algorithm was tested for further improvement in the image quality by applying hamming window. But it showed that windowing had no effect. The image quality remained the same or became worse. Increasing the bandwidth showed that for getting a good image quality, the ratio $\dfrac{\Delta n_d}{N_{samp}}$ should remain constant. Simulations performed by increasing the sampling frequency showed small improvement at lower array spacing but remained constant for higher array spacing.

Simulation was then performed by using all available array combinations. The simulations showed that further the elements are away from each other, the range cells become less correlated. This indicates that the array spacing cannot be increased infinitely. The simulations presented in this chapter shows that the non-linear combining process works well.

# Chapter 7
# Experimental System Design and Results

In chapter 6, simulation results were presented for the non-linear combining process. It was found that the non-linear combining process gives a better quality image. This algorithm was validated using both objective (PSNR) and subjective (SSIM) measures and the results were in good agreement with each other. Based on these results and observations, it was decided to perform real time experiments by building a hardware model incorporating the proposed algorithm.

## 7.1    Experimental parameters

The signal parameters used for experimental setup are given in table 7.1.

| *Signal* | **Chirp Signal** <br> *Duration   : 0.005s* <br> *Frequency : 325 kHz – 425 kHz* |
|---|---|
| *Bandwidth* | **100 kHz** |
| *Sampling Frequency* | **1 MHz** |
| *Number of hydrophone elements* | **4** |
| *Array Spacing* | **0.3 metres** |

**Table 7.1 Experimental parameters**

A chirp signal with a frequency sweep of 325 kHz to 425 kHz was used for the experimental setup. This is because the projector and hydrophone available in that frequency range. Thus the signal used has a bandwidth of 100 kHz which is same as the signal used for the simulation purposes. The following paragraphs summarize the various elements in the hardware setup.

## 7.2    Transducer frequency response

Due to budget constraints existing piezo-composite transducing hydrophones were used. The piezo-electric transducers have the ability to convert mechanical vibrations into electric signals and electric signals into mechanical vibrations.

The frequency response of the transducer has to be studied in order to determine the operating range of the transducers. The frequency response was determined by

applying a signal to transducers which is immersed in a tank of water. This transducer acts as the projector. The electrical signal applied is converted to pressure signal by the projector and travels through the medium. Another transducer is connected to the scope and immersed in water. This transducer acts as the hydrophone. The input signal frequency applied to the projector was changed constantly. The signal frequency was changed by keeping the signal amplitude constant. The signal produced by the hydrophone was noted. The experimental setup is shown in figure 7.1.
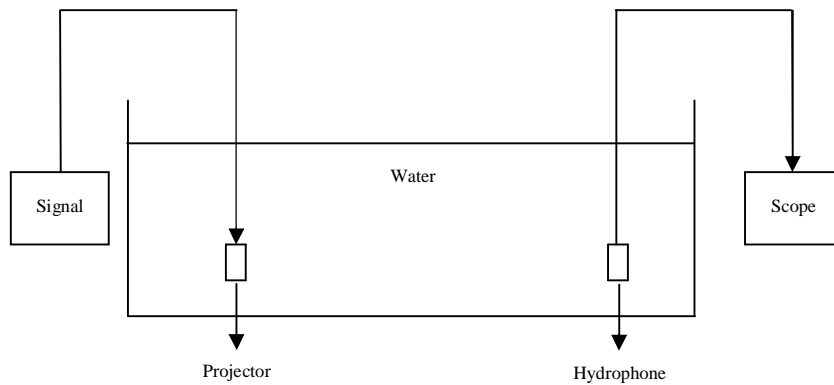


**Figure 7.1 Experiment setup to determine the frequency response of the transducer**
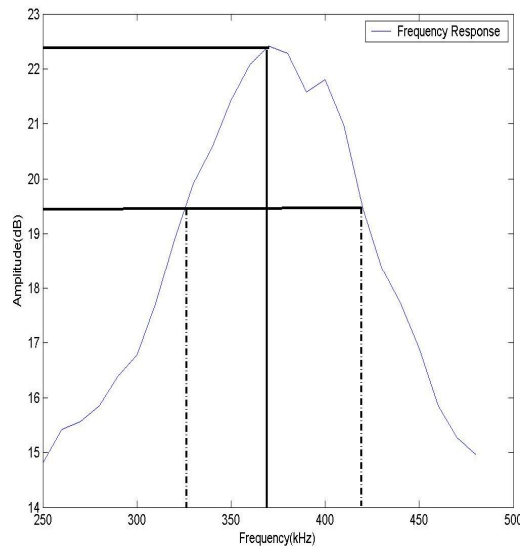


**Figure 7.2 Frequency response of the piezo-electric transducer**

The region in the frequency response graph where the response is the maximum is the operating range where the transducer would operate efficiently. The response

graph is shown in figure 7.2. Figure 7.2 shows that the transducer sensitivity is maximum in the frequency range 325 kHz – 425 kHz. Figure 7.2 indicates that at -3dB the bandwidth is 100 kHz.

## 7.3    Projector channel

The block diagram in figure 7.3 shows the main blocks of the projector channel.
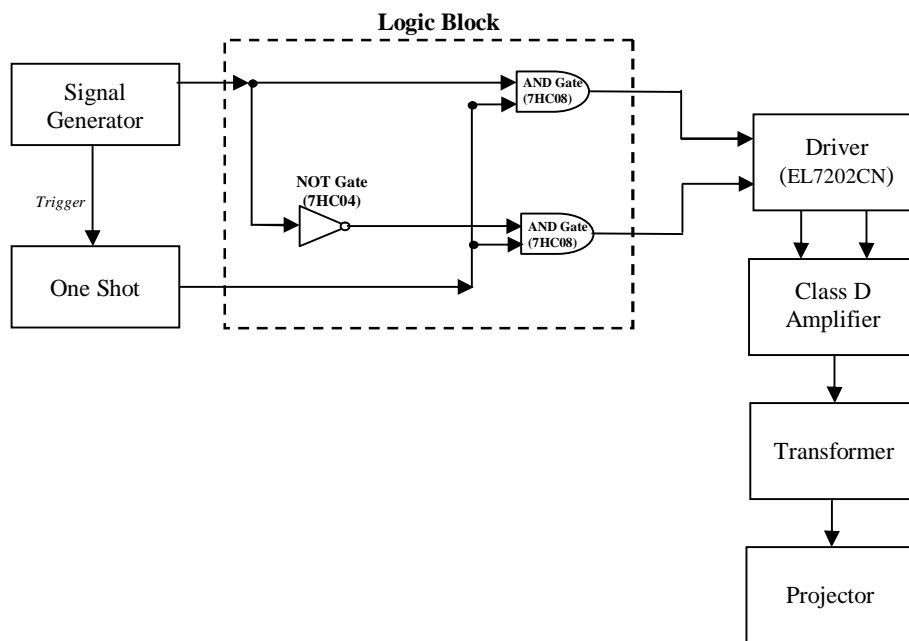


**Figure 7.3 Block diagram of the projector channel**

The projector channel consists of a signal generator which is capable of generating a chirp signal sweeping between 325 kHz – 425 kHz. An agilent signal generator available was capable of generating the continuous chirp signal in the given frequency range. For the purpose of the experiment it was required to have a single chirp pulse of duration 0.005s. This is achieved by using a one-shot circuit and a logic circuit. The one-shot circuit is shown in figure 7.4.
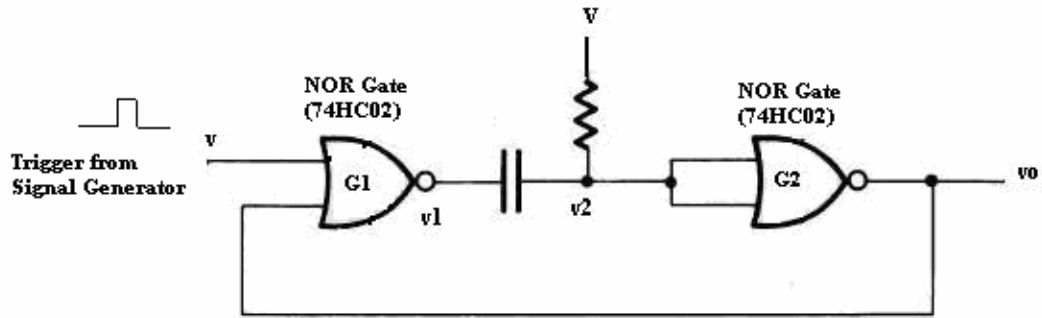
**Figure 7.4 One-shot using NOR gates [102]**

By choosing appropriate resistance and capacitance values for the circuit in figure 7.4, the one-shot circuit can be made to output a pulse with time duration of 0.005s. One-shot circuit is triggered using the *sync* output of the signal generator. The 0.005s pulse output is applied to the logic circuit which generates two outputs. One output is a 0.005s chirp signal whereas the other output is a complimentary pulse of duration 0.005s. Since the signal obtained from the signal generator is unipolar (varying between 0 and 1), these pulses are required to generate a bipolar signal which is applied to the projector.

The output of the logic circuit is applied to a MOSFET driver. The function of the driver circuit is to provide suitable current to the gate of the power MOSFET in order to enable fast switching. Though the output of the driver gives switched signals there is a necessity of large current to drive the primary of the transformer load. This can be achieved using a Class D amplifier which not only provides larger current outputs but at the same time acts as a switch. The circuit for the class D amplifier is shown in figure 7.5.

The Class D amplifiers are one in which the transistors are operated as switches. At each time two transistors are switched on (a p-type (*FQP12P10*) and an n-type (*IRF630*)) so that there is a flow of current through the transformer. The current through the transformer, when each pair of transistors conducts, flows in the opposite directions. The direction of current flow is shown in figure 7.5 using arrows. The output across transformer secondary would be an alternating waveform. The output amplitude depends on the transformer ratio. Class D amplifiers give the maximum efficiency when operated as a switch and hence they

184

are suited for battery operated systems. The transistors used (the p-type and the n-type) are selected in such a way that their switching, voltage and current characteristics match. The transformer used was a ferrite cored step up transformer with a turns ratio of 40.
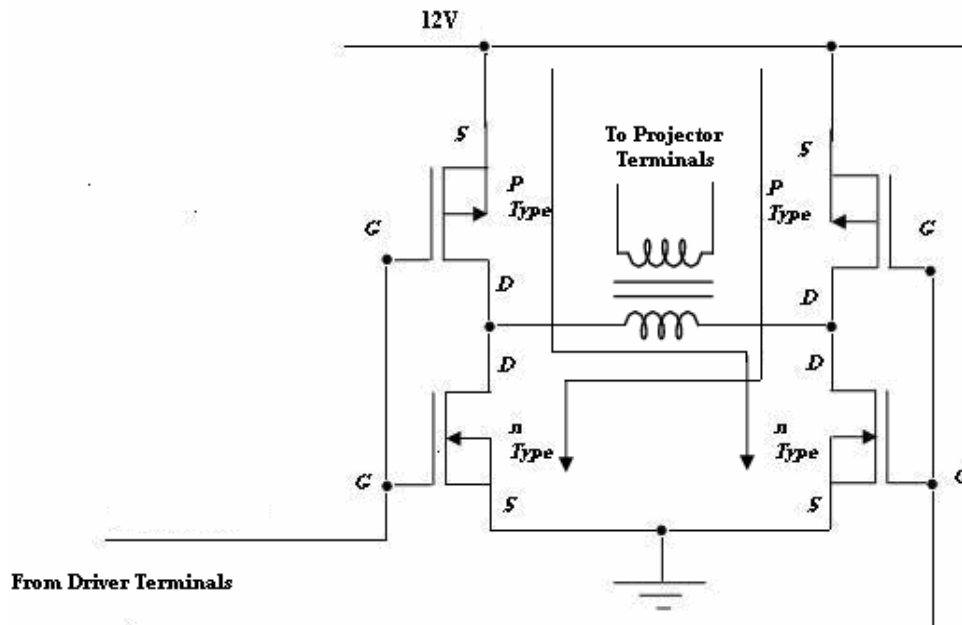


**Figure 7.5 Class D amplifier circuit [103]**

The peak value at the transformer secondary was 200V from which the source level is calculated. The RMS value can be given by

$$V_{rms} = \frac{V_A}{\sqrt{2}} = 141.4V \qquad 7.1$$

The sensitivity of the projector was 150 dB re.1µPa/1V@1m. Thus the source level is

$$SL = TS + 20\log_{10} V_{rms} = 193 \text{ dB re.1µPa @1m} \qquad 7.2$$

## 7.4 Receiver channels

Each receiver channel consists of a two stage filter-amplifier circuit built using an operational amplifier (LM833N) and connected to a data acquisition unit. The

operational amplifier (op-amp) chosen was a wideband amplifier with a large gain bandwidth product. The receiver has four channels with each channel having a similar filter-amplifier circuit. Each of the four transducers (hydrophones) was connected to their respective filter amplifier circuits feeding signals into the corresponding input in the data acquisition unit. The receiver channel is shown in the block diagram in figure 7.6.
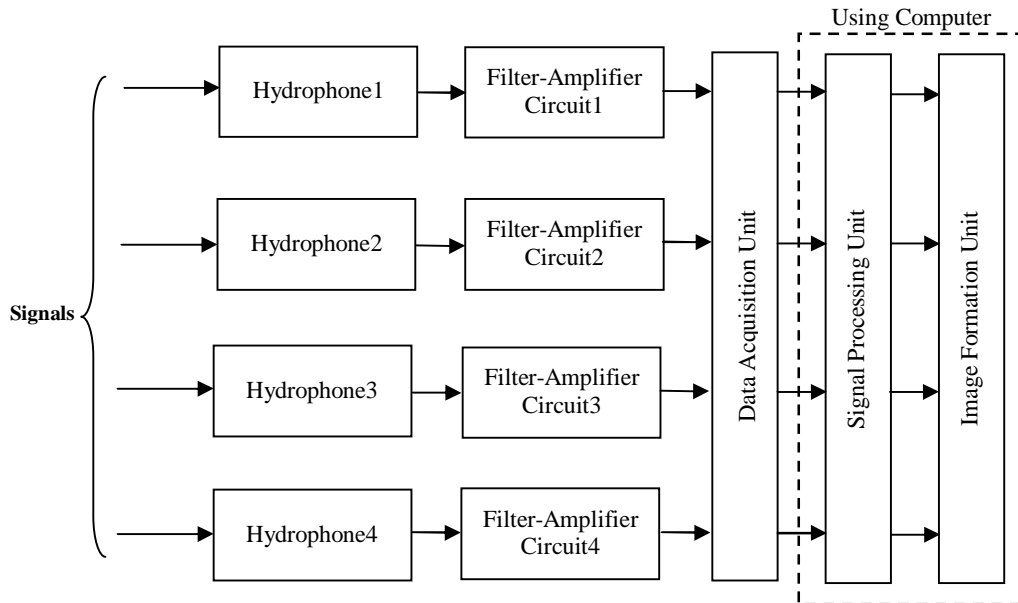


**Figure 7.6 Receiver structure**

One stage of the filter-amplifier is shown in figure 7.7.
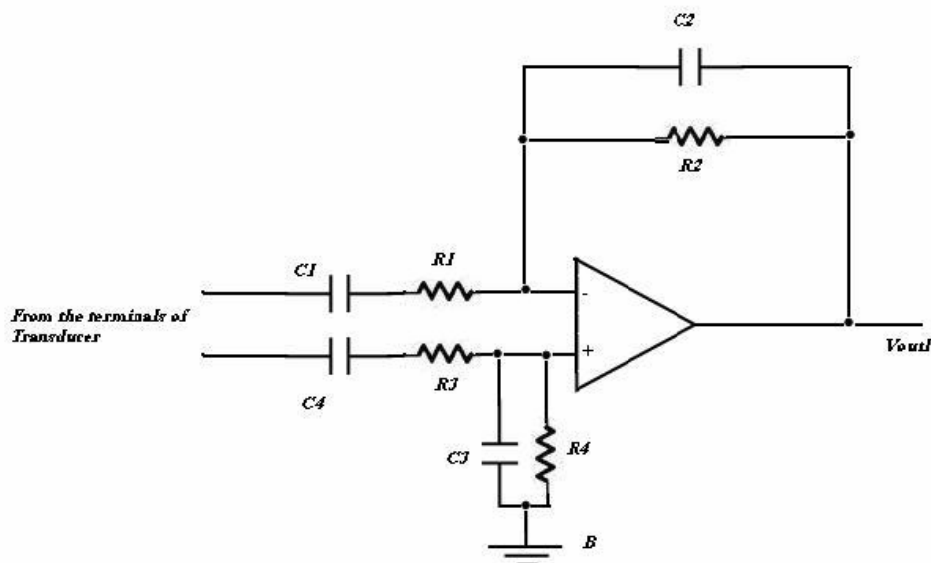


**Figure 7.7 One stage of filter-amplifier circuit [104]**

In figure 7.7 a bandpass filter is constructed using a lowpass filter and a highpass filter. The parallel *RC* circuit in figure 7.7 functions as a lowpass filter and the series *RC* circuit at the op-amp input perform the highpass filtering. The values of the resistors and the capacitors in figure 7.7 are chosen in order to have a passband of 325 kHz – 425 kHz and also to give an amplifier gain of 10. The output $V_{out}$ is connected to a similar op-amp circuit. The values of resistors and capacitors in the second stage will be same as the first stage. Thus this amplifier gives a further gain of 10. Thus theoretically, the total gain of the filter-amplifier circuit is 100. The frequency response of the filter-amplifier stage is shown in figure 7.8.
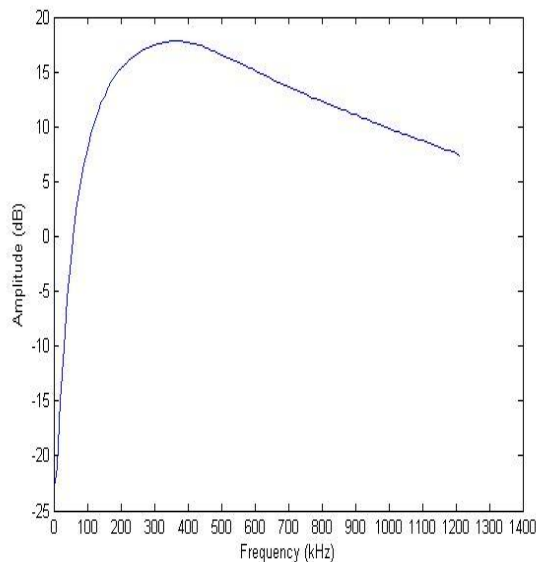


**Figure 7.8 Frequency response of filter-amplifier circuit**

The frequency response was determined by applying a 100 mV signal to the input of the filter-amplifier circuit. The maximum output voltage was obtained at 370 kHz frequency with output voltage amplitude of 7.81 V. Thus the gain obtained after the filter-amplifier stage is 78.1.

### 7.4.1   Data acquisition unit

The output of the filter-amplifier stage is connected to the data acquisition unit which converts the received analog signals to digital signals to facilitate storage

and further processing using computer. The data acquisition unit used was TiePie Handyscope HS4 which can sample at a maximum rate of 5MHz. The TiePie Handyscope had a 12 bit analog to digital converter (ADC). Thus the signal-to-quantisation noise ratio is 72dB. The instrument was powered using its universal serial bus (USB) which is connected to the computer. The data acquisition unit can be triggered externally to start recording of signals. The *sync* output provides a trigger pulse when the signal generator transmits a signal. The external trigger of the data acquisition unit is connected to the *sync* output of the signal generator. This causes the data acquisition unit to start recording at the instant when the projector transmits a 5ms chirp signal. The data acquisition unit has 4 channels to which the outputs from filter-amplifier circuits are connected. The received signal is stored in the computer as a binary file (.bin files).

## 7.5    Hardware

The hardware designed and the array setup is shown in figures 7.9, 7.10 and 7.11.
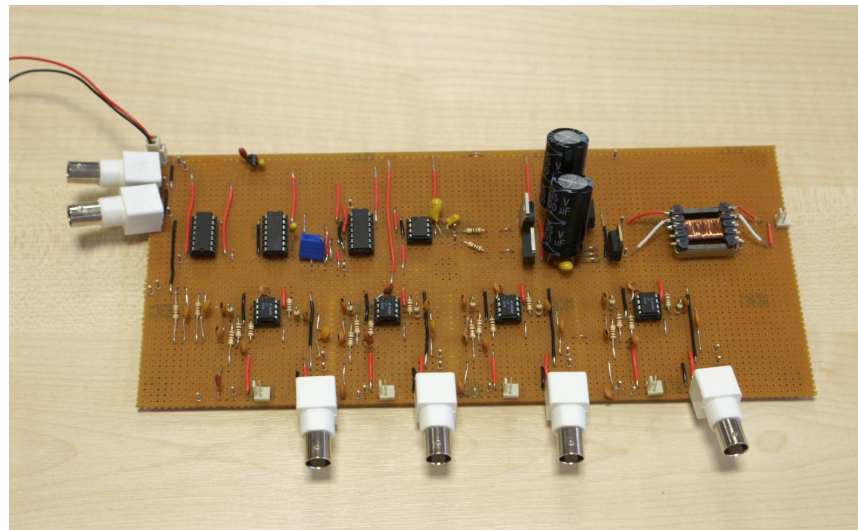


**Figure 7.9 Hardware circuit with a single channel for transmitter and four channels of receiver**

**Figure 7.10 Front view of the sonar array**



**Figure 7.11 Array view showing the number of piezo-electric elements**

The array elements of the hydrophone array in figures 7.10 and 7.11 were separated by 0.3m. The effective array length was 0.9m. The projector was located at the center of the array. The projector had a beamangle of approximately $10^0$. The hydrophone elements were fixed to an aluminium rod which was mounted on an aluminium frame.

The simulation results presented in Chapter 6 showed that the image quality depended on the profile considered. The best image quality was obtained for an array spacing of 0.25m to 0.3m. Equation 5.17 from Chapter 5, section 5.2.1.2 is approximated as

$$\Delta\theta \approx \left| \frac{c}{Bd} \right| \qquad\qquad 7.3$$

Using equation 7.3 an approximate plot for angular resolution can be obtained for array spacing between 0.1m – 0.5m and using the parameters in table 7.1. The plot is shown in figure 7.12
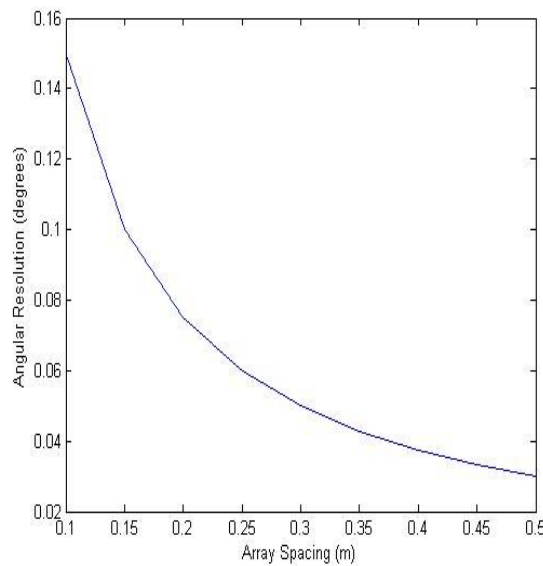


**Figure 7.12 Array spacing vs Angular Resolution**

**B = 100 kHz**

From figure 7.12 it is found that major change in angular resolution takes place at lower array spacing until 0.3m array spacing. After 0.3m array spacing, the angular resolution curve becomes asymptotic. This prompted 0.3m as a choice for array spacing in the experimental setup. As mentioned in section 7.2, due to budget constraints, existing piezo-electric composite hydrophones with a bandwidth of 100 kHz was chosen.

## 7.6    Experimental results

The hardware was tested in a tank in the Marine Engineering Department of the Newcastle University, UK. The hydrophone array was arranged for a forward looking configuration. The test tank was 35m long. A random package of bubble

wrap (a number of bubble wraps tied together) served as a target for the experiment. The target bubble wrap was chosen so that there was a change in density between the two mediums. The bubble wrap also served as a target with texture. The tank geometry is presented in figure 7.13.
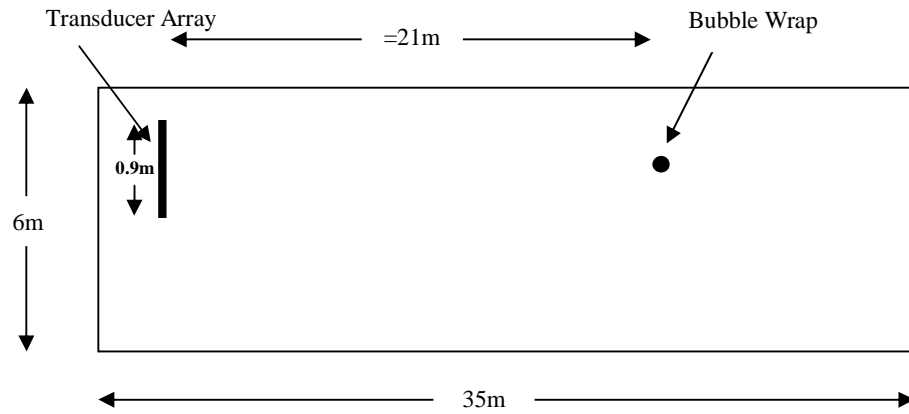


**Figure 7.13 Tank geometry**

The experiment is performed with the signal parameters in table 7.1. The return signals obtained in all the four channels by using the target bubble wrap is shown in figure 7.14.



**Figure 7.14 Signals received in 4 channels**

The spectrogram of the received signal on one channel is shown in figure 7.15.



**Figure 7.15 Spectrogram of received signal with a bubble wrap as target in the test tank**

The spectrogram in figure 7.15 shows three distinct target returns. Each return is marked on the spectrogram. One of the returns is due to the bubble wrap and the other two returns at the end are from the ends of the tank. The signals obtained after passing the received signals through matched filter is shown in figure 7.16.
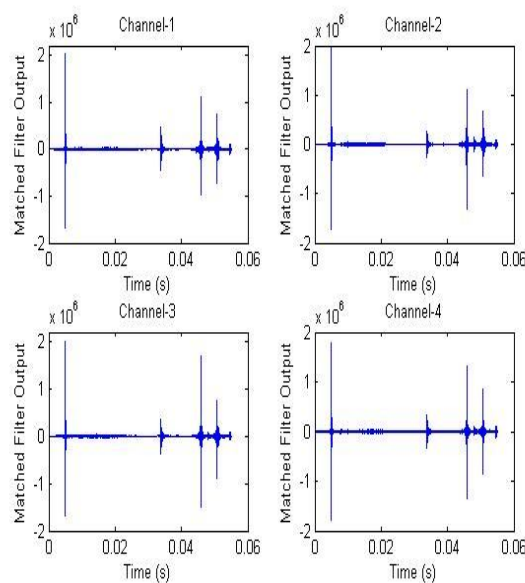


**Figure 7.16 Signals in the 4 channels after matched filtering**

The matched filter results clearly indicate the targets by the process of pulse compression. If there was any mismatch in the frequency of the received signal then the matched filter output would be low, distorted and clear peaks would not be seen. The signals obtained after applying TVG to all the four channels is shown in figure 7.17.
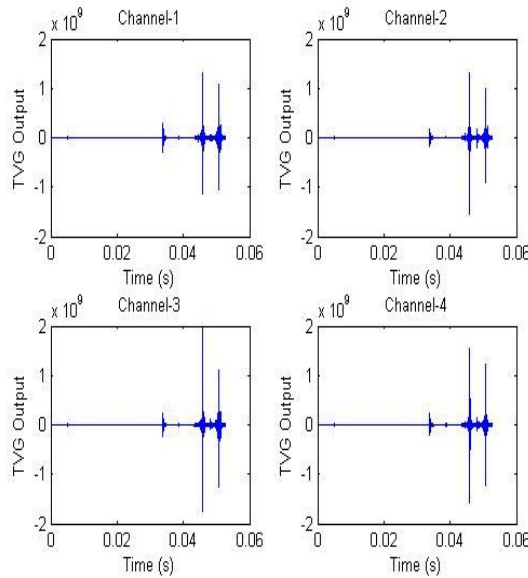


**Figure 7.17 Signals in figure 7.16 obtained after passing through TVG amplifier**

The images formed with the signals obtained from channel 1 and channel 2 for various values of $k_1$ and $k_2$ are shown in figures 7.18, 7.19 and 7.20. These images are obtained by using 0.75m range cell. The image obtained using 2.25m range cell is shown in figure 7.21.
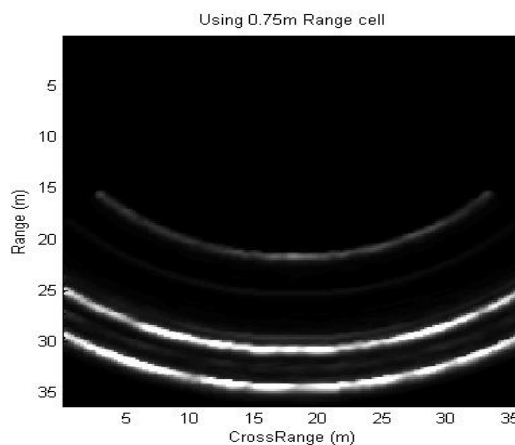


**Figure 7.18 Image formed using two elements with $k_1 = 0$, $k_2 = 0$, range cell size = 0.75m and overlap = 50%**
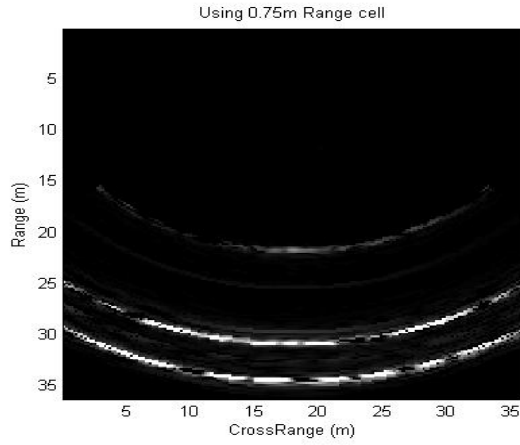
**Figure 7.19 Image formed using two elements with $k_1 = 0.5$, $k_2 = 0.5$, range cell size = 0.75m and overlap = 50%**
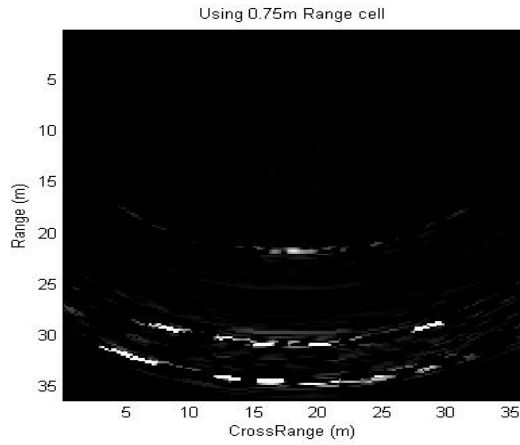


**Figure 7.20 Image formed using two elements with $k_1 = 1.0$, $k_2 = 1.0$, range cell size = 0.75m and overlap = 50%**
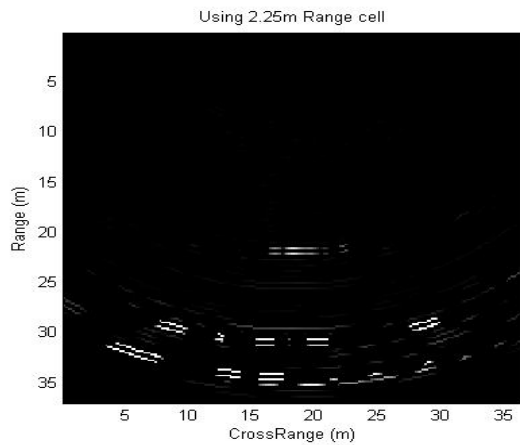


**Figure 7.21 Image formed using two elements with $k_1 = 1.0$, $k_2 = 1.0$, range cell size = 2.25m and overlap = 50%**

When $k_1 = 0$ and $k_2 = 0$, image is formed from the $r\theta$ matrix. When $k_1$ and $k_2$ are varied then different threshold levels were applied to $r\theta$ matrix obtained using two elements. The images formed using two elements (channel 1 and channel 2) in figure 7.18 show the bubble wrap, the return from tank ends and another ambiguous return in between them. Even the positions of the bubble wrap target and the ends of the tank are ambiguous. The image formed in figure 7.18 has no thresholding applied to it. The images formed in figures 7.19 and figure 7.20 has different intensity thresholding applied but still the position of the bubble wrap and the tank ends are ambiguous and cannot be distinguished. Thresholding was applied to the two element array in order to show that the image obtained using two elements cannot be further improved. The image formed in figure 7.22 uses 4 elements and the $r\theta$ matrices formed by the subarrays are combined using averaging.
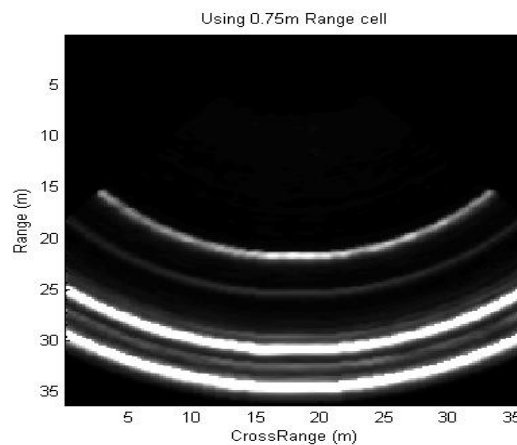


**Figure 7.22 Image formed using 4 elements, range cell size = 0.75m, overlap = 50% and averaging**

It is seen that averaging, which is a linear combination of the subarrays, has no effect in reducing the artifacts and the ambiguities mentioned still exists. Thresholding applied to resultant $r\theta$ matrix after averaging will show similar results as those obtained using 2 elements.

Image in figure 7.23 uses 4 array elements and non-linear combining with a range cell size of 0.75m. Image in figure 7.24 is obtained by using 4 elements and non-linear combining with a 2.25m range cell size. From figures 7.23 and figure 7.24 it can be seen that the position of the bubble wrap target is seen clearly. The ends

of the tank are seen as two different targets as there were two ramps at the each corner of the tank. It is also seen from the figures 7.23 and 7.24 that the ambiguous return in between the bubble wrap target and the ends of the tank has vanished as a result of non-linear combining. This shows that for largely spaced arrays forming an image using linear combination of elements does not work. Hence it is necessary that non-linear combination of elements is required for image formation.
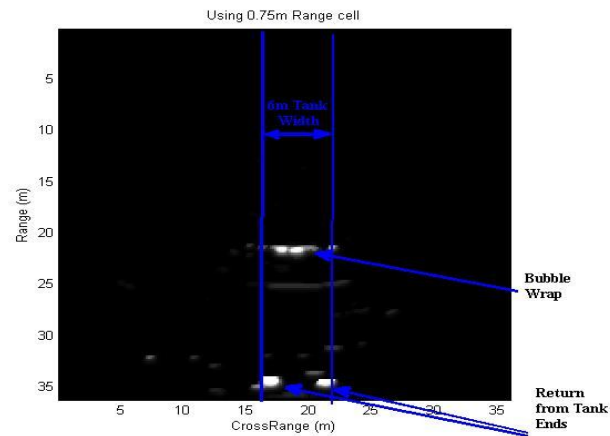


**Figure 7.23 Image formed using 4 elements with $k_1 = 1.0$, $k_2 = 1.0$, range cell size = 0.75m, overlap = 50% and non-linear combining**
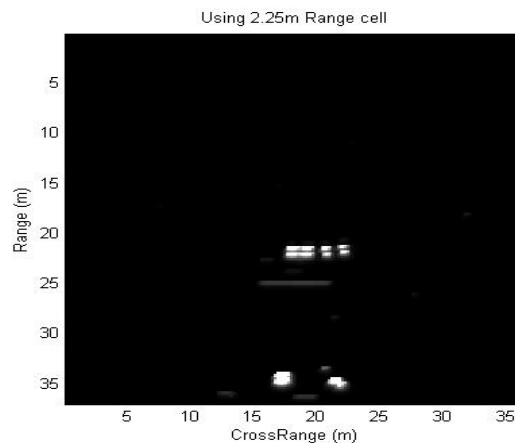


**Figure 7.24 Image formed using 4 elements with $k_1 = 1.0$, $k_2 = 1.0$, range cell size = 2.25m, overlap = 50% and non-linear combining**

From the results it is found that the non-linear combining algorithm works well. Following satisfactory results obtained from testing further experiments were conducted in a shallow water estuary near Blyth. The photograph of the target scene being imaged is shown in figure 7.25. A diagram showing the approximate

geometry of the illuminated area is shown in figure 7.26. The target scene shows wooden piers followed by a gap and then two moored ships.



**Figure 7.25 Target scene imaged**
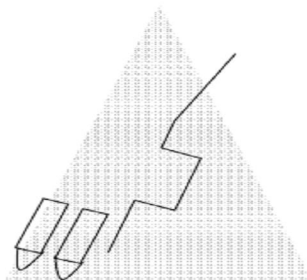


**Figure 7.26 Approximate geometry (illuminated area shaded)**

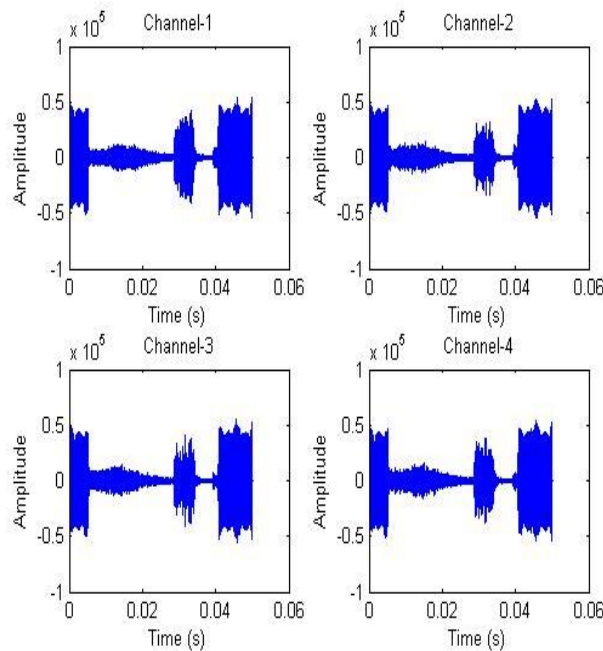The received signal on 4 channels is shown in figure 7.27.
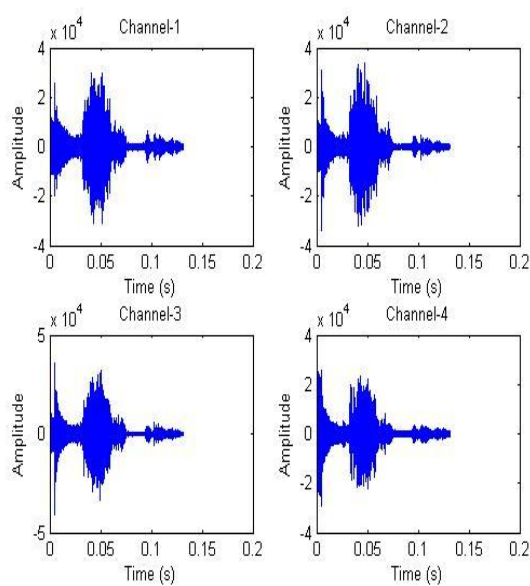


**Figure 7.27 Signals received in 4 channels in Blyth**

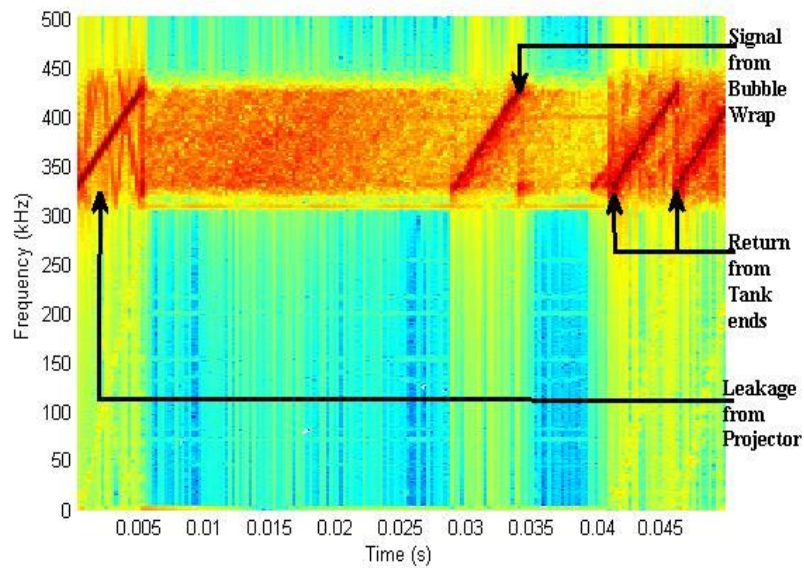The spectrogram of the received signal is shown in figure 7.28.
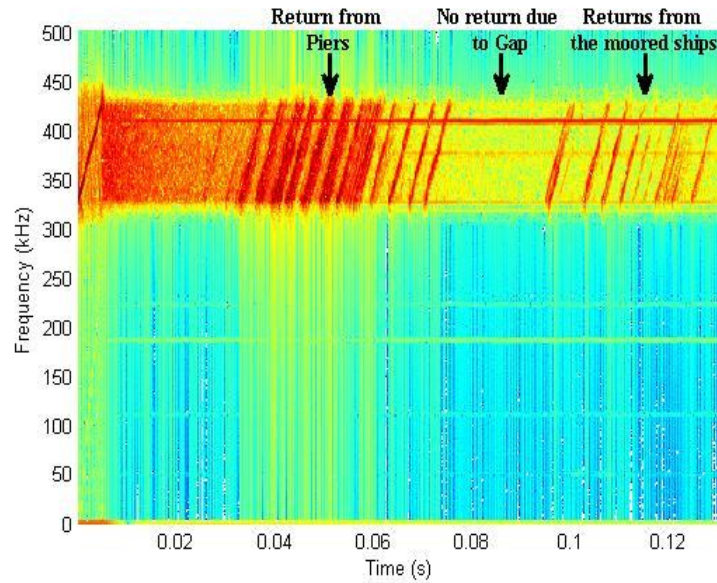


**Figure 7.28 Spectrogram of received signal in Blyth**

The matched filter response of the signals in 4 channels is shown in figure 7.29.
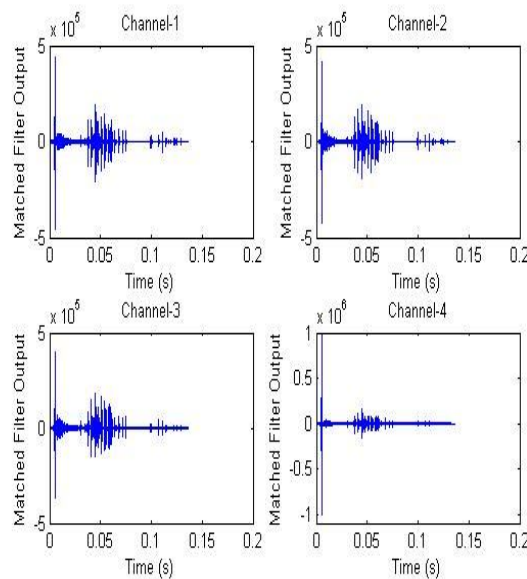


**Figure 7.29 Signals in the 4 channels obtained in Blyth after matched filtering**

In figure 7.29, the returns from the pier and the returns caused by the sterns of the moored ship are seen. The matched filter output shows a good SNR as any

frequency distortion or mismatch between the return signals would not give clear peaks. The output of TVG amplifier is shown in figure 7.30.
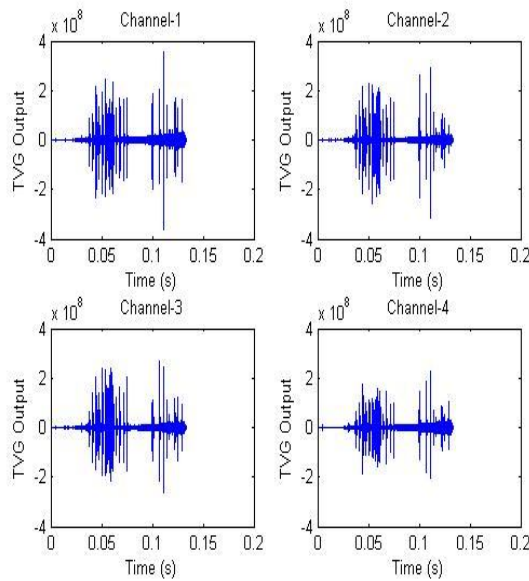


**Figure 7.30 Signals in figure 7.29 after passing through TVG amplifier**

The image obtained using the output of two channels (channel 1 and 2) is shown in figure 7.31. Figure 7.32 is obtained by applying thresholding to the image obtained using the output of two channels. The image formed in figure 7.31 and figure 7.32 is obtained using 0.75m range cell size. Various values of $k_1$ and $k_2$ were tried but there was no improvement in image quality.
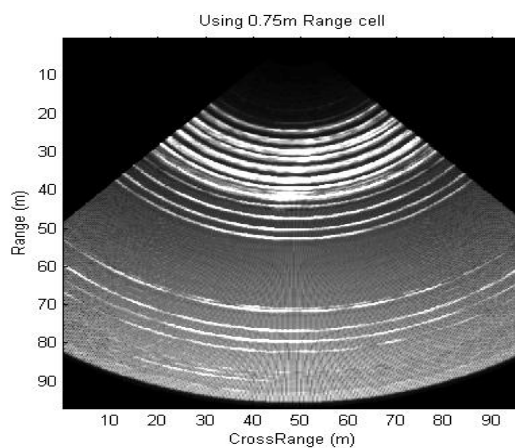


**Figure 7.31 Image formed by using data from Blyth with two elements, $k1 =$ 0.0, $k2 = 0.0$ and range cell = 0.75m**
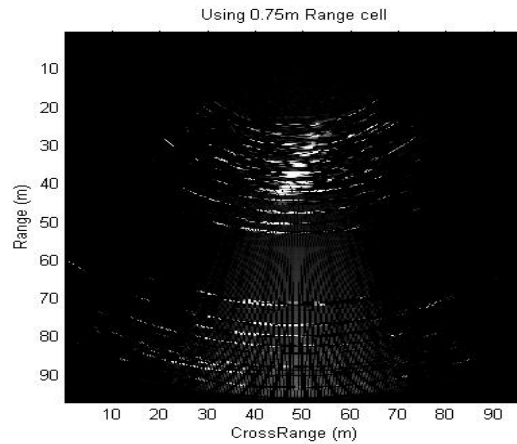
Figure 7.32 Image formed by using data from Blyth with two elements, *k1* =
1.0, *k2* = 1.0 and range cell = 0.75m

Figure 7.33 is formed by using two elements and a range cell size of 2.25m
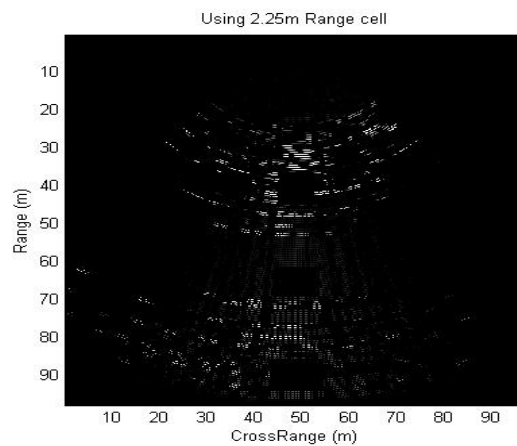


Figure 7.33 Image formed by using data from Blyth with two elements, *k1* =
1.0, *k2* = 1.0 and range cell = 2.25m

From the images presented it is clear that the images formed using two elements do not give good results even after thresholding. It is noted that high value of threshold reduces the quality of the image formed. Figure 7.34 shows the image obtained by using 4 elements and averaging. It can be seen that there is no reduction of artifacts corresponding to the results obtained previously. It should be noted that applying a threshold to the averaged result would only produce results similar to that obtained using two elements and thresholding.
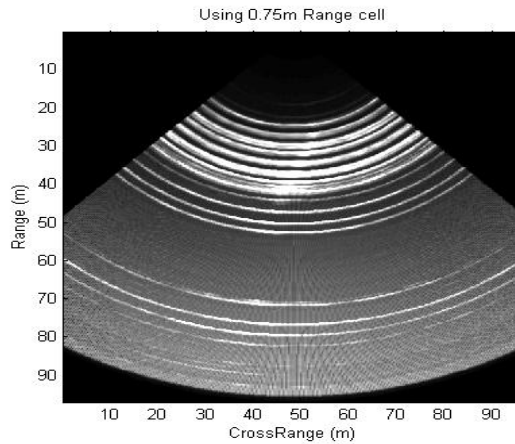
**Figure 7.34 Image formed by using data from Blyth with 4 elements, range cell = 0.75m and averaging**

Figure 7.35 and figure 7.36 show the images obtained using 4 elements and non-linear combining. A 0.75m range cell was used.
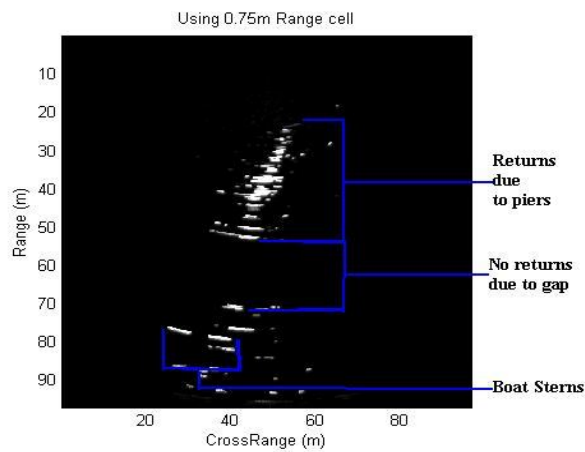


**Figure 7.35 Image formed by using data from Blyth with 4 elements, *k1* = 1.0, *k2* = 1.0, range cell = 0.75m and non-linear combining**
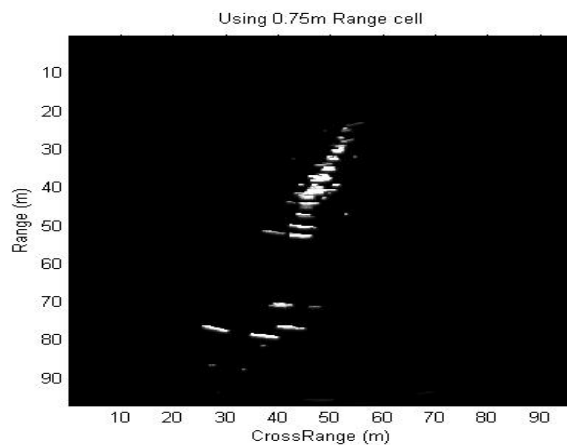


**Figure 7.36 Image formed by using data from Blyth with 4 elements, *k1* = 1.2, *k2* = 0.6, range cell = 0.75m and non-linear combining**

It was noted that the best image was obtained for $k1$ = 1.2 and $k2$ = 0.6. Figure 7.37 shows the image formed using 2.25m range cell.
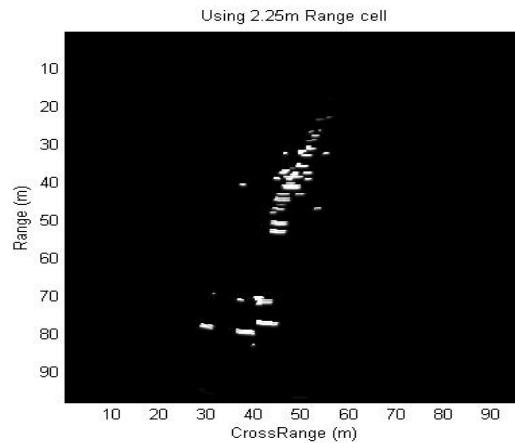


**Figure 7.37 Image formed by using data from Blyth with 4 elements, *k1* = 1.2, *k2* = 0.6, range cell = 2.25m and non-linear combining**

Figure 7.38 shows the image formed using all array combinations of a 4 element array.
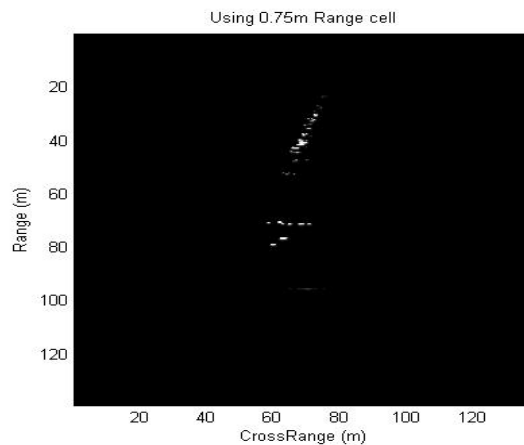


**Figure 7.38 Image formed by using data from Blyth with 4 elements (all combinations), *k1* = 1.2, *k2* = 0.6, range cell = 0.75m and non-linear combining**

Different values of *k1* and *k2* were tried in order to fine tune the image obtained. It was noted that the quality of image obtained was not getting better. This corresponds to the simulation results presented in Chapter 6 for all array combinations. Figure 7.38 was presented to show the same. This indicates that the array spacing can be increased only to a certain extent.

After imaging the piers, the sonar array was pointed towards the open sea. The chirp signal was transmitted and returns were recorded. Figure 7.39 shows the signal obtained in 4 channels.
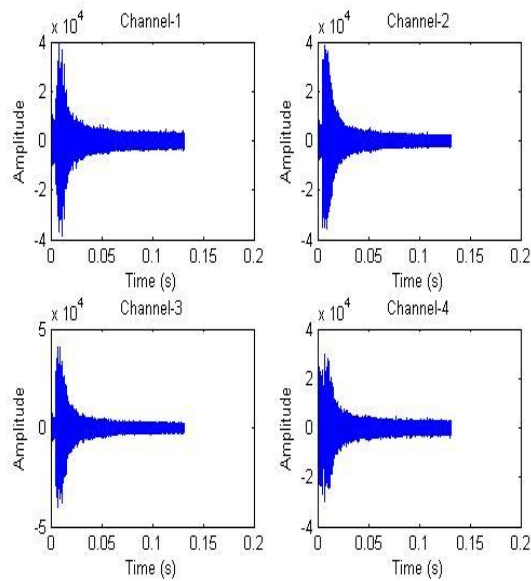


**Figure 7.39 Returns obtained with the sonar array pointed towards the sea at Blyth**

Figure 7.40 shows the spectrogram of the return signal.
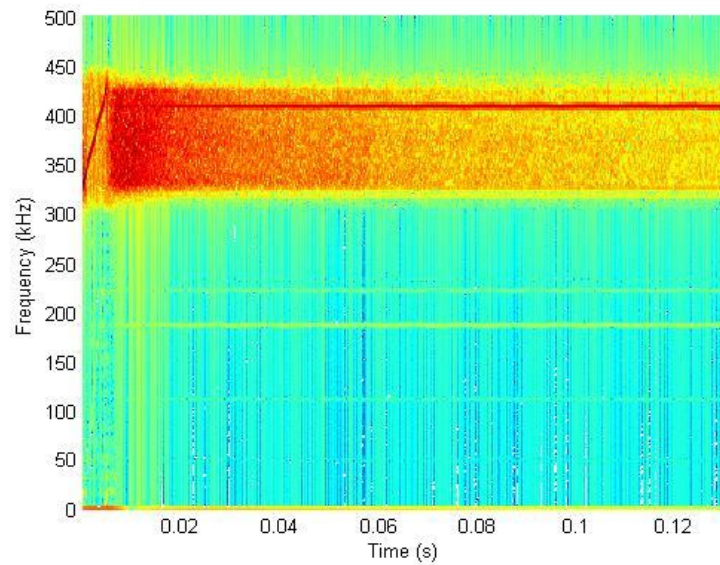


**Figure 7.40 Spectrogram obtained from the returns with the sonar array pointed towards the sea at Blyth**

The spectrogram in figure 7.40 shows that there is a single dominant frequency at 420 kHz. There are no other returns seen in the figure 7.40 indicating the absence of any target. The image formed using non-linear combining is shown in figure 7.41.
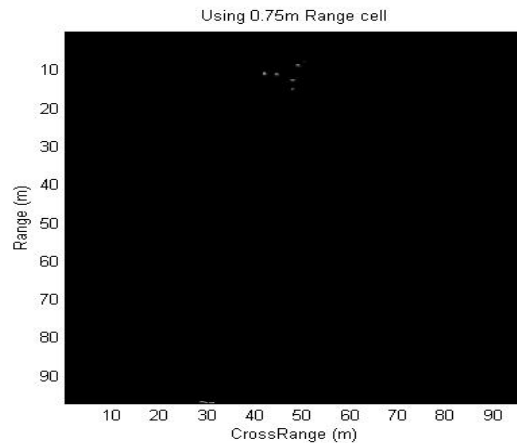


**Figure 7.41 Image formed with the sonar array pointed towards the sea, *k1* = 1.2, *k2* = 0.6, range cell = 0.75m and using non-linear combining**

The image formed confirms that there is no target in the signal path.

## 7.7　Few results from data provided by Tritech International

The bandpass filter used for the above experiment did not have sharp cutoff frequencies which was a cause of concern. Tritech International provided some of the data obtained from their separate trials using a 4 element array having an element spacing of 0.3m. The experiment was conducted in another shallow water dock site. The signal used for the experiment was a chirp signal with a frequency sweep of 325 kHz - 425 kHz. The sampling frequency used was 1 MHz. The sonar system used a 12 bit ADC. Tritech International had designed a bandpass filter with a better filter response than the one used for the trials in Blyth. The response of bandpass filter used by them is shown in figure 7.42. The purple line in figure 7.42 shows the final response of the bandpass filter used. Figure 7.42 shows that the bandpass filter used has much sharper cutoff frequencies than the filter in the system used in Blyth.
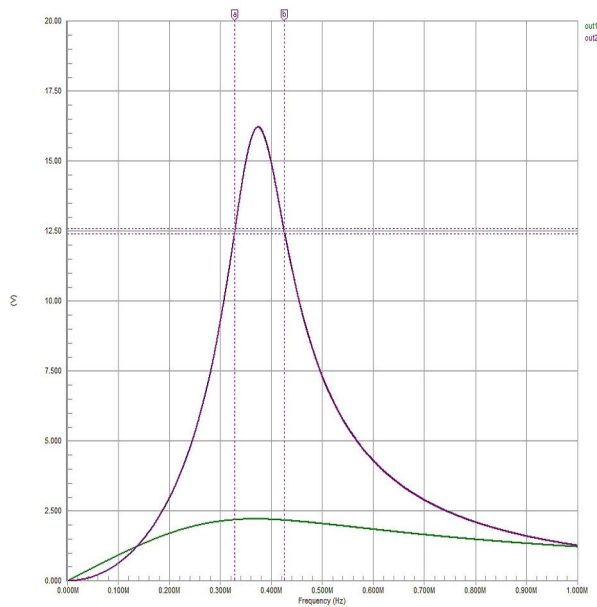
**Figure 7.42 Bandpass filter response of the system used by Tritech International**

The data provided was obtained by swinging the array from the dock walls to the open sea. The dock walls were located at about 35m from the boat. The results presented only shows the frames in which the dock walls were present.

Images formed using two elements are not included as it has already been shown that two elements do not provide a good quality image. Image formed by using 4 elements and averaging is shown in figure 7.43.
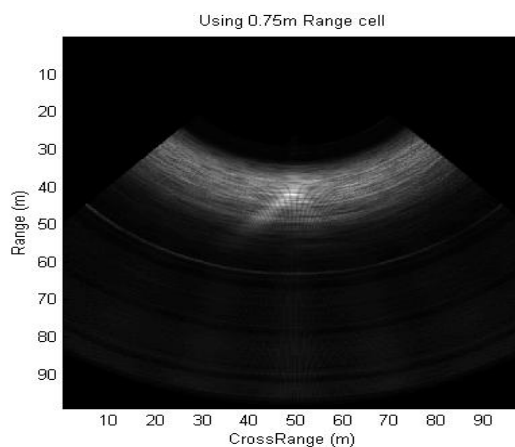


**Figure 7.43 Image formed by using data provided by Tritech International with 4 elements, range cell = 0.75m and averaging**

The image formed using non-linear combining is shown in figure 7.44. Figure 7.45 shows different image formed during the swing away from the dock wall. It can be found from these results that the image quality is improved and the non-linear combining algorithm works very well.
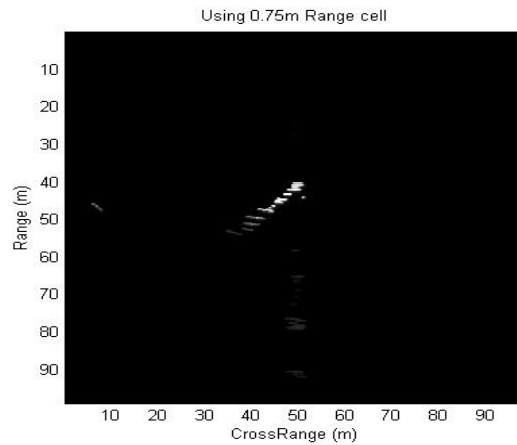


**Figure 7.44 Image formed by using data provided by Tritech International with 4 elements, *k1*=1.2, *k2* = 1.2, range cell = 0.75m and using non-linear combining**
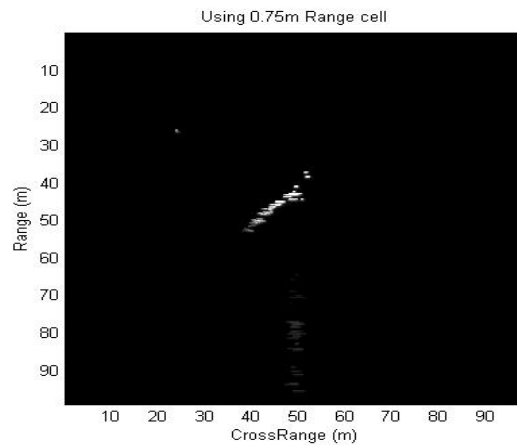


**Figure 7.45 Image formed by using data provided by Tritech International with 4 elements, *k1*=1.2, *k2* = 1.2, range cell = 0.75m and using non-linear combining – different frame**

## 7.8    Summary

This chapter presented the results obtained by performing real time experiments. Initially the experiment was conducted in a test tank at the marine engineering department of the Newcastle University. The result obtained from the two elements showed that it was difficult to identify the targets. The images obtained using two elements showed ambiguous target positions. Thresholding was applied to the results obtained using two elements but there was no improvement in the image quality. Increasing the number of array elements and applying averaging also showed no improvement in the quality of image formed and the ambiguity in determining the positions of the targets remained. Applying non-linear combining process to a 4 element array improved the image quality to a great extent. The position of the targets was also resolved using the non-linear combining process. This shows that the non-linear combining process works well. The experiment was also repeated at a shallow water estuary near Blyth. The results obtained confirmed the results of the tank tests.

One of the concerns of the sonar equipment used in the above trials was that the bandpass filter used did not have sharp cutoff frequency. This concern was overcome by using data gathered by the equipment designed by a commercial sonar manufacturer, Tritech International. The results obtained from real-time experiments further confirmed the performance of non-linear combining process thus verifying the simulation results presented in Chapter 6. The results obtained showed that by non-linearly combining the data from different subarrays of a uniform linear array, it is possible to have array separation of greater than $\lambda/2$.

# Chapter 8

# Conclusions

## 8.1    Conclusion

In this project, imaging sonar has been designed using the first principles of sonar. The sonar array used in this project has been assumed to have as few as four elements. Thus the objective of having an ultra-sparse array for the purpose of imaging is met. The inter-element spacing between the array elements was chosen to be many times the multiple of the wavelength. The array configuration chosen was such that it would give rise to ambiguous results for the DOA with the existing direction finding algorithms. This is because the existing DOA algorithms require the array elements to be spaced less than or equal to $\lambda/2$ in order to avoid phase ambiguities. The problem of phase ambiguities is overcome by using a broadband LFM signal and thus determining the time-difference of arrival. This successfully enabled the array elements to be separated by distances much greater than half the wavelength.

In Chapter 4, a novel non-linear combining process for estimation of multiple direction of arrival from the targets in the same range cell is presented. The non-linear combining process works by dividing the array into sub-array consisting of 2 elements. The following assumptions are made when developing the non-linear combining process.

1) The target being imaged is located in the far-field. This assumption is essential so that the DOA of the signals at each sub-array is equal.

2) The correlation artifacts vary when a cross-correlation is performed between the returns obtained from different hydrophones. This assumption is used to distinguish the true targets from the artifacts in the non-linear combining process.

208

The image of the target scene was formed by dividing the return signals into range cells. This reduces the range resolution of the sonar system and the range resolution would depend on the range cell size. It was shown that by overlapping the range cells, it is possible to increase the range-resolution. The DOA is determined by correlation of the corresponding range cells of two receivers. This shows that by trading off the range resolution, the angle of arrival is determined. It has been shown in Chapter 5 that the angular resolution is dependent on the signal bandwidth, the inter-element spacing and the angle subtended by the targets being imaged.

In Chapter 5, the simulation model that had been developed in this project has been explained in detail with the help of block diagrams. Three types of image quality measures 1) SNR 2) PSNR and 3) SSIM used are explained in Chapter 5. The SNR and PSNR are objective measures while SSIM is a subjective measure. Subjective image quality metric has never been used in predicting the quality of a sonar image formed. SSIM was chosen because it is better than the other subjective measures available. Another reason for the choice of SSIM is the ease with which this measure can be implemented. The SNR tries to reflect the amount of gain due to the application of the algorithm. Such a measure though not perfect was necessary because PSNR and SSIM describe the visual quality of the image. The complexity of the algorithm developed was calculated in-order to show the feasibility of application of the algorithm on digital signal processing (DSP) hardware. The calculations showed that this algorithm can be implemented on DSP hardware. A complex target was considered to be a collection of cluster of point targets. Different profiles were simulated by placing these clusters close together either in the form of a sine wave or a straight line or as a point target grid. Since the point targets are distributed randomly within the cluster, the simulated profiles can be considered equivalent to that of a similar realistic profile.

The results from the simulations were presented in Chapter 6. Simulations carried out with a two element array showed that the image formed contained correlation artifacts which degrade the image quality. The number of elements was increased to 4 and averaging was applied on the $r\theta$ matrices and the image was formed

using the resultant matrix. It was found that the correlation artifacts still existed and the image quality was not better than that formed using 2 elements. The graph obtained using the metrics confirmed the result. Then the non-linear combining process was applied which showed an improvement in the image quality. This was confirmed by the graphs obtained. In order to improve the image quality further the following processing were performed

1) Application of Hamming window – the results showed that applying window to the range cells before correlation did not have any effect in the improvement of image quality.

2) Increasing the sampling frequency – simulations were performed by increasing the sampling rate from 1 MHz to 5 MHz. The results obtained showed improvement in the image quality for small array spacing. The SNR also showed a small gain.

3) Increasing signal bandwidth to 200 kHz – simulations performed by increasing the signal bandwidth showed an improvement in SNR (gain) but the graphs of image quality metrics indicated very small or no improvement. Further investigation showed that this was due to the ratio $\dfrac{\Delta n_d}{N_{samp}}$. It was concluded that any improvement in the image quality can be observed only if the ratio $\dfrac{\Delta n_d}{N_{samp}}$ was kept constant. This indicated sampling at higher rate for higher bandwidth signals.

4) Simulations using all array combinations – simulations performed using all array combinations showed degradation in the image quality after reaching an effective array spacing of 0.7m. Comparing all array combinations for 3 and 4 elements showed that the quality of the images formed using 3 elements were better. Then the results obtained using 3 elements with all array combinations was compared with 4 elements results considering only equally spaced sub-arrays. The result showed that

in case of 3 elements using all combinations, the images formed using 0.25m had the same image quality as 0.5m spacing of 4 elements using equally spaced sub-arrays. This indicates that the correlation decreases when elements which are further apart are correlated. This is because when the elements are further apart the target signature present in the two range cells is less and hence the degree of correlation is low. This low degree of correlation caused parts of the true targets to be missing. While considering two close elements, the amount of target signature in the range cell considered is same and hence the degree of correlation is high. This indicates that the spacing between the array elements cannot be increased infinitely. The SNR measure which indicated the gain obtained using the algorithm was seen to oscillate at larger array spacing because the amount of artifacts present was very small when compared to the signal and hence at larger array spacing greater than 0.8m gain indicated by the SNR was not true. The PSNR and SSIM measures indicated the quality of the image formed.

5) The simulation performed indicated only a small improvement in the image quality when the non-linear combining process was applied. This was identified due to high threshold levels which were automatically chosen by the algorithm. Controlling the threshold levels showed that the non-linear combining process can be fine tuned to produce images of much better quality.

Chapter 7 presents the results obtained by performing real-time experiments. The non-linear combining process applied to the data obtained in the test tank showed good results. Further experiments were performed at Blyth which showed that the non-linear combining process works well. The bandpass filter used in the real-time experiments at Blyth did not have sharp cutoff frequencies which was a matter of concern. The non-linear combining process was then applied to the data provided by Tritech International whose bandpass filter response was much better than the response of the filter used at Blyth. The results showed that the non-linear combining process works.

This research has achieved the following

| No | Objective | Comments |
|---|---|---|
| 1 | Develop an imaging sonar system capable of forming recognizable images | Results shown in Chapter 6 and Chapter 7 |
| 2 | Build an imaging sonar with reduced number of hydrophone channels | Data fusion procedure given in Chapter 4 and results presented in Chapter 6 and Chapter 7 |
| 3 | Use a sparse array with array elements spaced greater than $\lambda/2$ | Data fusion procedure given in Chapter 4 and results presented in Chapter 6 and Chapter 7 |
| 4 | Investigate the possibility of trading off high range resolution obtained using high bandwidth signals for better angular resolution | Procedure described in Chapter 4 and Chapter 5. Results presented in Chapter 6 and Chapter 7. |
| 5 | Multiple angle of arrival in the same range cell | The targets profiles simulated were such that there are multiple targets in the same range cell. The non-linear combining process described in Chapter 4 and the results in Chapter 6 and Chapter 7 showed the capability of the algorithm. |
| 6 | Minimal Statistical assumptions | The non-linear combining process developed does not make any statistical assumptions on the signal received at the hydrophones. |
| 7 | Test the developed algorithm under realistic conditions | Hardware was built and the algorithm was tested under realistic conditions. The results are presented in Chapter 7. |

**Table 8.1 Table of objectives achieved**

### 8.1.1   Limitations of non-linear combining process

Some of the limitations of the non-linear combining process which was noted are presented.

1) When the inter-elemental spacing is large, the assumption that the angle of arrival of the signals at all sub-arrays remains the same fails. This degrades the image quality as the position of correlation peak formed by a target varies.

2) When the inter-elemental spacing is large, the range cell size should also be large so that sufficient amount of target signature is present in the range

cell for successful correlation. As the array spacing increases, the correlation between the range cells decreases. This occurs because for large array spacing the delay between the signals arriving is large such that the target signatures may not be in the same range cell. This causes loss of correlation and degrades the image quality.

3) Large range cells decrease the degree of correlation. When the range cells are large, there would be large number of targets in the range cell which arrive at the hydrophones having same time delay. This causes the correlation peaks to merge thus decreasing resolving capacity of the non-linear combining process. Thus the range cell should be chosen such that it is not very large or very small. This can only be done experimentally.

## 8.2    Future Work

The research has shown that it is possible to build imaging sonar with an ultra-sparse array. The research has been carried out using a linear array with equally spaced hydrophone elements. It might be possible to achieve better gain by using unequal array spacing or random array spacing and applying the non-linear combining process.

This research had aimed in building imaging sonar by assuming that the sonar platform and target is stationary. Thus the technique developed can only be used to form images of stationary targets. The effect of platform motion is another area that has been left for future investigation. It has been noted from this research that reduction in the number of hydrophone channels has come at a greater computational cost. But the primary aim was to reduce the system cost by reduction of the hydrophone channels and shifting the computational load to the DSP processors available. This allows the use of these DSP processors to their maximum capacity. Correlation had been used to determine the DOA by finding the lead or lag between the signals arriving at the hydrophone elements. There are many advanced signal processing algorithms using higher order spectral analysis techniques which are efficient but computationally complex than correlation. One

advantage of using the higher order spectral analysis (third order and above) is that if the noise is Gaussian then it would go to a zero in the higher order spectral domain.

The imaging sonar built in this project creates a 2D image. There is a possibility of investigating into building a 3D imaging sonar using the principle of sparse array. If such a system could be built up and if the performance is good then it could replace the present day imaging systems which use hundreds of transmitter and receiver elements. This would bring down the system cost by a great extent.

# References

[1] Murino V and Trucco A, *Three-Dimensional Image Generation and Processing in Underwater Acoustic Vision*, Proceedings of IEEE, Vol. 88, No. 12, December 2000, pp 1903-1946.

[2] Caimi F M, Kocak D M, Dalgleish F R and Watson J, *Underwater Imaging and Optics: Recent Advances*, Oceans 2008, 15-18 September 2008, pp 1-9.

[3] Jaffe J S, Moore K D, McLean J and Strand M P, *Underwater Optical Imaging: Status and Prospects, Oceanography*, Vol. 14, No.3, 2001, pp 64-75.

[4] Kocak D M, Dalgleish F R, Caimi F M and Schechner Y Y, *A Focus on Recent Developments and Trends in Underwater Imaging*, Marine Technology Society Journal, Vol. 42, No. 1, 2008, pp. 52-67.

[5] Costa B M, Battista T A, Pittman S J, *Comparative Evaluation of Airborne LIDAR and Ship-based Multibeam SoNAR Bathymetry and Intensity for Mapping Coral Reef Ecosystems*, Remote Sensing of Environment, Vol.113, 2009, pp. 1082-1100.

[6] Sutton J L, *Underwater Acoustic Imaging*, Proceedings of IEEE, Vol. 67, No. 4, April 1979, pp 564-566.

[7] *SM2000 Multibeam Imaging Sonar*, www.kongsberg-mesotech.com/pdf/ sonars/SM2000_200kHz_Sonar.pdf.

[8] Foote K G, Chu D and  Hammar T R, *Protocols for calibrating multibeam sonar*,  Journal of Acoustic Society of America, Vol. 117, No. 4, pp. 2013-2027, April 2005.

[9] Trees H L V, *Optimum Array Processing*, Detection, Estimation and Modulation Theory – Part IV, Wiley Interscience, ISBN 0-471-22110-4.

[10] Stefano Mosca S and Ciattaglia M, *Ant Colony Optimization Applied to Array Thinning*, Radar'08,  IEEE  Radar Conference, 26-30May 2008, pp. 1-3.

[11] Mosca M and Ciattaglia M, *Ant Colony Optimization Applied to Design Thinned Arrays*, Antennas and Propagation Society International Symposium 2006, 9-14 July 2006, pp. 4675 - 4678.

[12] Haupt R L, *Thinned arrays using genetic algorithms*, IEEE Transactions on Antennas and Propagation, Vol. 42, No. 7, July 1994, pp. 993–999.

[13] Sarajedini A, *Adaptive Array Thinning for Space-time Beamforming*, Conference Record of the Thirty-Third Asilomar Conference on Signals, Systems, and Computers, Vol. 2, 1999, pp. 1572-1576.

[14] Sherman C H and Butler J L, *Transducers and Arrays for Underwater Sound*, Springer, 2007, pp. 223.

[15] Chow L Y, On *Grating Plateaux of Non-uniformly spaced arrays*, IEEE Transactions of Antennas and Propogation, Vol. 13, Issue 2, pp. 208-215.

[16] Ishimaru A, *Theory of Unequally Spaced Arrays*, IRE Transactions on Antennas and Propogation, Nov 1962, pp. 691-702.

[17] Ishimaru A and Chen Y S, *Thinning and Broadbanding Antenna Arrays with Unequal Spacing*, IEEE Transactions on Antennas and Propagation, Vol. 13, Issue 1, pp.34-42.

[18] Panduro M A, Covarrubiasa D H, Brizuela C A and Marante F R, *A Multi-Objective Approach in the Linear Antenna Array Design*, International Journal of Electronics and Communications, Vol. 59, June 2005, pp. 205 – 212.

[19] Bray M G, Werner D H, Boeringer D W and Machuga D W, *Optimization of Thinned Aperiodic Arrays using Genetic Algorithms to Reduce Grating Lobes during Scanning*, IEEE Transactions on Antennas and Propagation, Vol. 50, No.12, December 2002.

[20] Palanisamy P, Kalayanasundaram N and Raghunathan A, *A New DOA Estimation for Wideband Signals in the Presence of Unknown Spatially Correlated Noise*, Signal Processing, Vol. 89, 2009, pp. 1921-1931.

[21] Sun-Yoon Y, *Direction of Arrival of Wideband Sources using Sensor Arrays*, Georgia Institute of Technology, PhD Thesis, July 2004.

[22] Repetto S, Palmese M, and Trucco A, *Design and Assessment of a Low-Cost 3-D Sonar Imaging System Based on a Sparse Array*, Proceedings of the IEEE Instrumentation and Measurement Technology Conference, IMTC 2006, 24-27 April 2006, pp. 410 – 415.

[23] Repetto S, Palmese M, and Trucco A, *High-resolution 3-D imaging by a sparse array: array optimization and image simulation*, Oceans 2005 - Europe, Vol. 2, 20-23 June 2005, pp. 763 – 768.

[24] Trucco A, Palmese M, and Repetto S, *Devising an Affordable Sonar System for Underwater 3-D Vision*, IEEE Transactions on Instrumentation and Measurement, Vol. 57, No. 10, October 2008, pp. 2348 – 2354.

[25] Lurton X, *Swath Bathymetry using Phase Difference: Theoretical Analysis of Acoustical Measurement Precision*, IEEE Journal of Oceanic Engineering, Vol. 25, No. 3, July 2000, pp. 351-363.

[26] Babb R J, *Feasibility of Interferometric Swath Bathymetry using Gloria, a long-range sidescan*, IEEE Journal of Oceanic Engineering, Vol. 14, No. 4, October 1989, pp. 299-305.

[27] Denbigh P N, *A Review of Rapid Depth Measuring Techniques and the Development of Bathymetric Side Scan Sonar*, Recent Developments in Side Scan Sonar Techniques, Edited W.G.A Russell-Cargill, 1982.

[28] Denbigh P N, *Stereoscopic Visualisation and Contour Mapping of the Seabed using a bathymetric sidescan sonar (BASS)*, Radio and Electronic Engineer, July-August 1983, Vol. 53, No. 7.8, pp. 301-307.

[29] Sintes C, Garello R and Gueriot D, *Interferometric Signal Denoised by Wavelets*, OCEANS 2006, September 2006, pp.1-6.

[30] Koyama H, Asada A, Ura T, Sakamaki T, Nose Y, Obara T and Nagahashi K, *Bathymetry by New Designed Interferometry Sonar Mounted on AUV*,

MTS/IEEE TECHNO-OCEAN '04, Vol. 2, 9-12 November 2004, pp.1160 – 1174.

[31] Denbigh P N, *Swath Bathymetry: Principles of Operation and an Analysis of Errors*, IEEE Journal of Oceanic Engineering, Vol. 14, No. 4, October 1989, pp. 289-298.

[32] Lesnikowski N S, *Deep Towed Interferometric Swath Bathymetry*, OCEANS '89 Proceedings, Volume 4, 18-21 September 1989 , pp.1130 – 1133.

[33] Lesnikowski N S, *A Decade of Isophase Swath Bathymetry*, OCEANS '99 MTS/IEEE. Riding the Crest into the 21st Century, Volume 2, 13-16 September 1999, pp. 901 – 903.

[34] Hunter A J, Hayes M P and Gough P T, *Simulation of Multiple-Receiver, Broadband Interferometric SAS Imagery*, OCEANS 2003 Proceedings, Volume: 5, pp. 2629- 2634.

[35] Wang L, Bellettini A, Hollett R, Tesei A, Pinto M, Chapman S and Gade K, *InSAS'00: Interferometric SAS and INS aided SAS imaging*, OCEANS 2001 MTS/IEEE Conference and Exhibition, Volume 1, 5th – 8th Nov 2001, pp.179 – 187.

[36] Chen J Y, Zhong X P and Feng X Z, *A Template Matching Method of Wideband Sonar Detection*, International Symposium on Instrumentation Science and Technology, Journal of Physics: Conference Series 48, 2006, pp. 54–58.

[37] Jing Z, Yuexian Z and Bo W, *Experimental Comparison of Cross Correlation-Based Time-Delay Algorithms for Acoustic Source Localization in Real Environment*, 3rd IEEE Conference on Industrial Electronics and Applications, ICIEA 2008, 3-5 June 2008, pp. 2517-2520.

[38] Kosalos J and Chayes D, *A Portable System for Ocean Bottom Imaging and Charting*, Proceedings of OCEANS '83, Vol. 15, August 1983, pp. 649-656.

[39] Winder A A, *Sonar System Technology*, IEEE Transactions on Sonics and Ultrasonics, Vol. SU-22, No. 5, September 1975, pp.291 -332.

[40] Coates R F W, *Underwater Acoustic Systems*, Macmillan New Electronic Series, 1990.

[41] Ehlers F, *Multi-Robot Teamwork in Multistatic Sonar*, International Conference on Emerging Security Technologies, 2010, pp.136-141.

[42] Waite A D, *SONAR for Practising Engineers*, Third Edition, John Wiley & Sons Ltd, 2002.

[43] Flemming B.W, *A Historical Introduction to Underwater Acoustics with Special Reference to Echo Sounding, Sub-Bottom Profiling and Side Scan Sonar, Recent Developments in Side Scan Sonar Techniques*, Edited W.G.A Russell-Cargill, 1982.

[44] Urick R J, *Principles of Underwater Sound for Engineers*, McGraw-Hill Book Company.

[45] Rossing T D, *Springer handbook of Acoustics*, Springer, 2007, pp. 157.

[46] Ratial P, Lai Y, and Makris M C, *Validity of the sonar equation and Babinet's principle for scattering in a stratified medium*, Journal of Acoustical Society of America, Vol. 112, No.5, November 2002, pp. 1797-1816.

[47] Papandreou-Suppappola A, and Suppappola S B, *Sonar Echo Ranging Using Signals With Nonlinear Time–Frequency Characteristics*, IEEE Signal Processing Letters, Vol. 11, No. 3, March 2004, pp. 393-396.

[48] Gonzalez J E, Pardo J M, Asensio A and Burgos M, *Digital Signal Generation for LFM-LPI Radars*, Electronics Letters, Vol. 39, No. 5, March 2003, pp. 464-465.

[49] Mahafza B R, *Radar System Analysis and Design using MATLAB*, Second Edition, Chapman and Hall/CRC, 2005.

[50] Lurton X, *An introduction to Underwater Acoustics*, Springer 2002.

[51] Collins T and Atkins P, *Nonlinear Frequency Modulation Chirps for Active Sonar, IEE Proceedings on Radar, Sonar and Navigation*, Vol. 146, Issue 6, December 1998, pp.312 – 316.

[52] Cook C E and Bernfield M, *Radar Signals An Introduction and Theory to Applications*, Academic Press, 1967.

[53] Levanon N and Mozeson E, *Radar Signals*, Wiley-Interscience, John Wiley and Sons Publications.

[54] Skolnik M L, *Introduction to Radar Systems*, Second Edition, McGraw Hill International Editions, 1981.

[55] Klein M, *A Modular Sonar System for Seabed Mapping*, Recent Developments in Side Scan Sonar Techniques, Edited W.G.A Russell-Cargill, 1982.

[56] Lawler M A, *A Real Time Parallel Processing System for Synthetic Aperture Sonar*, PhD Thesis, University of Newcastle, 1997.

[57] Marx D, Nelson M, Chang E, Gillespie W, Putney A, Warman K, *An Introduction to Synthetic Aperture Sonar*, Proceedings of the Tenth IEEE Workshop on Statistical Signal and Array Processing 2000, 14-16 August 2000, pp.717-721.

[58] Riyait V S, Lawlor M A, Adams A E, Hinton O R, Sharif B S, *Comparison of the Mapping Resolution of the ACID Synthetic Aperture Sonar with Existing Sidescan Sonar Systems*, OCEANS '94 'Oceans Engineering for Today's Technology and Tomorrow's Preservation' Proceedings, Vol. 3, 13-16 September 1994, pp.III/559 - III/564.

[59] Gough P T, *A Synthetic Aperture Sonar System Capable of Operating at High Speed and in Turbulent Media*, IEEE Journal Of Oceanic Engineering, Vol. OE-11, No. 2, April 1986, pp. 333-339.

[60] Douglas B L and Lee H, *Synthetic aperture active sonar imaging*, 1992 IEEE International Conference on Acoustics, Speech, and Signal Processing 1992 ICASSP-92, Vol. 3, 23-26 March 1992, pp. 37 – 40.

[61] Williams R E, *Creating an Acoustic Synthetic Aperture in the Ocean*, Journal of the Acoustical Society of America, Volume 60, Issue 1, July 1976, pp. 60-73.

[62] Brokloff N A, *Matrix algorithm for Doppler Sonar Navigation*, OCEANS '94, Oceans Engineering for Today's Technology and Tomorrow's Preservation, Proceedings, Vol.3, 13-16 Sep 1994, pp. III/378-III/383.

[63] Thompson R L and Zehner W J, *Frequency Steered Acoustic Beamforming and Process*, United States Patent, Patent No. 5,923,617, 13th July 1999.

[64] Thompson R L, Seawall J and Josserand T, *Two Dimensional and Three Dimensional Imaging Results using Blazed Arrays*, OCEANS 2001 MTS/IEEE.

[65] www.blueviewtech.com

[66] Dunham S J, Handal J T, Peterson T and O'Brien M, *High resolution bathymetric survey system*, MTTS/IEEE Techno-OCEAN '04, November 9-12 2004,Vol.2, pp.1139-1146.

[67] Stergiopoulos S, *Advanced Signal Processing Handbook – Theory and Implementation for Radar, Sonar and Medical Imaging Real-Time Systems*, CRC Press.

[68] Veen B D V and Buckley K M, *Beamforming: A Versatile Approach to Spatial Filtering*, IEEE Acoustic Speech and Signal Processing Magazine, Vol.5, No.2, April 1988, pp. 4-24.

[69] Ries S and Kaiser T, *Towards Beamforming for UWB Signals*, EUSIPCO '04, September 6-10 2004, pp. 829-832.

[70] Krim H and Viberg M, *Two Decades of Array Signal Processing*, IEEE Signal Processing Magazine, Vol.13, No.4, July 1996, pp.67-94.

[71] Rmhovde A, Yang L, TorfinnTaxt, and Holm S, *High-resolution beamforming for multibeam echo sounders using raw EM3000 data*, OCEANS '99 MTS/IEEE, Vol. 2, pp. 923-930.

[72] Kraeutner P H and Bird J S, *Beyond interferometry Resolving multiple angles-of-arrival in swath bathymetric imaging*, OCEANS '99 MTS/IEEE, 13th – 16th September 1999, Vol. 1,pp. 37-45.

[73] Johnson D H, *The Application of Spectral Estimation Methods to Bearing Estimation Problems*, Proceedings of IEEE, Vol. 70, No.9,September 1982, pp. 1018-1028.

[74] Nielsen R O, *Sonar Signal Processing*, Artech House.

[75] Proakis J G, Rader C M, Ling F, Nikias C L, Moonen M and Proudler I K, *Algorithms for Statistical signal Processing*, Prentice Hall, 2002.

[76] Schmidt R O, *Multiple Emitter Location and Signal Parameter Estimation*, IEEE Transactions on Antennas and Propagation, Vol. AP -34, No.3, March 1986, pp. 276-280.

[77] Balanis C A and Ioannides P I, *Introduction to Smart Antennas*, Synthesis Lectures on Antenna #5, Morgan and Claypool Publishers, 2007.

[78] Caiti A, Bergem O and Dybedal J, *Parametric Sonars for Seafloor Characterization*, Measasurement Science and Technology, Vol. 10, 1999, pp. 1105–1115.

[79] Moron P and Pihl J, *Sub-bottom Characterisation using a Parametric Sonar*, OCEANS '98 Conference Proceedings, 28th September-1st October 1998, Vol. 3, pp.1828-1832.

[80] Zheng M, Wang L, Stoner R and Coates R.F.W, *Underwater Digital Communication Utilising Parametric Sonar with M-ary DPSK Modulation*, IEE Proceedings Radar, Sonar and Navigation, Vol. 146, No. 4, August 1999, pp.213-218.

[81] Konrad W L and Carlton L F, *Design and Application of High Power Parametric Sonars*, OCEANS, September 1973, Vol. 5, pp. 310-315.

[82] Woodward B, Cook J C, Goodson A D and Lepper P A, *A Phase Steered Parametric Array for Sub-Bottom Profiling*, Electronic Engineering in Oceanography, 19-21 July 1994, Conference Publication No 394, IEE 1994.

[83] Moren P and Pihl J, *Sub-bottom Characterisation using a Parametric Sonar,* OCEANS '98 Conference Proceedings, Vol.3, 1998, pp. 1828-1832.

[84] Kritz J, *Parametric Array Doppler Sonar*, IEEE Journal of Oceanic Engineering, April 1977, Vol.2, Issue.2, pp. 190-200.

[85] Ghavami M, *Wideband Beamforming using Rectangular Arrays without Phase Shifting*, Euroropean Transactions on Telecommunications, December 2003, Vol. 14, Issue 5, pp. 449–456.

[86] Ksendzuk A V, Volosyuk V K and Sologub N S, *Advantages of the Wideband and Ultrawideband Signals in the Remote Sensing Systems*, Second International Workshop on Ultrawideband and Ultrashort Impulse Signals, 19-22 September, 2004, pp. 240-242.

[87] Steinberg B D, *Principles of Aperture and Array System Design*, John Wiley and Sons, 1976.

[88] Mitra S K, *Digital Signal Processing A Computer Based Approach*, Second Edition, Tata Mcgraw Hill.

[89] Gonzalez R C and Woods R E, *Digital Image Processing*, Fifth Indian Reprint 2000, Addison Wesley.

[90] Hyvärinen A and Oja E, *Independent Component Analysis: Algorithms and Applications*, Neural Networks, 13(4-5), pp. 411-430, 2000.

[91] Stojanovic M, *On the relationship between capacity and distance in an underwater acoustic channel*, Proc. First ACM International Workshop on Underwater Networks (WUWNeT'06)/MobiCom 2006, Los Angeles, CA, September 2006.

[92] Domingo M C, *Overview of channel models for underwater wireless communication networks*, Physical Communication, No. 1, 2008).pp.163-182.

[93] Wang Z and Bovik A C, *Modern Image Quality Assessment*, San Rafael, CA: Morgan and Claypool 2006.

[94] Sheikh H R, Bovik, A C and Veciana G D, *An Information Fidelity Criterion for Image Quality Assessment Using Natural Scene Statistics*, IEEE Transactions on Image Processing, Vol. 14, No. 12, December 2005.

[95] Damera-Venkata N, Kite T D, Evans B L and Bovik A C, *Image Quality Assessment based on a Degradation Model*, IEEE Transactions on Image Processing, Vol 9, No 4, pp. 636-650, April 2000.

[96] Thu Q U and Ghanbari M, *Scope of Validity of PSNR in Image/Video Quality Assessment*, Electronic Letters, Vol. 44, No. 13, 19th June 2008, pp.800-801.

[97] Welstead S T, *Fractal and Wavelet Image Compression Techniques*, SPIE-The International Society for Optical Engineering, 1999.

[98] Winkler S, *Digital Video Quality Vision and Metrics*, John Wiley and Sons, 2005.

[99] Dosselmann R and Yang X D, *An Empirical Assessment of the Structural Similarity Index*, Canadian Conference on Electrical and Computer Engineering 2009, CCECE '09, pp.112-116.

[100] Wang Z, Bovik A C, H. R. Sheikh and E. P. Simoncelli, *Image Quality Assessment: From Error Visibility to Structural Similarity*, IEEE Transactions on Image Processing, Vol. 13, No. 4, pp. 600-612, April 2004.

[101] Wang Z and Bovik A C, *A Universal Image Quality Index*, IEEE Signal Processing Letters, Vol. 9, pp. 81–84, March 2002.

[102] Kumar A A, *Fundamentals of Digital Circuits*, Prentice Hall of India Private Ltd, 2006.

[103] Hung T P, Rode J, Larson L E and Asbeck P M, *Design of H-Bridge Class D Power Amplifiers for Digital Pulse Modulation Transmitters*, IEEE Transaction for Microwave Theory and Techniques, Vol. 55, No. 12 December 2007, pp.2845-2855.

[104] Eccles W J, *Pragmatic Circuits: Signals and Filters*, Morgan and Claypool Publishers, 2006.

# Appendix A

## A.1    Code showing the formation of $r\theta$ matrix

```matlab
function [FIMG] = Proc_First(nRC,Arrsp,S_Freq,Overlap,R_sig,B)


  %nRC          - Number of samples in range cell
  %Arrap        - Array Spacing
  %S_Freq       - Sampling Frequency
  %R_Sig        - Received Signal
  %B            - Bandwidth

  global C PI;                                 %C-Speed of Sound
  c = fir1(16,B*2/S_Freq);
  len_f = (length(c)+1)/2;



  A11  = R_sig(:,1);
  A12  = R_sig(:,2);

  LEN  = length(A11);

  IMG  = [];
  RCELL = nRC;
  OVERLAP = floor(RCELL-RCELL*Overlap/100);

  nd_max    = Arrsp*cos(PI/4)*S_Freq/C;        %nd_max - Maximum
                                               %number of range cells
                                                %samples to be
                                                %considered


  for i = 1:OVERLAP:LEN

    a11 = (A11(i:i+RCELL-1));                   %Division into range
    a12 = (A12(i:i+RCELL-1));                   %cells


    cor = abs(xcorr(a11,a12));                 % Correlation between
                                               %range cells


    cor = conv(c,cor);
    cor = cor(len_f:end)';
    IMG = [IMG;cor];

  end;

  IMG1   = zeros(size(IMG));

  IMG1( : ,RCELL-round(n_dmax):RCELL+round(n_dmax)) = IMG( : ,RCELL-
                                round(n_dmax):RCELL+round(n_dmax));


  FIMG   = IMG1;
```

## A.2 Code for image formation

```matlab
function [GH] = IMGE_First(FIMG,Arrsp,xr,nRC,S_Freq,Overlap)


    global C PI;
    RCELL = nRC;
    RCELL1= xr;

    nd_max = Arrsp*cos(PI/4)*S_Freq/C;

        IMG   = FIMG(:,Rcell-round(nd_max):Rcell+round(nd_max));

        s  = size(IMG);

    clear G;

    G = zeros(300,300);
    r = size(G);
    center = ceil((r(1)+1)*0.5);
    M = 1;
    I = (1-Overlap/100)*RCELL1/2;

    for i = 1:s(1)
      N = 1;
      for j = -floor(nd_max):floor(nd_max)

        K = j*C/S_Freq;                          % K - delay distance

         if(K<0)
           an = pi/2-asin((abs(K))/Arrspa);
           X = I*cos(an);
           Y = ceil(I*sin(an));
           Pos = round((center - X));
           G(Y,Pos) = (G(Y,Pos)+IMG(M,N));
          else
            an= pi/2-asin((abs(K))/Arrspa);
           X = I*cos(an);
           Y = ceil(I*sin(an));
           Pos = round(center + X);
           G(Y,Pos) = (G(Y,Pos)+IMG(M,N));
         end;
         N = N+1;
       end;
       I = I + (1-Overlap/100)*RCELL1/2;           % Range calculation

       M = M+1;
    end;
    GH = G(:,:);
```

## A.3    Code for non-linear combining

```matlab
function [img1] = Thr1_First(IMGG)


% IMGG        - 3D Matrix containing all the r-theta matrices
% img1        - final combined matrix
% S           - Number of r-theta matrices
% S1          - Number of range cells
% Temp        - Threshold

S = size(IMGG,3);
S1= size(IMGG,1);
img1 = [];

for i = 1:S1

   Temp = ME_AN(IMGG(i,:,:));
   tt   = Comb_First(IMGG(i,:,:),Temp);
   img1 = [img1; tt];

end;

img1    = img1/S;




function M = ME_AN(IMGG)
% Function to determine the Threshold

S1 = size(IMGG,3);
M  = 0;

% Loop for determining initial Threshold
for i = 1:S1

   d    = find(IMGG(:,:,i)~=0);
   temp = IMGG(:,min(d):max(d),i);
   M    = mean(temp)+M;

end;

M = M/S1;

STd = 0;

% Loop for determining Modified Threshold
for i = 1:S1

    d = find(IMGG(:,:,i)~=0);
    temp = IMGG(:,min(d):max(d),i)-M;
    temp(find(temp<0)) = 0;
    STd = STd + std(temp);

end;

M = M+STd/S1;   % Modified Threshold
```

```matlab
function [img1] = Comb_First(IMGG,Temp)
% Function to combine the r-theta matrices

S  = size(IMGG,3);
S1 = size(IMGG,1);

T1 = zeros(size(IMGG,1),size(IMGG,2));
IM = [];


  for j = 1:S1
    T1   = IMGG(j,:,1);          %Taking one range cell
                                 % of first r-theta  matrix
    for i = 2:S
      T1 = imgAnd(T1,IMGG(j,:,i),Temp);
    end;
    IM = [IM; T1];
  end;


function [TT] = imgAnd(A,B,Temp)

 % Function to perform AND operation

TT1 = (A>Temp)&(B>Temp);

A(~TT1) = 0;
B(~TT1) = 0;

TT      = (A+B);
```